Lipid Modulation of Ligand-Gated Ion channels

Anna Ananchenko

Thesis submitted to the University of Ottawa
in partial fulfillment of the requirements
for the Doctorate in Philosophy in Biochemistry

Department of Biochemistry, Microbiology and Immunology
Faculty of Medicine
University of Ottawa

Abstract

Ligand-gated ion channels (LGICs) are a diverse family of membrane proteins which play a key role in neuronal communication. The neuronal lipid membrane in which LGICs are embedded is a complex and dynamic environment which, over decades of LGIC research, has been shown to influence the function of these proteins. The specific lipid requirements and functional effects of membrane lipids differ by LGIC type. The presence of polyunsaturated fatty acids (PUFAs) modulates the pH response of acid-sensing ion channels (ASICs), and in the case of subtype ASIC3, can even activate the channels at physiological pH. Another type of LGIC, the nicotinic acetylcholine receptor (nAChR), requires the presence of anionic lipids and/or cholesterol for function. It has been proposed that lipids exert their function on LGICs through direct interactions at lipid binding sites. To date, however, these binding sites are poorly described, and their existence remains uncertain. High resolution cryo-EM structures of ASICs and nAChRs have been solved in recent years showing density attributed to bound lipids. Using multiscale molecular dynamics (MD simulations), I embed high-resolution structures of ASIC and the nAChR in membrane patches of interest to observe the dynamics of specific lipid interactions with these channels. My simulations suggest prolonged, direct interactions of functionally relevant lipids with the transmembrane domains (TMDs) of ASICs and nAChRs. Key arginine residues at the outer leaflet region of ASIC TMDs coordinate high-occupancy PUFA interactions which can be disrupted by *in-silico* mutagenesis. Similarly, the activity-promoting lipids phosphatidic acid (PA) and cholesterol bind to specific sites with longer duration than the lipid phosphatidylcholine (PC), which does not promote activity. The relative binding free energy of PA and PC was calculated using free energy perturbation at a conserved nAChR inner leaflet site, estimating a 1.5 kcal/mol difference between the two lipids, revealing slight preferential binding for PA. Together these

findings suggest that activity-promoting lipids species bind to specific lipid binding sites which higher affinity than bulk membrane lipids, and these interactions could stabilize active or activatable states of LGICs.

Acknowledgements

I would first and foremost like to express my gratitude to my supervisors. To Dr. Musgaard with whom I started my PhD, thank you for supporting my curiosity and shaping my passion for science. To Dr. Baenziger, thank you for taking the chance of accepting me into your lab to continue my PhD and providing me with immeasurable guidance and opportunities to pursue computational biophysics. To Dr. Dehez, thank you for your constant encouragement and mentorship.

I would like to thank my TAC committee, Dr. Corrie DaCosta and Dr. Steffany Bennett who consistently provided me with feedback and guidance and played a significant role in the completion of this thesis. I also thank my scientific mentors Dr. Benoit Roux and Dr. Christophe Chipot with whom I have had countless exciting scientific discussions and who challenged and encouraged me to expand my MD simulation skills.

Thank you to the various colleagues with whom I have had the pleasure of working during my PhD. From the Musgaard lab, Mariam, Megan and Becca. From the Baenziger lab, Toka, Deepansh, Mack, Camille, Serena and Rui Yan. Thank you also to all my colleagues at Laboratoire de Physique et Chimie Théoriques (LPCT), especially Flo, for her collaboration and insight in a particularly challenging project. I had the pleasure of mentoring two hard working undergraduate students, Jamal and Rui Yan, who both were able to add valuable insight to our shared projects.

My PhD was supported financially by uOttawa, NSERC and CIHR. Westgrid, Compute Canada and LPCT provided computational resources for these projects.

Preface

Over the course of my PhD, I used MD simulations extensively to study lipid interactions with LGICs as well as the structural dynamics of LGIC functional states. In addition to the manuscripts presented below, the first paper that I published as a co-first author in 2021 describes the motions of a wild type and mutant β11-β12 linker in ASICs, which plays an important role in the channel's recovery from desensitization. I am also a co-author on two papers relating to structural studies of the nAChR. In the first, I performed MD simulations of wild type and mutant M2-M3 nAChR linkers to study allosteric communication between the extracellular and transmembrane domains, and in the second, I used MD simulations to study the pore dynamics and hydration of nAChR unliganded, diliganded and primed states. In this thesis, I chose to focus on my work relating to lipid-LGIC interactions. I therefore present my data in the form of the three manuscripts below:

Manuscript 1: Ananchenko, A., Musgaard, M. (2023) Multiscale molecular dynamics simulations predict arachidonic acid binding sites in human ASIC1a and ASIC3 transmembrane domains. J. Gen. Physiol. 155 (3): e202213259

doi: 10.1085/jgp.202213259

Manuscript 2: Ananchenko, A., Gao, R.Y., Dehez, F., Baenziger, J.E. (2024) State-dependent binding of cholesterol and an anionic lipid to the muscle-type *Torpedo* nicotinic acetylcholine receptor. Commun. Biol. 7(1):437

doi: 10.1038/s42003-024-06106-8

Manuscript 3: Ananchenko, A., Szczepaniak, F., Roux, B., Baenziger, J.E., Dehez, F. (2025)

Differences in lipid affinity and binding dynamics at conserved nAChR lipid binding sites. *To be submitted*

Table of Contents

List of Figures

List of Tables

List of Movies

2.1 hASIC3 interactions with AA in CG simulation. AA molecules within 5 Å of the hASIC3 protein are shown. The protein is shown in cyan. The residues $R65_{hASIC3}$, $R68_{hASIC3}$, and $R63_{hASIC3}$ are shown as purple VDW spheres. Interactions over 1 μs of simulation time (from 4–5 μs) are shown in one CG simulation repeat of hASIC3 in the open state. The movie illustrates approximately 0.75 ns/frame; played at a speed of ~1 μs/min.

2.2 Example of a stable salt bridge interaction of the AA carboxylic acid headgroup with the sidechain of R65hASIC3, as well as interactions with Y58hASIC3. The ASIC protein is shown as cyan cartoon with interacting residues shown as cyan sticks. AA is shown as orange sticks. Interactions for a 200 ns section of a simulation with a total length of 500 ns are shown. The movie illustrates approximately 0.1 ns/frame, played at a speed of ~200 ns/min.

2.3 Example of a stable salt bridge interaction of the AA carboxylic acid headgroup with the sidechain of R68hASIC3, with simultaneous interactions with R65hASIC3and also interactions with Y58hASIC3. The ASIC protein is shown as cyan cartoon with interacting residues shown as cyan sticks. AA is shown as orange sticks. Interactions for a 200 ns section of a simulation with a total length of 500 ns are shown. The movie illustrates approximately 0.1 ns/frame, played at a speed of ~200 ns/min.

3.1 Supplementary Movie 1. Movie starts at 2.6 μs into a CG simulation repeat of the nAChR apo state in a 3:2 PC:Chol membrane and continues to 30 μs. Each frame duration is 2 ns with a frame rate of 60 fps. Chol is shown as green VDW beads with the bead corresponding to the

hydroxyl group in red. The α and γ subunits are shown in pastel cyan and pink respectively, with the S235 bead shown in darker magenta. Subunits are shown as VDW beads with bonds as sticks

3.2 Supplementary Movie 2. The movie shows a 250 ns simulation of the apo nAChR in a 3:2 PC:Chol membrane. Each frame duration is 0.1 ns with a frame rate of 60 frames per second. Chol is shown as green sticks with the hydroxyl oxygen shown in red. The β and α subunits are shown as yellow and cyan cartoon respectively, with residues within 5 Å of the Chol molecules appearing as sticks.

List of Abbreviations

5HT	5-hydroxytryptamine (serotonin)
5-HT3R	Serotonin receptor
AA	arachidonic acid
AMBER	Assisted Model Building with Energy Refinement
AMPA	α-amino-3-hydroxy-5-methyl-4-isoxazolepropionic acid
ASIC	acid-sending ion channel
cASIC	chicken acid-sensing ion channel
CG	coarse-grained
CG2AT	coarse-grained to atomistic
CHARMM	Chemistry at Harvard macromolecular mechanics
Chol	cholesterol
CHS	cholesteryl hemisuccinate
CRAC	Cholesterol recognition amino acid consensus
cryo-EM	cryogenic electron microscpoy
DEG	degenerin channels
DHA	docosahexaenoic acid
EC_{50}	half maximum effective concentration
ECD	extracellular domain
ELIC	erwinia ligand-gated ion channel
ENaC	epithelial sodium channel
FEP	free energy perturbation
$GABA_AR$	γ-aminobutyric acid type A receptor
GAS	glycine-alanine-serine
GLIC	Gloeobacter violaceus ligand-gated ion channel
GROMACS	Groningen machine for chemical simulations
GUI	guided user interface
hASIC	human acid-sensing ion channel
HCN	Hyperpolarization-activated cyclic nucleotide-gated channels
Imax	maximum current
ICD	intracellular domain
K+	potassium ion
Kir	inward rectifying potassium channel
KV	voltage-gated potassium channel
Ld	liquid disordered
Lo	liquid ordered
LGIC	ligand-gated ion channel
LINCS	linear contraint solver

LPC	lysophosphatidylcholine
MD	molecular dynamics
MSP2N2	Membrane scaffold protein 2N2
mV	millivolt
Na+	sodium ion
nAChR	nicotinic acetylcholine receptor
NAMD	nanoscale molecular dynamics
NMDA	N-methyl-D-aspartate
NMR	nuclear magnetic resonance
NPT	isothermal-isobaric ensemble
ns	nanosecond
PA	phosphatidic acid
PC	phosphatidylcholine
PDB	protein data bank
PE	phosphatidylethanolamine
pH	potential of hydrogen
PG	phosphatidylglycerol
PIP2	Phosphatidylinositol 4,5-bisphosphate
pLGIC	pentameric ligand-gated ion channel
PME	particle mesh ewald
POPA	1-palmitoyl-2-oleoyl-sn-glycero-3-phosphatidic acid
POPC	1-palmitoyl-2-oleoyl-sn-glycero-3-phosphocholine
POPE	1-palmitoyl-2-oleoyl-sn-glycero-3-phosphoethanolamine
ps	picosecond
PS	phosphatidylserine
PUFA	polyunsaturated fatty acid
RESPA	reference system propagator algorithm
SAFEP	streamlined alchemical free energy perturbation
SDPC	1-stearoyl-2-docosahexaenoyl-sn-glycero-3-phosphocholine
TIP3P	transferable intermolecular potential 3P
TM	transmembrane
TM1	transmembrane helix 1
TM2	transmembrane helix 2
TMD	transmembrane domain
VDW	van der Waals
VMD	visual molecular dynamics
WT	wild type

Chapter 1. Introduction

1.1 Signal transduction in the nervous system

Neurons are the structural units of the nervous system. These massive cells consist of a central cellbody which contains the nucleus, and a long axon which conducts impulses along the neuron. Radiating from the cell body and axon are branchlike structures, dendrites and axon termini, which facilitate communication with other neurons.

At rest, the cytosol of a neuron is negatively charged relative to the extracellular region. This creates a voltage across the neuronal membrane of approximately -70 mV, known as the resting membrane potential. This is primarily caused by a difference in the ionic composition of the cell cytosol and extracellular fluid, and the difference in permeability of the cell membrane to different species of ions contained in these fluids.

A change is this membrane potential acts as a communication signal in the neuron. Typically, depolarization, where the membrane potential becomes less negative, produces nerve impulses. Hyperpolarization on the other hand, when the membrane potential becomes more negative, decreases the chances of nerve impulses.

Neurons are connected by synapses, which mediate communication transfer from one neuron to another. The arrival of an electrical signal at the axon terminal causes the release of neurotransmitter from synaptic vesicles in the presynaptic neuron, which diffuse across the synaptic cleft and bind to neurotransmitter-specific receptors on the postsynaptic neuron surface (Figure 1.1). These receptors, or ion channels, open, and allow for ions to move across the membrane and thereby change the local membrane potential in the postsynaptic neuron.

Figure 1.1. Neuronal Synapse. Left: Two motor neurons. Middle inset: close-up view of a neuronal synapse. Neurotransmitter is depicted as red spheres. Several ion channels in different states are shown embedded in the presynaptic and postsynaptic membrane. Right inset: Close up view of ion channel in the open state with bound neurotransmitter. Ion channel is embedded in a phospholipid bilayer and conducts sodium, shown in purple spheres.

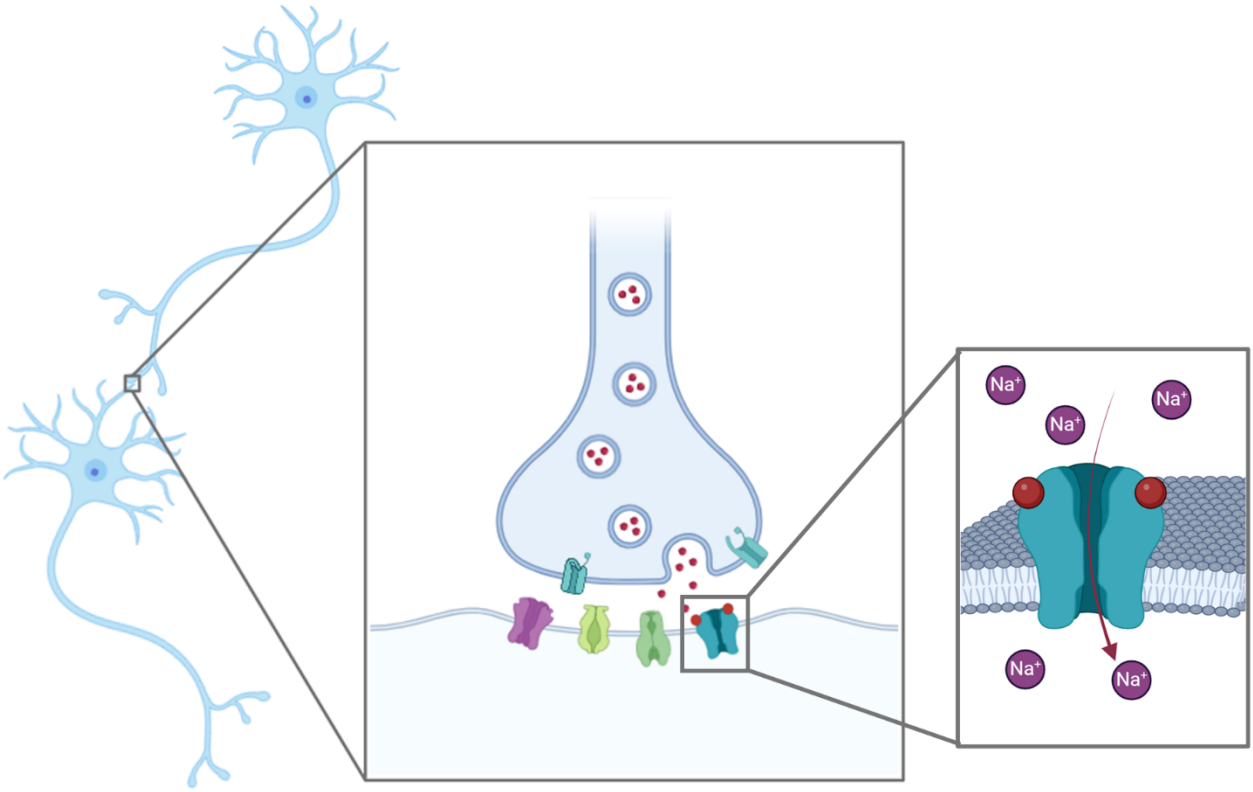
Na+
Na+
Na+
Na+
Na+

Synaptic communication is tightly regulated by enhancing or inhibiting neurotransmitter release or destruction, and through control of ion channel function. Even minor dysfunction of these systems leads to serious nervous system pathologies.

1.2 Neuronal lipid composition

Cells are encapsulated by lipid membranes, which are made from spontaneously forming bilayers of amphipathic lipids. The apolar components of lipids aggregate together towards the bilayer center with the polar lipid headgroup components contacting the intracellular and extracellular fluids (Figure 1.2). This creates a semi-permeable bilayer. Cell membranes are constituted of phospholipids, glycolipids, and cholesterol (Chol), with phospholipids forming most of the lipid composition. Specific plasma membrane lipid composition in mammals differs by species, cell type, and other biological factors such as age, disease and diet. Because of this complexity, the exact lipidome of different membrane types, including neuronal membranes, and under different physiological conditions, is poorly characterized.

The neuronal membrane composition (Bozek et al., 2015; Ingólfsson et al., 2017) differs from other mammalian plasma membranes in its thickness, fluidity and lipid content, which further differs between nervous system regions. Neuronal membranes are enriched in ceramides and cholesterol, the latter constitutes as much as 35% of these membranes (Fitzner et al., 2020). The zwitterionic lipid types, phosphatidylinositol (PE) and phosphatidylcholine (PC), are the primary phospholipid constituents of neuronal plasma membranes (Bozek et al., 2015; Cotman et al., 1969; Fitzner et al., 2020). Other phospholipid types, such as the negatively charged phosphatidic acid (PA) and phosphatidylserine (PS), are found in much smaller molar ratios in neuronal membranes. Neuronal membranes also tend to be thicker than other mammalian plasma membranes due to a

high proportion of phospholipids containing longer polyunsaturated fatty acyl chains relative to those in other plasma membranes. Specifically, they have a higher relative proportion of 20-24 carbon fatty acyl chains compared to 16-18 carbon fatty acyl chains, the latter being more abundant in the plasma membranes of other mammalian cells (Stillwell, 2016). Polyunsaturated fatty acids (PUFAs), such as docosahexaenoic acid (DHA), eicosapentaenoic acid and arachidonic acid (AA) are also present in trace amounts and play an important role in cell signaling and synaptic function (Di Miceli et al., 2020). PUFAs are released from phospholipids by phospholipase A2, the function of which is regulated by physiological processes such as inflammation and neurotransmission, thereby altering the availability of free PUFAs in the brain. PUFAs, in turn, may affect neuronal function by altering the function of ion channels or membrane fluidity, or be further used to synthesize oxylipins which participate in cell signalling pathways involved in inflammation, neurotransmission modulation, and immune modulation.

Figure 1.2. Membrane lipid bilayer. A. Chemical structures of neuronal plasma membrane constituents. B. Simplified schematic of ion channels embedded in a plasma membrane. Bulk phospholipids are shown in gray. Chol, PUFAs and charged lipid species are shown in orange. Schematic representations of ion channels are shown in turquoise and purple in the membrane. Purple circles represent Na+ and green triangles represent K+.

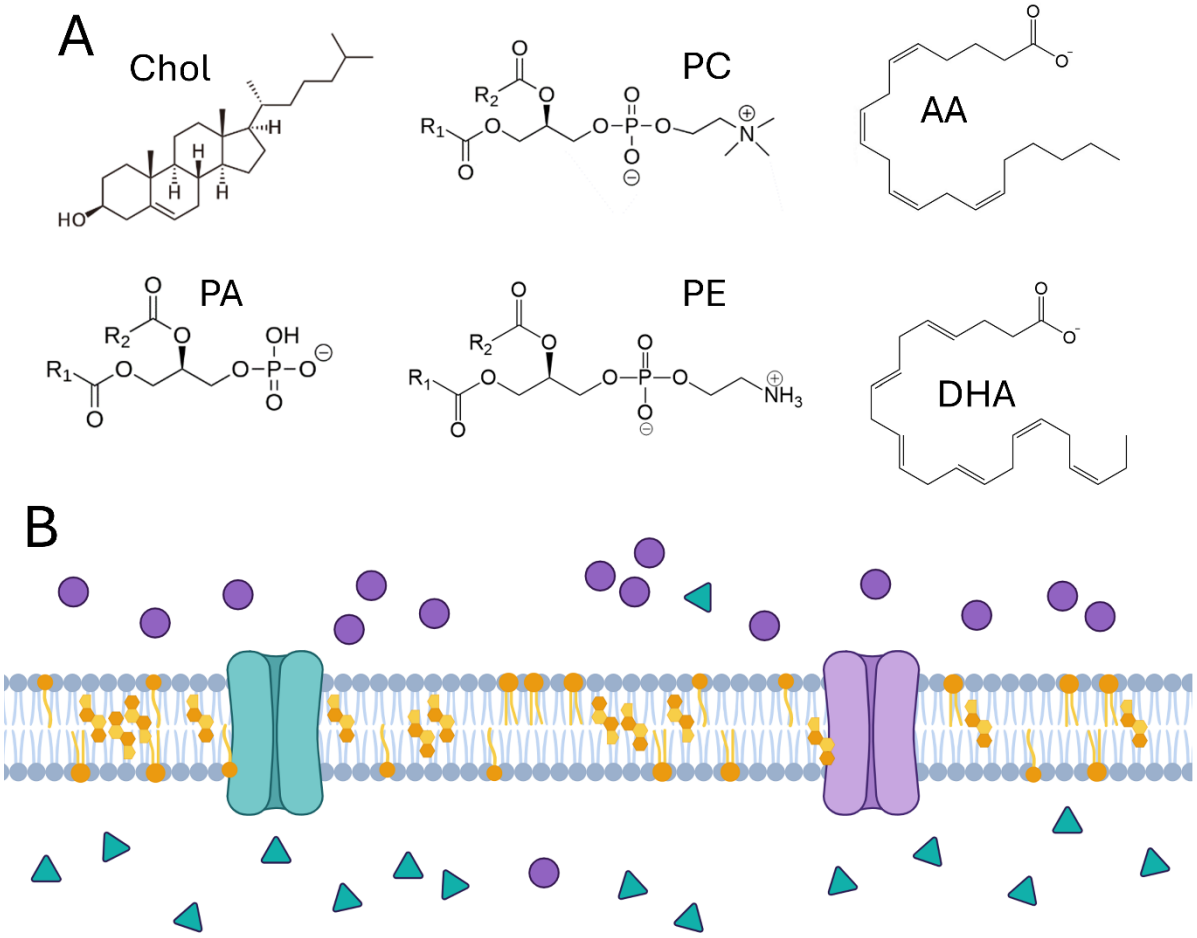
A
Chol
PC
AA
PA
PE
DHA
B

Lipid membranes are fluid, dynamic structures, containing a multitude of membrane proteins, which participate in transport of molecules in and out of the cell, communication, and maintaining cell structure. The lipid bilayer is not of uniform composition or fluidity, rather, it is a heterogenous mix of components, with some lipids such as cholesterol being able to self-associate and form structures called lipid rafts (Lingwood et al., 2009; Simons & Ikonen, 1997). Heterogenous mixing of lipids creates regions of differing fluidity, or lipid phases in the membrane. Liquid ordered (L_o) and liquid disordered (L_d) phases are regions of less fluid and more fluid lipid environments, respectively (Honerkamp-Smith et al., 2008). Lipid rafts and lipid phases may play an important role in protein sorting and trafficking (Schütte et al., 2017), including ion channels.

The neuronal plasma membrane is a dynamic environment, with changes to the composition or mixing of lipids influencing neuronal function. It is not surprising that changes in membrane composition are correlated with neurological disease (Ledesma et al., 2012; Martin et al., 2010).

1.3 Ligand-gated ion channels

Ion channels are a broad class of proteins making up 18% of all current small molecule drug targets (Santos et al., 2016) with an estimated $12 billion USD in sales (Wickenden et al., 2012). They are membrane proteins that open in response to neurotransmitter binding to mediate fast synaptic transmission. In general, ion channels are comprised of several protein subunits arranged around a central pore. The ion channel pore, through constriction size and ion coordination, is selective to the charge and size of ions it conducts.

Ion channels respond to a variety of stimuli, including voltage, mechanical stress, or chemical ligands. The latter class are known as ligand-gated ion channels (LGICs). In the absence of agonist and at resting membrane potential, LGICs adopt a structure with a closed pore, known as the apo or resting state. Upon agonist binding, they undergo a structural rearrangement to the open state

allowing ions to pass down their electrochemical gradient either into or out of the cell (Figure 1.1) thus altering the relative concentrations of ions in the cytosol and extracellular fluid to change the transmembrane potential. The process of ion channel opening in response to a stimulus is known as gating. Upon prolonged agonist binding, LGICs adopt a desensitized state, whereby the pore is closed while agonist affinity remains high. This terminates the membrane depolarization caused by the stimulus, preventing additional ion flux while ion pumps recover the resting membrane potential.

Electrophysiology experiments are used to measure agonist-induced ion currents *in vitro*. Whole-cell ion currents are described by the I_{max} value, which is the maximum ion current produced, and the EC_{50}, which is the agonist concentration needed to produce half of the maximum current. The relative proportions of the resting, open and desensitized states and the rate of transitions between them determine the temporal nature of ion current produced in a cell. While these three states underlie general ion channel function, LGICs can adopt several other physiologically relevant states. Intermediate (Carignano et al., 2016), primed (Tessier et al., 2022), and uncoupled (daCosta & Baenziger, 2009) states have been described.

LGICs include pentameric, tetrameric and trimeric ion channel families. Tetrameric ligand-gated ion channels are comprised of four protein subunits and include ionotropic glutamate receptors further characterized as NMDA, AMPA and kainite receptors. The focus of this thesis is on the function of trimeric and pentameric ligand-gated ion channels, which are further discussed below.

Trimeric ligand-gated ion channels: acid-sensing ion channels

The trimeric ligand-gated ion channel family includes P2X receptors, epithelial sodium channels (ENaC), degenerin channels (DEG) and acid-sensing ion channels (ASICs), which vary widely in

their physiological function and activation mechanism. This family is characterized by a trimeric subunit arrangement, with each subunit containing a large extracellular domain (ECD), two transmembrane (TM) helices forming the pore, and a re-entrant intracellular domain (ICD).

ASICs are found in the central and peripheral nervous system and are particularly important in inflammatory pain pathways. They also participate in fear conditioning (Chiang et al., 2015), pain sensing (Bohlen et al., 2011), and neuronal death during acidosis (Wang et al., 2015), such as in the event of a stroke.

Several types of ASICs exist, with variants of each, including major types 1-4. These subtypes assemble as homo or hetero-trimers and differ in their function, sensitivity and localization. Some ASIC subtypes, such as the 1a/2a heterotrimer, have relatively low proton sensitivity and activate at low pH (4.8-5.4), other subtypes, such as ASIC3 and ASIC1a homotrimers, are activated in conditions only slightly more acidic than physiological pH (6.4-6.7), allowing them to sense more subtle changes in proton concentration (Gründer, 2018). ASIC subtypes also vary in their activation and desensitization rates, allowing this family of ion channels to sense both subtle, prolonged changes in pH as well as short periods of significant acidification.

ASICs are activated by acidification, a process which is thought to occur through protonation of acidic residues in the ECD, leading to a conformational change in the TM helices and opening of the ion channel pore (Yoder et al., 2018). The ECD structure is described by a clenched fist analogy, containing a primarily beta sheet palm and β-ball domain, and primarily alpha helix thumb, finger and knuckle domains (Figure 1.3). The resting state of the channel has an expanded ECD with the finger and thumb domains arranged further from the threefold axis and an expanded acidic pocket found at subunit interfaces. Upon acidification, residues in the acidic pocket are protonated which contracts the acidic pocket and stabilizes contact between the thumb, finger and palm domains.

These rearrangements cause a concerted rotation subunits leading to the flexing of the palm domain towards that plasma membrane and inducing a translation of the alpha helices forming the TMD away from the threefold axis.

Figure 1.3. Structure of an ASIC protein. A. Surface representation of ASIC1a trimer (PDB: 7VTK) with colours representing different subunits. Lateral fenestration is highlighted in white dotted triangle. B. Same as A but a top-down view. C. Structure of an ASIC monomer. ECD is shown as purple cartoon and TMD is shown as turquoise cartoon. Re-entrant loop is shown as green cartoon. The other two subunits are shown as light grey surface. D. ASIC subunit subdomains shown in one subunit, with the other two subunits shown as transparent white surface for clarity.

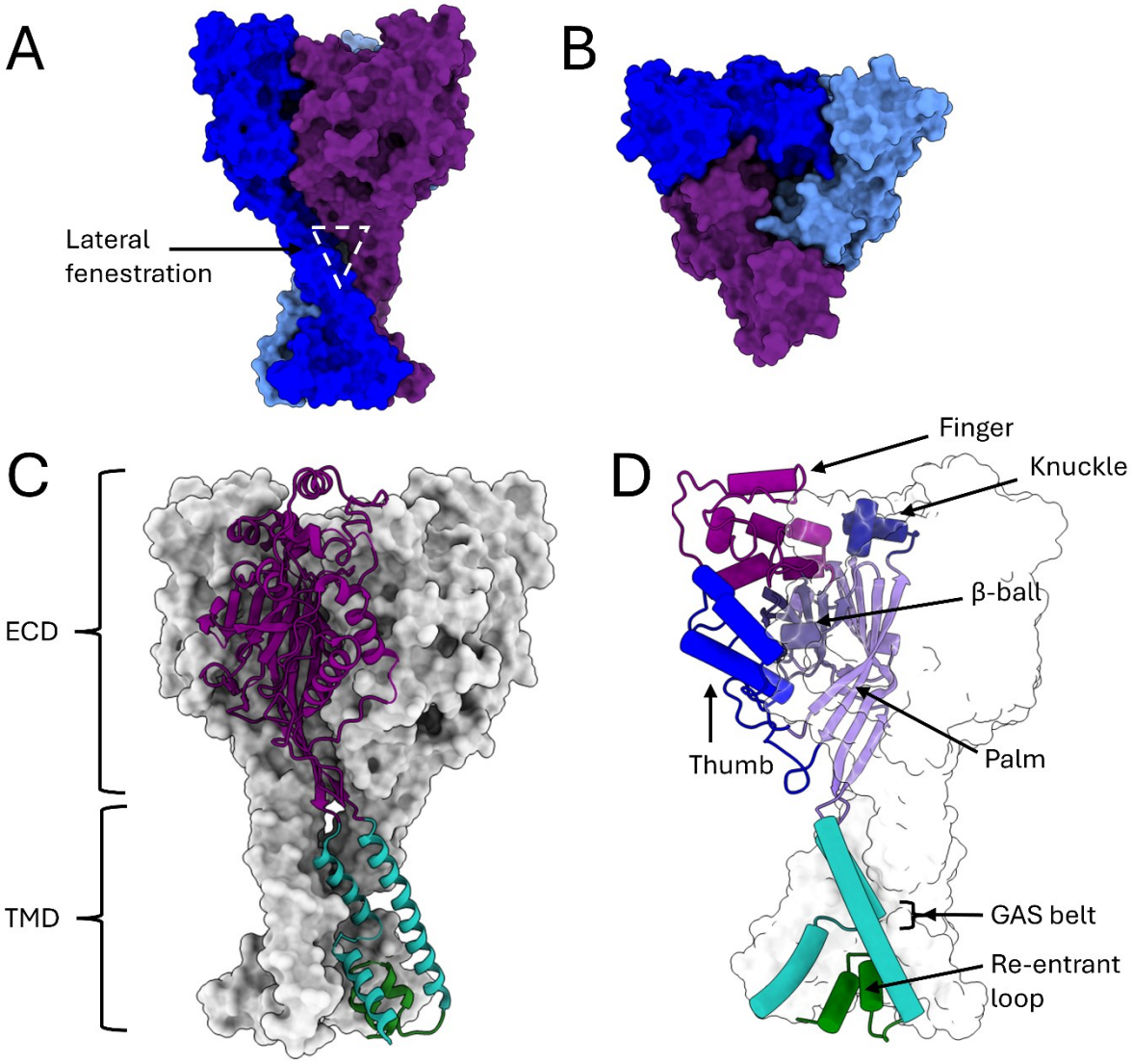
A
Lateral
fenestration
B
C
ECD
TMD
D
Finger
Knuckle
β-ball
Thumb
Palm
GAS belt
Re-entrant
loop

The ASIC TMD is composed of the inner, pore lining TM2 helix and the outer TM1 helix which makes extensive contact with membrane lipids. The TM2 helices undergo a domain swap, creating a non-alpha helical, extended region near the center of the TMD, which is perpendicular to the rest of the TMD and contains the conserved glycine-alanine-serine (GAS) motif, suggested to be important to ion selectivity (Baconguis et al., 2014) . Ions enter the pore via the upper and central vestibules in the ECD, as well as through lateral fenestrations located between the TMD and ECD near the outer surface of the membrane (Gonzales et al., 2009). The lower region of the TMD is a re-entrant pre-TM1 loop (Yoder & Gouaux, 2020), which contains a conserved histidine-glycine motif situated below the GAS belt towards the cytoplasm (Figure 1.3).

Pentameric ligand-gated ion channels: nicotinic acetylcholine receptors

Pentameric ligand-gated ion channels (pLGICs), also known as Cys-loop receptors, are a diverse super-family of ion channels all featuring an assembly of five subunits, with each subunit containing a large primarily β-sheet ECD, an α-helical transmembrane domain (TMD), and a largely disordered ICD (Figure 1.4). The ligand binding sites are at subunit interfaces in the ECD. In mammals, this family exhibits a characteristic the 13-amino-acid Cys loop, containing a pair of disulphide-bonded Cys residues, located in the ECD. The pLGIC superfamily includes four main families, the excitatory cation-selective nicotinic acetylcholine receptors (nAChRs) and 5-hydroxytriptamine receptors (5-HT3Rs), and the inhibitory anion selective γ-aminobutyric acid receptors (GABARs) and glycine receptors (GlyRs).

nAChRs are sensitive to the neurotransmitter, acetylcholine, but can also be activated by agonist analogs, such as carbamylcholine, and the exogenous ligand nicotine. Sixteen different subunit types (α1-7, α9, α10, β1-4, γ, δ, ε) are found in mammals and assemble as homo or heteropentamers, creating many subtypes of nAChRs that vary in localization and neurotransmitter

sensitivity. In humans, nAChRs are categorized as neuronal, which are found primarily in the brain, and muscle-type, which are present at neuromuscular junctions. Muscle-type nAChRs assemble as $(\alpha 1)_2\beta 1\delta(\gamma/\varepsilon)$ heteropentamers, with neonatal nAChRs containing a γ subunit and the adult form containing an ε subunit (Hesselmans et al., 1993). Many other types of nAChRs also exist in non-mammalian species, making this an extremely diverse protein family.

The best studied nAChR is the nAChR from the electric ray, *Torpedo*, which is homologous to the human muscle-type nAChR. It is a heteropentamer composed of two α subunits, one β, one δ and one γ subunit. It contains two agonist binding sites in the ECD at the α_γ-γ and α_δ-δ subunit interfaces. Each subunit contains 5 TMD α-helices; the pore lining M2 helix, the outer M4 helix which makes extensive contacts with the surrounding lipid membrane, M1 and M3 which form an intermediate layer between M2 and M4, and a short MX helix, which is parallel to the membrane surface and is located at the interface between the membrane and the cytosol. Agonist binding causes conformational changes of the loops surrounding the binding site in the ECD which lead to quaternary rearrangements that ultimately translate into opening of the ion channel pore (Zarkadas et al., 2022). Upon agonist binding, loop C of the principal subunit closes around the binding pocket and loop F of the complimentary subunit rocks upwards towards the binding pocket pivoting outward from the pore axis. The capping of loop C leads to a pivoting of the β9 and β10 towards the adjacent γ/δ subunits. This ultimately leads to a tilt of M1 towards the β/γ subunits and thus an outward movement of the M2-M3 linker so that the M2 and M3 helices to tilt out away from the pore axis to open the channel gate (Figure 1.4).

Figure 1.4. ***Torpedo*** **nAChR Structure.** A. Side view of an nAChR with one monomer shown in cartoon representation and the rest as light grey surface. The ECD is shown in purple, the TMD is shown in turquoise, and the ICD is shown in green. B. Top-down view of nAChR pentamer. The α subunits are shown in purple. The rest of the subunits are coloured as follows: β - dark blue, δ – turquoise, γ – light blue. C. Top-down view of the TMD. Individual TMD helices are highlighted in one subunit, the other subunits are shown as white cartoon. Figure adapted from Ananchenko et al. 2024. D. Subdomains of nAChR subunits. Two subunits shown forming a binding site, with complimentary subunit in blue. Agonist is shown in red spheres.

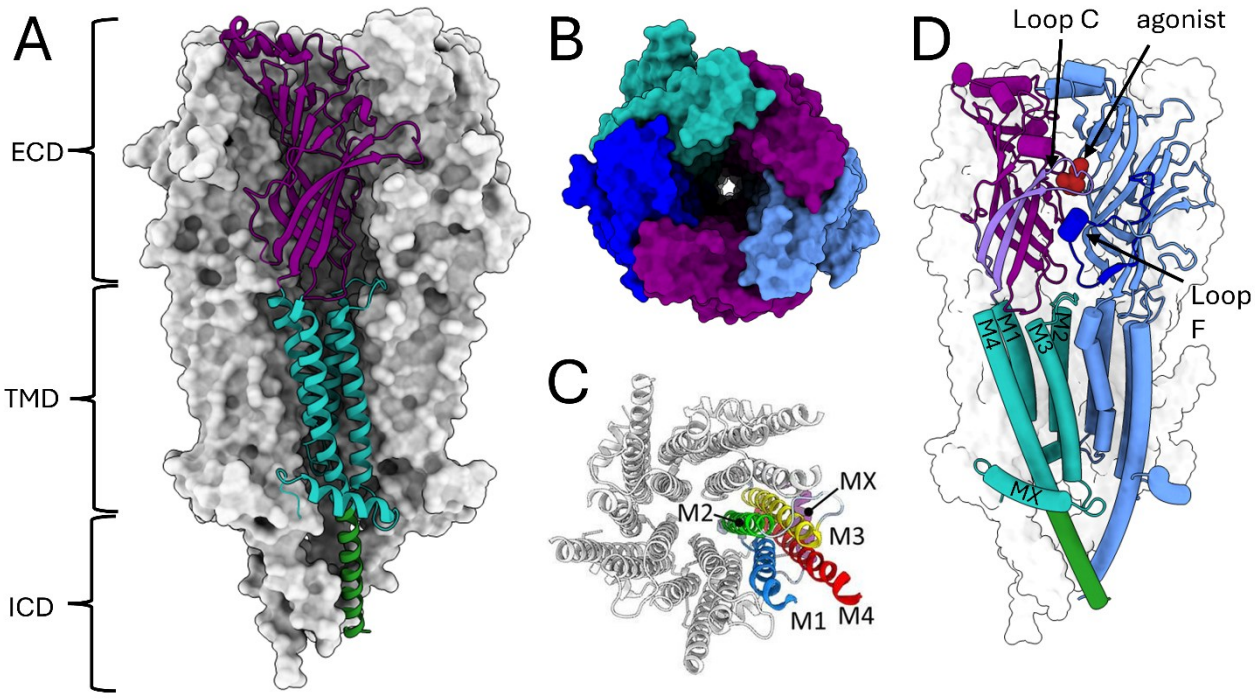
A
ECD
TMD
ICD
B
C
MX
M2
M3
M1
M4
D
Loop C
agonist
Loop
F
M1
M4
M2
M3
MX

1.4 Role of lipids in ligand-gated ion channel function

Decades of biophysical research have shown that the membrane environment of ion channels modulates their function. Membrane lipids can either activate ion channels directly or potentiate their response to agonists. Two ways that the presence of certain lipid species affect channel function have been proposed. First, lipids may bind to defined sites on ion channels and exert their function directly by modifying the ion channel structure or stabilizing a functional state. For example, signalling lipid phosphatidylinositol 4,5-bisphosphate (PIP2) is shown in structures to be well coordinated at distinct sites on inward rectifying potassium (Kir2.2) channels (Hansen et al., 2011) and voltage-gated potassium (KV) channels (Sun & MacKinnon, 2020), leading to enhanced coupling between distinct regulatory and transmembrane pore domains. There is also evidence that lipids can exert their functions on LGICs through bulk membrane properties, such as membrane tension, curvature or fluidity. Hyperpolarization-activated cyclic nucleotide-gated (HCN) channels exhibit domain rearrangement depending on their localization to different membrane compartments (Handlin & Dai, 2023). Their activity is potentiated by the disruption of L_o domains in the cell membrane. Membrane lipids have been noted to affect the function of many ion channels though diverse mechanisms (Thompson & Baenziger, 2020).

Modulation of ASIC function by lipids

PUFAs are of particular importance to ASIC function. Most prominently, the PUFAs AA and DHA alter the voltage dependence and maximum current of ASICs (Klipp & Bankston, 2022; Marra et al., 2016). During inflammation, hydrolysis of phospholipids generates AA and lysophosphatidylcholine (LPC). Whole-cell electrophysiology studies demonstrated that increasing concentrations of AA, DHA and LPC shifted the activation currents of ASIC to a higher pH_{50}, with differing lipid sensitivity between ASIC subtypes. AA and DHA increase the proton

sensitivity of ASIC1a, increasing the pH_{50} and I_{max} (Klipp & Bankston, 2022; Smith et al., 2007), suggesting that the presence of PUFAs favours an open channel state. In the case of ASIC3, the presence of PUFAs shift the pH_{50} dramatically to 7.4, allowing for activation of ASIC3 without extracellular acidification (Marra et al., 2016), essentially allowing PUFAs to act as agonists. The modulatory effects of PUFAs on ASICs are dependent on the chemical structure of the PUFA, with increased potentiation seen with longer fatty acid chains containing a larger number of double bonds (Klipp & Bankston, 2022; Smith et al., 2007). Specifically, stearic (18:0) and linoleic (18:2) acids do not appreciably potentiate ASICs while eicosapentaenoic acid (20:5) and DHA (22:6) have the largest modulatory effect.

While a PUFA binding site on ASICs has not been identified, there is evidence for direct PUFA binding over bulk membrane effects. It was originally proposed that increased concentrations of AA could potentiate ASIC currents through membrane deformation (Allen & Attwell, 2002), however, it was later shown that changes in membrane stretch, and membrane fluidity do not potentiate ASIC currents (Smith et al., 2007). Additionally, neutralization of an arginine residue, which is located near the extracellular side of the transmembrane domain near the channel's lateral fenestrations, eliminated the potentiation of ASIC3 and ASIC1a by DHA (Klipp & Bankston, 2022). Arginine residues in this region may form salt bridges with adjacent glutamate residues on the TM2 helix, with these salt bridges only existing which exists only in the resting state of the channel (Yoder et al., 2018). On the other hand, a specific role for these arginine residues in ASIC function has not been described. Importantly, the arginine to glutamine neutralization mutation did not change the pH_{50} for activation in the absence of PUFAs, suggesting that this mutation only affects modulation by PUFAs and not channel activation itself.

Modulation of nAChR function by lipids

The effects of lipids on nAChR function have been studied over several decades, with by far the most studies using the prototypic pLGIC, the *Torpedo* nAChR. Early studies showed that purified receptors must be reconstituted into membranes containing anionic lipids and Chol for channel gating, with nAChRs reconstituted into a 3:1:1 mixture of PC, PA and Chol being able to undergo agonist-induced response as effectively as in native membranes (Baenziger et al., 2000; Criado et al., 1982; daCosta et al., 2004; Fong & McNamee, 1986; Sunshine & McNamee, 1992). Lipids modulate nAChR function via a conformational selection mechanism, whereby specific membrane compositions, such as native or 3:1:1 PC:PA:Chol membranes, stabilize an activatable resting state of the receptor, whereas other membranes, such as pure PC membranes, stabilize an uncoupled conformation (daCosta et al., 2013; daCosta & Baenziger, 2009). The uncoupled conformation is characterized by the ability to bind ligand with a similar affinity to the resting state, however without pore opening in response to ligand binding (daCosta & Baenziger, 2009).

Though the initial studies suggested that both Chol and anionic lipids such as PA were essential for nAChR function, subsequent work demonstrated that neither lipid type was strictly required and that nAChR specificity for modulating lipids was relatively low. Independently, increasing levels of either PA or Chol in a PC membrane stabilized increasing proportions of an activatable nAChR state (Baenziger et al., 2000; Hamouda et al., 2006). In the presence of anionic lipids, several types of neutral lipids can be substituted for Chol to support nAChR function (Addona et al., 2003; Sunshine & McNamee, 1992). Similarly, in the presence of Chol, other types of anionic lipids, such as PS or phosphatidylglycerol (PG), yield activatable nAChRs (Addona et al., 2003; daCosta et al., 2009; Sunshine & McNamee, 1992). In the absence of Chol, however, PA is particularly effective at stabilizing a large proportion of activatable receptors (daCosta et al., 2009).

Some evidence from these functional studies suggests that lipids influence nAChR function through bulk membrane properties, for example, although thicker membranes containing PC lipids with longer acyl chains stabilize an uncoupled state, these membranes promote slow conformational transitions from the uncoupled to "coupled" states (i.e., resting, open and desensitized) in the absence of anionic lipids or Chol (daCosta et al., 2013).

1.5 Cryo-EM structures of ion channels with resolved lipids

Developments in cryo-EM technology have yielded a multitude of high-resolution ion channel structures in recent years. The ability to reconstitute membrane proteins in lipid nanodiscs gives us the ability to solve structures in the presence of native or functionally relevant lipids, which has yielded structures of LGICs with resolved bound lipids. The number and pattern of bound lipids in these structures may depend on sample preparation (Rahman et al., 2022) and nanodisc size (Flayhan et al., 2018). Furthermore, assignment of LGIC functional states from cryo-EM structures is not always clear, for example, structures which appear open in cryo-EM datasets may collapse to a closed-pore state in molecular dynamics (MD) simulations (Zarkadas et al., 2022). It may therefore be difficult to discern specific state-dependent lipid binding in cryo-EM structures. These structures are nonetheless a powerful tool combined with *in-vitro* and *in-silico* studies to describe mechanisms of lipid binding and modulation.

Structures of ASICs with resolved lipids

Structures of the chicken ASIC1 attributed to open (Baconguis et al., 2014), resting and desensitized (Yoder et al., 2018) states solved by X-ray crystallography do not show any bound lipids. More, recently, a resting state structure of chicken ASIC1 has been solved by cryo-EM with density attributed to lipids adjacent to the TMD (Yoder & Gouaux, 2020). These lipids densities

resemble pairs of adjacent of lipid acyl chains. Due to the lack of headgroup density, it is possible that these densities represent ordered lipids near the TMD rather than lipid binding sites. A structure of human ASIC1a solved by cryo-EM in the presence of cholesteryl hemisuccinate (CHS) also revealed CHS density in the outer leaflet of the TMD near the lateral fenestrations (Figure 1.5). There is a lack of structural information for functionally relevant lipids, such as PUFAs, bound to ASICs, likely due to the low concentration of these lipids in native membranes.

Structures of pLGICs with resolved lipids

The first almost complete structure of a pLGIC pentamer was a cryo-EM structure of the *Torpedo* nAChR solved in 2005 at 4 Å resolution (Unwin, 2005). Full-length X-ray crystallography structures were subsequently solved of the prokaryotic pLGICs, Erwinia ligand-gated ion channel (ELIC) (Hilf & Dutzler, 2008) and Gloeobacter violaceus (GLIC), the latter with resolved lipids (Bocquet et al., 2008). In 2019, a high-resolution structure of ELIC was solved in a lipid-bound state (Hénault et al., 2019). Many more cryo-EM structures of members of the pLGIC family in nanodiscs have been solved in subsequent years, several of which show lipids bound to the transmembrane domain. Two cryo-EM studies of GlyRs show many regions of density attributed to acyl chains on the TMD surface (Yu et al., 2021; Zhu & Gouaux, 2021) without, however, any modelled lipid headgroups. A structure of the α1β3γ2 $GABA_AR$ shows well-coordinated PIP2 inner leaflet sites on the TMD (Sente et al., 2022). The prokaryotic pLGIC, Erwinia ligand-gated ion channel (ELIC), shows cardiolipin and PG sites at its TMD in recent cryo-EM structures (Kumar et al., 2021).

Figure 1.5. Density attributed to bound lipids in ASIC structures. A. Lipid density (blue) at chicken ASIC1 TMD (PDB: 7VTK). Lipids were not modelled but density resembles phospholipid tails. B. CHS density (orange) at TMD of human ASIC1a (PDB: 7CFS). ASIC TMD is shown as light grey surface.

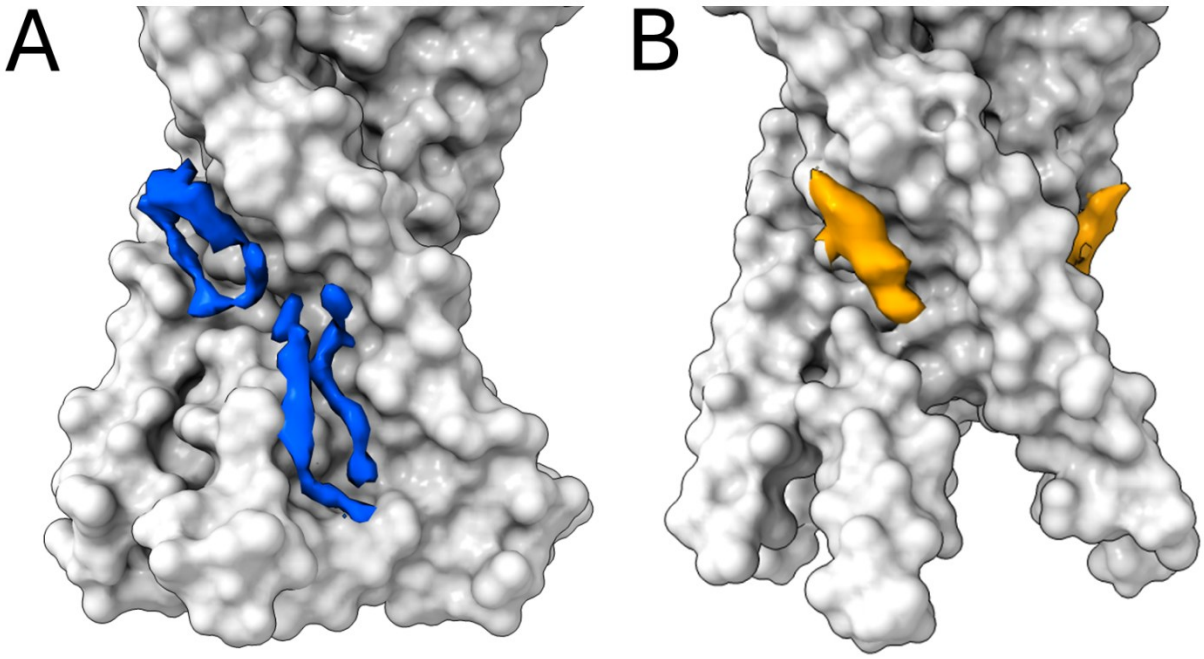
A
B

The first structural evidence of lipid binding to nAChRs came from cryo-EM structures of human detergent-solubilized neuronal α4β2 (Walsh et al., 2018) and nanodisc-reconstituted α3β4 (Gharpure et al., 2019) nAChRs. The structures in these studies were solved in the presence of CHS, with density attributed to CHS observed at the periphery of the TMD located at subunit interfaces. Diffuse density attributed to cholesterol was also observed in detergent-solubilized human α7 nAChR structures, with one cholesterol molecule modelled at each subunit-subunit interface (Zhao et al., 2021).

Several recent cryo-EM studies have been performed which showed density attributed to bound lipids on the *Torpedo* nAChR TMD. These structures, solved in azolectin nanodiscs with or without supplemented cholesterol, have been particularly informative, providing insight into both cholesterol and phospholipid binding (Rahman et al., 2022; Zarkadas et al., 2022). Several densities attributed to bound phospholipids were observed both in the inner and outer leaflet of the TMD at subunit interfaces of the nAChR. The inner leaflet site suggests a conserved phospholipid binding motif, where the phosphate group of the lipids is coordinated by an arginine located on the M3 helix of the principal subunit at each interface, and a lysine or arginine residue located on the complementary M4 helix (Figure 1.6). At subunit interfaces with a complementary α subunit, the coordinating M4 residue is replaced with a histidine. Additional coordinating interactions with a histidine on the principal M3-MX linker and aromatic residue on the complementary M1 helix were resolved. While the lipid poses differ slightly between subunits, these coordinating interactions are consistent at each subunit interface.

Table 1.1. Summery of available nAChR Cryo-EM structures

nAChR structure	**PDB**	**year**	**Bound lipids**
Torpedo	2BG9	2005	none
Human α4β2	6CNJ, 6CNK	2018	CHS
Human α3β4	6PV7, 6PV8	2019	CHS
Human α7	7EKI, 7EKT, 7EKP	2021	Chol
Torpedo	7QL5, 7QKO, 7QL6	2022	Phospholipids
Torpedo	7SMQ, 7SMM, 7SMR, 7SMS, 7SMT	2022	Phospholipids, Chol, additional Chol sites when supplemented

Figure 1.6. Density attributed to bound lipids at nAChR TMD. A. Phospholipid density at inner and outer leaflet sites on nAChR TMD surface (blue). Density was modelled at PC (PDB:7QL5). B. Chol density at nAChR TMD in sample prepared with exogenous cholesterol (orange). Inner leaflet sites were deemed high affinity, while outer leaflet sites were deemed low affinity (PDB:7SMQ). TMD shown as light gray surface. C. Putative conserved phospholipid site shown at the α_{γ}-γ subunit interface. Protein is shown as gray cartoon with two shades representing two subunits. Lipid is shown as blue sticks coloured by heteroatom. Coordinating residues are shown as turquoise sticks.

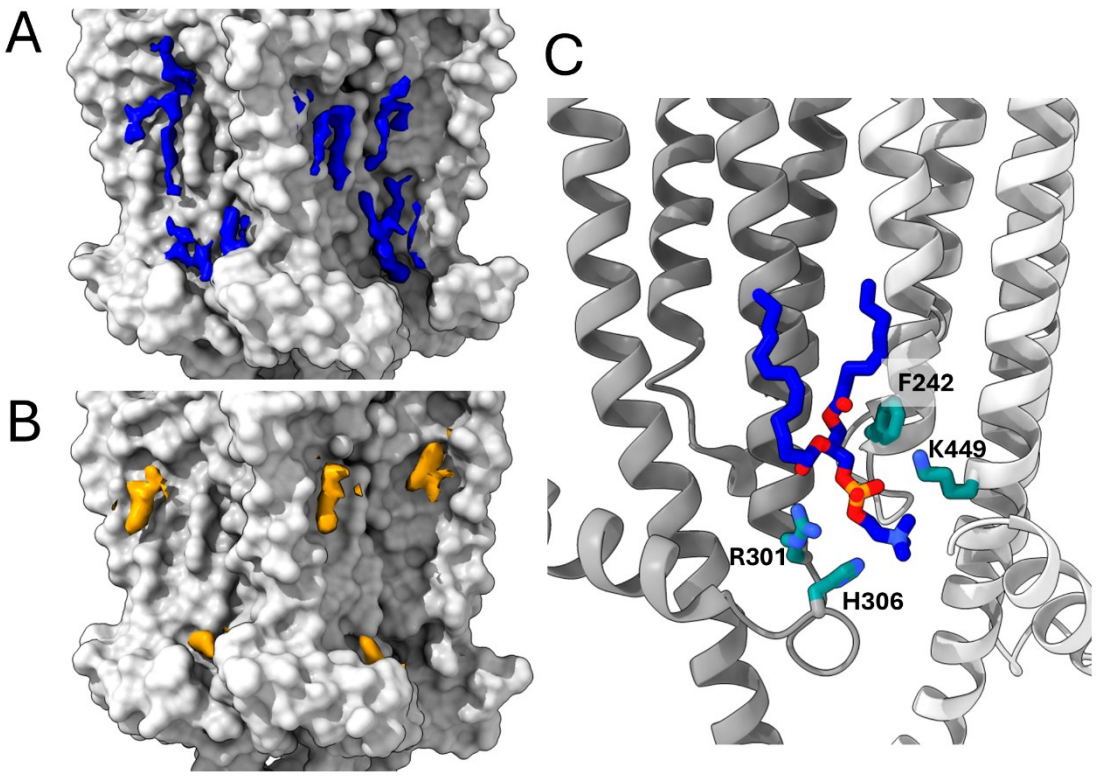
A
B
C
F242
K449
R301
H306

Torpedo nAChR cryo-EM structures exhibit differences in cholesterol density depending on sample preparation. Purified nAChR that was washed, while bound to the nAChR-affinity resin, with detergent-solubilized azolectin to facilitate lipid exchange does not show any density attributable to cholesterol (Zarkadas et al., 2022). In contrast, purified nAChR that was not washed, while bound to the affinity resin, with detergent solubilized lipid exhibit regions of density that were attributed to endogenous cholesterol, proposed to be high affinity cholesterol binding sites (Rahman et al., 2022). These cholesterol molecules are bound in the inner leaflet in a pocket formed by M4, M3 and MX, and observed on three of five subunits. In addition, a structure solved in the presence of added exogenous cholesterol reveals additional regions of cholesterol density in the outer leaflet, sites deemed to be low affinity (Figure 1.6).

1.6 In-silico studies of lipid-ion channel interactions

Molecular dynamics (MD) simulations are a computational tool which use a general model of physics governing interatomic interactions to predict how atoms in a biomolecular system move over time. Using known static molecular structures as starting points, MD simulations model the positions of atoms at femtosecond temporal resolution. They were first performed on simple gasses almost 70 years ago (Alder & Wainwright, 1957), and are now at the point of being able to predict atomic motions in a whole cell (Stevens et al., 2023). These techniques are now increasingly used alongside experimental structural biology for interpretation of experimental results and generating new hypotheses. MD simulations in which positions of atoms are simply allowed to evolve in given conditions are known as brute force simulations and are generally limited to a local region of the energetic landscape, such as local motions within protein domains or simple ligand binding, due to their prohibitive computational cost. Another form of MD simulations, known as enhanced sampling techniques, artificially accelerate the exploration of conformational space and allow for

the study of slow or rare events. This can be done through adding external potentials to overcome high energy barriers, steering the simulation towards desired endpoints, or simulating multiple shorter replicas of a system at different conditions. MD simulations also allow for the perturbation of a system, for example, free energy perturbation (FEP) can be used to compute binding affinities of a ligand to a protein by transforming one ligand into another in a binding site (alchemical route) or using restraints to "pull" a ligand out of a binding site (geometrical route) (Fu et al., 2022).

Cryo-EM structures provide information on the location and interactions of putative bound lipids but are not able to give information on lipid binding dynamics. A further limitation of structural studies is the inability to probe binding of different lipid species, especially those present in low amounts in sample preparation. MD simulations can predict dynamic lipid binding behaviour at atomistic resolution, which are not currently available in experiments, albeit over very short timescales. With recent advances in computing, simulations at atomistic resolution are routinely performed for up to a microsecond, while coarse grained (CG) simulations, where properties of several atoms are generalized into one bead, are performed for tens or hundreds of microseconds. CG-MD studies of large plasma membrane patches have been performed to study lipid dynamics and organization of both mammalian (Ingólfsson et al., 2014) and neuronal (Ingólfsson et al., 2017) plasma membranes with experimentally defined lipid compositions.

Several MD simulation studies have investigated lipid interactions with ion channels, including lipid interactions with high resolution pLGIC structures solved by cryo-EM in different functional states. A multiscale simulation study of lipid binding to the active and inactive states of the GlyR suggested differences in lipid organizational patterns between different lipid species and state-dependent cholesterol interactions (Dämgen & Biggin, 2021). The study reliably predicted lipid sites previously seen in cryo-EM structures as well as novel sites. Another study used CG-MD to

study lipid interactions with the active, inhibited and desensitized states of the human neuronal α7 nAChR, suggesting differences in cholesterol binding to these states (Zhuang et al., 2022). A cholesterol site on the desensitized state was similar to that seen for the positive allosteric modulator PNU biding to an intermediate desensitized/activated state in cryo-EM structures (Zhao et al., 2021). A study in which long atomistic simulations of up to 20 microseconds were performed showed 1-stearoyl-2-docosahexaenoyl-sn-glyerco-3-phosphocholine (SDPC) lipid tails inserting into the interhelical space between the M1 and M4 helices of a mouse 5-HT_{3A} TMD (Guros et al., 2020). This intrahelical space was suggested to expand upon prolonged 5HT binding, suggesting a possible role for lipids in state transitions.

MD simulations have also been used to probe lipid interactions with the *Torpedo* nAChR, notably studies in complex membranes using the pioneering 4Å structure (PDB: 2BG9) (Sharp et al., 2019; Sharp & Brannigan, 2021). These models provided preliminary insight into nAChR interactions with several types of lipids. The 2BG9 structure, however, lacks the MX helix which frames lipid binding to inner leaflet sites, as well as exhibiting an error in the register of the amino acid sequence within the TMD. These issues limit the conclusions that can be derived from this simulation data.

As previously stated, a major limitation of MD simulations is their computational cost, making it challenging to study relatively slow biomolecular processes such as lipid diffusion and organization around an ion channel. While CG-MD allows for longer simulation times to study lipid diffusion, the unphysical secondary structure of proteins at this resolution requires the use of strong restraints, making it impossible to observe protein conformational changes. Ion channel state transitions occur over milliseconds (Akk & Auerbach, 1999), while current atomistic simulation capabilities are limited to timescales of tens of microseconds. Furthermore, MD

simulations are limited by the quality of the structural information obtained from X-ray crystallography and cryo-EM structures. The current criteria to determine the usefulness of structural models for MD simulations is limited to adequate resolution and correct modelling of sidechains to yield normal behaviour of the model in simulations. Other criteria, such as the accurate annotation of a functional state, or the physiological relevance of the structural model based on the given sample preparation, can only be explored from the analysis of the resulting MD simulation and comparison to experimental data.

1.7 Summary of thesis and objectives

While there is evidence for both bulk membrane and direct lipid binding effects on pLGICs as discussed above, I focus here on direct interactions. This allows for direct comparisons to lipid resolved in recently solved structures which serves to validate the binding sites observed in simulations. Using *in-silico* studies, I seek to bridge the recent structural and experimental insight into lipid effects on pLGIC function. My hypothesis is that lipids which exert an effect on ASIC and nAChR function have distinct binding patterns on the TMD of these proteins, and that the relative affinities of lipid species to these sites in different states reflects their physiological effect. This thesis is presented as a series of articles which investigate lipid interactions with ASICs and nAChRs. These studies focus on direct lipid interactions of functionally relevant lipid species with recent structures of both proteins using CG, atomistic, and FEP MD simulations.

Chapter 2 contains the first manuscript completed in this PhD in which I predict PUFA binding sites on human ASIC1a and ASIC3 in their open and resting states, which have been shown experimentally to respond differently to increasing concentrations of PUFAs like AA and DHA. Using CG-MD, I suggest differences in PUFA interaction patterns between these two ASIC subtypes, which are reversed by *in-silico* mutagenesis. I then propose key coordinating interactions

between PUFAs and positively charged residues in the outer leaflet region of the TMD using atomistic simulations.

Chapter 3 contains a manuscript in which I similarly use multiscale MD simulations to investigate phospholipid and cholesterol interactions with the *Torpedo* nAChR in the apo and diliganded states. These simulations suggest differences in localization between the functionally relevant lipids PA, PC and Chol, with particularly long duration interacting events with the activity-promoting lipids PA and Chol compared to the inactivating lipid PC. I also describe putative general interaction sites for phospholipids, distinct from high affinity Chol sites, in agreement with recent structural data.

Chapter 4 contains the final manuscript completed during my PhD, in which I delve deeper into phospholipid-nAChR interactions using atomistic simulations and free energy perturbation (FEP). I describe subtle differences in PA and PC binding behaviour at the conserved inner leaflet phospholipid site which may explain the differences in affinity between these two lipid species. I use FEP to compare the biding affinity between PA and PC to one of these conserved sites, estimating a higher affinity for PA.

Chapter 5 presents a discussion of the new information on lipid-pLGIC interactions obtained from my simulation studies and how future studies can be used to gain additional insights into the mechanisms by which lipids affect pLGIC function

Chapter 2: Manuscript 1: Multiscale molecular dynamics simulations predict arachidonic acid binding sites in human ASIC1a and ASIC3 transmembrane domains

Ananchenko, A., Musgaard, M. (2023)

2.1 Preface

This is the first MD simulation study that I undertook in my PhD to study lipid-LGIC interactions and focused on PUFA interactions with ASICs. The Musgaard lab at the time was interested in studying the response of ASICs to protonation of residues in the acidic pocket and to PUFAs in the local membrane environment. The mechanisms underlying ASIC activation were not well known at the time, and no structural information was available regarding interactions with PUFAs or any other lipids. Given the functional information available on this topic, I hypothesised that direct PUFA binding sites exist on the ASIC TMD surface and differ between ASIC subtypes.

To probe this, I conducted multiscale MD simulations of hASIC1 hASIC3 homology models, which I built from solved X-ray crystallography structures of chicken ASIC proteins. I used CG simulations initially to study the general pattern of PUFA interactions with the two ASIC subtypes and find areas of preferential PUFA interactions and then perturbed these sites though in -silico mutagenesis. I then used atomistic simulations to investigate the atomic details of PUFA-ASIC interactions. I critically analyzed the resulting simulation data under the guidance of Dr. Maria Musgaard. I wrote the initial draft of this manuscript, which was edited and finalized by both myself and Dr. Musgaard.

2.2 Abstract

Acid-sensing ion channels (ASICs) play important roles in inflammatory pathways by conducting ions across the neuronal membrane in response to proton binding under acidic conditions. Recent studies have shown that ASICs can be modulated by arachidonic acid (AA), and, in the case of the ASIC3 subtype, even activated by AA at physiological pH. However, the mechanism by which these fatty acids act on the channel is still unknown. Here, we have used multiscale molecular dynamics simulations to predict a putative, general binding region of AA to models of the human ASIC protein. We have identified, in agreement with recent studies, residues in the outer leaflet transmembrane region which interact with AA. In addition, despite their similar modulation, we observe subtle differences in the AA interaction pattern between human ASIC1a and human ASIC3, which can be reversed by mutating three key residues at the outer leaflet portion of TM1. We further probed interactions with these residues in hASIC3 using atomistic simulations and identified possible AA coordinating interactions; salt bridge interactions of AA with $R65_{hASIC3}$ and $R68_{hASIC3}$ and AA tail interactions with the $Y58_{hASIC3}$ aromatic ring. We have shown that longer fatty acid tails with more double bonds have increased relative occupancy in this region of the channel, a finding supported by recent functional studies. We further proposed that the modulatory effect of AA on ASIC does not result from changes in local membrane curvature. Rather, we speculate that it may occur through structural changes to the ion channel upon AA binding.

2.3 Introduction

Acid-sensing ion channels (ASICs) are trimeric proton-sensitive cation channels found in the central and peripheral nervous system. Identified as part of the family of degenerin/epithelial sodium channels, ASICs play an especially important role in inflammatory pain pathways (Cheng et al., 2018). Several ASIC subunit types exist, including the major types ASIC1, ASIC2, ASIC3, and ASIC4 and their variants. Different ASIC subtypes have distinct function and nervous system localization (Kweon and Suh, 2013) and may assemble as homo- or heterotrimers. All ASIC types share a similar structure (Fig. 2.1, A and B). Each subunit contains a large extracellular domain (ECD), two transmembrane helices (TM1 and TM2) forming the transmembrane domain (Jasti et al., 2007; Fig. 2.1, A and B), and a recently resolved re-entrant intracellular domain (ICD; Yoder and Gouaux, 2020). ASICs are activated at acidic pH, presumably through protonation of acidic residues in the ECD, leading to rearrangements and subsequent opening of the ion pore in the transmembrane domain (Jasti et al, 2007; Yoder et al, 2018). In this way, ASICs act as important sensors of tissue acidosis in the central and peripheral nervous systems.

Figure 2.1 Model of the hASIC3 and structure of PUFAs. A. Homology model of hASIC3. One subunit of the trimer is highlighted in color while the rest of the channel is shown in transparent gray cartoon. The ECD is shown in orange cartoon, while the TMD is in blue cartoon, with TM1 in royal blue and TM2 in dark cyan. The dashed lines illustrate the approximate position of the membrane. **B.** Surface representation of the open state of hASIC3, colored as in A. Residues $R63_{hASIC3}$, $R65_{hASIC3}$, and $R68_{hASIC3}$ are highlighted in cyan and labeled in one subunit. The dashed triangle indicates the location of lateral fenestrations. **C.** Structures of AA (20:4, top) and DHA (22:6, bottom).

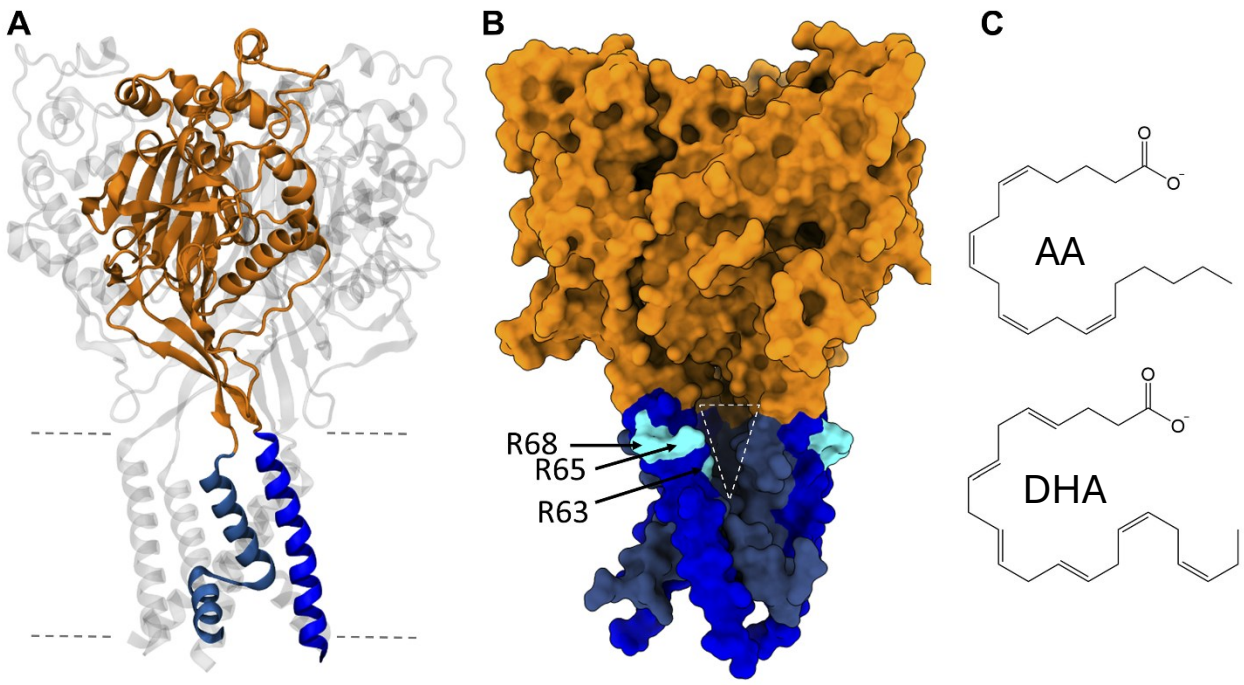
A
B
C
R68
R65
R63
AA
DHA

The neuronal membrane environment plays an important role in the function of ion channels. For example, pentameric ligand-gated ion channels, such as the nicotinic acetylcholine receptors, are functionally sensitive to the lipid composition of their surrounding membrane (Baenziger et al., 2000; daCosta et al., 2013; Ananchenko et al., 2022). It has also been shown that several voltage-gated ion channels are functionally affected by polyunsaturated fatty acids (PUFAs), with the presence of PUFAs altering the voltage dependence and maximal current of these channels (Elinder and Liin, 2017; Tong et al., 2019). PUFAs such as docosahexaenoic acid (DHA) and arachidonic acid (AA; Fig. 2.1 C) are abundant in neuronal membranes in their esterified form as phospholipid tails (Salem et al., 1996). The concentration of PUFAs as free fatty acids has been estimated to be between 1 and 50 μM in plasma (De Caterina et al., 2000; Fraser et al., 2003); however, the exact concentration in the neuronal plasma membrane, and its physiological relevance, is unknown. It is suggested that the PUFA concentration, in particular DHA and AA, in neuronal membranes can be affected by factors such as diet or sex (Chen et al., 2020). Physiological conditions can also affect the free fatty acid abundance of AA, e.g., inflammation increases the AA concentration (Marra et al., 2016). The importance of PUFAs in neuronal function, in particular through their effects on ion channels, is an evolving field.

Recent studies have illustrated that ASICs can be modulated by fatty acids, most prominently by AA (Smith et al., 2007; Marra et al., 2016). Modulation by AA has been shown to occur in several ASIC subtypes (Smith et al., 2007). AA has been suggested to shift the pH dependence of the channel, leading to increased activation at higher pH, i.e., smaller proton concentration (Allen and Attwell, 2002; Smith et al., 2007; Klipp and Bankston, 2022). Evidence suggests that this occurs through a direct binding mechanism, rather than through changes in the bilayer properties (Smith et al., 2007). Interestingly, the ASIC3 subtype can be activated by AA at physiological pH (Marra

et al., 2016), potentially due to a more extreme shift in pH50 or a higher initial pH50, whereas ASIC1a does not open without a drop in pH, despite the presence of AA (Marra et al., 2016). pH50 is the pH that yields half maximal response. However, other studies suggest that AA acts in the same manner on both the ASIC1 and ASIC3 subtypes (Klipp and Bankston, 2022). Other PUFAs also have a modulatory effect on ASICs, the potency of which is suggested to correlate with tail length and saturation (Smith et al., 2007; Klipp and Bankston, 2022). AA itself is an important inflammatory marker in the nervous system, with increased levels of AA seen in exudates of patients with rheumatoid arthritis (Marra et al., 2016) and psoriasis (Hammarström et al., 1975).

Until very recently, the binding site, if any, for AA on ASICs has remained unknown. A recent study has suggested that $R64_{hASIC1}$ ($R63_{hASIC3}$, Fig. 1 B) could play an important role in binding of, and potentiation by, AA in both ASIC1 and ASIC3 (Klipp and Bankston, 2022). This functional study gives promising evidence of AA modulation of ASICs through structural effects; however, evidence of direct AA binding to this residue is yet to be shown. In addition, recent structures of chicken ASIC1 solved in styrene maleic anhydride nanodiscs reveal electron densities attributed to lipids (Yoder and Gouaux, 2020). However, the identity of these lipids and their functional relevance are unknown. Overall, the exact mechanism by which AA modulates or even activates ASICs remains unclear.

In this study, we identify a putative binding region for AA in the extracellular half of the TMD. This binding region is similar between the human ASIC3 (hASIC3) and hASIC1a subtypes, consistent with the general modulatory effect of AA on several ASIC isoforms. We observed subtle differences in the AA coordination pattern between the two isoforms, with the largest differences seen in residues which are conserved within their respective ASIC subtypes. Importantly, we suggest that AA can form stable, direct interactions with ASICs. This is, for example, shown by

the observation from simulations that the hASIC3 residue R65hASIC3, located near the transmembrane domain (TMD) fenestrations, forms a stable salt bridge with the carboxylic acid headgroup of AA. To expand upon recent studies such as Klipp and Bankston (2022), we speculate that modulation of ASIC by AA does not occur solely through effects on the structure of TMD fenestrations directly, but rather through a more complex mechanism involving changes in contacts and conformation between TM1 and TM2. We proposed that several coordinating interactions, rather than a single binding residue, may contribute to the overall ASIC-AA binding affinities and modulatory mechanism.

2.4 Materials and Methods

Homology modeling and system setup

Homology models of hASIC1a and hASIC3 were constructed from crystal structures of chicken ASIC1 in both the open and resting states (PDB: 4NTX, 5WKU; Baconguis et al, 2014; Yoder and Gouaux, 2020) using Modeller (Eswar et al., 2006). The following sequences from the Uniprot database (Bateman et al., 2021) were used: Q1XA74 for chicken ASIC1, P78348 for hASIC1a (89.35% sequence identity with chicken ASIC1), and Q9UHC3 for hASIC3 (49.71% sequence identity with chicken ASIC1). A disordered extracellular loop (residues 291–304 in hASIC3 numbering) was removed from the hASIC3 structure due to poor modeling and to reduce the solvated box size. Rather, our models incorporate a direct link between residues 290 and 305 in hASIC3. This extended loop in hASIC3 relative to ASIC1 is found in the ECD and thus not believed to affect the potential interaction of PUFAs with the TMD. 100 structures were made for each homology model and the structure with the lowest molpdf score (Eswar et al., 2006) was chosen for simulations. The resulting all-atom homology models were converted to coarse-grain (CG) representation using the martinize.py script and the MARTINI2.2 CG forcefield (Marrink et al., 2007). The secondary, tertiary, and quaternary structures of the protein models were restrained using an elastic network with a force constant of 1,000 kJ/mol and a cut-off radius (Rc) value of 1.05 nm, constructed by the martinize.py script. These values were chosen to stabilize the specific functional states and to maintain the root mean square deviation of each CG structure within 4 Å. The insane.py script (Wassenaar et al., 2015) was used to embed the CG models in a bilayer in a 140 × 140 × 150 Å3 cubic box, solvated in MARTINI CG water with 0.15 mM NaCl, with additional neutralizing Na+ ions added to systems containing AA. Each system contained ~25,000

CG beads. Insane.py randomly places lipids in the intra- and extracellular leaflets. Therefore, repeats of simulations were set up independently to randomize lipid placement.

Initial simulations, using CG structures of the open and resting states, were set up with a membrane containing an 8:1:1 ratio of palmitoyl-oleoyl-phosphatidylcholine (POPC), lysophosphatidylcholine (LPC) and AA. A 10 μM solution of AA has been used in electrophysiology recordings to invoke ASIC3 currents at physiological pH (Marra et al., 2016), a concentration which is not attainable in the membrane patch size used in our simulations. We initially set up systems containing six molecules each of AA and LPC in each leaflet (1% AA); however, we found this to be insufficient for sampling interactions over 30 μs. We therefore increased the number of modulatory lipids 10-fold to 60 molecules per leaflet (10% AA) to ensure adequate sampling of lipid–protein interactions. This AA concentration is well above that of a physiological membrane composition. However, it allowed us to probe a large number of contacts between AA and the ASIC protein. In this way, it provided us the ability to reproducibly measure lipid occupancy and interaction duration, without deforming the membrane. Additional control simulations were set up the same way but containing only POPC in the membrane. Headgroup density calculations were performed using the 8:1:1 POPC:LPC:AA membranes. No specific associations between LPC and ASIC models were seen in the initial simulations, so subsequent simulations were performed using a 9:1 ratio of POPC:AA.

Mutations were created in the atomistic homology models of hASIC1a and hASIC3 using the ChimeraX (Pettersen et al., 2021) rotamers tool, selecting rotamers to minimize clash. The resulting atomistic mutant structures were subsequently coarse-grained and embedded in a 90:10 POPC:AA membrane as described above. For all structures, all ionizable residues were kept in their standard state. ASICs are believed to be activated by protonation of a number of acidic

residues in the ECD. In this case, however, where AA is proposed to be able to activate ASIC3 without a drop in pH, presumably by shifting pH50, we did not want to bias our simulations toward the open state as we wanted to capture the "pure" AA effect. Therefore, we probed AA interactions with the channel in the absence of additional proton activation.

Coarse-grained simulations

The GROMACS (van der Spoel et al., 2005; Abraham et al., 2015) 2019 simulation engine was used for all simulations. Energy minimization was performed for three rounds of 5,000 steps using steepest descent. Systems were equilibrated using the NPT ensemble (constant number of atoms and constant pressure and temperature) for a total of 4.75 ns with gradual lowering of protein position restraints from 1,000 to 50 kJmol−1nm−2 and lipid position restraints from 200 to 10 kJmol−1nm−2. Equilibration was performed with temperature held at 310 K using the v-rescale thermostat (Bussi et al., 2007) and pressure held at 1 bar with the Berendsen barostat (Berendsen et al., 1995). Production runs were simulated in triplicate for 30 μs each. Production runs were simulated with a timestep of 20 fs using an NPT ensemble with v-rescale set to 310 K and semi-isotropic Parinello-Rahman pressure coupling (Parrinello and Rahman, 1998) set to 1 bar.

Simulations with DHA and palmitic acid instead of AA were set up following the above protocol, using the open state CG structure, with a 9:1 ratio of POPC:FA where FA is the fatty acid of interest.

Atomistic simulations

Frames from the last 100 ns of CG simulations were selected, for which AA was seen to interact with the protein at least two upper TMD sites. One frame was selected from each repeat of relevant systems. Frames were backmapped to atomistic resolution using the CG2AT tool (Vickery and Stansfeld, 2021). A higher resolution structure of the ASIC1 open state (PDB: 4NTW; Baconguis

et al., 2014) was used to create an atomistic homology model as described in the homology modeling section above, and this model was subsequently used as the reference structure for alignment in the CG2AT protocol. One CG2AT system was created for each repeat of simulations containing the open and resting states of ASIC bound to at least two AA molecules at the extracellular TMD, solvated in TIP3P water. A total of 500 ns of simulation were performed for each starting system. AA parameters were obtained from the CHARMM-GUI lipid library (Lee et al., 2016).

Atomistic simulations were performed using the GROMACS 2019 simulation engine (van der Spoel et al., 2005; Abraham et al., 2015) and the CHARMM36 forcefield (Best et al., 2012; Huang and Mackerell, 2013). The resulting backmapped system was energy minimized for 5,000 steps or until a maximum force of 1,000 kJmol−1nm−1 on any atom was reached using the steepest descent algorithm. Equilibration was performed using the NPT ensemble for a total of 1 ns with temperature held at 310 K using the Berendsen thermostat, and pressure held at 1 bar using the Berendsen barostat. Production runs were performed for 500 ns in the NPT ensemble using the Nose-Hoover thermostat (Evans and Holian, 1998) with temperature set to 310 K and pressure held at 1 bar using the Parinello-Rahman barostat. The Verlet cut-off scheme (Verlet, 1967) was used throughout all steps with a force-switch modifier starting at 10 Å and a cutoff of 12 Å. The particle mesh Ewald (Darden et al., 1998) method was used for long-range electrostatics and a cutoff of 12 Å was used for short-range electrostatics. Covalent bonds including hydrogen atoms were constrained using the LINCS algorithm (Hess et al., 1997).

Analysis

Lipid occupancies and residence times at individual residues were calculated using the PyLipID tool (Song et al., 2022), with 0.475 nm and 1.1 nm lower and upper cutoffs, respectively. In-house

tcl scripts and VMD (Humphrey et al., 1996) were used for calculating density maps of lipid occupancies and membrane curvature. All other analysis was performed using in-house MDAnalysis (Michaud-Agrawal et al., 2011; Gowers et al., 2016) scripts. Figures were created in VMD (Humphrey et al., 1996) and Chimera X (Pettersen et al., 2021).

For analysis, the charged "COO" bead was used to define the headgroup of fatty acids, and the "PO4" bead was used as the headgroup phosphate of POPC.

Online supplemental material

The supplementary data includes information on the optimization of cut-offs for use with the PyLipID software (Figure 2.11). In addition, supplemental distance and interaction measurements for all chains, as shown in the main text Figure 2.6, are illustrated in Figure 2.12. Movie 2.1 shows a representative CG simulation where AA interactions with the relevant sites are sampled. Movie 2.2 illustrates a 200 ns section of a 500 ns simulation with one example of an AA molecule interacting with $R65_{hASIC3}$, $R68_{hASIC3}$, and $Y58_{hASIC3}$. Movie 2.3 illustrates another 200 ns section of a 500 ns simulation with a different example of an AA molecule interacting with $R65_{hASIC3}$, $R68_{hASIC3}$, and $Y58_{hASIC3}$.

2.5 Results

In order to computationally investigate lipid interactions with ASICs, we employed the MARTINI forcefield and performed CG MD simulations (Marrink et al., 2007). By restraining the channel to its original conformation and allowing lipids to sample the transmembrane surface of the protein, we were able to sample sites that are specific to the structurally resolved conformation of the protein. At the time when simulations were initiated, the only solved ASIC structures available were those of chicken ASIC1 without a resolved ICD. We therefore used these available structures to create homology models of hASIC1a and hASIC3. Subsequently, additional ASIC structures were solved of hASIC1a in an inhibited state (Wu et al., 2021) and chicken ASIC1 with additional ICD regions resolved in the form of re-entrant loops (Yoder and Gouaux, 2020). No structure of the ASIC protein is yet available in the open state with resolved re-entrant loops. For these reasons, in order to specifically sample AA interactions with the open and resting states of the channel, we continued to use homology models of hASIC1 and hASIC3 created from the chicken ASIC1 structures without the ICD, as outlined in the Materials and methods section. Furthermore, due to only the incomplete structures being available at the time, we chose to focus on AA interactions with the extracellular half of the TMD. In a recent study, it was demonstrated that fatty acids act on the channel in the extracellular membrane leaflet (Klipp and Bankston, 2022), making it likely that key interacting residues are located towards the extracellular end of the TMD. It was shown in the more recent structures of chicken ASIC1 in the desensitized state that the conformation of the TMD helices near the intracellular side appears unaffected by the presence of re-entrant ICD helices, although the side chain orientations in this region are altered (Yoder and Gouaux, 2020). Given the minimal effect of the re-entrant loop on the overall structure, we therefore assumed that

lipid interactions in the upper TMD region are not affected by the missing ICD re-entrant helices in our models.

AA specifically localizes to hASIC3 and hASIC1a channels

AA has been postulated to affect ASIC function through direct binding to the channel, rather than through membrane deformation (Smith et al., 2007). We wanted to test whether AA interacts specifically with ASICs in silico. We first investigated whether hASIC1a and hASIC3 preferentially interacted with AA in a membrane containing 10% LPC, 80% POPC, and 10% AA. As outlined above, we focus on the extracellular side of the TMD due to uncertainty of the structure of the intracellular component of the TMD. From a total of three 30 μs simulations per system, the average lipid occupancy was calculated using either all 60 AA carboxylic acid headgroups, or 60 randomly selected POPC headgroups for comparison. The AA carboxylic acid headgroups showed a higher average occupancy near the open state hASIC3 transmembrane domain in comparison to the POPC headgroups (Figure 2.2). AA also specifically localized around hASIC1, albeit at a slightly lower apparent density than for hASIC3. In both cases, the AA occupancy was especially high around the outer region of TM1, the outer transmembrane helix of ASIC (Figure 2.1). Interestingly, the general region of POPC localization correlated with electron densities attributed to lipids in recent structures (Yoder and Gouaux, 2020), showing possible lipid tail density at the lipid-exposed surface of TM2 (Fig. 2). On the contrary, AA density localized at TM1, toward the periphery of the channel (density from simulations only). This supports the idea that AA exhibits specific interactions with ASICs, which differs from that of phospholipids such as POPC.

Figure 2.2 AA accumulates around ASICs. AA headgroup occupancy maps colored by occupancy as a fraction of frames. **(A)** Occupancy of AA headgroups, as defined by the charged COO bead, around hASIC3 channel. **(B)** Occupancy of AA headgroups around hASIC1 channel. **(C)** Occupancy of a subsample of 60 randomly selected POPC headgroups, as defined by the PO4 bead, around hASIC3 channel. Maps show an average of occupancy across three repeats of 30 μs simulations for each system. The systems were aligned on the TMD of the protein prior to calculating the occupancy. Top-down view of hASIC3 homology model TMD is displayed as surface and colored as in Fig. 1. **(D)** Left: Example of calculated AA density from 500 ns atomistic simulation of hASIC3 open state. Middle: Example of calculated POPC density from 100 ns atomistic simulation. Right: Electron density attributed to lipids in recently solved chicken ASIC1 desensitized state structure (PDB: 6VTK; Yoder et al., 2020).

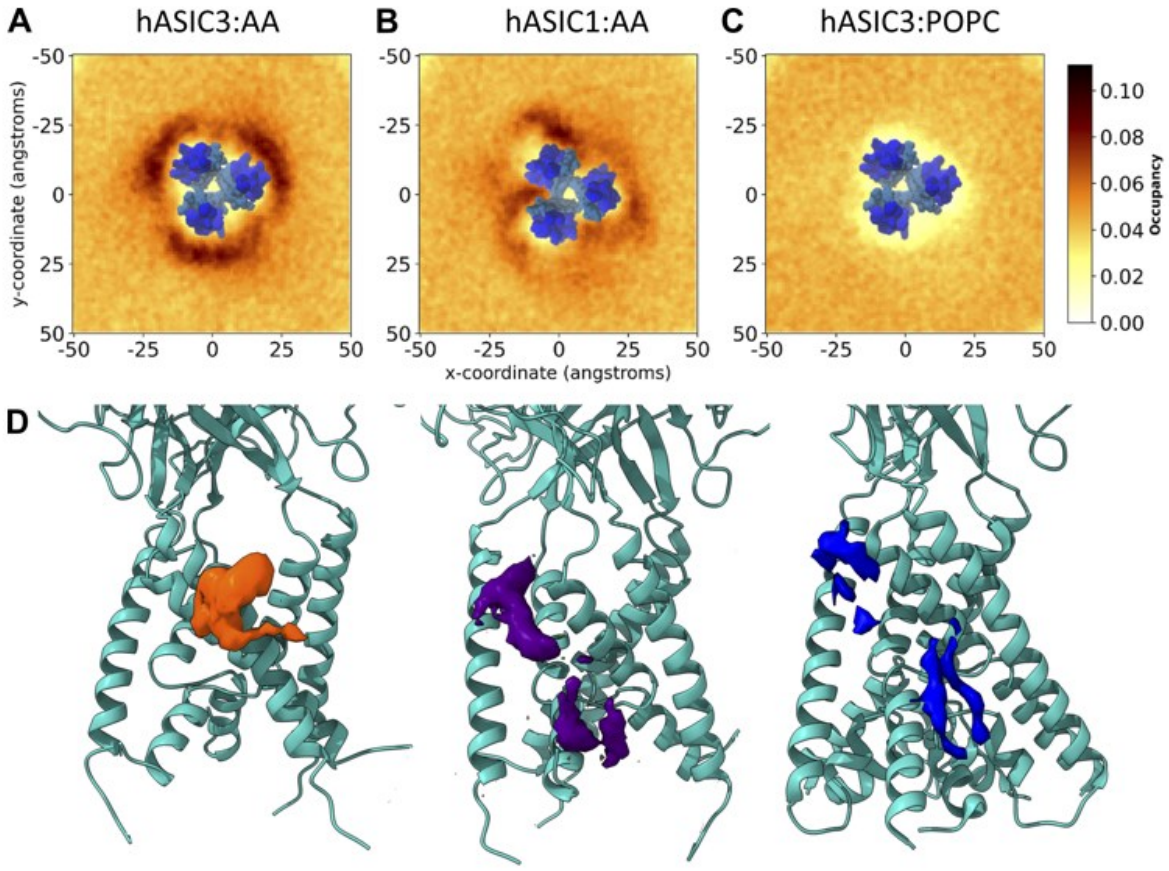
A
hASIC3:AA
B
hASIC1:AA
C
hASIC3:POPC
y-coordinate (angstroms)
x-coordinate (angstroms)
-50
-25
0
25
50
Occupancy
0.10
0.08
0.06
0.04
0.02
0.00
D

AA interacts at upper TM1 residues

First, using our models of hASIC3 in the open and resting state, we set out to identify transmembrane sites which participate in interactions with AA. We first compared AA occupancies between the open and resting states of hASIC3. Occupancy is measured as a percentage of total simulation time in which any AA molecule is within range of a lower distance cutoff (4.75 Å) from any bead of a residue. Distance cutoffs were previously optimized by sampling lipid interactions with a variety of distance cutoffs as described for the PyLipID method (Song et al., 2022). A lower cutoff of 4.75 Å was sufficiently short to select for specific interactions between AA and ASICs, while also allowing for sufficient sampling of lipid binding sites (Figure 2.11). Surprisingly, AA occupancy did not appreciably differ between the two hASIC3 states (Figure 2.3 A). An example of AA sampling the hASIC3 open state TMD is illustrated in Video 1. For further comparison, we measured the average AA interaction duration time for the TMD residues (Figure 2.3 B), with an interaction considered to begin when an AA molecule is within range of the lower cutoff, and continuing until the molecule exits the upper cut-off range of 1.1 Å. Notably, the hASIC3 open state model exhibited longer interactions at R63, a residue lining the lateral fenestrations (Figure 2.1 A) and previously suggested to be involved in AA interactions with ASIC (Klipp and Bankston, 2022), as well as in the proton sensitivity of the channel (Chen et al., 2021).

Figure 2.3 AA participates in longer interactions with hASIC3 open state compared to resting state. A. Occupancies of AA at TM1 residues for the hASIC3 open state in cyan and the resting state in light blue. **B.** Average interaction duration of AA at TM1 residues. All values calculated as averages over three chains in three repeats of 30 μs (i.e., each value is an average of nine samples). Standard deviations are shown as black lines. Bars represent averages, while points represent individual samples.

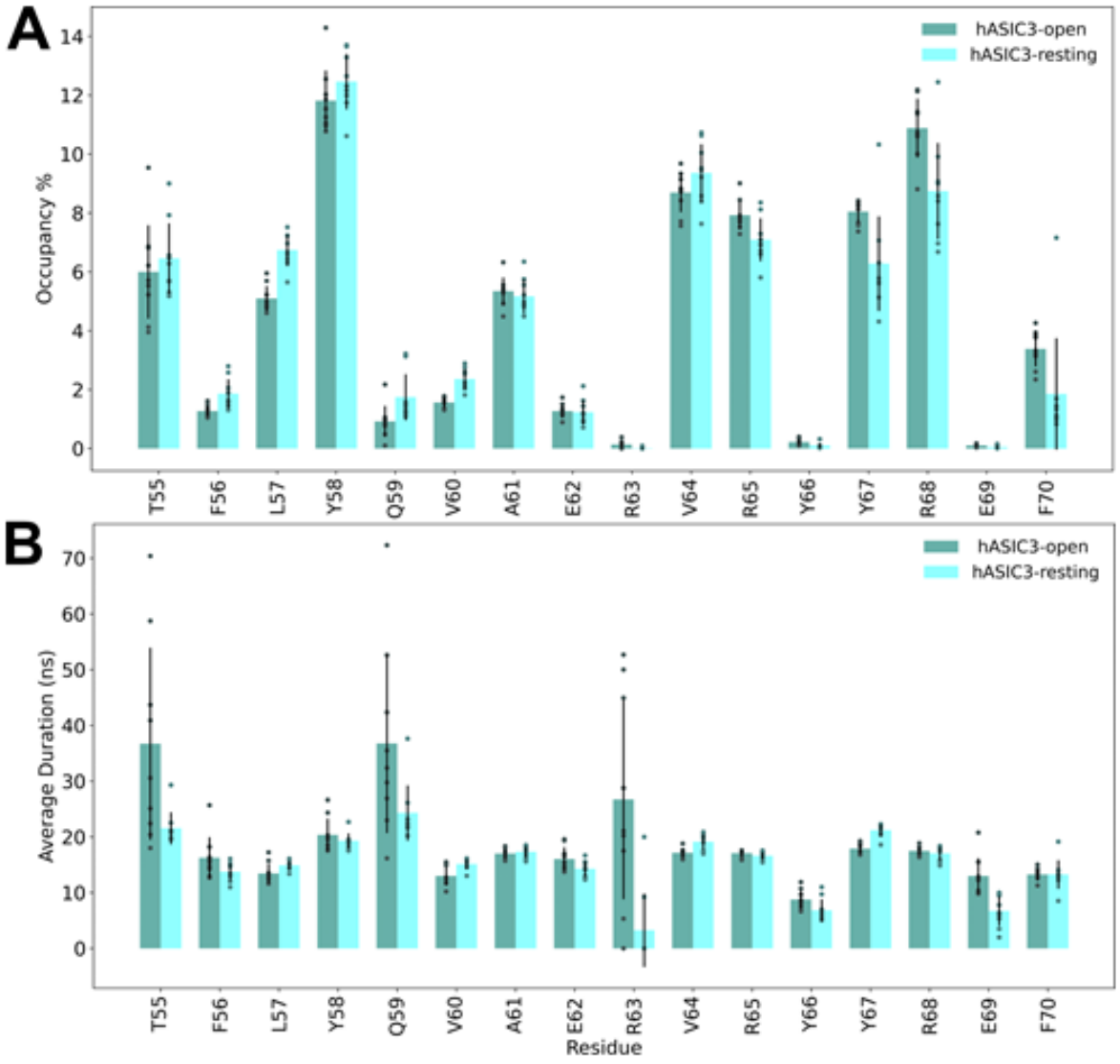
A
Occupancy %
hASIC3-open
hASIC3-resting
T55
F56
L57
Y58
Q59
V60
A61
E62
R63
V64
R65
Y66
Y67
R68
E69
F70
B
Average Duration (ns)
Residue

We then set out to elucidate the structural determinants of specific AA interactions with the hASIC1 and hASIC3 transmembrane domains in the open state. Such determinants were expected to account for specific interaction of AA with ASICs and furthermore illustrate a level of conservation of a potential AA binding site between hASIC1 and hASIC3. To determine which residues of the TM domain AA preferentially interacts with, if any, we calculated the occupancy of AA at each residue in TM1 and TM2 in the same way as for Figure 2.3 A. The occupancy was calculated as an average for three homomeric chains in three 30 μs simulations in both hASIC1 and hASIC3, respectively, thereby predicting which residues are potential interacting partners for AA. Such residues could constitute a potential binding site. We compared occupancies at each residue in the upper region of TM1 (Figure 2.4 A) and TM2 (Figure 2.4 B) between hASIC1 and hASIC3 to identify conserved interactions but also predict potential interactions that may account for the subtle differences in overall occupancy as seen above (Figure 2.2).

Figure 2.4 AA interacts preferably with residues located at the extracellular side of TM1. AA occupancy at residues in the upper region of the TM1 and TM2 helices calculated as averages over three chains in three repeats of 30 μs each. Residues on the x-axis are labeled with the hASIC3 residue on the left and the hASIC1a residue on the right, in the form hASIC3/hASIC1a. **A.** Occupancies of AA at TM1 residues for hASIC3 in cyan and hASIC1a in orange. Black lines show standard deviations, bars show averages, and points show individual samples. **B.** Occupancies of AA at TM2 residues (colors like A). **C.** The same occupancy information as in A and B presented as a heatmap superimposed on models of hASIC1a and hASIC3.

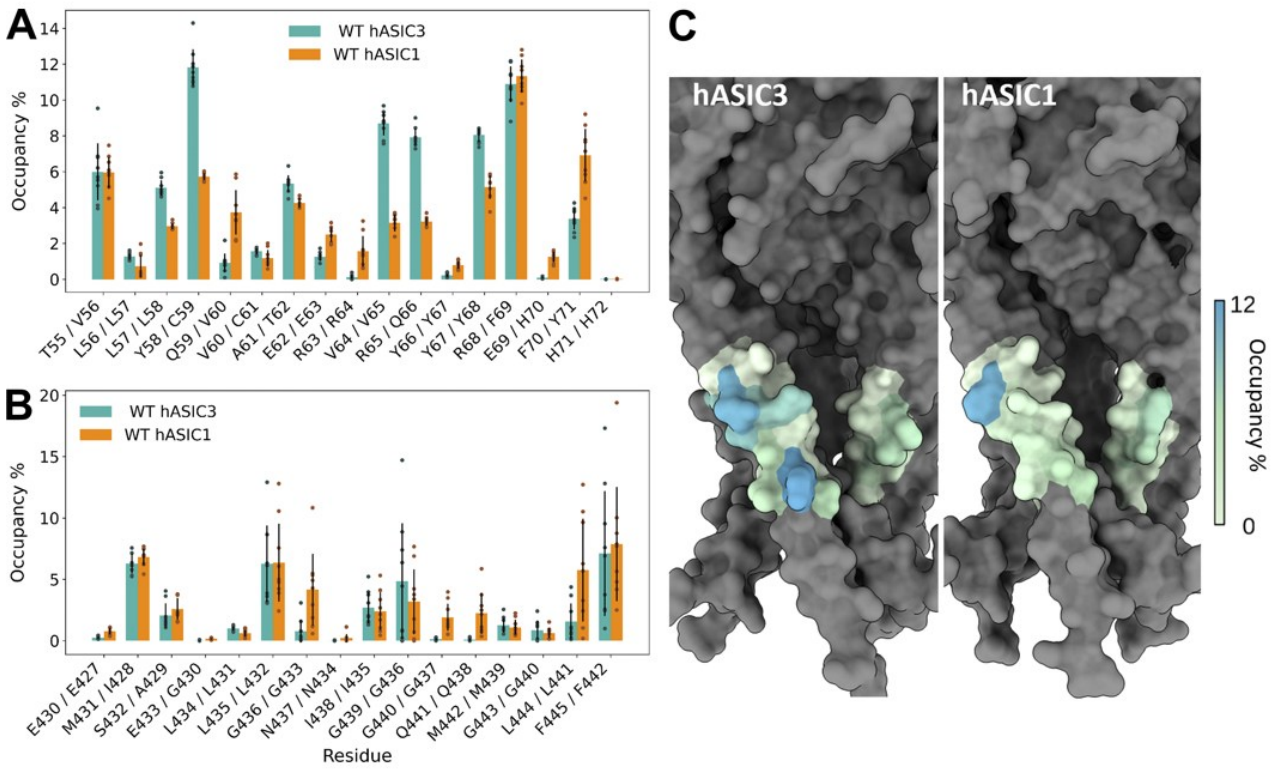
A
WT hASIC3
WT hASIC1
Occupancy %
T55 / V56
L56 / L57
L57 / L58
Y58 / C59
Q59 / V60
V60 / C61
A61 / T62
E62 / E63
R63 / R64
V64 / V65
R65 / Q66
Y66 / Y67
Y67 / Y68
R68 / F69
E69 / H70
F70 / Y71
H71 / H72
B
WT hASIC3
WT hASIC1
Occupancy %
E430 / E427
M431 / I428
S432 / A429
E433 / G430
L434 / L431
L435 / L432
G436 / G433
N437 / N434
I438 / I435
G439 / G436
G440 / G437
Q441 / Q438
M442 / M439
G443 / G440
L444 / L441
F445 / F442
Residue
C
hASIC3
hASIC1
12
Occupancy %
0

There were no clear differences in occupancies at residues in TM2 (Figure 2.4 B) between hASIC1 and hASIC3. Although certain residues in TM2 have high occupancies, their large variability between chains and simulations, as shown by the standard deviations, make this data unclear. Likely, this is due to the reduction in lipid accessibility of TM2 compared to TM1, resulting in less frequent lipid interactions and therefore less sampling. However, there were residues of particular interest in TM1. Occupancy was high at both $R68_{hASIC3}$ in hASIC3 and $F69_{hASIC1}$ in hASIC1—the occupancy at these residues was above 10% and thus higher than expected given the AA concentration of the membrane. Occupancies at $Y58_{hASIC3}$, $R65_{hASIC3}$, and $Y67_{hASIC3}$ were noticeably higher in hASIC3 than for the equivalent residues in hASIC1 (Figure 2.4 A and C). We also observed higher occupancy at $V64_{hASIC3}$; however, we rationalized that this higher occupancy at valine may be a product of its adjacency to $R65_{hASIC3}$. On the other hand, the AA occupancy at $Y71_{hASIC1}$ in hASIC1 was approximately twofold higher than at $F70_{hASIC3}$ in hASIC3. Interestingly, despite AA modulating, and therefore interacting with, both ASIC subtypes, $Y58_{hASIC3}$ and $R65_{hASIC3}$ are conserved in the ASIC3 subtype, but not ASIC1, while $Y71_{hASIC1}$ is conserved in the ASIC1 subtype, but not ASIC3 (Figure 2.5 A). We next wondered whether the two identified hASIC3 residues, $Y58_{hASIC3}$ and $R65_{hASIC3}$, could constitute a single AA binding site on hASIC3. A representative binding pose from PyLipID analysis (Figure 2.5 B) supports the presence of such a site. Briefly, binding sites are predicted based on community analysis of interaction networks. The most sampled binding poses are then clustered and scored based on density. This method is described in detail in Song et al. (2022). These data may suggest that while both hASIC1a and hASIC3 interact with AA at the outer leaflet region of TM1, the specific binding motif may vary somewhat between the two subtypes.

Figure 2.5 Interaction site residues differ between subunit types. A. Alignment of the upper part of TM1 for ASIC1 and ASIC3 subtypes from different species. **B.** Representative binding pose (CG representation) of AA at conserved ASIC3 residues determined by PyLipID clustering analysis, as described in Song et al. (2022). The red bead near R65 represents the charged headgroup as defined by the COO bead.

A

Chicken ASIC1	60-	L	V	C	T	N	R	I	Q	Y	Y	F	L	Y-	72
Human ASIC1a	59-	C	V	C	T	E	R	V	Q	Y	Y	F	H	Y-	71
Rat ASIC1a	59-	C	V	C	T	E	R	V	Q	Y	Y	F	C	Y-	71
Mouse ASIC1a	59-	C	V	C	T	E	R	V	Q	Y	Y	F	C	Y-	71
Human ASIC3	58-	Y	Q	V	A	E	R	V	R	Y	Y	R	E	F-	70
Rat ASIC3	59-	Y	Q	V	A	E	R	V	R	Y	Y	G	E	F-	71
Mouse ASIC3	59-	Y	Q	V	A	E	R	V	R	Y	Y	G	E	F-	71

B

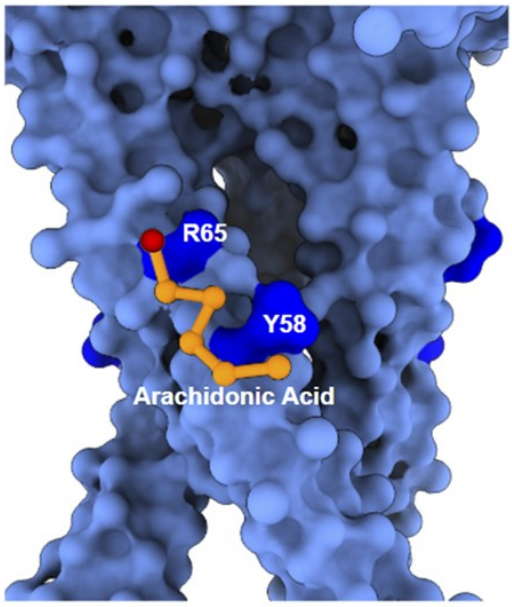

AA forms a putative stable salt bridge with R65

Given that hASIC3 had slightly higher AA occupancy overall compared to hASIC1a, we backmapped selected simulation frames from our hASIC3 CG simulations to atomistic resolution for further simulations of 500 ns to determine whether the interactions observed in coarse-grained simulations remained stable. We observed further time-resolved AA interactions with $R65_{hASIC3}$ and $Y58_{hASIC3}$ (Movies 2.2 and 2.3), as well as notable salt bridge interactions with $R68_{hASCI3}$. Defining an interaction as a distance <4.5 Å between a non-hydrogen atom of AA and a non-hydrogen atom of a protein residue, we observed that an interaction is present >50% of the total trajectory length between $R65_{hASIC3}$ and an AA headgroup in some individual chains of ASIC. Taking the chains together, this interaction is present at 100% of the trajectory in at least one of three chains (Figure 2.6 and 2.12). Taking the initially bound AA molecules, we measured the distance between the carboxylic acid carbon atom and the C-ζ atom of the arginine that it was interacting with. Stable interactions (distance <4.5 Å) were observed in all chains, with stable interactions lasting as long as 300 ns (Figure 2.6 and 2.12). This interaction appears to be a salt bridge between the carboxylic acid of AA and the guanidinium group of $R65_{hASIC3}$ (Figure 2.6 C). The AA carboxylic acid headgroup can also form occasional simultaneous salt bridges with $R65_{hASIC3}$ and $R68_{hASIC3}$ (Movies 2.2 and 2.3). These observations from our atomistic simulations support that ASICs can stably bind AA.

Figure 2.6 AA shows long-lived interactions with protein sites in atomistic simulations. A. Time-resolved occupancy of AA at three sites in one of three 500 ns repeats of a backmapped atomistic setup. Dark blue indicates presence of AA, i.e., when the carboxylic acid carbon of AA is within 4.5 Å of the $R65_{hASIC3}$ sidechain. **B.** Distances between the carboxylic acid carbon of AA and ζ-carbon of $R65_{hASIC3}$ over time of three initially bound AA molecules at three chains. **C.** An example of a putative salt bridge interaction between the headgroup of AA and guanidinium groups of $R65_{hASIC3}$ and $R68_{hASIC3}$, with a potential van der Waals interaction of the AA tail with $Y58_{hASIC3}$. The protein structure is shown in cyan cartoon, while residues of interest are shown as sticks with carbon atoms colored in cyan. AA is shown as stick representation with carbon atoms colored in orange.

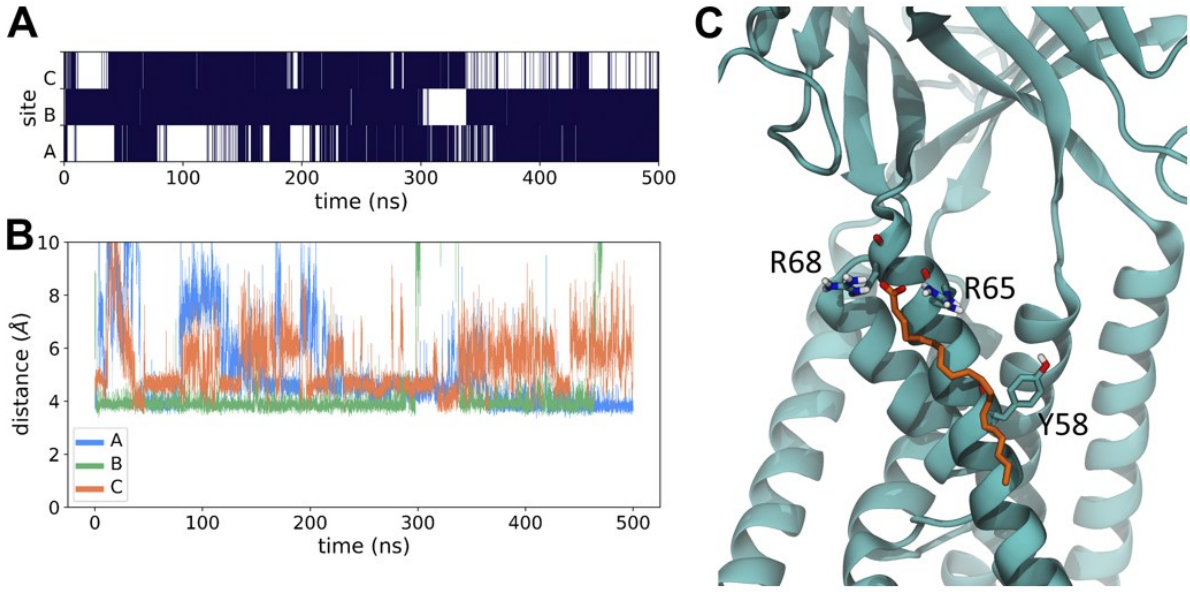
A
site
C
B
A
0
100
200
300
400
500
time (ns)
B
distance (Å)
10
8
6
4
2
0
A
B
C
0
100
200
300
400
500
time (ns)
C
R68
R65
Y58

Mutation of three key interacting residues reverses AA interaction pattern

To investigate whether the two identified residues with high AA occupancy ($Y58_{hASIC3}$, $R65_{hASIC3}$), and the additional coordinating residue $R68_{hASIC3}$, influence the overall interaction pattern of AA at the hASIC1/3 TM1, we mutated the three sites in hASIC3 to their equivalent residues in hASIC1 and vice versa. We saw that simulating hASIC3 with the mutations Y58C, R65Q, and R68F in a 90:10 POPC:AA membrane yielded a TM1 interaction pattern similar to wild-type hASIC1 (Figure 2.7 A). hASIC1 with the reverse mutations (C59Y, Q66R, F69R) yielded a similar pattern to wild-type hASIC3 (Figure 2.7 B). Significantly, these three mutations changed the overall occupancy at all residues in the upper portion of TM1, and not only at these three positions (Figure 2.7). We speculate therefore that these three sites could be responsible for the subtle differences in overall occupancy between hASIC1a and hASIC3 observed in Figure 2.2 and give rise to different binding motifs on the two channels, despite the similarity in modulation.

Figure 2.7 Mutations to three key residues change AA interaction pattern. A. AA occupancy comparison between WT hASIC3 (cyan) and triple mutant hASIC3 (orange). The occupancy data is averaged over three chains from three repeats simulated for 30 μs each, and standard deviations are shown with black lines. Bars show averages while points show individual samples. Residue numbering corresponds to hASIC3. **B.** AA occupancy comparison between WT hASIC3 (cyan) and triple mutant hASIC1a (orange). Mutated residues are indicated with arrowheads. Residue numbering corresponds to hASIC1a.

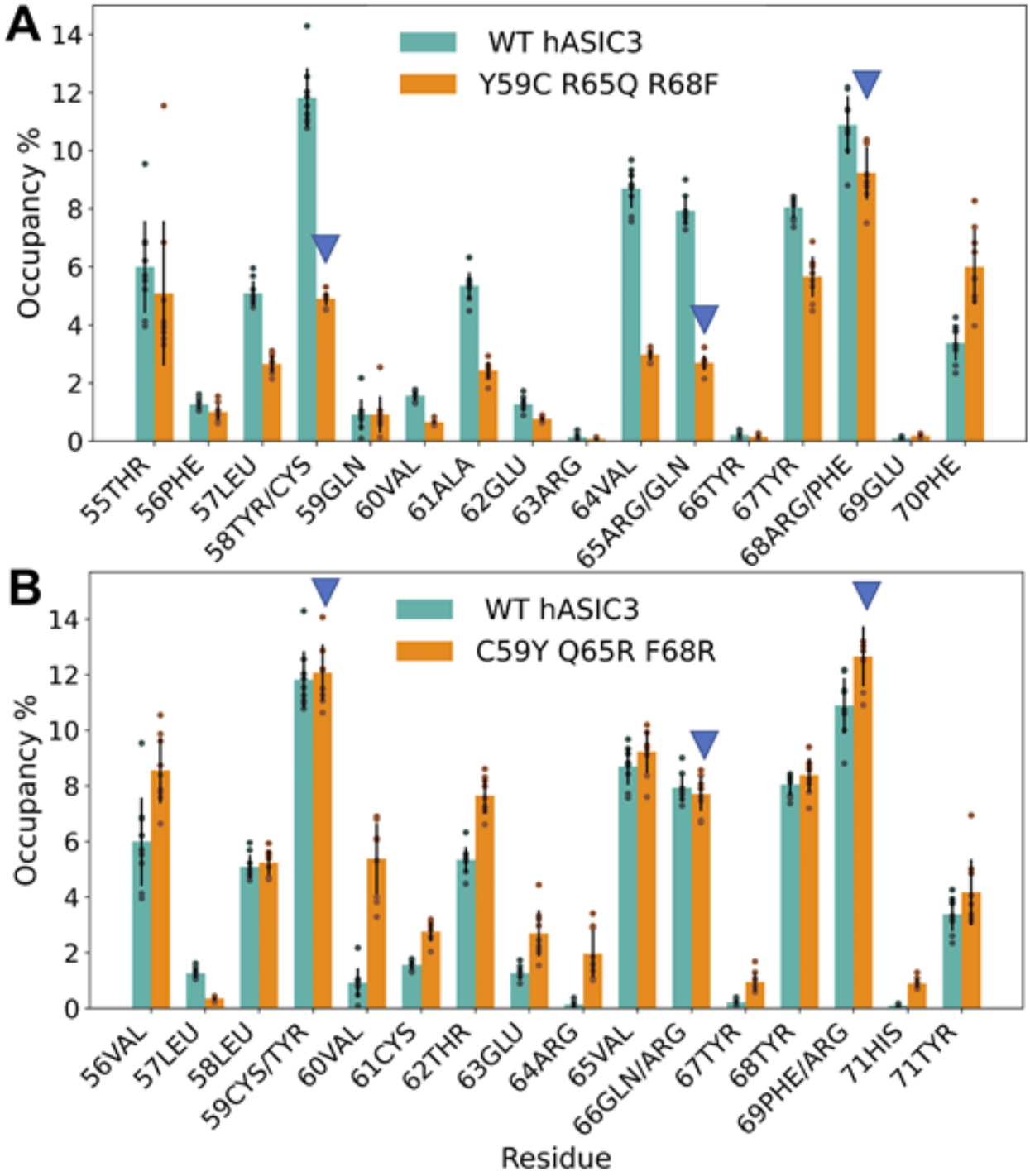
A
WT hASIC3
Y59C R65Q R68F
Occupancy %
0
2
4
6
8
10
12
14
55THR
56PHE
57LEU
58TYR/CYS
59GLN
60VAL
61ALA
62GLU
63ARG
64VAL
65ARG/GLN
66TYR
67TYR
68ARG/PHE
69GLU
70PHE
B
WT hASIC3
C59Y Q65R F68R
Occupancy %
0
2
4
6
8
10
12
14
56VAL
57LEU
58LEU
59CYS/TYR
60VAL
61CYS
62THR
63GLU
64ARG
65VAL
66GLN/ARG
67TYR
68TYR
69PHE/ARG
71HIS
71TYR
Residue

Fatty acid interactions with ASIC are correlated with acyl chain length and saturation

Early studies showed that a larger number of double bonds in the fatty acid tail increased ASIC potentiation by fatty acids, whereas a smaller number of double bonds decreased potentiation (Smith et al., 2007). Similarly, it has been shown that at least three double bonds are required for potentiation by fatty acids with 20- or 22-carbon tails (Klipp and Bankston, 2022). It was therefore suggested that the number of double bonds determines the degree of potentiation (Klipp and Bankston, 2022). Furthermore, cis double bonds, specifically, increase the flexibility of fatty acid tails and can potentiate, e.g., voltage-gated ion channels (Elinder and Liin, 2017). Fatty acids with trans double bonds, on the other hand, are ineffective.

Thus, we probed whether changing the acyl tail length or saturation affected the occupancy of fatty acids at the ASIC transmembrane domain. We speculated that increasing PUFA tail unsaturation increased tail flexibility, and thus allowed for fatty acid positioning at the slightly concave transmembrane domain of ASICs. Indeed, DHA, which has six cis double bonds and a 22-carbon tail, showed an overall slightly higher occupancy along the upper TM1 residues with a conserved binding pattern, compared to AA. In contrast, palmitic acid, which has 16 carbon atoms in its tail and no double bonds, has significantly decreased occupancy for all residues (Figure 2.8). Our data therefore support that for AA interactions with ASICs, a flexible tail with multiple cis double bonds is indeed required. This is consistent with recent functional data (Klipp and Bankston, 2022) showing that multiple cis double bonds as well as a negatively charged headgroup are important in interactions with the ASIC channel.

Figure 2.8 Fatty acid tail length and saturation affect interactions with hASIC3. **A.** Occupancies of palmitic (C16:0), arachidonic (C20:4), and docosahexaenoic (C22:6) acid at the TM1 helix. **B.** Occupancies of palmitic, arachidonic, and docosahexaenoic acid at the TM2 helix. The occupancy data is averaged over three chains from three repeats simulated for 30 μs each, and standard deviations are shown with black lines. Bars represent averages while points represent individual samples.

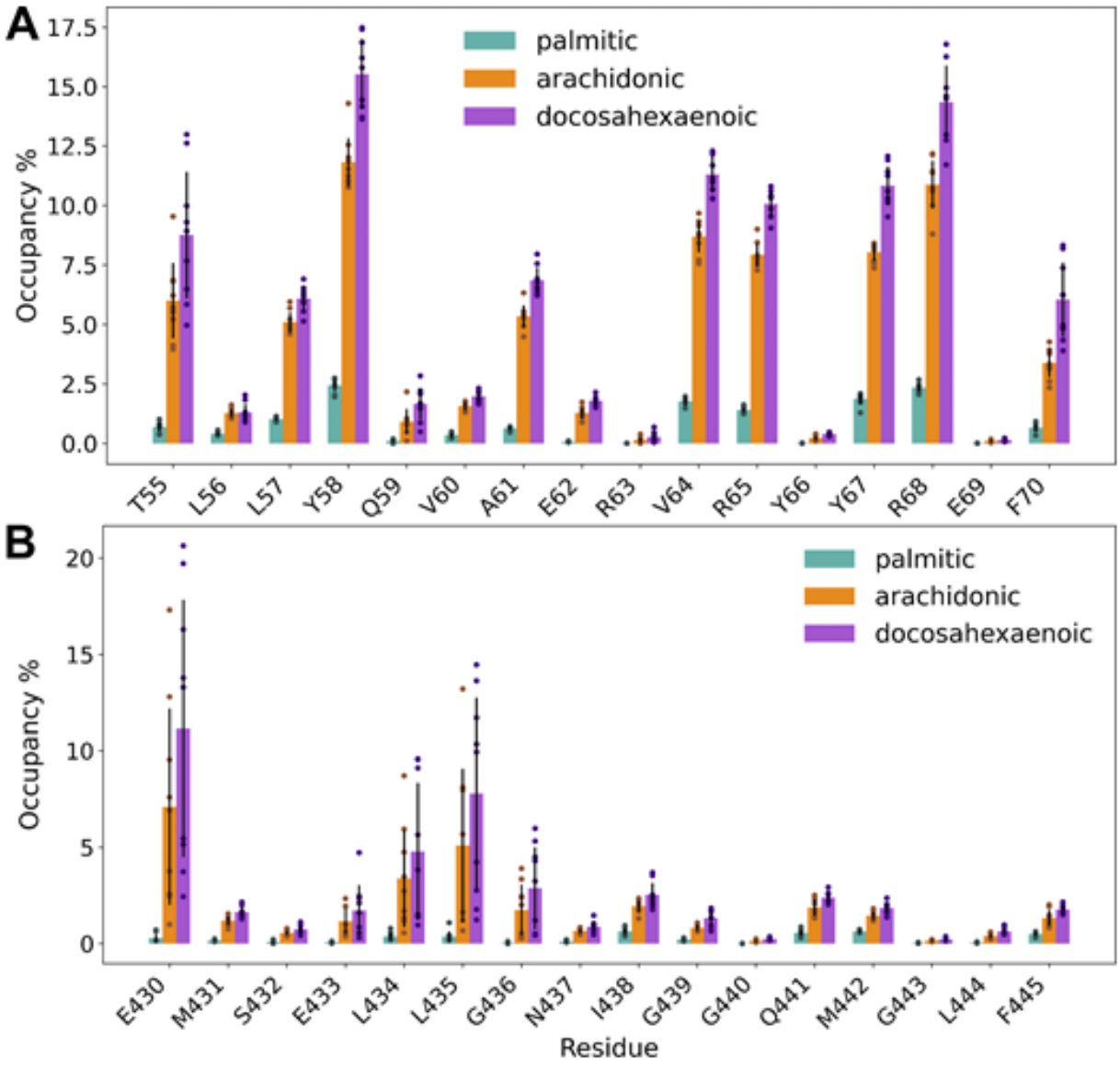
A
Occupancy %
17.5
15.0
12.5
10.0
7.5
5.0
2.5
0.0
palmitic
arachidonic
docosahexaenoic
T55
L56
L57
Y58
Q59
V60
A61
E62
R63
V64
R65
Y66
Y67
R68
E69
F70
B
Occupancy %
20
15
10
5
0
palmitic
arachidonic
docosahexaenoic
E430
M431
S432
E433
L434
L435
G436
N437
I438
G439
G440
Q441
M442
G443
L444
F445
Residue

AA effects on ASIC are not likely caused by changes in membrane curvature

We noticed that R65 is located slightly below the polar headgroup region of the membrane bilayer, with AA therefore interacting with this residue below the overall headgroup region. We wondered whether binding of AA at the ASIC TMD could create a local deviation in the membrane curvature immediately adjacent to the lateral fenestrations located in the upper region of the TMD (Figure 2.1), which have been proposed to conduct ions through the pore (Gründer and Chen, 2010). This could subsequently increase the ion flow through the fenestrations and present a possible mechanism for ASIC modulation by AA and alter pH dependence of the channel by influencing Imax overall and thereby shifting the pH50 activation curve. To probe this, we analyzed the local membrane curvature surrounding the open state of hASIC3 in a 10% AA membrane as well as that in a pure POPC membrane. We did not observe a noticeable difference in local membrane curvature between the two membrane types (Figure 2.9). We therefore proposed that modulation of ASICs by AA occurs through direct structural changes due to AA biding, which are likely to occur at a timescale beyond the current capabilities of our atomistic simulations.

Figure 2.9 Average upper leaflet membrane curvature around ASIC3 TMD in 10% AA and 0% AA membranes. A. Local membrane curvature averaged over each of the three repeats of 500 ns atomistic simulations in membranes containing 10% AA. Surface is colored by degree of deviation from membrane normal; positive deviation is colored in blue and negative deviation is colored in red. Analysis developed by Lea Thøgersen, as used in Sonntag et al. (2011). **B.** Local membrane curvature in three repeats of 500 ns atomistic simulations in POPC-only membranes. **C.** Local membrane curvature with embedded ASIC3 average structure (cyan cartoon) in one simulation repeat with a membrane containing 10% AA.

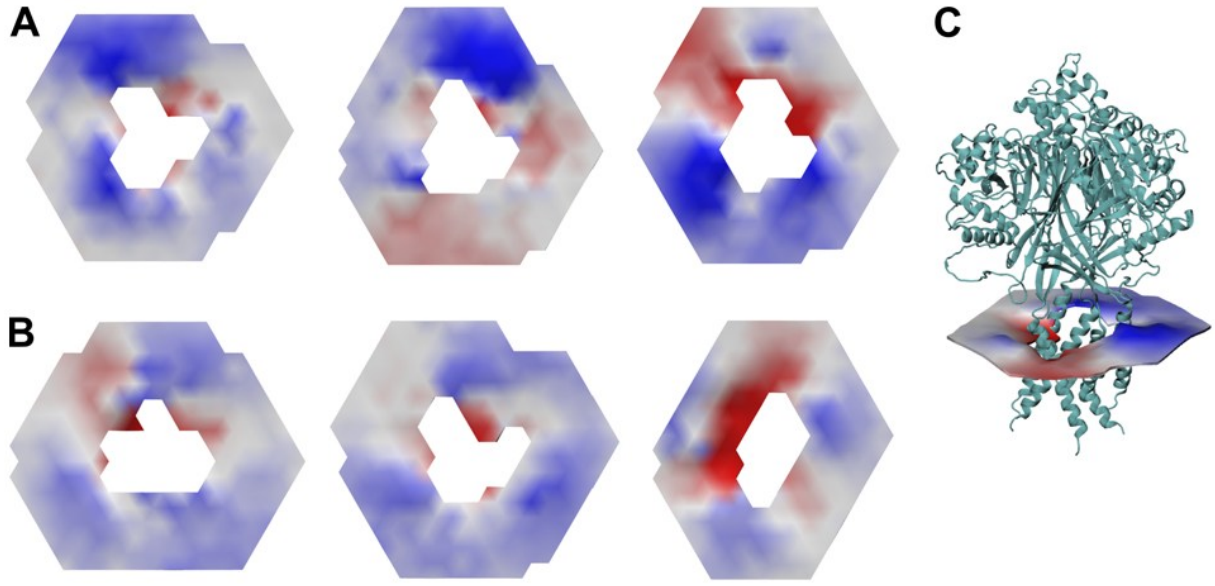
A
B
C

2.6 Discussion

In this molecular dynamics simulation study, we have described a potential AA binding pattern for ASICs. Both hASIC3 and hASIC1a exhibit accumulation of AA and high-occupancy AA interactions at the outer leaflet region of TM1, albeit with differences in the pattern of coordinating residues. AA interacts with hASIC3 primarily at three residues; $Y58_{hASIC3}$, $R65_{hASIC3}$, and $R68_{hASIC3}$, with $Y58_{hASIC3}$ and $R65_{hASIC3}$ conserved among the ASIC3 subtype. On the other hand, the residue $Y71_{hASIC1}$, which is conserved in the ASIC1 subtype, exhibits high occupancy interactions in hASIC1. If these interactions play a role in the modulatory effects of AA, these residues could therefore cause potential differences in the extent of lipid modulation of these two ASIC subtypes, affecting perhaps affinity or efficacy. Furthermore, by comparing AA occupancies to those of other fatty acids, we show that fatty acid tail length and number of double bonds may be important to their affinity to ASICs. This finding agrees with experimental data illustrating functional differences depending on the number of double bonds or the tail length (Smith et al., 2007; Elinder and Liin, 2017; Klipp and Bankston, 2022).

n both ASIC subtypes, our simulations suggest that the charged fatty acid headgroup participates in electrostatic/polar interactions with residues in the upper region of TM1, while the tail interacts with hydrophobic residues several turns lower on the same helix. We proposed that in hASIC3, the charged AA headgroup forms salt bridges with $R65_{hASIC3}$ and $R68_{hASIC3}$, while in hASIC1, AA could form an ion–dipole interaction with $Y71_{hASIC1}$. Our atomistic simulations support that AA participates in stable interactions with $R65_{hASIC3.}$

Since R65 and R68 are on the same face of TM1 in hASIC3, we speculate that these two residues could contribute to a region of positive electrostatic potential in this area. Compared to hASIC1, which does not have positively charged residues in this region, this could create a larger

accumulation of AA in the upper TM1 region, as was seen in our simulations (Figure 2.2). We proposed that this slightly higher degree of attraction, and therefore greater degree of AA accumulation, could affect the affinity or efficacy of hASIC3 modulation by AA.

Surprisingly, we did not see high AA occupancy at the arginine at position 63_{hASIC3}, which is conserved among both ASIC3 and ASIC1 types. We did, however, despite this low occupancy, see relatively longer-lived interactions at this residue in the open state of our hASIC3 model compared to the resting state. This could suggest that, although MD simulations are not able to capture extensive interactions between AA and $R63_{hASIC3}$, this residue could participate in AA interactions and constitute part of the modulatory mechanism. In a recent study, mutation of this arginine residue to glutamine in rat ASIC3 and ASIC1a eliminated potentiation by the fatty acid DHA (Klipp and Bankston, 2022). We proposed two reasons for this discrepancy between our CG molecular dynamics (CG-MD) simulations and the electrophysiology results. Firstly, $R63_{hASIC3}$, compared to $R65_{hASIC3}$ and $R68_{hASIC3}$, is oriented toward the TMD helix bundle rather than toward the membrane environment. Since we restrained the tertiary and quaternary structure of ASIC to the conformation of the solved crystal structure, the position of the TMD helices cannot readily change to accommodate lipid binding between tightly packed helices. However, without restraints, protein secondary and tertiary structure does not remain stable in CG simulations. Therefore, in our simulations, $R63_{hASIC3}$ is less solvent exposed and does not interact readily with AA, potentially due to the inherent properties of CG-MD. Furthermore, we did not observe interactions between AA and $R63_{hASIC3}$ in our atomistic simulations, in which the protein was unrestrained, although this lack of sampling could additionally be caused by the relatively shorter timescales of atomistic simulations. This may also suggest that this residue remains poorly solvent exposed even when restraints are removed, at least in our hands.

Moreover, the structure of the resting state of chicken ASIC1 shows a possible salt bridge between $R65_{cASIC1}$ and $E413_{cASIC1}$, which is broken in the open state structure (Figure 2.10 A and B). The corresponding interaction between $R63_{hASIC3}$ and $E430_{hASIC3}$ remains stable in our atomistic simulations of the resting state of hASIC3 (Figure 2.10 C) but only sometimes re-forms in simulations of the open state (Figure 2.10 D). An $R63Q_{hASIC3}$ mutation will eliminate this salt bridge, and in doing so, potentially destabilize the resting state of the channel. This is supported by the fact that, in the absence of potentiating fatty acids, this mutation still shifted the pH50 of both rat ASIC1a and ASIC3 to slightly more alkaline pH (Klipp and Bankston, 2022). In rat ASIC3, this shift in pH50 caused by the $R63Q_{hASIC3}$ mutation was similar to that observed for WT ASIC3 when potentiated by DHA (Klipp and Bankston, 2022). The equivalent residue has also been previously shown to be involved in proton-mediated gating of hASIC1 (Chen et al., 2021). It is therefore unclear whether this mutation is directly involved in AA binding, or whether it is involved in structural changes relating to the activation and gating of the ASIC channel. To build on these experimental findings, as well as our simulation data, we suggest that $R63_{hASIC3}$ could be involved in ASIC modulation by AA, but the mechanism may be more complex and involve a conformational bias toward the open state of the channel.

Figure 2.10 Potential salt bridge between R63 hASIC3 and E430 hASIC3 . **(A)** Top-down view of the transmembrane domain of a structure of the cASIC1 resting state (PDB: 5WKU) shown as cyan cartoon. Conserved residues $R65_{cASICa}$ and $E413_{cASIC1}$ are shown as sticks. **(B)** The same representation as A, however, of the open state structure of cASIC1 (PDB: 4NTW). A change in the position of $R65_{cASIC1}$ and $E413_{cASIC1}$ suggests a breaking of this salt bridge in the open state of the channel upon rotation and opening of the TM helices. **(C)** Position of residues $R63_{hASIC3}$ and $E430_{hASIC3}$ sampled in one atomistic simulation of the resting hASIC3 state. **(D)** Position of residues $R63_{hASIC3}$ and $E430_{hASIC3}$ sampled in one atomistic simulation of the open hASIC3 state.

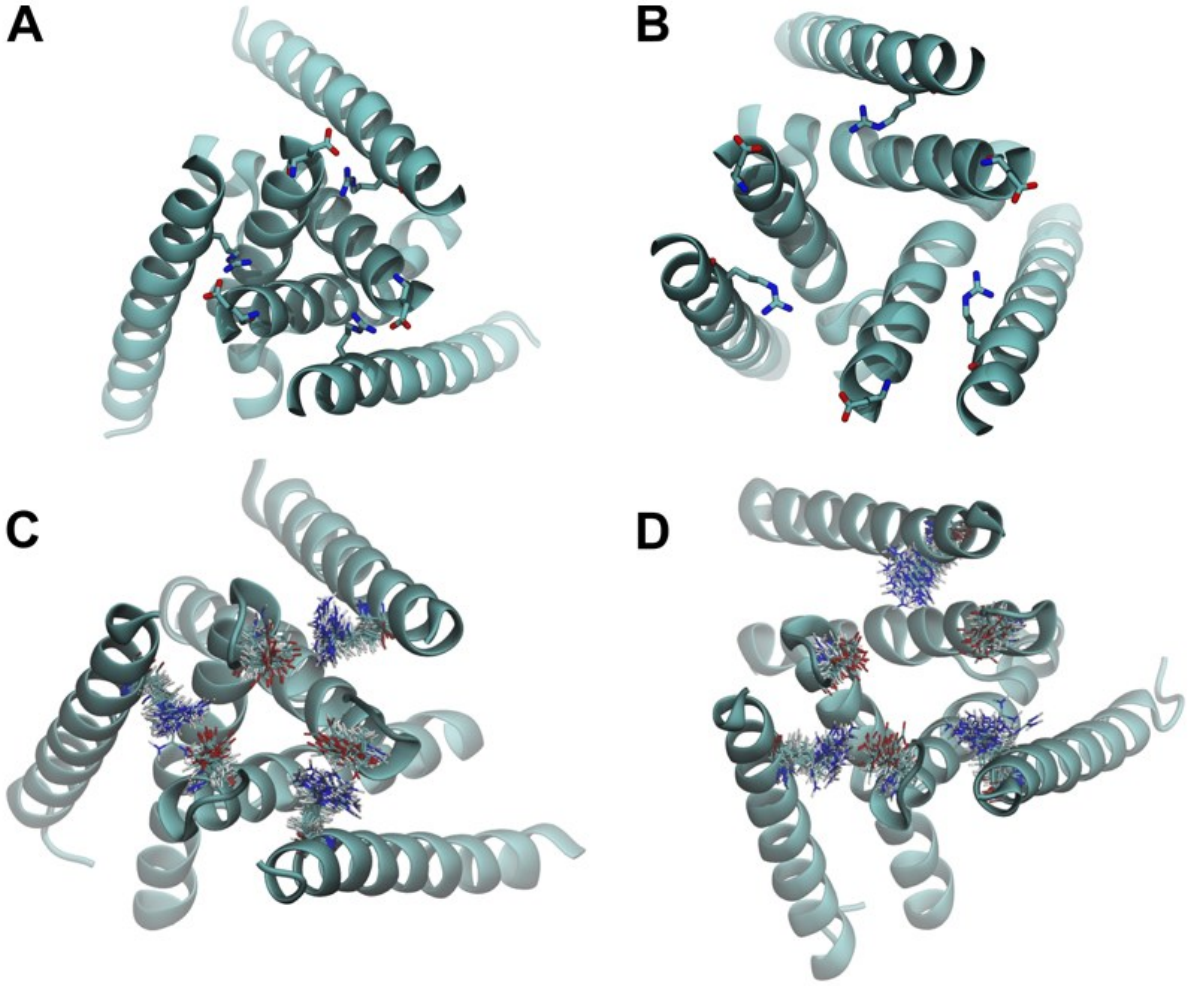
A
B
C
D

We finally predict that the effect of AA on ASICs does not arise from changes in local membrane curvature, and thus further support that AA binding may have direct effects on the conformation of the ion channel. However, such conformational changes are likely to occur at timescales inaccessible to atomistic simulations. Further functional studies are needed to confirm the presence of the proposed regulatory sites, as well as to investigate whether these sites cause small differences in AA modulation between hASIC1a and hASIC3. A combination of mutagenesis and electrophysiological recordings in membranes containing AA could determine whether these identified residues play a functional role in ASIC activation, desensitization, ion conductance and PUFA modulation, after which more detailed simulation studies could shed further light on the molecular mechanism of fatty acid modulation of ASICs. In combination with functional studies, additional in silico mutants, such as the additional mutations (e.g., Y67 in both ASIC subtypes) studied in the work of Klipp and Bankston, could give a more detailed overview of AA interactions in this region. This could further be elaborated on by performing free energy calculations to study the identified ASIC-AA interactions. Given the complex nature of fatty acid effects on ASIC function, and more broadly, lipid effects on ion channel function, it would furthermore be valuable to simulate these channels in complex bilayers containing other lipid species found in neuronal membranes to better understand the interplay between the protein and its cell environment.

2.7 References

Abraham, M.J., T. Murtola, R. Schulz, S. Páll, J.C. Smith, B. Hess, and E. Lindahl. 2015. GROMACS: High performance molecular simulations through multi-level parallelism from laptops to supercomputers. SoftwareX. 1–2:19–25. https://doi.org/10.1016/j.softx.2015.06.001

Allen, N.J., and D. Attwell. 2002. Modulation of ASIC channels in rat cerebellar Purkinje neurons by ischaemia-related signals. J. Physiol. 543:521–529. https://doi.org/10.1113/jphysiol.2002.020297

Ananchenko, A., T.O.K. Hussein, D. Mody, M.J. Thompson, and J.E. Baenziger. 2022. Recent insight into lipid binding and lipid modulation of pentameric ligand-gated ion channels. Biomolecules. 12:814. https://doi.org/10.3390/biom12060814

Baconguis, I., C.J. Bohlen, A. Goehring, D. Julius, and E. Gouaux. 2014. X-ray structure of acid-sensing ion channel 1-snake toxin complex reveals open state of a Na(+)-selective channel. Cell. 156:717–729. https://doi.org/10.1016/j.cell.2014.01.011

Baenziger, J.E., M.L. Morris, T.E. Darsaut, and S.E. Ryan. 2000. Effect of membrane lipid composition on the conformational equilibria of the nicotinic acetylcholine receptor. J. Biol. Chem. 275:777–784. https://doi.org/10.1074/jbc.275.2.777

Bateman, A., M.-J. Martin, S. Orchard, M. Magrane, R. Agivetova, S. Ahmad, E. Alpi, E.H. Bowler-Barnett, R. Britto, B. Bursteinas, et al. 2021. UniProt: The universal protein knowledgebase in 2021. Nucleic Acids Res. 49:D480–D489. https://doi.org/10.1093/nar/gkaa1100

Berendsen, H.J.C., D. van der Spoel, and R. van Drunen. 1995. GROMACS: A message-passing parallel molecular dynamics implementation. Comput. Phys. Commun. 91:43–56. https://doi.org/10.1016/0010-4655(95)00042-E

Best, R.B., X. Zhu, J. Shim, P.E. Lopes, J. Mittal, M. Feig, and A.D. Mackerell Jr. 2012. Optimization of the additive CHARMM all-atom protein force field targeting improved sampling of the backbone φ, ψ and side-chain χ(1) and χ(2) dihedral angles. J. Chem. Theory Comput. 8:3257–3273. https://doi.org/10.1021/ct300400x

Bussi, G., D. Donadio, and M. Parrinello. 2007. Canonical sampling through velocity rescaling. J. Chem. Phys. 126:014101. https://doi.org/10.1063/1.2408420

De Caterina, R., J.K. Liao, and P. Libby. 2000. Fatty acid modulation of endothelial activation. Am. J. Clin. Nutr. 71:213S–223S. https://doi.org/10.1093/ajcn/71.1.213S

Chen, C.T., S. Haven, L. Lecaj, M. Borgstrom, M. Torabi, J.P. SanGiovanni, and J.R. Hibbeln. 2020. Brain PUFA concentrations are differentially affected by interactions of diet, sex, brain regions, and phospholipid pools in mice. J. Nutr. 150:3123–3132. https://doi.org/10.1093/jn/nxaa307

Chen, Z., G. Kuenze, J. Meiler, and C.M. Canessa. 2021. An arginine residue in the outer segment of hASIC1a TM1 affects both proton affinity and channel desensitization. J. Gen. Physiol. 153:e202012802. https://doi.org/10.1085/jgp.202012802

Cheng, Y.R., B.Y. Jiang, and C.C. Chen. 2018. Acid-sensing ion channels: Dual function proteins for chemo-sensing and mechano-sensing. J.Biomed. Sci. 25:46. https://doi.org/10.1186/s12929-018-0448-y

daCosta, C.J.B., L. Dey, J.P. Therien, and J.E. Baenziger. 2013. A distinct mechanism for activating uncoupled nicotinic acetylcholine receptors. Nat. Chem. Biol. 9:701–707. https://doi.org/10.1038/nchembio.1338

Darden, T., D. York, and L. Pedersen. 1998. Particle mesh Ewald: An N-log(N) method for Ewald sums in large systems. J. Chem. Phys. 98:10089–10092. https://doi.org/10.1063/1.464397

Elinder, F., and S.I. Liin. 2017. Actions and mechanisms of polyunsaturated fatty acids on voltage-gated ion channels. Front. Physiol. 8:43. https://doi.org/10.3389/fphys.2017.00043

Eswar, N., and A. Sali. 2006. Comparative protein structure modeling using modeller. Curr. Protoc. Bioinformatics. 5:5–6. https://doi.org/10.1002/0471250953.bi0506s15

Evans, D.J., and B.L. Holian. 1998. The Nose–Hoover thermostat. J. Chem. Phys. 83:4069–4074. https://doi.org/10.1063/1.449071

Fraser, D.D., S. Whiting, R.D. Andrew, E.A. Macdonald, K. Musa-Veloso, and S.C. Cunnane. 2003. Elevated polyunsaturated fatty acids in blood serum obtained from children on the ketogenic diet. Neurology. 60:1026–1029. https://doi.org/10.1212/01.WNL.0000049974.74242.C6

Gowers, R.J., M. Linky, J. Barnoud, T.J.E. Reddy, M.N. Melo, S.L. Seyer, J. Domanski, D.L. Dotson, S. Buchoux, I.M. Kenney, and O. Beckstein. 2016. MDAnalysis: A Python package for the rapid analysis of molecular dynamics simulations. Proc. 15th Python Sci. Conf. 98–105. https://doi.org/10.25080/Majora-629e541a-00e

Gründer, S., and X. Chen. 2010. Structure, function, and pharmacology of acid-sensing ion channels (ASICs): Focus on ASIC1a. Int. J. Physiol. Pathophysiol. Pharmacol. 2:73–94

Hammarström, S., M. Hamberg, B. Samuelsson, E.A. Duell, M. Stawiski, and J.J. Voorhees. 1975. Increased concentrations of nonesterified arachidonic acid, 12L-hydroxy-5,8,10,14-eicosatetraenoic acid, prostaglandin E2, and prostaglandin F2alpha in epidermis of psoriasis. Proc. Natl. Acad. Sci. USA. 72:5130–5134. https://doi.org/10.1073/pnas.72.12.5130

Hess, B., H. Bekker, H.J.C. Berendsen, and J.G.E.M. Fraaije. 1997. LINCS: A linear constraint solver for molecular simulations. J. Comput. Chem. 18:1463–1472. https://doi.org/10.1002/(SICI)1096-987X(199709)18:12<1463::AID-JCC4>3.0.CO;2-H

Huang, J., and A.D. MacKerell Jr. 2013. CHARMM36 all-atom additive protein force field: Validation based on comparison to NMR data. J. Comput. Chem. 34:2135–2145. https://doi.org/10.1002/jcc.23354

Humphrey, W., A. Dalke, and K. Schulten. 1996. VMD: Visual molecular dynamics. J. Mol. Graph. 14:33–38. https://doi.org/10.1016/0263-7855(96)00018-5

Jasti, J., H. Furukawa, E.B. Gonzales, and E. Gouaux. 2007. Structure of acid-sensing ion channel 1 at 1.9 A resolution and low pH. Nature. 449:316–323. https://doi.org/10.1038/nature06163

Klipp, R.C., and J.R. Bankston. 2022. Structural determinants of acid-sensing ion channel potentiation by single chain lipids. J. Gen. Physiol. 154:e202213156. https://doi.org/10.1085/jgp.202213156

Kweon, H.J., and B.C. Suh. 2013. Acid-sensing ion channels (ASICs): Therapeutic targets for neurological diseases and their regulation. BMB Rep. 46:295–304. https://doi.org/10.5483/bmbrep.2013.46.6.121

Lee, J., X. Cheng, J.M. Swails, M.S. Yeom, P.K. Eastman, J.A. Lemkul, S. Wei, J. Buckner, J.C. Jeong, Y. Qi, et al. 2016. CHARMM-GUI input generator for NAMD, GROMACS, AMBER, OpenMM, and CHARMM/OpenMM simulations using the CHARMM36 additive force field. J. Chem. Theory Comput. 12:405–413. https://doi.org/10.1021/acs.jctc.5b00935

Marra, S., R. Ferru-Clément, V. Breuil, A. Delaunay, M. Christin, V. Friend, S. Sebille, C. Cognard, T. Ferreira, C. Roux, et al. 2016. Non-acidic activation of pain-related acid-sensing ion channel 3 by lipids. EMBO J. 35:414–428. https://doi.org/10.15252/embj.201592335

Marrink, S.J., H.J. Risselada, S. Yefimov, D.P. Tieleman, and A.H. de Vries. 2007. The MARTINI force field: Coarse grained model for biomolecular simulations. J. Phys. Chem. B. 111:7812–7824. https://doi.org/10.1021/jp071097f

Michaud-Agrawal, N., E.J. Denning, T.B. Woolf, and O. Beckstein. 2011. MDAnalysis: A toolkit for the analysis of molecular dynamics simulations. J. Comput. Chem. 32:2319–2327. https://doi.org/10.1002/jcc.21787

Parrinello, M., and A. Rahman. 1998. Polymorphic transitions in single crystals: A new molecular dynamics method. J. Appl. Phys. 52:7182–7190. https://doi.org/10.1063/1.328693

Pettersen, E.F., T.D. Goddard, C.C. Huang, E.C. Meng, G.S. Couch, T.I. Croll, J.H. Morris, and T.E. Ferrin. 2021. UCSF ChimeraX: Structure visualization for researchers, educators, and developers. Protein Sci. 30:70–82. https://doi.org/10.1002/pro.3943

Salem, N., Jr, B. Wegher, P. Mena, and R. Uauy. 1996. Arachidonic and docosahexaenoic acids are biosynthesized from their 18-carbon precursors in human infants. Proc. Natl. Acad. Sci. USA. 93:49–54. https://doi.org/10.1073/pnas.93.1.49

Smith, E.S., H. Cadiou, and P.A. McNaughton. 2007. Arachidonic acid potentiates acid-sensing ion channels in rat sensory neurons by a direct action. Neuroscience. 145:686–698. https://doi.org/10.1016/j.neuroscience.2006.12.024

Song, W., R.A. Corey, T.B. Ansell, C.K. Cassidy, M.R. Horrell, A.L. Duncan, P.J. Stansfeld, and M.S.P. Sansom. 2022. PyLipID: A Python package for analysis of protein–lipid interactions from

molecular dynamics simulations. J. Chem. Theory Comput. 18:1188–1201. https://doi.org/10.1021/acs.jctc.1c00708

Sonntag, Y., M. Musgaard, C. Olesen, B. Schiøtt, J.V. Møller, P. Nissen, and L. Thøgersen. 2011. Mutual adaptation of a membrane protein and its lipid bilayer during conformational changes. Nat Commun. 2:304. https://doi.org/10.1038/ncomms1307

van der Spoel, D., E. Lindahl, B. Hess, G. Groenhof, A.E. Mark, and H.J. Berendsen. 2005. GROMACS: Fast, Flexible, and Free. J. Comput. Chem. 1701–1718. https://doi.org/10.1002/jcc.20291

Tong, A., J.T. Petroff II, F.F. Hsu, P.A. Schmidpeter, C.M. Nimigean, L. Sharp, G. Brannigan, and W.W. Cheng. 2019. Direct binding of phosphatidylglycerol at specific sites modulates desensitization of a ligand-gated ion channel. Elife. 8:e50766. https://doi.org/10.7554/eLife.50766

Verlet, L. 1967. Computer “experiments” on classical fluids. I. Thermodynamical properties of Lennard-Jones molecules. Phys. Rev. 159:98–103. https://doi.org/10.1103/PhysRev.159.98

Vickery, O.N., and P.J. Stansfeld. 2021. CG2AT2: An enhanced fragment-based approach for serial multi-scale molecular dynamics simulations. J. Chem. Theory Comput. 17:6472–6482. https://doi.org/10.1021/acs.jctc.1c00295

Wassenaar, T.A., H.I. Ingólfsson, R.A. Böckmann, D.P. Tieleman, and S.J. Marrink. 2015. Computational lipidomics with insane: A versatile tool for generating custom membranes for molecular simulations. J. Chem. Theory Comput. 11:2144–2155. https://doi.org/10.1021/acs.jctc.5b00209

Wu, Y., Z. Chen, F.J. Sigworth, and C.M. Canessa. 2021. Structure and analysis of nanobody binding to the human ASIC1a ion channel. Elife. 10:e67115. https://doi.org/10.7554/eLife.67115

Yoder, N., and E. Gouaux. 2020. The His-Gly motif of acid-sensing ion channels resides in a reentrant “loop” implicated in gating and ion selectivity. Elife. 9:1–18. https://doi.org/10.7554/eLife.56527

Yoder, N., C. Yoshioka, and E. Gouaux. 2018. Gating mechanisms of acid-sensing ion channels. Nature. 555:397–401. https://doi.org/10.1038/nature25782

2.8 Supplementary Information

Figure 2.11. Selection of distance cutoffs for PyLipID analysis. A. Minimum distance between AA headgroup bead and sidechain of any interacting residue over a 30 μs simulation. Contacts start at ~4.1 Å and peak at 5 Å. **B.** Number of detected binding sites (based on PyLipID software network analysis) as a product of selected cut-off pairs, with cut-off pairs shown on the x-axis as (lower, upper). Any pair with a lower cutoff of 4.75 Å yielded the largest number of detected binding sites.

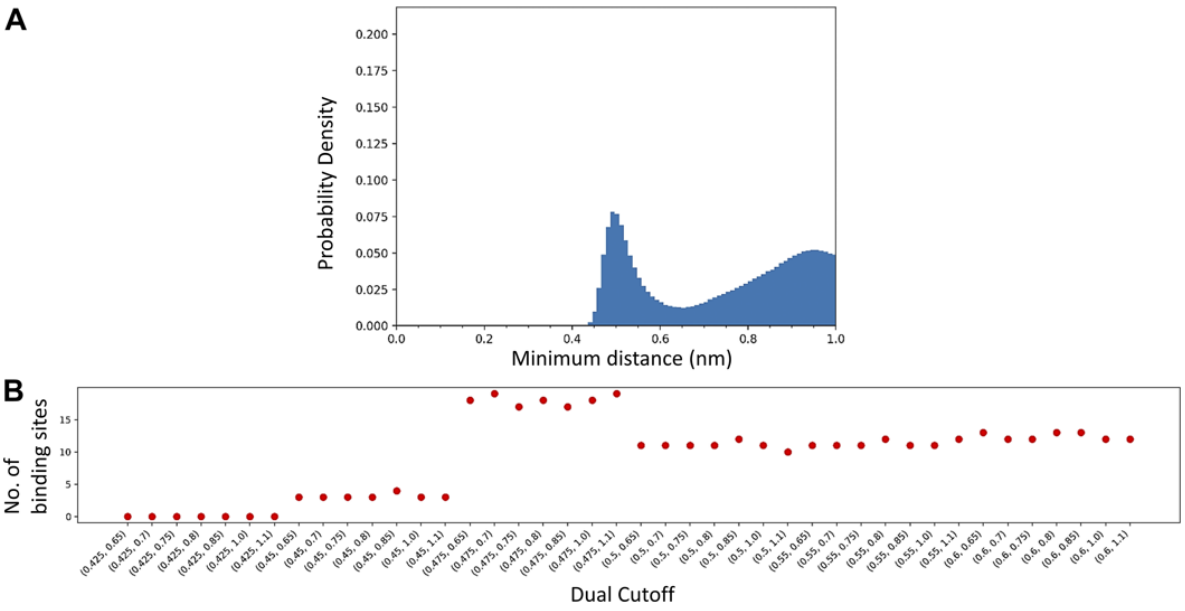
A
Probability Density
0.200
0.175
0.150
0.125
0.100
0.075
0.050
0.025
0.000
0.0
0.2
0.4
0.6
0.8
1.0
Minimum distance (nm)
B
No. of binding sites
15
10
5
0
(0.425, 0.65)
(0.425, 0.7)
(0.425, 0.75)
(0.425, 0.8)
(0.425, 0.85)
(0.425, 1.0)
(0.425, 1.1)
(0.45, 0.65)
(0.45, 0.7)
(0.45, 0.75)
(0.45, 0.8)
(0.45, 0.85)
(0.45, 1.0)
(0.45, 1.1)
(0.475, 0.65)
(0.475, 0.7)
(0.475, 0.75)
(0.475, 0.8)
(0.475, 0.85)
(0.475, 1.0)
(0.475, 1.1)
(0.5, 0.65)
(0.5, 0.7)
(0.5, 0.75)
(0.5, 0.8)
(0.5, 0.85)
(0.5, 1.0)
(0.5, 1.1)
(0.55, 0.65)
(0.55, 0.7)
(0.55, 0.75)
(0.55, 0.8)
(0.55, 0.85)
(0.55, 1.0)
(0.55, 1.1)
(0.6, 0.65)
(0.6, 0.7)
(0.6, 0.75)
(0.6, 0.8)
(0.6, 0.85)
(0.6, 1.0)
(0.6, 1.1)
Dual Cutoff

Figure 2.12. Interactions between AA headgroup and R65 hASIC3 in atomistic simulations. **A.** Time-resolved occupancy of AA at three sites in two 500 ns repeats of a backmapped atomistic simulations. Dark blue indicates presence of AA, i.e., when the carboxylic acid carbon of AA is within 4.5 Å of the $R65_{hASIC3}$ sidechain. **B.** Distances between the carboxylic acid carbon of AA and ζ-carbon of $R65_{hASIC3}$ over time of initially bound AA molecules at hASIC3 subunits in two 500 ns atomistic simulation repeats.

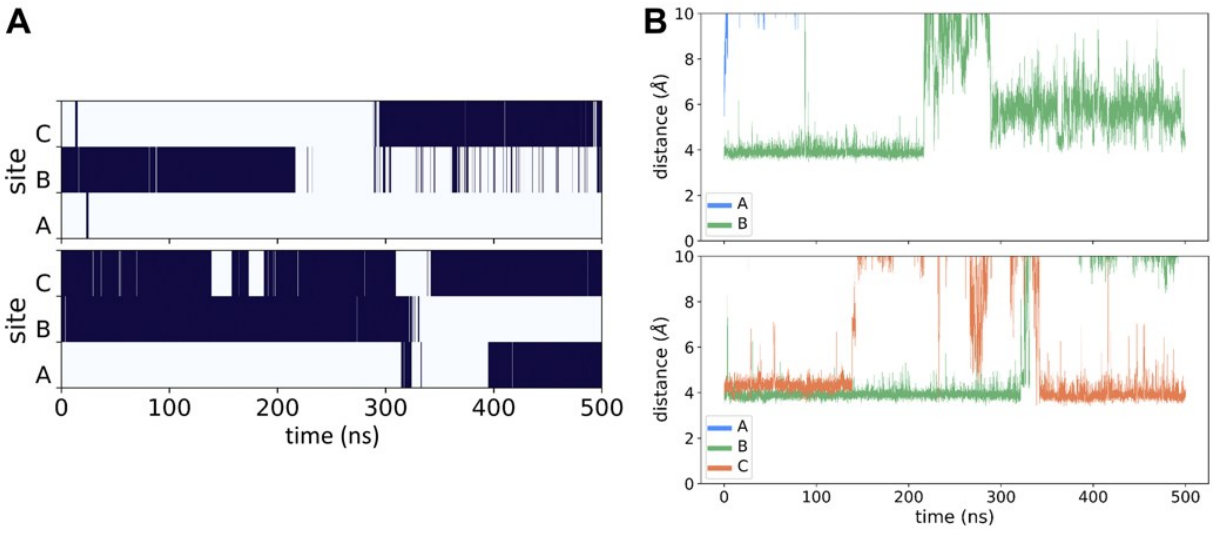
A
site
C
B
A
site
C
B
A
0
100
200
300
400
500
time (ns)
B
distance (Å)
0
2
4
6
8
10
A
B
distance (Å)
A
B
C
0
100
200
300
400
500
time (ns)

Chapter 3: Manuscript 2: State-dependent binding of cholesterol and an anionic lipid to the muscle-type *Torpedo* nicotinic acetylcholine receptor

Ananchenko, A., Gao, R. Y., Dehez, F., Baenziger, J. E. (2024)

3.1 Preface

I joined the Baenziger lab in the second half of 2021 just after the group, in collaboration with researchers at the Institut de Biologie Structurale, had solved new cryo-EM structures of the *Torpedo* nAChR at high resolution and were getting ready to publish. Given that Dr. Baenziger is an expert in lipid-nAChR interactions, and the new structures showed potentially important phospholipid binding sites, this was an exciting opportunity for me to investigate lipid interactions with these new structures using MD simulations. I performed CG-MD simulations of the apo and nicotine-bound states, starting from the new structures, in simple membranes composed of PA, PC and Chol. I then backmapped frames from the CG simulations in which lipids were seen binding to sites of interest for subsequent atomistic simulations. I analyzed the data from these simulations, focusing on phospholipid binding sites, while my coauthor Rui Yan Gao focused on Chol interactions. I wrote the manuscript with input from Dr. Baenziger and Dr. Dehez. I participated in editing the manuscript with the other co-authors and made the majority of the figures and movies.

3.2 Abstract

The ability of the *Torpedo* nicotinic acetylcholine receptor (nAChR) to undergo agonist-induced conformational transitions requires the presence of cholesterol and/or anionic lipids. Here we use recently solved structures along with multiscale molecular dynamics simulations to examine lipid binding to the nAChR in bilayers that have defined effects on nAChR function. We examine how phosphatidic acid and cholesterol, lipids that support conformational transitions, individually compete for binding with phosphatidylcholine, a lipid that does not. We also examine how the two lipids work synergistically to stabilize an agonist-responsive nAChR. We identify rapidly exchanging lipid binding sites, including both phospholipid sites with a high affinity for phosphatidic acid and promiscuous cholesterol binding sites in the grooves between adjacent transmembrane α-helices. A high affinity cholesterol site is confirmed in the inner leaflet framed by a key tryptophan residue on the MX α-helix. Our data provide insight into the dynamic nature of lipid-nAChR interactions and set the stage for a detailed understanding of the mechanisms by which lipids facilitate nAChR function at the neuromuscular junction.

3.3 Introduction

The lipid composition of neuronal membranes is essential to healthy brain function, with changes in the levels of lipids correlating with aging and neurodegenerative disease (Ledesma et al., 2012; Martin et al., 2010). In this broad medical context, it is intriguing that the activities of many proteins implicated in neuronal communication, including post-synaptic pentameric ligand-gated ion channels (pLGICs), are modulated by lipids (Ananchenko et al., 2022; Baenziger et al., 2017; Dadsena et al., 2019; Elinder & Liin, 2017; Hammond & Martin, 1987; Marra et al., 2016; Thompson & Baenziger, 2020a, 2020b). Decades of biophysical and biochemical studies have established that the activity of the prototypic pLGIC, the muscle-type nicotinic acetylcholine receptor (nAChR) from *Torpedo*, is sensitive to a variety of lipids, including neutral lipids, such as cholesterol (Chol), and anionic lipids, such as phosphatidic acid (PA) (Criado et al., 1982, 1984; Fong & McNamee, 1986). Although the nAChR exhibits only weak structural specificity for both lipid types (Baenziger et al., 2000; Sunshine & McNamee, 1992), PA is particularly effective at stabilizing an agonist-responsive conformation (daCosta et al., 2004; Hamouda et al., 2006; Sturgeon & Baenziger, 2010). Also, a 3:1:1 molar ratio of phosphatidylcholine (PC), PA, and Chol is as effective as native membranes in stabilizing an agonist-responsive nAChR (daCosta & Baenziger, 2009; Fong & McNamee, 1986). Lipids influence the magnitude of the agonist-induced response via a conformational selection mechanism whereby they stabilize different proportions of activatable resting versus non-activatable desensitized or uncoupled states (Baenziger et al., 2000; daCosta et al., 2009; daCosta & Baenziger, 2009). Lipids also influence the kinetics of conformational transitions (daCosta et al., 2013). It remains to be determined whether lipids select conformations by binding to allosteric sites, altering bulk membrane-protein interactions, or a combination of both.

Recent cryo-electron microscopy (cryo-EM) structures determined in apo, agonist-bound, and toxin/inhibitor-bound states reveal densities in both the outer extracellular and inner cytoplasmic leaflets at the periphery of the TMD that have been attributed to bound lipids (Gharpure et al., 2019; Noviello et al., 2021; Rahman et al., 2020, 2022; Walsh et al., 2018; Zarkadas et al., 2022) (Figure 3.1, see also (Unwin, 2022)). A conserved inner leaflet phospholipid site, modeled with bound PC, is located at each subunit-subunit interface with the headgroup phosphate framed by an arginine and histidine on the M3 α-helix from the principal subunit (+M3) and a positive lysine or arginine on the M4 α-helix from the complementary subunit (-M4)(Zarkadas et al., 2022). Both the absence of residues coordinating the modeled choline headgroup and the variability in head group poses from one subunit to another suggests that these sites may accommodate a variety of phospholipids, including PA. Diffuse density was also modeled as bound Chol, including sites deemed both high and low affinity, with the former occurring in the inner leaflet of the bilayer (Rahman et al., 2022). Densities attributed to Chol have also been observed in similar regions in cryo-EM images of the nAChR in native membranes (Unwin, 2020, 2021). Notably, some of the modeled phospholipid and Chol binding sites overlap while others do not. The structures raise the possibility that neutral and anionic lipids bind to multiple overlapping allosteric sites but with different affinities and thus potentially different efficacies for stabilizing activatable versus non-activatable conformations.

Figure 3.1. Cryo-EM structures with bound lipids and functional lipid sensitivity of the nAChR. A. Structure of the nAChR with bound lipids. Left: side view of the nicotine-bound nAChR (PDB: 7QL5) represented as a white surface, with the α_γ subunit highlighted as cartoon colored by α-helices: M1, blue; M2, green; M3, yellow; M4, red; MX, purple. Middle top: Side view of the nicotine-bound nAChR TMD with bound PC shown as blue sticks. Middle bottom: Side view of the apo nAChR (PDB:7SMQ) with bound Chol shown as green sticks. Right: Top-down view of the TMD. **B.** Kinetic binding of ethidium bromide (EthBr) assess the functional state of reconstituted nAChR membranes. EthBr binds to the TMD pore with an ~1000-fold higher affinity to *open* and *desensitized* rather than *resting* or *uncoupled* states, with its fluorescence increasing dramatically upon nAChR-binding (Sun et al., 2017). High affinity EthBr binding prior to agonist (carbamylcholine, Carb) addition likely reflects binding to pre-existing *desensitized* nAChRs. The addition of Carb transitions *resting* nAChRs to *open* and then *desensitized* states. The local anesthetic, dibucaine (Dib), competitively displaces EthBr binding. Left: the nAChR in *i*. native, *ii*. 3:1:1 PC:PA:Chol, and *iii*. PC-only membranes. Right: the nAChR in *i*. 3:2 PC:PA, *ii*. 3:2 PC:phosphatidylserine (PS), *iii*. 3:2 PC:Chol, and *iv*. PC-only membranes. Mixtures of PC:PA are more effective than mixtures of PC and other anionic lipids, such as PS, in stabilizing an agonist-responsive nAChR. Note that the left and right panels were acquired with different excitation/emission slit widths leading to different arbitrary fluorescence units (au). Data modified from refs (daCosta et al., 2009; daCosta & Baenziger, 2009). **C.** Chemical structures of nAChR-interacting lipids.

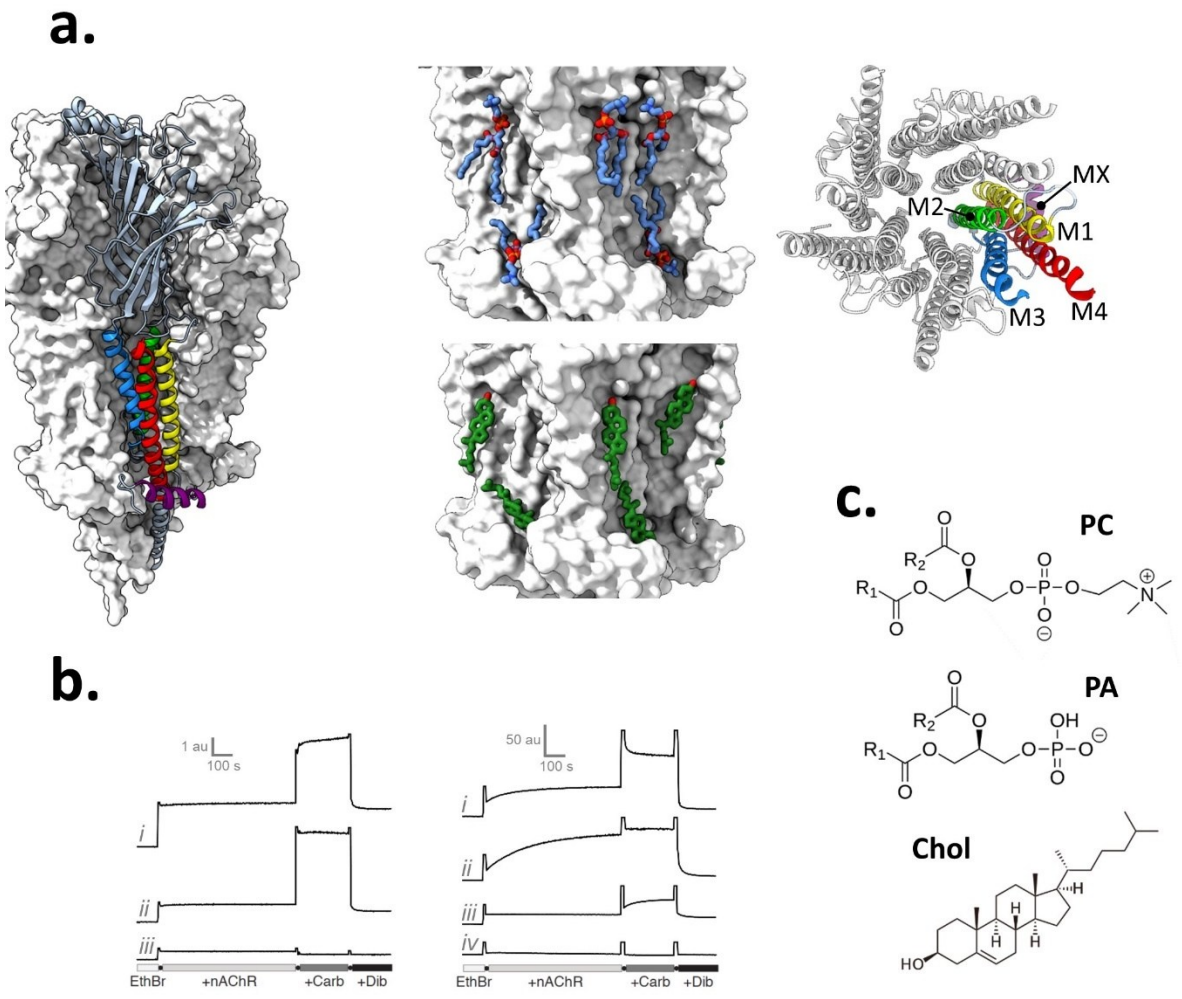
a.
MX
M2
M1
M3
M4
b.
1 au
100 s
50 au
100 s
i
ii
iii
iv
EthBr
+nAChR
+Carb
+Dib
c.
PC
PA
Chol
HO

Molecular dynamics (MD) simulations have been used to probe the dynamic interactions between lipids and the *Torpedo* nAChR using models ranging from individual transmembrane domain (TMD) α-helices imbedded in simple PC bilayers to the pioneering full-length 4 Å resolution *Torpedo* structure (PDB code, 2BG9) imbedded in complex neuronal-like membranes (Antollini et al., 2005; Brannigan et al., 2008; Sharp et al., 2019; Sharp & Brannigan, 2021; Xu et al., 2005). Although these models provided preliminary insight into the nature of lipid-nAChR interactions, the 2BG9 structure exhibits an error in the register of the amino acid sequence within the TMD and lacks the short MX α-helix in each subunit (Rahman et al., 2020), the latter frames lipid binding to the above noted inner leaflet sites (Figure 3.1). These and other errors alter how the modeled TMD interacts with its lipid environment thus limiting the conclusions derived from the simulation data.

With recent advancements in both computational methods and power, MD simulations are now poised to explore the dynamic nature of lipid-protein interactions, even with relatively large proteins such as the nAChR (Corradi et al., 2018, 2019; Muller et al., 2019). A coarse-grained MD (CG-MD) approach simplifies the system to reduce computational costs thus allowing simulation timescales long enough to sample in an unbiased manner both lipid association and dissociation events (Siewert J. Marrink et al., 2007). Individual frames from CG-MD simulations can be back-mapped to all-atom structures for simulations that shed light on the nature of the lipid-protein associations. MD simulations have been used to study lipid binding to a variety of pLGICs (Sharp & Brannigan, 2021), with multi-timescale simulation approaches recently applied to the neuronal α7 nAChR (Zhuang et al., 2022), glycine receptor (Dämgen & Biggin, 2021), acid-sensing ion

channels (Ananchenko & Musgaard, 2023), and the voltage-gated potassium channel, Kv1.2 (Kasimova et al., 2014).

Here, we use a multiscale MD simulation approach to characterize dynamic lipid binding to both apo and nicotine-bound structures (2.9 and 2.5 Å resolution, respectively) of the *Torpedo* nAChR. We focus on simple bilayers, containing PC, PA and Chol, whose effects on nAChR function have been characterized in vitro, with the goal of elucidating how PA and Chol, two lipids that support conformational transitions, both individually and synergistically compete for binding to the nAChR with PC, a lipid that does not support conformational transitions. Our simulations reveal state-dependent interactions at subunit specific sites thus providing a framework for understanding the mechanisms by which lipids influence nAChR function.

3.4 Methods

Molecular samples

We focused our MD simulations on recently published structures of the nAChR (Zarkadas et al., 2022) solved in the apo (resting state, PDB: 7QKO) and nicotine-bound (desensitized-like with a capped loop C around the agonist and an open Leu9'/Val13' gate, see Discussion in (Zarkadas et al., 2022), PDB: 7QL5) states at 2.9 Å and 2.5 Å resolution, respectively. Glycosylation sites were removed from the structures, and nicotine was removed from the nicotine-bound structure. The insane.py script (Wassenaar et al., 2015) was used to embed the CG models in a bilayer in a $180 \times 180 \times 200$ Å^3 cubic box, solvated in MARTINI CG water with 0.15 mM NaCl, with additional neutralizing Na+ ions added to systems containing phosphatidic acid. Insane.py randomly places lipids in the intra- and extracellular leaflets, thus three repeats of simulations were set up independently to randomize lipid placement. Each structure was embedded in membranes composed of PC, 3:2 mol:mol PC/PA, 3:2 mol:mol PC/Chol, and 3:1:1 mol:mol:mol PC:PA:Chol. Membrane compositions were selected based on known lipid ratios that stabilize resting-to-desensitized conformational transitions of the nAChR, as discussed in the Results and shown in Figure 3.1 (Baenziger et al., 2000; daCosta & Baenziger, 2009). Simulation systems are summarized in Tables 3.1 and 3.2.

Fluorescence experiments

Ethidium bromide fluorescence experiments were performed on a Cary Eclipse fluorescence spectrophotometer (Varian Inc.) (daCosta et al., 2009; daCosta & Baenziger, 2009). The fluorescence intensity at 590 nm was monitored as a function of time (2.0 s sampling time), while ethidium was excited at 500 nm. At the indicated times, ~250 nM (left panel) or ~50 nM (right

panel) nAChR, 500 μM Carb, and 500 μM dibucaine were added to a 0.3 μM solution of ethidium bromide in *Torpedo* Ringer buffer (5 mM Tris, 250 mM NaCl, 5 mM KCl, 2 mM $MgCl_2$, and 3 mM $CaCl_2$, pH 7.0). The data in the left and right panels were acquired with ±5 nm and ±20 nm excitation/emission slits, respectively.

Coarse-grained simulations

The PDB files, with ligands and bound lipids removed, were converted to coarse-grain (CG) representation using the martinize.py script and the MARTINI2.2 CG forcefield (Siewert J. Marrink et al., 2007). The 3D structure of the CG proteins was restrained using the ElNeDyn network (Periole et al., 2009) using the default force constant of 500 kJ mol-1 and default lower and upper cutoffs of 0.5 and 0.9 nm respectively. The GROMACS (Abraham et al., 2015; Berendsen et al., 1995; Van Der Spoel et al., 2005) 2021 simulation engine was used for CG simulations. Soft-core energy minimization was performed for 5000 steps, then double-precision minimization for an additional 5000 steps using the steepest descent algorithm, or until a maximum force of 1000 kJmol−1 nm−1 on any atom was reached. Systems were equilibrated using the NPT ensemble for a total of 4.75 ns with gradual lowering of protein position restraints from 1000 to 50 kJ. Temperature held at 310 K during equilibration steps using the v-rescale thermostat (Bussi et al., 2007) and pressure was held at 1 bar with the Berendsen barostat (Berendsen et al., 1998). Production runs were performed for 30 μs each with a timestep of 20 fs using an NPT ensemble with v-rescale set to 310 K and semi-isotropic Parrinello-Rahman pressure coupling (Parrinello & Rahman, 1998) set to 1 bar. Three simulation repeats were performed for each system.

Atomistic simulations

A single frame was selected from each CG simulation repeat for each system, where lipids of interest were bound to possible identified binding sites. The CG2AT script (Vickery & Stansfeld, 2021) was used to backmap the system to an atomistic representation, with the box size reduced to $130 \times 130 \times 190$ Å^3, resulting in a system size of approximately 300,000 atoms. The original cryo-EM structures were used for steered-MD alignment of the backmapped coarse grained structure as described in (Vickery & Stansfeld, 2021).

Proteins, lipids and ions were modeled using the CHARMM36 force field (Huang & Mackerell, 2013), and water was described by the TIP3P model (Jorgensen & Jenson, 1998). Salt concentration was again brought to 0.15 M of NaCl, with some ions added to neutralize systems containing PA. The NAMD 3.11 simulation software (Phillips et al., 2020) was used for atomistic simulations. The backmapped systems were minimized for 1000 steps. Systems were equilibrated for 5 ns with soft harmonic positional restrains on all heavy protein atoms, followed by 5 ns of equilibration with positional restraints on heavy backbone atoms only. Production runs were performed with no positional restrains for two repeats of 250 ns for each backmapped system. Hydrogen mass repartitioning (Hopkins et al., 2015) was used for all atomistic simulations, allowing for a timestep of 4 fs. A timestep of 8 and 4 fs was used for long- and short-range interactions respectively, using the r-RESPA multiple time-stepping algorithm (Tuckerman et al., 1992). Temperature was held constant at 300 K using the Langevin thermostat (Feller et al., 1995) and pressure was held at 1 atm using the Langevin piston method. The SETTLE algorithm (Miyamoto & Kollman, 1992) was used for water and the SHAKE/RATTLE algorithms (Andersen, 1983; Ryckaert et al., 1977) were used for constraining covalent bonds involving hydrogen atoms to their experimental lengths.

Analysis

Lipid density was calculated using built-in functions within the package MDAnalysis (Gowers et al., 2016; Michaud-Agrawal et al., 2011). Briefly, trajectories are aligned on the nAChR and positions of the lipid bead of interest are histogrammed on a grid with 1 Å spacing, resulting in a density measurement expressed in $Å^{-3}$. Upper and inner leaflets were defined by first identifying the membrane thickness based on average phosphate group positions, then dividing the membrane thickness into equal upper and lower portions. Figures of upper and lower densities are shown as summations along the z-axis of the density volume. Each leaflet thickness is approximately 16 Å. Cholesterol flip-flopping was detected using the tool LiPyPlilic (Smith & Lorenz, 2021).

For each simulation, we quantified the occupancy and interaction durations of each lipid with each residue in the nAChR TMD using the package PyLipID (Song et al., 2022). Occupancy is defined as the percentage of total simulation frames for which a lipid headgroup is within 5 Å of a coarse-grained "bead". To quantify interaction durations, a dual cut-off approach was used where an interaction was deemed to start when a lipid headgroup is within the lower cut-off distance (5 Å) of a residue and continues until the headgroup-residue distance exceeds the upper cut-off (8.5 Å). The cut-off distances were first established based on the interaction behavior of the PC headgroup with the nAChR in pure PC bilayers, based on the optimization protocol used in ref. (Song et al., 2022) (Supplementary figure 3.21). The lower cutoff was chosen based on the highest probability minimum distance from the lipid headgroup to any interacting residue, corresponding to specific lipid interactions, while the upper cutoff was chosen in order to account for the "rattling-in-cage" effect and to be able to sample long interactions. For consistency, the same cut-off values were then used to quantify the occupancy and interaction durations of each lipid in the multi-component lipid bilayers. See Supplementary Note 1 for a discussion of data convergence (Supplementary figure 3.22).

The VMD program (Humphrey et al., 1996) was used for visualization of MD trajectories. Cavities in Cryo-EM structures were calculated using the KVFinder webtool (Guerra et al., 2023). The python package MDAnalysis (Gowers et al., 2016; Michaud-Agrawal et al., 2011) was used for protein-lipid distance measurements. Figures were created using VMD (Humphrey et al., 1996), ChimeraX (Pettersen et al., 2021) and the Matplotlib python package.

Statistics and reproducibility

All occupancy and maximum duration averages and standard deviations are calculated from the three replicates performed for each CG simulation. Replicates were defined by re-generating the given nAChR/membrane system with new lipid positions within the membrane. In atomistic simulations, replicates are defined by re-assigning initial atom velocities to the chosen backmapped frame at the beginning of equilibration. Lipid headgroup densities and patterns of high occupancy/duration are consistent between repeats, showing reproducibility.

3.5 Results

As a first step towards understanding the mechanisms by which neutral and anionic lipids modulate *Torpedo* nAChR function, we performed 3 × 30 μs long CG-MD simulations with both apo and nicotine-bound nAChR structures imbedded in pure PC, 3:2 PC:PA, 3:2 PC:Chol, and 3:1:1 PC:PA:Chol membranes (all molar ratios). These lipid mixtures were chosen for three reasons. First, the agonist-induced response of the nAChR in each of the membranes has been characterized in vitro (Figure 3.1). The nAChR in PC-only membranes is stabilized in an uncoupled conformation that normally does not undergo agonist-induced conformational transitions (Baenziger et al., 2000; daCosta & Baenziger, 2009). The 3:2 molar ratios of PC:PA and PC:Chol are the optimal ratios of both PA and Chol in a PC membrane for stabilizing an agonist-responsive nAChR, although mixtures of PC and PA are more effective in this regard (Figure 3.1) (Baenziger et al., 2000). The 3:1:1 PC:PA:Chol membrane is as effective as native membranes at stabilizing an agonist-responsive nAChR and thus serves as a surrogate for a native membrane environment (Figure 3.1 B). Second, simulations of the nAChR in these four simple membranes allow us to directly assess how PA and Chol, lipids that in reconstituted membranes are particularly effective at supporting an agonist-induced response, both individually and synergistically compete for binding to the nAChR with PC, a lipid that does not support an agonist-induced response. Finally, the relatively high levels of PA and Chol enhance the sampling of lipid binding to provide unprecedented insight into the dynamic nature of PA and Chol interactions with the nAChR. We first describe the dynamic patterns of lipid binding to the apo nAChR followed by a discussion of state dependent lipid-nAChR interactions. We then explore the nature of PC, PA and Chol interactions using atomistic simulations performed on select frames back mapped from the CG-MD simulations.

Lipid organization at the nAChR-lipid interface

2-D headgroup density projections (phosphate for PC and PA, hydroxyl for Chol) averaged over the combined set of three repeat trajectories show that all three lipids localize preferentially around the nAChR with concentric rings of diminishing density radiating out from the TMD (Figures 3.2 3.3 and Supplementary figure 3.8) suggesting the nAChR influences lipid organization beyond a single shell of "boundary" lipids (Marsh & Barrantes, 1978). Localized regions of high headgroup density are observed in contact with the TMD. For the two phospholipids, side views show that these headgroup densities delineate the bilayer-water interface of both the outer and inner leaflets, although in a few select regions the head groups concentrate slightly higher to interact transiently with the Cys (β6-β7) loop of the extracellular domain or the β10-M1 linker. For Chol, additional head group density is located near the middle of the bilayer suggesting that the hydroxyl either bobs or dives into the membrane to interact with the TMD. The same global pattern of lipid organization around the nAChR, including both the concentric rings of lipid density radiating out from the nAChR and the local regions of high headgroup density immediately adjacent to the TMD is observed for both the apo and nicotine-bound structures.

Figure 3.2. PC, PA and Chol localization in simulations of the apo nAChR in membranes composed of PC, 3:2 PC:PA, and 3:2 PC:Chol. The top two rows correspond to top-down 2D lipid headgroup density plots for **A.** the PO_4 bead of PC, **B.** the PO_4 bead of PA, and **C.** the OH bead of Chol in each case averaged over 3 × 30 μs CG-MD simulations for the outer (top row) and inner (middle row) bilayer leaflets. The bottom row shows side views of the headgroup densities adjacent to the apo nAChR at the α_γ-γ interface, with the coarse-grained nAChR shown as silver van der Waals beads.

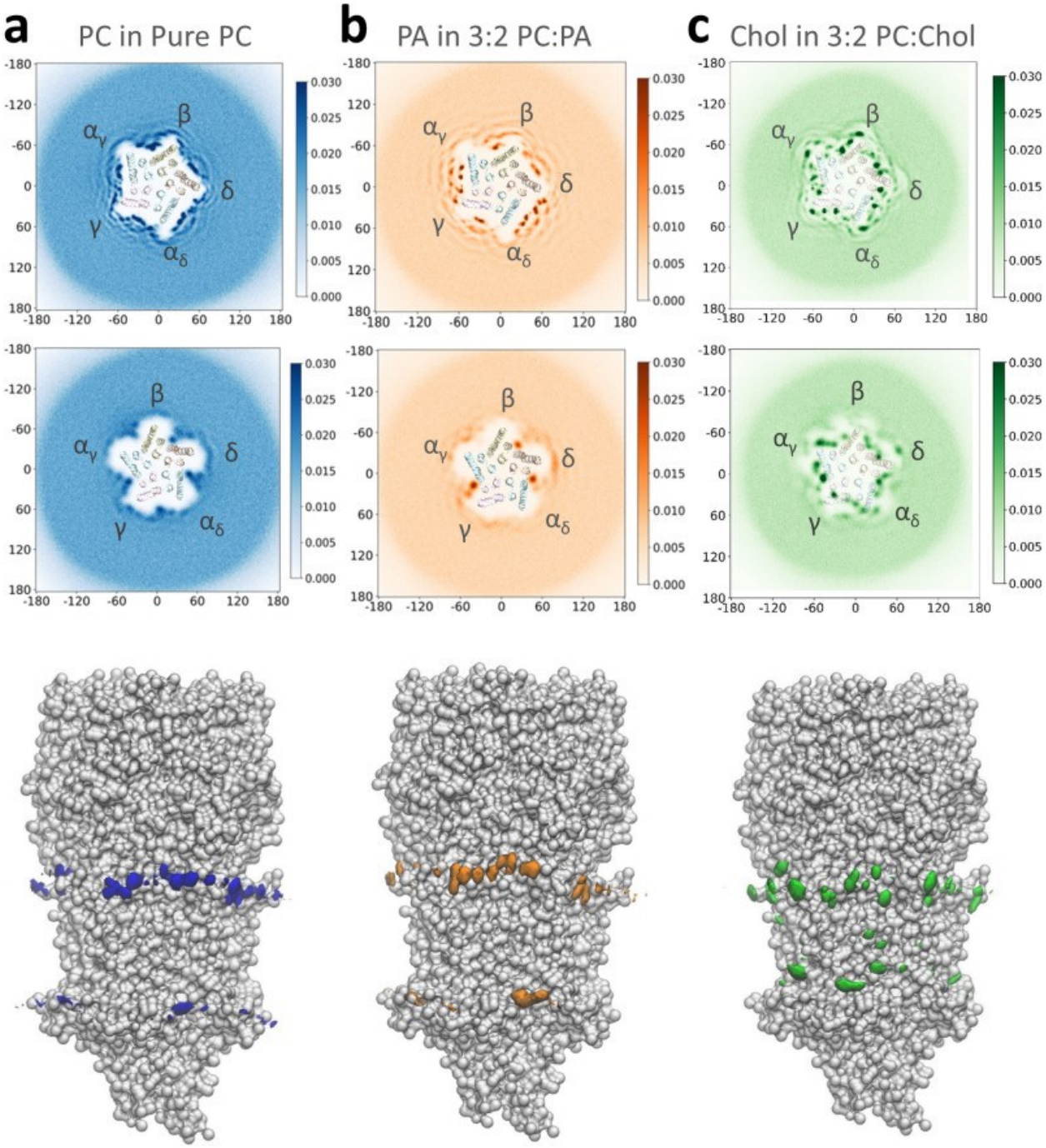
a
PC in Pure PC
b
PA in 3:2 PC:PA
c
Chol in 3:2 PC:Chol
β
δ
γ
α_γ
α_δ
-180 -120 -60 0 60 120 180
0.030 0.025 0.020 0.015 0.010 0.005 0.000

Figure 3.3. Top-down 2D headgroup density plots for PC, PA and Chol in the inner leaflet from simulations of the apo nAChR. Each density plot represents the lipid headgroup densities averaged over 3 × 30 μs CG-MD trajectories.

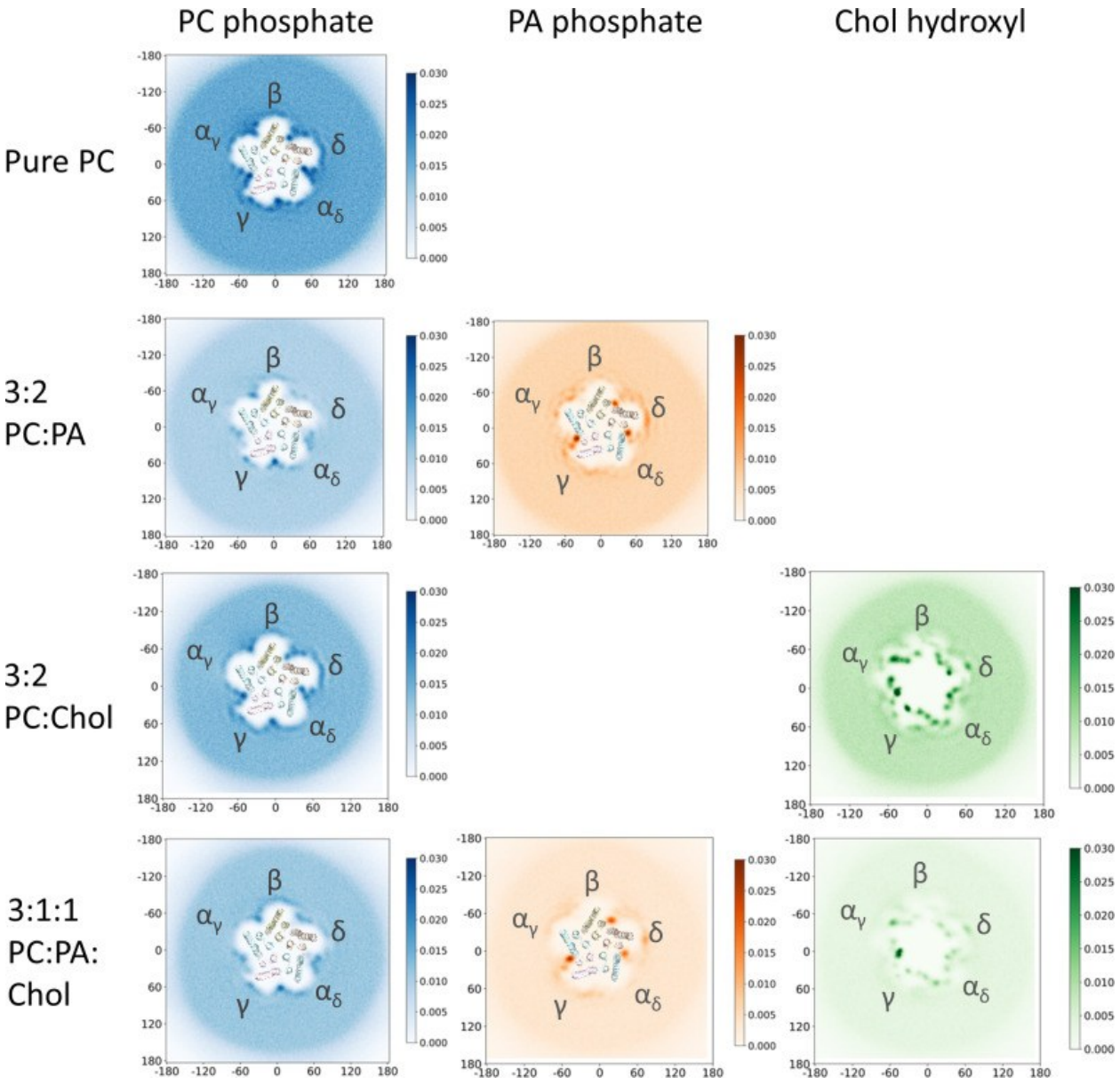
PC phosphate
PA phosphate
Chol hydroxyl
Pure PC
3:2 PC:PA
3:2 PC:Chol
3:1:1 PC:PA: Chol
β
αγ
δ
γ
αδ

PC exchanges rapidly between nAChR-bound sites and the bulk membrane

In pure PC membranes, the PC headgroup in the outer leaflet localizes to numerous sites on each of the five roughly concave surfaces located between pairs of M4 α-helices from adjacent subunits, with lower lipid headgroup density surrounding the periphery of each of the M4 α-helices (Figures 3.2, 3.3). Both the number of localized regions and their exact positions differ from one concave surface to another. Although these high-density regions reflect relatively high occupancy in that the phosphate is located at each site in a large percentage of simulation frames, the durations of binding are relatively short (Figures 3.4, Supplementary figures 3.9-3.11) suggesting that the bound PC is in rapid exchange with PC in the bulk membrane.

In the inner leaflet, PC exhibits longer duration binding to five inner leaflet pockets framed by the +M3 and +MX α-helices from the principal subunit and the -M1, -MX and -M4 α-helices from the complementary subunit. PC binds deeper (i.e., closer to the ion pore) to the α_γ-γ, α_δ-δ, and δ-β inner leaflet pockets with its phosphate coordinated by an arginine on +M3 (e.g., δArg315), a histidine located between +M3 and +MX (e.g., δHis320) and a positively charged lysine or arginine on -M4 (e.g., βArg437) (Figure 3.4). PC binds more superficially to the β-α_γ and γ-α_δ inner leaflet sites with its phosphate positioned on the lipid-facing surface of +M3, with deeper access to the pockets sterically restricted by the C-terminus of -MX (Figure 3.4 B). Binding deeper to the site may also be less favorable because the positively charged lysine/arginine residue on -M4 is replaced by His (αHis408). In one prominent pose at the β-α_γ and γ-α_δ inner leaflet sites, the phosphate interacts directly with the +M3 arginine side chain and the choline projects downwards toward the groove between the adjacent +MX and -MX α-helices.

Figure 3.4. Phospholipid interactions at "high" and "low" affinity PA inner leaflet binding sites of the apo nAChR. **A.** Top left panel shows the bound PC modeled at the δ-β inner leaflet site of the apo nAChR (PDB: 7QKO) with the subunits shown as cartoons and both lipid and coordinating residues shown as sticks. Top right dual-axis plots showing the % occupancy (% of frames with bound lipid) and average maximum durations (average of the longest interaction duration from each of the three simulation trajectories) from CG-MD simulations of lipid binding to the δ-β inner leaflet site. Error bars represent standard deviations. Overlaid points represent occupancy or maximum duration values from each repeat. Interactions were determined using the dual cutoff method (see Methods). The top plot summarizes PC binding in pure PC membranes while the middle and bottom plots summarize PC and PA binding, respectively, in 3:2 PC:PA membranes. The bottom three panels in (**A.**) are histograms depicting the interaction durations of each lipid with δR315 using both linear and log (inset) time scales. **B.** Same data as in (**A.**) but for lipid binding to the low PA affinity β-α_γ inner leaflet site.

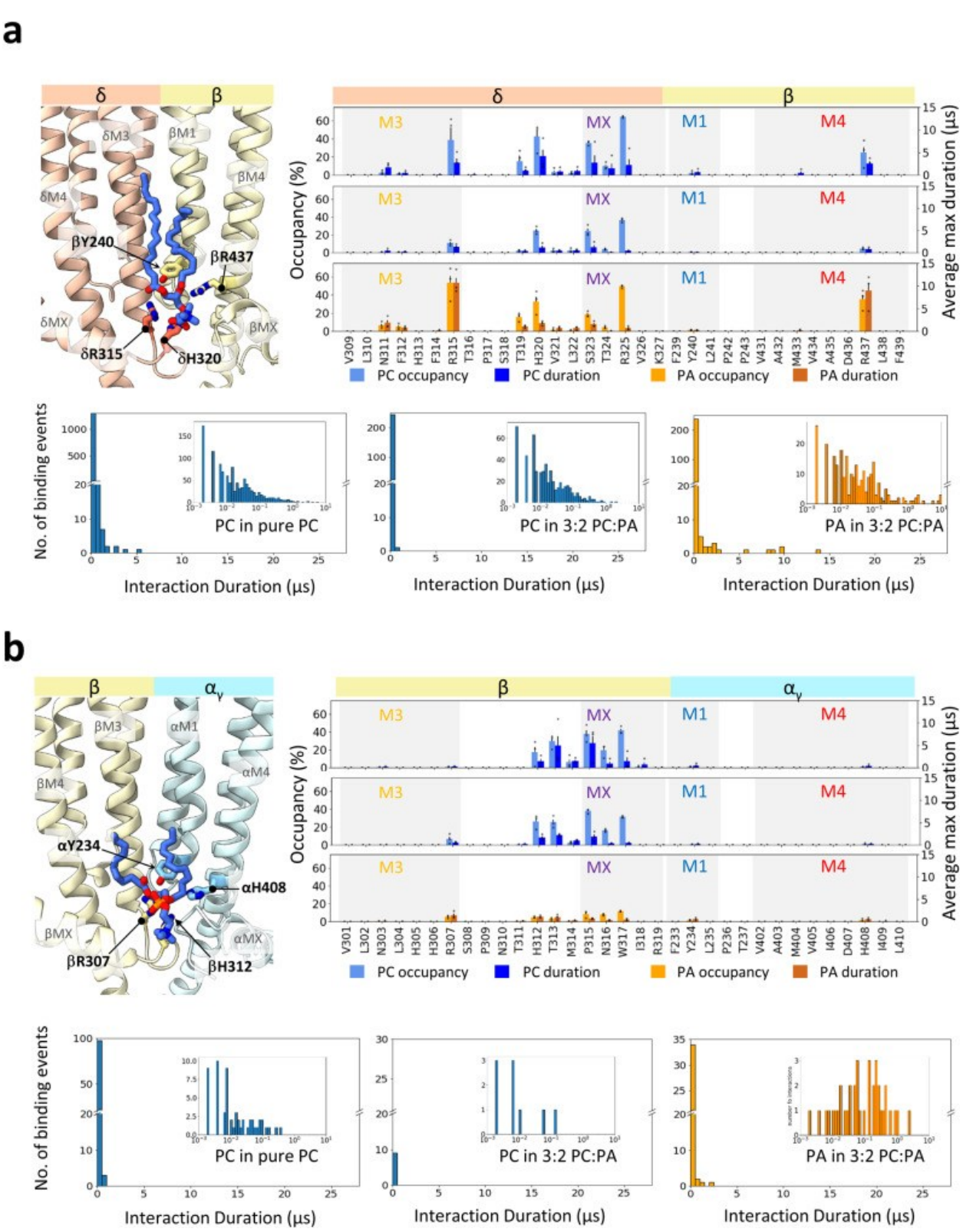
a
δ
β
δM3
βM1
βM4
δM4
βY240
βR437
δMX
βMX
δR315
δH320
M3
MX
M1
M4
Occupancy (%)
Average max duration (μs)
PC occupancy
PC duration
PA occupancy
PA duration
No. of binding events
PC in pure PC
PC in 3:2 PC:PA
PA in 3:2 PC:PA
Interaction Duration (μs)
b
β
αγ
βM3
αM1
αM4
βM4
αY234
αH408
βMX
αMX
βR307
βH312

The observed pattern of PC binding correlates with the pattern of phospholipid binding observed in cryo-EM structures (Rahman et al., 2022; Zarkadas et al., 2022). As in the CG-MD simulations, the structures also detect phospholipids (modeled as PC) bound to variable sites in the outer leaflet along with phospholipids bound to the same five pockets at subunit interfaces in the inner leaflet. The structures even capture PC binding deeper within the pocket at the α_γ-γ, α_δ-δ and δ-β interfaces. Both the MD simulations and the cryo-EM structures present a unified picture of phospholipid binding, albeit with the simulations showing that most of the bound PC exchanges rapidly with PC in the bulk membrane. A diagram depicting how the lipid binding poses of PC, PA and Chol detected in our simulations compare with the binding poses observed in cryo-EM structures is presented in Figure 3.12.

PA exhibits long-duration binding to subunit-selective inner leaflet pockets

The patterns of both PC and PA binding in 3:2 PC:PA membranes are similar to that of PC binding in pure PC membranes suggesting that the two phospholipids compete for overlapping sites (Figures 3.2, 3.3, Supplementary figure 3.8). In the outer leaflet, both bind to numerous sites along each concave surface between pairs of M4 α-helices from adjacent subunits (Supplementary figure 3.8) with the locations of these sites differing from one interface to another. The headgroup densities corresponding to PA are generally more intense than those of PC, particularly along the α_γ-γ and the α_δ-δ interfaces. PA binding to β10-M1 is more prominent in the δ subunit where two contiguous positively charged residues, δArg222 and δLys223, project towards the lipid bilayer (Supplementary figure 3.13). The durations of these interactions for both PC and PA, however, are again relatively short.

In the inner leaflet, PC and PA compete for the same five inner leaflet pockets but with different affinities (Figure 3.3). PA selectively displaces PC from the pockets at the α_γ-γ, α_δ-δ, and δ-β

interfaces. In fact, two PA molecules are observed binding to the α_γ-γ pocket in approximately 25% of the simulation frames. The enhanced occupancy of PA at these three sites is due primarily to longer binding durations (Figure 3.4, 3.9, Supplementary figure 3.13). For example, PA undergoes many interactions with the +M3 arginine that last between 5 and 15 μs, the latter corresponding to half of a 30 μs simulation trajectory. In contrast, PC maintains preferential binding to the inner leaflet pockets at the γ-α_δ and β-α_γ interfaces. As in the pure PC membranes, the bound PC still interacts extensively with residues in the loop between +M3 and +MX.

PA exists in both monoanionic and dianionic forms, with the equilibrium between the two in a PC:PA 3:2 membrane exhibiting a pK_a of 6.5 (Sturgeon & Baenziger, 2010). While there are contrasting reports as to whether the monoanionic or dianionic forms of PA are responsible for its unique effects on channel function, we noted that the MARTINI v2.2 lipidome assigns PA a charge of −2. Given the cationic nature of the inner leaflet pockets, we repeated the CG-MD simulations using monoanionic PA. 2D headgroup density plots show that the monoanionic form of PA competes effectively with PC and thus binds deeply to the inner leaflet binding sites at the α_γ-γ, α_δ-δ, and δ-β interfaces, although binding is slightly more diffuse. As with dianionic PA, the enhanced affinity of PA for these three sites is due to its relatively long interaction durations (Supplementary Figure 3.14). Monoanionic PA competes more effectively with PC for binding to the γ-α_δ and β-α_γ inner leaflet pockets, although its ability to do so was not observed in all simulation repeats. The single cationic charge (γArg310 and βArg307) at the γ-α_δ and β-α_γ inner leaflet pockets may "solvate" monoanionic PA better than dianionic PA.

Chol exhibits promiscuous long duration binding

The binding of PC in the 3:2 PC:Chol membranes is essentially identical to that observed in the absence of Chol. Chol has little effect on PC binding because the headgroup of the bound Chol is

typically positioned lower and thus closer to the middle of the bilayer with the sterol ring penetrating the grooves between adjacent lipid-exposed α-helices, while the PC headgroup typically binds higher and closer to the aqueous interface in poses restricted to the lipid-exposed surfaces of the TMD α-helices. These poses are highlighted in the atomistic simulations discussed below (Supplementary figure 3.16). The flexible acyl chains of PC adapt around the bound sterol ring so that the two lipids collectively form a highly complementary interface with the TMD.

In contrast, Chol exhibits a pattern of binding to the nAChR in 3:2 PC:Chol membranes that is strikingly distinct from the binding pattern of PC (Figure 3.3, Supplementary figure 3.8,3.15). In the extracellular leaflet, Chol binding is centered around four main sites along each of the five concave surfaces between the M4 α-helices from adjacent subunits (Figure 3.2, Supplementary figure 3.8). Three of these sites are in contact with the principal face, with one of these located on the +M4 surface and the other two in the grooves between the +M4/+M3 and the +M3/-M1 α-helices. These three distinct poses are most clearly seen at the β-α_γ and γ-α_δ interfaces. The fourth site is located on the complementary face in the -M3/-M4 groove, although binding to this site is variable leading to blurring of the headgroup density in the 2D density plots. Notably, the interactions between non-polar residues and the sterol ring are typically longer than those involving the polar hydroxyl (Figure 3.5). Together, these interactions lead to substantially longer Chol binding durations to the +M4/+M3 and +M3/-M1 grooves than to either the +M4 or the -M1/-M4 groove. Chol binding to the +M4/+M3 and +M3/-M1 grooves is also longer in duration than the binding of either PC or PA to their outer leaflet sites.

Figure 3.5. Chol interactions at upper and lower leaflet sites in PC:Chol 3:2 membranes. **A.** Top left panel shows Chol bound at the β-α_γ upper leaflet site in the structure of the apo + Chol nAChR (PDB: 7SMQ). The subunits are shown as cartoon, while the lipid and Chol-interacting side chains are shown as sticks. Top right dual-axis plots showing % occupancy and average maximum durations (see Figure 3.4) for the Chol hydroxyl and sterol ring interacting with residues at the same β-α_γ interface. Error bars represent standard deviations. Overlaid points represent occupancy or maximum duration values from each repeat. The bottom four panels in (**a**) show interaction duration histograms for the Chol hydroxyl with βR282 and αV216 and for the Chol sterol ring with βF286 and αI2220. **B.** Same data as in (**A.**) but for Chol interacting with the inner leaflet site at the α_γ-γ interface. The interaction duration histograms are for the Chol hydroxyl interacting with α_γW399 and α_γR301, and the Chol sterol interacting with α_γI406 and α_γI291.

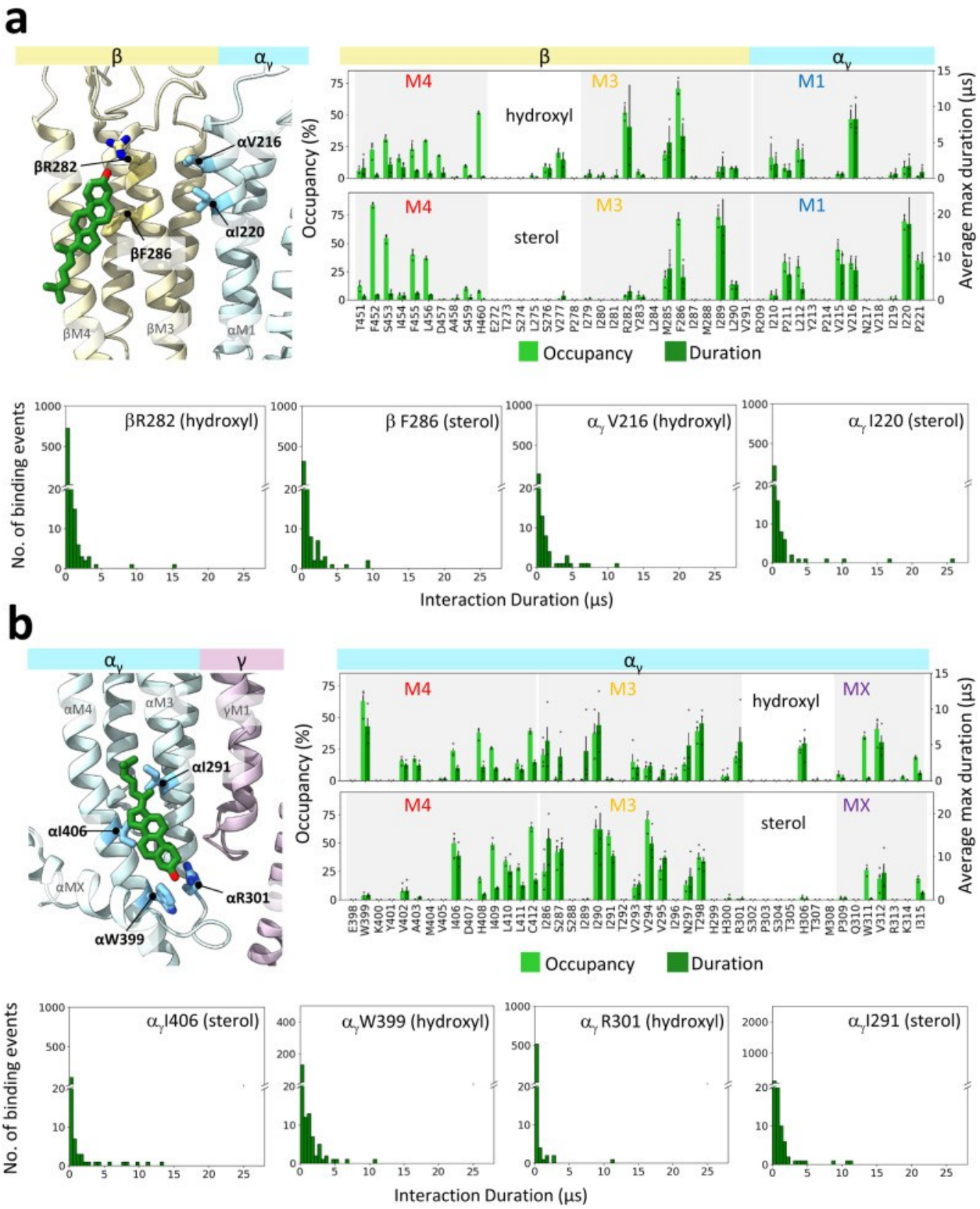
a
β
αγ
βR282
αV216
αI220
βF286
βM4
βM3
αM1
M4
M3
M1
hydroxyl
sterol
Occupancy (%)
Average max duration (μs)
Occupancy
Duration
βR282 (hydroxyl)
β F286 (sterol)
αγ V216 (hydroxyl)
αγ I220 (sterol)
No. of binding events
Interaction Duration (μs)
b
αγ
γ
αM4
αM3
γM1
αI291
αI406
αMX
αR301
αW399
MX
αγ I406 (sterol)
αγ W399 (hydroxyl)
αγ R301 (hydroxyl)
αγ I291 (sterol)

Chol binds to the same inner leaflet pocket that binds phospholipids, but with its hydroxyl located closer to the middle of the bilayer and deeper towards the ion pore (Supplementary figure 3.12). Chol also binds on the principal face of the inner leaflet pocket with its sterol positioned in the +M4/+M3 groove and its hydroxyl buried in a pocket framed by the +M4, +M3, and +MX where it can interact with the same conserved +M3 arginine that plays a critical role in phospholipid binding. The framing of this pocket at the α_{γ}-γ, α_{δ}-δ, and β-α_{γ} interfaces is facilitated by a bulky tryptophan (e.g., αTrp311) on +MX, with Chol binding at these three sites exhibiting higher occupancy and longer interaction durations than binding to the same sites at the γ-α_{δ}, and δ-β interfaces. High affinity Chol binding is observed at these α_{γ}-γ, α_{δ}-δ, and β-α_{γ} inner leaflet pockets in cryo-EM structures (Supplementary figure 3.10).

In addition to binding within the outer and inner leaflets, the Chol hydroxyl often bobs up/down or dives into the membrane to interact with the TMD, the latter orienting the sterol ring roughly parallel to the bilayer surface (Supplementary figure 3.16). Supplemental movie 3.1 captures a single Chol in the outer leaflet that binds to the TMD, bobs down into the inner leaflet, flips its orientation, and then dives up so that its hydroxyl interacts with γSer235 for the remainder of the simulation trajectory. Surprisingly, the Chol hydroxyl interacts frequently with numerous polar and hydrophobic residues within the TMD suggesting that bobbing and diving events for Chol are common. The extensive sampling of the lipid exposed TMD surface facilitates movements of Chol from one leaflet of the bilayer to the other, although it does not change the distribution of Chol in either leaflet (Supplementary figure 3.17).

Synergistic effects of PA and Chol

Although most of the binding sites for PC, PA, and Chol are maintained in the 3:1:1 PC:PA:Chol membrane, many exhibit reduced occupancies. In the outer leaflet, both PC and PA still bind to multiple sites along each concave surface between the M4 α-helices from adjacent subunits, with PA binding slightly more prevalent than PC (Supplementary figure 3.8). The interactions of PC and PA in the outer leaflet are still of relatively short duration and likely represent non-specific binding. Many of the localized regions of Chol binding to the outer leaflet also exhibit reduced occupancy. For example, although three distinct Chol binding poses are observed along the principal face of both β-α_γ and γ-α_δ in the 3:2 PC:Chol membranes, these poses are only observed at the γ-α_δ interface in the 3:1:1 PC:PA:Chol membrane.

Notably, PC or PA still bind preferentially to the inner leaflet pockets, with PA displacing PC at the α_γ-γ, α_δ-δ, and δ-β sites. Both the intensities of PA and PC binding to these sites (Figure 3.3) and their interaction durations are similar to those observed in the 3:2 PC:PA membrane. In contrast, the majority of the Chol binding events in the inner leaflet scale roughly proportionally with the reduced levels of Chol, the one exception being Chol binding to the principal face at the α_γ-γ interface. The ability of Chol to maintain binding highlights a potential modulatory role for this site in Chol action at the nAChR.

State dependent lipid interactions

We repeated the CG-MD simulations with the nicotine-bound structure of the nAChR, which has a capped loop C around the agonist and an open Leu9'/Val13' gate. The patterns of lipid binding to the apo and nicotine-bound structures are similar (Figure 3.6), with three notable exceptions:

Figure 3.6. Top-down 2D headgroup density plots for PC, PA and Chol in the inner leaflet from simulations of the nicotine-bound nAChR. Each density plot represents the lipid headgroup densities averaged over 3 × 30 μs CG-MD trajectories.

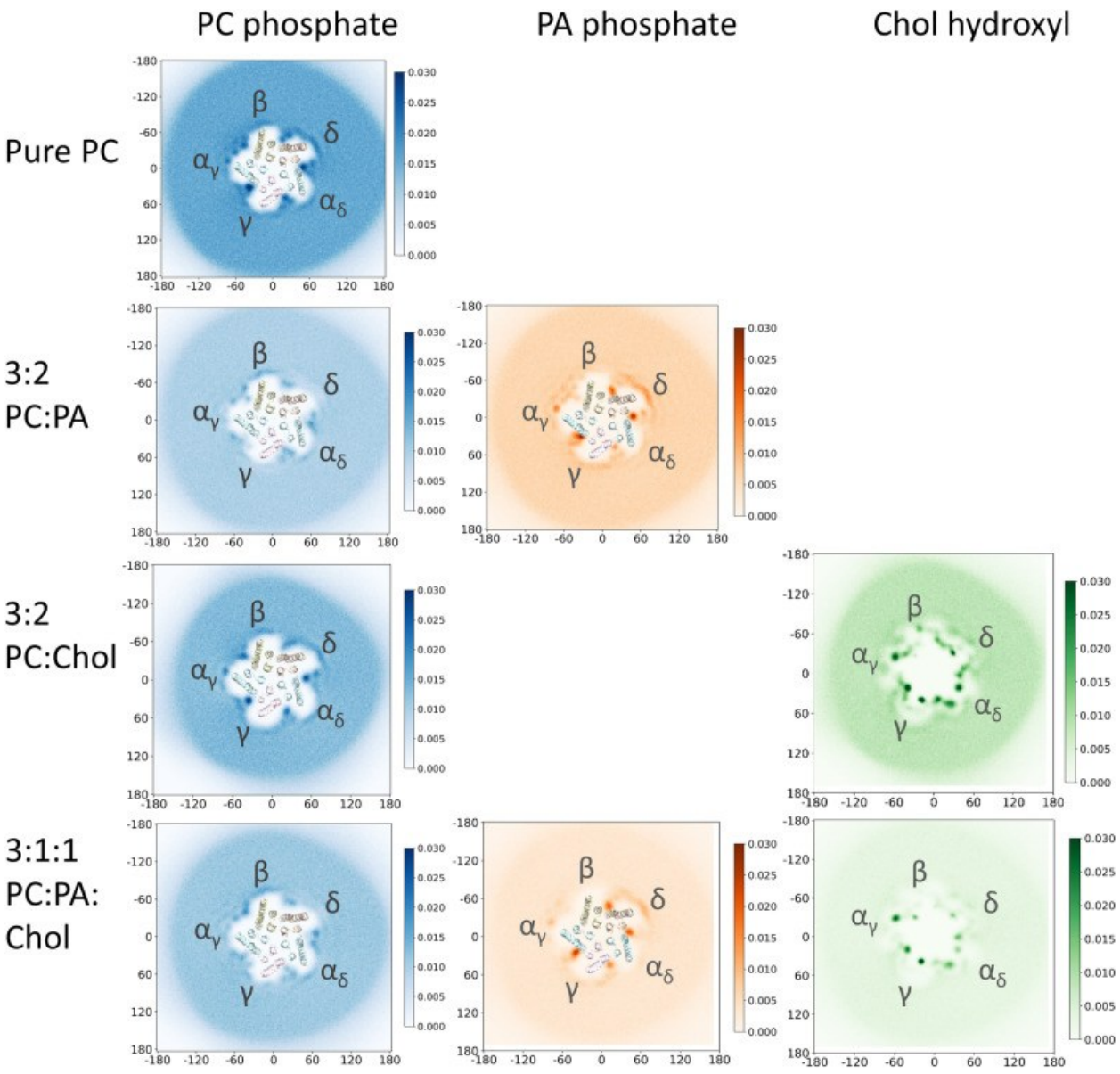
PC phosphate
PA phosphate
Chol hydroxyl
Pure PC
3:2 PC:PA
3:2 PC:Chol
3:1:1 PC:PA: Chol
β
δ
α_γ
α_δ
γ

First, although PC and PA still exhibit a similar pattern of binding to the α_γ-γ, α_δ-δ, δ-β and β-α_γ inner leaflet pockets as in the apo state, subtle agonist-induced movements of the α_δ MX α-helix allow PC to penetrate deeper into the γ-α_δ inner leaflet pocket in both the pure PC and 3:2 PC:Chol membranes leading to slightly longer interaction durations. The subtle opening of the γ-α_δ inner leaflet pocket also allows PA to penetrate more effectively and out compete PC for binding.

Second, nicotine binding subtly alters the pattern of Chol interactions with the TMD of each subunit. For example, Chol interactions in the inner leaflet at the α_γ-γ interface are longer in duration and are centered on a more condensed region in the apo versus the nicotine-bound state, while interactions at the same site at the α_δ-δ interface are similar in both states.

Third, a new site for Chol binding to the nicotine-bound state is observed deep within the TMD at the β-α_γ interface. This site corresponds to Chol diving into the bilayer so that its hydroxyl penetrates an enlarged hydrophobic pocket framed by βAla292, βIle296 and α_γLeu228 to interact with βLeu256 on the lipid-facing side of the pore-lining M2 α-helix (Supplementary Figure 3.18). Notably, the allosteric potentiator PNU binds to a similar site on the α7 nAChR, with binding possibly stabilizing the open state (Zhao et al., 2021) MD simulations show that Chol binds to the same PNU site on the desensitized α7 nAChR (Zhuang et al., 2022). The binding of Chol to this hydrophobic pocket on the *Torpedo* nAChR could help stabilize an agonist-responsive nAChR.

Finally, although previous structures have revealed a tilting of the M4 α-helices in the agonist-bound state (Rahman et al., 2022; Zarkadas et al., 2022), which could lead to enhanced lipid binding at the M4-M1/M3 interface, we did not detect major changes in either the lipid occupancy or interaction durations at this interface in the nicotine bound state.

Atomistic simulations

To explore the nature of the physical interactions that drive lipid binding, we back mapped select frames from the apo and nicotine-bound CG-MD simulations and performed 2 × 250 ns long all atom simulations. We focus here on atomistic simulations of the nAChR in PC, 3:2 PC:PA and 3:2 PC:Chol membranes as these highlight the nature of the interactions between each lipid and the nAChR. For PC and 3:2 PC:PA, we back-mapped frames where PC or PA, respectively, is bound to each of the three α_γ-γ, α_δ-δ, and δ-β inner leaflet pockets and to at least one of the γ-α_δ or β-α_γ inner leaflet pockets. The all-atomistic simulations were performed with PA in the monoanionic state. For the 3:2 PC:Chol membrane, we back mapped frames that had the largest number of residues with both Chol occupancies above 40% and average longest Chol interaction durations >3 μs.

All but one of the six PC molecules and all six PA molecules remain bound to the α_γ-γ, α_δ-δ, and δ-β inner leaflet pockets (two repeats of three sites) over the course of the 250 ns simulation trajectories. For both lipids, one of the headgroup phosphate oxygen atoms remains within 3 Å (a distance indicative of a salt bridge) of one of the nitrogen atoms on either the +M3 arginine or the -M4 arginine/lysine essentially throughout the simulation trajectory (Figure 3.7). A similar PA interaction has been proposed with the α2β4 nAChR (Cheng et al., 2009). At the same time, the phosphate and glycerol backbone oxygens form transient interactions with polar residues, including αHis306 and αAsn297, respectively, while the acyl chains interact with previously identified lipid-coordinating residues on -M1, such as γPhe241 and βTyr240. The choline headgroup of PC is relatively dynamic and does not form long duration interactions with any side chain. The all-atom simulations suggest that an oscillating salt bridge between the lipid phosphate and either the +M3 arginine or the -M4 lysine/arginine is the main stabilizing interaction at each of these three sites.

Figure 3.7. PA and Chol binding characterized by atomistic simulations. A. A time-course plot of the distances between one phosphate oxygen of PA and the nitrogen of both αR301 and δR355 over the course of one 250 ns atomistic simulation trajectory of the apo nAChR in a 3:2 PC:PA membrane. The starting configuration was back-mapped from a CG-MD simulation. "Swarm images" showing different binding poses over the course of one 250 ns atomistic simulation trajectory are presented for (**B.**) PA binding to the α_{δ}-δ inner leaflet site in 3:2 PC:PA membranes, (**C.**) Chol binding to the α_{γ}-γ inner leaflet site in 3:2 PC:Chol membranes, and (**D.**) Chol binding to the β-α_{γ} outer leaflet site in 3:2 PC:Chol membranes. Each swarm image reflects the position of the lipid and coordinating residues at 8 ns intervals (200 simulation frame intervals) over the course of a 250 ns atomistic simulation. Images were aligned on the relevant lipid-interacting transmembrane helices.

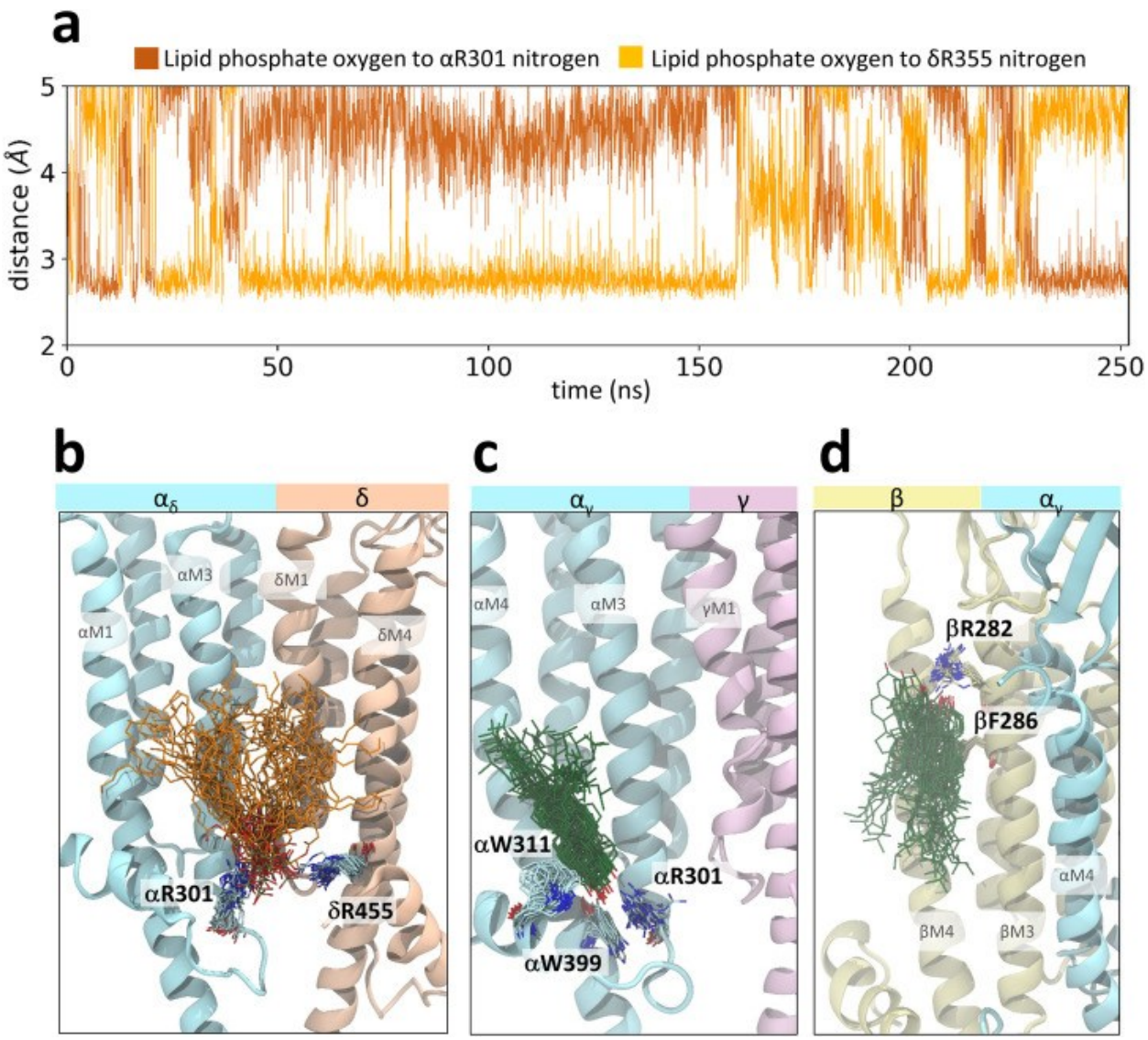
a
Lipid phosphate oxygen to αR301 nitrogen
Lipid phosphate oxygen to δR355 nitrogen
distance (Å)
time (ns)
b
αδ
δ
αM3
δM1
αM1
δM4
αR301
δR455
c
αγ
γ
αM4
αM3
γM1
αW311
αR301
αW399
d
β
αγ
βR282
βF286
αM4
βM4
βM3

Although PC or PA bound to the γ-α_δ and β-α_γ interfaces in the apo state still form interactions of less than 3 Å distance with the + M3 arginine, these are sporadic. The PC phosphate also binds transiently to γSer316/βThr313 with the choline headgroup simultaneously interacting with γGlu319 at the γ-α_δ interface – interactions at β-α_γ were not well sampled due to frame selection. Notably, the –MX helix at the γ-α_δ interface is shorter and the inner leaflet pocket more "open" in the nicotine-bound state thus allowing PA to form a salt bridge with the +M3 arginine that lasts roughly half of each simulation trajectory. This long duration interaction accounts for the ability of PA to outcompete PC for binding to this site in the agonist-bound state.

Chol binding appears to be governed by non-specific van der Waals and polar interactions involving the sterol ring and the hydroxyl, respectively. Chol binding to a β-α_γ outer leaflet site and the α_γ-γ inner leaflet pocket highlight the general nature of Chol-nAChR interactions (Figure 3.7 C, D). At the β-α_γ outer leaflet site, one trajectory captures Chol initially adopting a pose with its sterol ring oriented diagonally across the +M4/+M3 groove and its hydroxyl interacting with βArg282 (Supplementary Movie 3.2). Midway through the simulation, however, the sterol ring inserts into the +M4/+M3 groove, with this parallel orientation over the course of the simulation eventually breaking the interaction between the hydroxyl and βArg282. Such competing sterol ring/hydroxyl interactions were observed frequently in the atomistic simulations. In contrast, the binding pose of Chol at the α_γ-γ inner leaflet is relatively stable over the entire simulation trajectory likely because the sterol ring is tightly sandwiched between the +M4/+M3 groove and +MX. In this pose, the Chol hydroxyl simultaneously forms transient interactions with several residues including αArg301, αHis306 and αTrp399.

3.6 Discussion

Here, we have taken a unique multiscale MD simulation approach to study lipid binding to the nAChR in that we have focused on simple, defined membranes containing levels of PC, PA and/or Chol that are known to stabilize the nAChR in reconstituted membranes in different conformational states. These simulations allow us to correlate lipid binding patterns directly with documented effects of lipids on the function of the nAChR in reconstituted liposomes. Specifically, we set out to understand how lipids, PA and Chol, that support an agonist-induced response compete for binding to the nAChR with a lipid, PC, that does not. The relatively high levels of PA and Chol also enhance the sampling of lipid binding. The simulations provide direct insight into the dynamic nature of lipid binding to both the apo and agonist-bound *Torpedo* nAChR that is complementary to the static snapshots of lipid binding detected in cryo-EM structures (Supplementary figure 3.12). The resulting data not only set the stage for functional measurements, which should provide detailed insight into the mechanisms by which lipid binding influences nAChR function, but also reconcile observations from previous biophysical studies that are foundational to our understanding of lipid-nAChR interactions.

First, simulations detect sites of lipid binding on the surface of the TMD, although most of the bound lipids exchange rapidly with lipids in the bulk membrane. Notably, PA and Chol bind to sites with longer durations and thus higher occupancy than PC. Both observations are consistent with electron spin resonance experiments that detect rapidly exchanging nAChR-bound lipids in both native and reconstituted membranes, albeit with larger fractions of immobilized PA and Chol (Ellena et al., 1983; Marsh & Barrantes, 1978). In addition, the electron spin resonance experiments estimate rates of exchange between the bulk and immobilized lipids between 10^5 s^{-1} and 5×10^7 s^{-1} (Ellena et al., 1983; Marsh & Barrantes, 1978), which are consistent with the ns to μs lipid residence times detected in the MD simulations (Figures 3.4 and 3.5). The MD

simulations and electron spin resonance data thus present a unified snapshot of lipid-nAChR interactions.

Second, simulations address a long-standing controversy regarding the existence of "non-annular" Chol binding sites on the nAChR. These sites located deep within each subunit's α-helical TMD bundle were originally proposed based on the observation that the nAChR's intrinsic tryptophan fluorescence is quenched to a greater extent by brominated Chol than by brominated PC, suggesting that Chol accesses sites that are PC inaccessible (Jones & Mcnamee, 2002). Based on the early 4 Å resolution 2BG9 *Torpedo* structure, it was suggested that Chol fits into cavities between TMD α-helices to stabilize the TMD, although the detected cavities are *absent* in higher resolution nAChR structures (Supplementary figure 3.19) (Brannigan et al., 2008). While neither the cryo-EM structures nor our MD simulations support the existence of deeply buried non-annular Chol sites, the simulations show that the relatively small sterol ring of Chol penetrates the shallow grooves between adjacent lipid-exposed transmembrane α-helices while the larger phospholipids are restricted to the lipid-exposed α-helical surfaces (Supplementary figure 3.16). The simulations also capture Chol bobbing and diving into the membrane to interact with the TMD near the middle of the bilayer. These unique, albeit bulk lipid exposed, Chol binding poses likely account for the enhanced fluorescence quenching by brominated Chol.

Third, the observed Chol binding patterns shed light on the general nature of Chol-protein interactions. It has been suggested that Chol binding to membrane proteins is localized by CRAC ((L/V)-X_{1-5}-(Y)-X_{1-5}-(K/R)) and CARC (K/R)-X(1,5)-Y-X(1,5)-[L/V] motifs (Baier et al., 2011; Jamin et al., 2005). The locations of these putative motifs on the nAChR, however, do not correlate with the prominent sites of Chol binding observed in our simulations (Supplementary figure 3.20). In fact, although we observe that Chol binds promiscuously over the entire lipid exposed TMD

surface, high occupancy/long duration interactions occur in grooves between adjacent TMD α-helices – i.e., the sites for Chol binding are framed by residues that are on adjacent α-helices and that are thus distant from each other in the nAChR sequence. Binding sites are typically formed by a patch of hydrophobic residues (contributions from residues located on adjacent α-helices), which interact with the sterol ring, and a polar side chain, which interacts with the hydroxyl. Long duration binding is typically driven by van der Waals interactions between the hydrophobic residues and the sterol ring. Although both CRAC and CARC motifs fit the general pattern required for Chol binding, the simulations suggest that a *local* sequence specific Chol binding motif does not exist on the nAChR.

Fourth, the simulations and structural data reveal numerous binding sites for both phospholipids and Chol that likely facilitate roles for lipids in nAChR folding and/or function (Supplementary figure 3.10), although the correlations between lipid binding and channel function are likely complex. The phospholipids, PC and PA, compete for multiple binding sites, with both lipids exhibiting high occupancy at five inner leaflet pockets framed by the +M3 and +MX α-helices from the principal subunit and the -M1, -MX and -M4 α-helices from the complementary subunit. High occupancy Chol binding is also observed in both the outer and inner leaflets, most notably on the principal face of the same inner leaflet pockets that bind phospholipids. Significantly, both PC and Chol binding is modeled at the same sites in cryo-EM structures (Rahman et al., 2022; Zarkadas et al., 2022). The simulation and structural data thus provide cohesive evidence for high affinity phospholipid and Chol binding to the nAChR.

The inner leaflet phospholipid binding pockets may serve as allosteric sites that regulate folding and/or function. Both PC and PA bind to the α_{γ}-γ, α_{δ}-δ, and δ-β inner leaflet pockets with their phosphates coordinated by a conserved arginine on +M3 and a positively charged lysine or arginine

on -M4. In both cases, the bound lipid phosphate oscillates between forming a salt bridge with one or the other positively charged residue. Significantly, a steric clash between the large choline headgroup and the -MX α-helix renders these interactions with PC relatively unstable. In contrast, the small headgroup facilitates PA access to these three sites leading to substantially longer interactions indicative of high affinity binding, consistent with previous MD simulations showing anionic lipid binding in the same region of the 2BG9 *Torpedo* structure (Sharp & Brannigan, 2021). PA may be more effective than other phospholipids in stabilizing an agonist-responsive nAChR because its small headgroup facilitates access to these sites leading to high affinity binding, with such high affinity binding possibly required to stabilize an agonist-responsive resting conformation.

Alternatively, the preferential binding of PC to the β-α_γ and γ-α_δ inner leaflet pockets may favor the non-responsive uncoupled nAChR. These sites lack a positively charged arginine/lysine residue on -M4 and exhibit a unique conformation of -MX that limits phospholipid binding deep in the pocket. Phospholipids bind to these two inner leaflet pockets with their phosphates typically positioned on the lipid exposed side of the +M3 α-helix. Structures of the uncoupled nAChR are required to fully understand whether preferential PC binding to these sites favors an uncoupled state.

The MD simulations suggest several potential mechanisms by which Chol could work synergistically with anionic lipids to stabilize agonist responsive nAChRs. Chol may influence function by binding close to the same high affinity α_γ-γ, α_δ-δ, and δ-β inner leaflet pockets to facilitate PA binding. Chol may also bind to the principal face of the α_γ-γ inner leaflet pocket where it exhibits high occupancy even in the presence of both PC and PA. The synergistic effects of Chol on nAChR function could also arise from Chol binding to other regions of the TMD surface. The

simulations highlight a propensity for the sterol ring to bind to the shallow grooves between TMD α-helices. Such binding could easily influence packing of the TMD α-helices in a manner that favors one conformation over another or that influences the relative movements of TMD α-helices during conformational transitions. In addition, Chol frequently bobs and dives into the membrane to interact with residues on the TMD surface.

Although a complete map of the nAChR conformational landscape remains to be defined, we observe numerous conformational specific interactions that could further underlie the effects of PA and Chol on nAChR function. Agonist-binding leads to movement of the -MX α-helix that open slightly the γ-α_δ interface allowing PC to penetrate deeper in the pocket leading, with PA competing with PC for binding in the nicotine bound state. Enhanced PA interactions at this site could promote channel function. Especially interesting are the instances where the hydroxyl of Chol dives into the membrane to insert deeply at the β-α_γ interface to contact residues on M2 in the nicotine bound state. The binding of Chol to a similar M2 site has been observed in a state-dependent fashion in CG-MD simulations of the GlyR (Dämgen & Biggin, 2021) and the α7 nAChR (Zhuang et al., 2022). The mechanistic importance of these and other observed lipid binding sites must be verified by functional measurements.

Finally, our data suggest features that likely impact on our understanding of lipid interactions at other pLGICs, including prokaryotic pLGICs, such as GLIC and ELIC (Carswell, Hénault, et al., 2015; Carswell, Sun, et al., 2015). PIP_2 and PE/PG bind to similar inner leaflet pockets on the $GABA_AR$ (Laverty et al., 2019) and on ELIC (Hénault et al., 2019), respectively. The binding of phospholipids with larger headgroups to these two pLGICs is likely facilitated by the absence of MX α-helices, which frame the inner leaflet sites in the nAChR. In fact, the MX α-helices undergo subtle conformational changes that may impact on state dependent lipid binding to the nAChR. It

has been suggested that phospholipid binding to outer leaflet sites on ELIC plays a role in channel function (Petroff et al., 2022). While such binding is important in ELIC, our simulations suggest that phospholipid binding to outer leaflet sites on the nAChR are of short durations and thus likely reflect non-specific binding.

3.7 References

Abraham, M. J., Murtola, T., Schulz, R., Páll, S., Smith, J. C., Hess, B., & Lindahl, E. (2015). GROMACS: High performance molecular simulations through multi-level parallelism from laptops to supercomputers. SoftwareX, 1–2, 19–25. https://doi.org/10.1016/J.SOFTX.2015.06.001

Ananchenko, A. ;, Hussein, T. O. K. ;, Mody, D. ;, Thompson, M. J. ;, Baenziger, J. E., Ananchenko, A., Hussein, T. O. K., Mody, D., Thompson, M. J., & Baenziger, J. E. (2022). Recent Insight into Lipid Binding and Lipid Modulation of Pentameric Ligand-Gated Ion Channels. Biomolecules 2022, Vol. 12, Page 814, 12(6), 814. https://doi.org/10.3390/BIOM12060814

Ananchenko, A., & Musgaard, M. (2023). Multiscale molecular dynamics simulations predict arachidonic acid binding sites in human ASIC1a and ASIC3 transmembrane domains. The Journal of General Physiology, 155(3). https://doi.org/10.1085/JGP.202213259/213797

Andersen, H. C. (1983). Rattle: A "velocity" version of the shake algorithm for molecular dynamics calculations. Journal of Computational Physics, 52(1), 24–34. https://doi.org/10.1016/0021-9991(83)90014-1

Antollini, S. S., Xu, Y., Jiang, H., & Barrantes, F. J. (2005). Fluorescence and molecular dynamics studies of the acetylcholine receptor gammaM4 transmembrane peptide in reconstituted systems. Molecular Membrane Biology, 22(6), 471–483. https://doi.org/10.1080/09687860500367915

Baenziger, J. E., Domville, J. A., & Therien, J. P. D. (2017). The Role of Cholesterol in the Activation of Nicotinic Acetylcholine Receptors. Current Topics in Membranes, 80, 95–137. https://doi.org/10.1016/BS.CTM.2017.05.002

Baenziger, J. E., Morris, M. L., Darsaut, T. E., & Ryan, S. E. (2000). Effect of membrane lipid composition on the conformational equilibria of the nicotinic acetylcholine receptor. Journal of Biological Chemistry, 275(2), 777–784. https://doi.org/10.1074/jbc.275.2.777

Baier, C. J., Fantini, J., & Barrantes, F. J. (2011). Disclosure of cholesterol recognition motifs in transmembrane domains of the human nicotinic acetylcholine receptor. Scientific Reports 2011 1:1, 1(1), 1–7. https://doi.org/10.1038/srep00069

Berendsen, H. J. C., Postma, J. P. M., Van Gunsteren, W. F., Dinola, A., & Haak, J. R. (1998). Molecular dynamics with coupling to an external bath. The Journal of Chemical Physics, 81(8), 3684. https://doi.org/10.1063/1.448118

Berendsen, H. J. C., van der Spoel, D., & van Drunen, R. (1995). GROMACS: A message-passing parallel molecular dynamics implementation. Computer Physics Communications, 91(1–3), 43–56. https://doi.org/10.1016/0010-4655(95)00042-E

Brannigan, G., Hénin, J., Law, R., Eckenhoff, R., & Klein, M. L. (2008). Embedded cholesterol in the nicotinic acetylcholine receptor. Proceedings of the National Academy of Sciences of the United States of America, 105(38), 14418–14423. https://doi.org/10.1073/pnas.0803029105

Bussi, G., Donadio, D., & Parrinello, M. (2007). Canonical sampling through velocity rescaling. The Journal of Chemical Physics, 126(1), 014101. https://doi.org/10.1063/1.2408420

Carswell, C. L., Hénault, C. M., Murlidaran, S., Therien, J. P. D., Juranka, P. F., Surujballi, J. A., Brannigan, G., & Baenziger, J. E. (2015). Role of the Fourth Transmembrane α Helix in the Allosteric Modulation of Pentameric Ligand-Gated Ion Channels. Structure, 23(9), 1655–1664. https://doi.org/10.1016/J.STR.2015.06.020

Carswell, C. L., Sun, J., & Baenziger, J. E. (2015). Intramembrane Aromatic Interactions Influence the Lipid Sensitivities of Pentameric Ligand-gated Ion Channels. The Journal of Biological Chemistry, 290(4), 2496. https://doi.org/10.1074/JBC.M114.624395

Cheng, M. H., Xu, Y., & Tang, P. (2009). Anionic lipid and cholesterol interactions with α4β2 nAChR: Insights from MD simulations. Journal of Physical Chemistry B, 113(19), 6964–6970. https://doi.org/10.1021/JP900714B/ASSET/IMAGES/LARGE/JP-2009-00714B_0001.JPEG

Corradi, V., Mendez-Villuendas, E., Ingólfsson, H. I., Gu, R. X., Siuda, I., Melo, M. N., Moussatova, A., Degagné, L. J., Sejdiu, B. I., Singh, G., Wassenaar, T. A., Delgado Magnero, K., Marrink, S. J., & Tieleman, D. P. (2018). Lipid-Protein Interactions Are Unique Fingerprints for Membrane Proteins. ACS Central Science, 4(6), 709–717. https://doi.org/10.1021/acscentsci.8b00143

Corradi, V., Sejdiu, B. I., Mesa-Galloso, H., Abdizadeh, H., Noskov, S. Y., Marrink, S. J., & Tieleman, D. P. (2019). Emerging Diversity in Lipid-Protein Interactions. In Chemical Reviews (Vol. 119, Issue 9, pp. 5775–5848). American Chemical Society. https://doi.org/10.1021/acs.chemrev.8b00451

Criado, M., Eibl, H., & Barrantes, F. J. (1982). Effects of lipids on acetylcholine receptor. Essential need of cholesterol for maintenance of agonist-induced state transitions in lipid vesicles. Biochemistry, 21(15), 3622–3629. https://doi.org/10.1021/bi00258a015

Criado, M., Eibl, H., & Barrantes, F. J. (1984). Functional properties of the acetylcholine receptor incorporated in model lipid membranes. Differential effects of chain length and head group of phospholipids on receptor affinity states and receptor-mediated ion translocation. Journal of Biological Chemistry, 259(14), 9188–9198. https://doi.org/10.1016/S0021-9258(17)47283-8

daCosta, C. J. B., & Baenziger, J. E. (2009). A Lipid-dependent Uncoupled Conformation of the Acetylcholine Receptor. The Journal of Biological Chemistry, 284(26), 17819. https://doi.org/10.1074/JBC.M900030200

daCosta, C. J. B., Dey, L., Therien, J. P. D., & Baenziger, J. E. (2013). A distinct mechanism for activating uncoupled nicotinic acetylcholine receptors. Nature Chemical Biology 2013 9:11, 9(11), 701–707. https://doi.org/10.1038/nchembio.1338

daCosta, C. J. B., Medaglia, S. A., Lavigne, N., Wang, S., Carswell, C. L., & Baenziger, J. E. (2009). Anionic Lipids Allosterically Modulate Multiple Nicotinic Acetylcholine Receptor Conformational Equilibria. The Journal of Biological Chemistry, 284(49), 33841. https://doi.org/10.1074/JBC.M109.048280

daCosta, C. J. B., Wagg, I. D., McKay, M. E., & Baenziger, J. E. (2004). Phosphatidic acid and phosphatidylserine have distinct structural and functional interactions with the nicotinic acetylcholine receptor. Journal of Biological Chemistry, 279(15), 14967–14974. https://doi.org/10.1074/jbc.M310037200

Dadsena, S., Bockelmann, S., Mina, J. G. M., Hassan, D. G., Korneev, S., Razzera, G., Jahn, H., Niekamp, P., Müller, D., Schneider, M., Tafesse, F. G., Marrink, S. J., Melo, M. N., & Holthuis, J. C. M. (2019). Ceramides bind VDAC2 to trigger mitochondrial apoptosis. Nature Communications, 10(1), 1–12. https://doi.org/10.1038/s41467-019-09654-4

Dämgen, M. A., & Biggin, P. C. (2021). State-dependent protein-lipid interactions of a pentameric ligand-gated ion channel in a neuronal membrane. PLoS Computational Biology, 17(2). https://doi.org/10.1371/JOURNAL.PCBI.1007856

Elinder, F., & Liin, S. I. (2017). Actions and mechanisms of polyunsaturated fatty acids on voltage-gated ion channels. Frontiers in Physiology, 8(FEB), 43. https://doi.org/10.3389/FPHYS.2017.00043/BIBTEX

Ellena, J. F., Blazing, M. A., & McNamee, M. G. (1983). Lipid-Protein Interactions in Reconstituted Membranes Containing Acetylcholine Receptor. Biochemistry, 22(24), 5523–5535. https://doi.org/10.1021/BI00293A012/ASSET/BI00293A012.FP.PNG_V03

Feller, S. E., Zhang, Y., Pastor, R. W., & Brooks, B. R. (1995). Constant pressure molecular dynamics simulation: The Langevin piston method. The Journal of Chemical Physics, 103(11), 4613–4621. https://doi.org/10.1063/1.470648

Fong, T. M., & McNamee, M. G. (1986). Correlation between Acetylcholine Receptor Function and Structural Properties of Membranes. Biochemistry, 25(4), 830–840. https://doi.org/10.1021/bi00352a015

Gharpure, A., Teng, J., Zhuang, Y., Noviello, C. M., Walsh, R. M., Cabuco, R., Howard, R. J., Zaveri, N. T., Lindahl, E., & Hibbs, R. E. (2019). Agonist Selectivity and Ion Permeation in the α3β4 Ganglionic Nicotinic Receptor. Neuron, 104(3), 501-511.e6. https://doi.org/10.1016/J.NEURON.2019.07.030

Gowers, R., Linke, M., Barnoud, J., Reddy, T., Melo, M., Seyler, S., Domański, J., Dotson, D., Buchoux, S., Kenney, I., & Beckstein, O. (2016). MDAnalysis: A Python Package for the Rapid Analysis of Molecular Dynamics Simulations. Proceedings of the 15th Python in Science Conference, 98–105. https://doi.org/10.25080/majora-629e541a-00e

Guerra, J. V. S., Ribeiro-Filho, H. V., Pereira, J. G. C., & Lopes-De-Oliveira, P. S. (2023). KVFinder-web: a web-based application for detecting and characterizing biomolecular cavities. Nucleic Acids Research, 51(W1), W289–W297. https://doi.org/10.1093/NAR/GKAD324

Hammond, J. R., & Martin, I. L. (1987). Modulation of [3H]flunitrazepam binding to rat cerebellar benzodiazepine receptors by phosphatidylserine. European Journal of Pharmacology, 137(1), 49–58. https://doi.org/10.1016/0014-2999(87)90181-6

Hamouda, A. K., Sanghvi, M., Sauls, D., Machu, T. K., & Blanton, M. P. (2006). Assessing the lipid requirements of the Torpedo californica nicotinic acetylcholine receptor. Biochemistry, 45(13), 4327–4337. https://doi.org/10.1021/bi052281z

Hénault, C. M., Govaerts, C., Spurny, R., Brams, M., Estrada-Mondragon, A., Lynch, J., Bertrand, D., Pardon, E., Evans, G. L., Woods, K., Elberson, B. W., Cuello, L. G., Brannigan, G., Nury, H., Steyaert, J., Baenziger, J. E., & Ulens, C. (2019). A lipid site shapes the agonist response of a pentameric ligand-gated ion channel. Nature Chemical Biology, 15(12), 1156–1164. https://doi.org/10.1038/s41589-019-0369-4

Hopkins, C. W., Le Grand, S., Walker, R. C., & Roitberg, A. E. (2015). Long-time-step molecular dynamics through hydrogen mass repartitioning. Journal of Chemical Theory and Computation, 11(4), 1864–1874. https://doi.org/10.1021/CT5010406/ASSET/IMAGES/LARGE/CT-2014-010406_0017.JPEG

Huang, J., & Mackerell, A. D. (2013). CHARMM36 all-atom additive protein force field: Validation based on comparison to NMR data. Journal of Computational Chemistry, 34(25), 2135–2145. https://doi.org/10.1002/JCC.23354

Humphrey, W., Dalke, A., & Schulten, K. (1996). VMD: Visual molecular dynamics. Journal of Molecular Graphics, 14(1), 33–38. https://doi.org/10.1016/0263-7855(96)00018-5

Jamin, N., Neumann, J. M., Ostuni, M. A., Vu, T. K. N., Yao, Z. X., Murail, S., Robert, J. C., Giatzakis, C., Papadopoulos, V., & Lacapère, J. J. (2005). Characterization of the Cholesterol Recognition Amino Acid Consensus Sequence of the Peripheral-Type Benzodiazepine Receptor. Molecular Endocrinology, 19(3), 588–594. https://doi.org/10.1210/ME.2004-0308

Jones, O. T., & Mcnamee, M. G. (2002). Annular and nonannular binding sites for cholesterol associated with the nicotinic acetylcholine receptor. Biochemistry, 27(7), 2364–2374. https://doi.org/10.1021/BI00407A018

Jorgensen, W. L., & Jenson, C. (1998). Temperature Dependence of TIP3P, SPC, and TIP4P Water from NPT Monte Carlo Simulations: Seeking Temperatures of Maximum Density. J Comput Chem, 19, 11791186. https://doi.org/10.1002/(SICI)1096-987X(19980730)19:10

Kasimova, M. A., Tarek, M., Shaytan, A. K., Shaitan, K. V., & Delemotte, L. (2014). Voltage-gated ion channel modulation by lipids: Insights from molecular dynamics simulations. Biochimica et Biophysica Acta (BBA) - Biomembranes, 1838(5), 1322–1331. https://doi.org/10.1016/J.BBAMEM.2014.01.024

Laverty, D., Desai, R., Uchański, T., Masiulis, S., Stec, W. J., Malinauskas, T., Zivanov, J., Pardon, E., Steyaert, J., Miller, K. W., & Aricescu, A. R. (2019). Cryo-EM structure of the human α1β3γ2 GABAA receptor in a lipid bilayer. Nature 2019 565:7740, 565(7740), 516–520. https://doi.org/10.1038/s41586-018-0833-4

Ledesma, M. D., Martin, M. G., & Dotti, C. G. (2012). Lipid changes in the aged brain: Effect on synaptic function and neuronal survival. Progress in Lipid Research, 51(1), 23–35. https://doi.org/10.1016/J.PLIPRES.2011.11.004

Marra, S., Ferru-Clément, R., Breuil, V., Delaunay, A., Christin, M., Friend, V., Sebille, S., Cognard, C., Ferreira, T., Roux, C., Euller-Ziegler, L., Noel, J., Lingueglia, E., & Deval, E. (2016). Non-acidic activation of pain-related Acid-Sensing Ion Channel 3 by lipids. The EMBO Journal, 35(4), 414–428. https://doi.org/10.15252/embj.201592335

Marsh, D., & Barrantes, F. J. (1978). Immobilized lipid in acetylcholine receptor-rich membranes from Torpedo marmorata. Proceedings of the National Academy of Sciences, 75(9), 4329–4333. https://doi.org/10.1073/PNAS.75.9.4329

Martin, M., Dotti, C. G., & Ledesma, M. D. (2010). Brain cholesterol in normal and pathological aging. Biochimica et Biophysica Acta (BBA) - Molecular and Cell Biology of Lipids, 1801(8), 934–944. https://doi.org/10.1016/J.BBALIP.2010.03.011

Michaud-Agrawal, N., Denning, E. J., Woolf, T. B., & Beckstein, O. (2011). MDAnalysis: A toolkit for the analysis of molecular dynamics simulations. Journal of Computational Chemistry, 32(10), 2319–2327. https://doi.org/10.1002/jcc.21787

Miyamoto, S., & Kollman, P. A. (1992). Settle: An analytical version of the SHAKE and RATTLE algorithm for rigid water models. Journal of Computational Chemistry, 13(8), 952–962. https://doi.org/10.1002/jcc.540130805

Muller, M. P., Jiang, T., Sun, C., Lihan, M., Pant, S., Mahinthichaichan, P., Trifan, A., & Tajkhorshid, E. (2019). Characterization of Lipid-Protein Interactions and Lipid-Mediated Modulation of Membrane Protein Function through Molecular Simulation. In Chemical Reviews (Vol. 119, Issue 9, pp. 6086–6161). https://doi.org/10.1021/acs.chemrev.8b00608

Noviello, C. M., Gharpure, A., Mukhtasimova, N., Cabuco, R., Baxter, L., Borek, D., Sine, S. M., & Hibbs, R. E. (2021). Structure and gating mechanism of the α7 nicotinic acetylcholine receptor. Cell, 184(8), 2121-2134.e13. https://doi.org/10.1016/J.CELL.2021.02.049

Parrinello, M., & Rahman, A. (1998). Polymorphic transitions in single crystals: A new molecular dynamics method. Journal of Applied Physics, 52(12), 7182. https://doi.org/10.1063/1.328693

Periole, X., Cavalli, M., Marrink, S. J., & Ceruso, M. A. (2009). Combining an elastic network with a coarse-grained molecular force field: Structure, dynamics, and intermolecular recognition. Journal of Chemical Theory and Computation, 5(9), 2531–2543. https://doi.org/10.1021/ct9002114

Petroff, J. T., Dietzen, N. M., Santiago-McRae, E., Deng, B., Washington, M. S., Chen, L. J., Trent Moreland, K., Deng, Z., Rau, M., Fitzpatrick, J. A. J., Yuan, P., Joseph, T. T., Hénin, J., Brannigan, G., & Cheng, W. W. L. (2022). Open-channel structure of a pentameric ligand-gated ion channel reveals a mechanism of leaflet-specific phospholipid modulation. Nature Communications 2022 13:1, 13(1), 1–16. https://doi.org/10.1038/s41467-022-34813-5

Pettersen, E. F., Goddard, T. D., Huang, C. C., Meng, E. C., Couch, G. S., Croll, T. I., Morris, J. H., & Ferrin, T. E. (2021). UCSF ChimeraX: Structure visualization for researchers, educators, and developers. Protein Science : A Publication of the Protein Society, 30(1), 70. https://doi.org/10.1002/PRO.3943

Phillips, J. C., Hardy, D. J., Maia, J. D. C., Stone, J. E., Ribeiro, J. V., Bernardi, R. C., Buch, R., Fiorin, G., Hénin, J., Jiang, W., McGreevy, R., Melo, M. C. R., Radak, B. K., Skeel, R. D., Singharoy, A., Wang, Y., Roux, B., Aksimentiev, A., Luthey-Schulten, Z., … Tajkhorshid, E. (2020). Scalable molecular dynamics on CPU and GPU architectures with NAMD. The Journal of Chemical Physics, 153(4), 44130. https://doi.org/10.1063/5.0014475

Rahman, M. M., Basta, T., Teng, J., Lee, M., Worrell, B. T., Stowell, M. H. B., & Hibbs, R. E. (2022). Structural mechanism of muscle nicotinic receptor desensitization and block by curare. Nature Structural and Molecular Biology, 29(4), 386–394. https://doi.org/10.1038/s41594-022-00737-3

Rahman, M. M., Teng, J., Worrell, B. T., Noviello, C. M., Lee, M., Karlin, A., Stowell, M. H. B., & Hibbs, R. E. (2020). Structure of the Native Muscle-type Nicotinic Receptor and Inhibition by Snake Venom Toxins. Neuron, 106(6), 952-962.e5. https://doi.org/10.1016/J.NEURON.2020.03.012

Ryckaert, J. P., Ciccotti, G., & Berendsen, H. J. C. (1977). Numerical integration of the cartesian equations of motion of a system with constraints: molecular dynamics of n-alkanes. Journal of Computational Physics, 23(3), 327–341. https://doi.org/10.1016/0021-9991(77)90098-5

Sharp, L., & Brannigan, G. (2021). Spontaneous lipid binding to the nicotinic acetylcholine receptor in a native membrane. The Journal of Chemical Physics, 154(18), 185102. https://doi.org/10.1063/5.0046333

Sharp, L., Salari, R., & Brannigan, G. (2019). Boundary lipids of the nicotinic acetylcholine receptor: spontaneous partitioning via coarse-grained molecular dynamics simulation. Biochimica et Biophysica Acta. Biomembranes, 1861(4), 887. https://doi.org/10.1016/J.BBAMEM.2019.01.005

Siewert J. Marrink, *,†, H. Jelger Risselada, †, Serge Yefimov, ‡, D. Peter Tieleman, § and, & Vries†, A. H. de. (2007). The MARTINI Force Field: Coarse Grained Model for Biomolecular Simulations. https://doi.org/10.1021/JP071097F

Smith, P., & Lorenz, C. D. (2021). LiPyphilic: A Python Toolkit for the Analysis of Lipid Membrane Simulations. Journal of Chemical Theory and Computation, 17(9), 5907–5919. https://doi.org/10.1021/ACS.JCTC.1C00447/ASSET/IMAGES/LARGE/CT1C00447_0011.JPEG

Song, W., Corey, R. A., Ansell, T. B., Cassidy, C. K., Horrell, M. R., Duncan, A. L., Stansfeld, P. J., & Sansom, M. S. P. (2022). PyLipID: A Python Package for Analysis of Protein-Lipid Interactions from Molecular Dynamics Simulations. Journal of Chemical Theory and Computation, 18(2), 1188–1201. https://doi.org/10.1021/acs.jctc.1c00708

Sturgeon, R. M., & Baenziger, J. E. (2010). Cations Mediate Interactions between the Nicotinic Acetylcholine Receptor and Anionic Lipids. Biophysical Journal, 98(6), 989–998. https://doi.org/10.1016/J.BPJ.2009.11.030

Sun, J., Comeau, J. F., & Baenziger, J. E. (2017). Probing the structure of the uncoupled nicotinic acetylcholine receptor. BBA - Biomembranes, 1859(2), 146–154.

Sunshine, C., & McNamee, M. G. (1992). Lipid modulation of nicotinic acetylcholine receptor function: the role of neutral and negatively charged lipids. Biochimica et Biophysica Acta (BBA) - Biomembranes, 1108(2), 240–246. https://doi.org/10.1016/0005-2736(92)90031-G

Thompson, M. J., & Baenziger, J. E. (2020a). Ion channels as lipid sensors: from structures to mechanisms. Nature Chemical Biology 2020 16:12, 16(12), 1331–1342. https://doi.org/10.1038/s41589-020-00693-3

Thompson, M. J., & Baenziger, J. E. (2020b). Structural basis for the modulation of pentameric ligand-gated ion channel function by lipids. Biochimica et Biophysica Acta (BBA) - Biomembranes, 1862(9), 183304. https://doi.org/10.1016/J.BBAMEM.2020.183304

Tuckerman, M., Berne, B. J., & Martyna, G. J. (1992). Reversible multiple time scale molecular dynamics. The Journal of Chemical Physics, 97(3), 1990–2001. https://doi.org/10.1063/1.463137

Unwin, N. (2020). Protein–lipid architecture of a cholinergic postsynaptic membrane. IUCrJ, 7(Pt 5), 852. https://doi.org/10.1107/S2052252520009446

Unwin, N. (2021). Protein–lipid interplay at the neuromuscular junction. Microscopy, 2021, 1–6. https://doi.org/10.1093/JMICRO/DFAB023

Unwin, N. (2022). Structure of a cholinergic cell membrane. Proceedings of the National Academy of Sciences of the United States of America, 119(34), e2207641119. https://doi.org/10.1073/PNAS.2207641119/SUPPL_FILE/PNAS.2207641119.SAPP.PDF

Van Der Spoel, D., Lindahl, E., Hess, B., Groenhof, G., Mark, A. E., & Berendsen, H. J. C. (2005). GROMACS: Fast, flexible, and free. In Journal of Computational Chemistry (Vol. 26, Issue 16, pp. 1701–1718). John Wiley & Sons, Ltd. https://doi.org/10.1002/jcc.20291

Vickery, O. N., & Stansfeld, P. J. (2021). CG2AT2: An Enhanced Fragment-Based Approach for Serial Multi-scale Molecular Dynamics Simulations. Journal of Chemical Theory and Computation, 17(10), 6472–6482. https://doi.org/10.1021/ACS.JCTC.1C00295/SUPPL_FILE/CT1C00295_SI_001.PDF

Walsh, R. M., Roh, S.-H., Gharpure, A., Morales-Perez, C. L., Teng, J., & Hibbs, R. E. (2018). Structural principles of distinct assemblies of the human α4β2 nicotinic receptor. Nature 2018 557:7704, 557(7704), 261–265. https://doi.org/10.1038/s41586-018-0081-7

Wassenaar, T. A., Ingólfsson, H. I., Böckmann, R. A., Tieleman, D. P., & Marrink, S. J. (2015). Computational Lipidomics with insane : A Versatile Tool for Generating Custom Membranes for Molecular Simulations. Journal of Chemical Theory and Computation, 11(5), 2144–2155. https://doi.org/10.1021/acs.jctc.5b00209

Xu, Y., Barrantes, F. J., Luo, X., Chen, K., Shen, J., & Jiang, H. (2005). Conformational dynamics of the nicotinic acetylcholine receptor channel: A 35-ns molecular dynamics simulation study. Journal of the American Chemical Society, 127(4), 1291–1299. https://doi.org/10.1021/JA044577I/SUPPL_FILE/JA044577ISI20041112_085428.PDF

Zarkadas, E., Pebay-Peyroula, E., Thompson, M. J., Schoehn, G., Uchański, T., Steyaert, J., Chipot, C., Dehez, F., Baenziger, J. E., & Nury, H. (2022). Conformational transitions and ligand-binding to a muscle-type nicotinic acetylcholine receptor. Neuron, 110(8), 1358-1370.e5. https://doi.org/10.1016/j.neuron.2022.01.013

Zhao, Y., Liu, S., Zhou, Y., Zhang, M., Chen, H., Eric Xu, H., Sun, D., Liu, L., & Tian, C. (2021). Structural basis of human α7 nicotinic acetylcholine receptor activation. Cell Research 2021 31:6, 31(6), 713–716. https://doi.org/10.1038/s41422-021-00509-6

Zhuang, Y., Noviello, C. M., Hibbs, R. E., Howard, R. J., & Lindahl, E. (2022). Differential interactions of resting, activated, and desensitized states of the α7 nicotinic acetylcholine receptor with lipidic modulators. Proceedings of the National Academy of Sciences, 119(43), e2208081119. https://doi.org/10.1073/PNAS.2208081119

3.8 Supplementary Information

Table 3.1. CG simulations system setup

System	Lipids	No. of repeats	Box Size	No. of Atoms	No. of Water Molecules	Salt Concentration
Nicotine-bound state, Pure PC	947 POPC	3	180 x 180 x 200 Å	55355	38515	0.15 mM
Apo state, Pure PC	942 POPC	3	180 x 180 x 200 Å	55290	38493	0.15 mM
Nicotine-bound state, 3:2 PC:PA	378 POPA 569 POPC	3	180 x 180 x 200 Å	55374	38172	0.15 mM
Apo state, 3:2 PC:PA	377 POPA 566 POPC	3	180 x 180 x 200 Å	55339	38169	0.15 mM
Nicotine-bound state, 3:2 PC:Chol	378 CHOL 568 POPC	3	180 x 180 x 200 Å	54218	38906	0.15 mM
Apo state, 3:2 PC:Chol	377 CHOL 566 POPC	3	180 x 180 x 200 Å	54195	38910	0.15 mM
Nicotine-bound state, 3:1:1 PC:PA:Chol	189 CHOL 189 POPA 568 POPC	3	180 x 180 x 200 Å	54790	38533	0.15 mM
Apo state, 3:1:1 PC:PA:Chol	188 CHOL 188 POPA 566 POPC	3	180 x 180 x 200 Å	54771	38552	0.15 mM
Nicotine-bound state, 3:2 PC:monoanionic PA	378 mono-POPA 568 POPC	3	180 x 180 x 200 Å	55380	38556	0.15 mM
Apo state, 3:2 PC:monoanionic PA	377 mono-POPA 566 POPC	3	180 x 180 x 200 Å	55345	38550	0.15 mM

Table 3.2. Atomistic simulations system setup

System	Lipids	No. of repeats	Box Size	No. of Atoms	No. of Water Molecules	Salt Concentration
Nicotine-bound state, Pure PC	367 POPC	2	130 x 130 x 190 Å	315132	78192	0.15 mM
Apo state, Pure PC	378 POPC	2	130 x 130 x 190 Å	316587	78148	0.15 mM
Nicotine-bound state, 3:2 PC:PA	150 POPA 221 POPC	2	130 x 130 x 190 Å	316485	78836	0.15 mM
Apo state, 3:2 PC:PA	160 POPA 218 POPC	2	130 x 130 x 190 Å	317123	78756	0.15 mM
Nicotine-bound state, 3:2 PC:Chol	247 CHOL 312 POPC	2	130 x 130 x 190 Å	325203	77460	0.15 mM
Apo state, 3:2 PC:Chol	239 CHOL 317 POPC	2	130 x 130 x 190 Å	325030	77324	0.15 mM
Nicotine-bound state, 3:1:1 PC:PA:Chol	94 POPA 101 CHOL 266 POPC	2	130 x 130 x 190 Å	320966	78044	0.15 mM
Apo state, 3:1:1 PC:PA:Chol	93 POPA 102 CHOL 261 POPC	2	130 x 130 x 190 Å	321640	78476	0.15 mM

Figure 3.8. Top-down 2D density plots for lipid headgroups localizing around the apo nAChR in the outer leaflet. Density calculated over the course of 3 x 30μs CG-MD simulations. Density is based on the "PO4" bead for both PA and PC, and the "ROH" bead for cholesterol. Top-down subunit arrangement is shown.

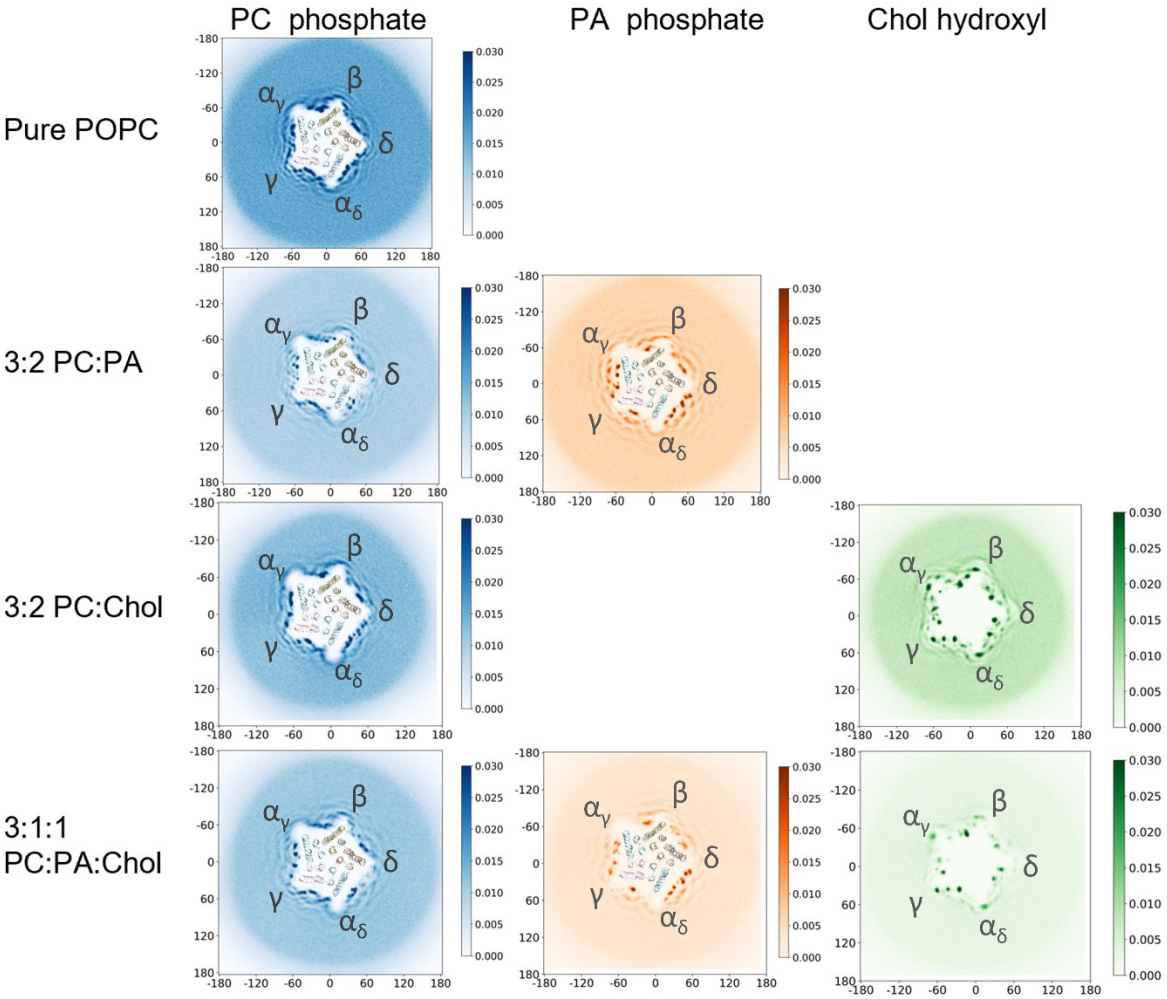
PC phosphate
PA phosphate
Chol hydroxyl
Pure POPC
3:2 PC:PA
3:2 PC:Chol
3:1:1
PC:PA:Chol
β
δ
γ
α_γ
α_δ
-180 -120 -60 0 60 120 180
0.030 0.025 0.020 0.015 0.010 0.005 0.000

Figure 3.9. Occupancy and average maximum duration profiles for lipids interacting with the apo state. A) Occupancy values (% of frames with an interacting lipid) for residues interacting with the headgroups of PC, PA or Chol (left to right blue, orange, green) are mapped onto the atomistic apo nAChR structure (PDB: 7QKO). In each case, a side view of the α_{γ}-γ subunit interface is shown. **B)** The average maximum duration for lipid headgroup binding (the average of the single longest interaction in each of three CG-MD simulation repeats of 30 μs) mapped onto the atomistic apo nAChR structure at each subunit interface. Top, PC (blue); middle, PA (orange); bottom, Chol (green).

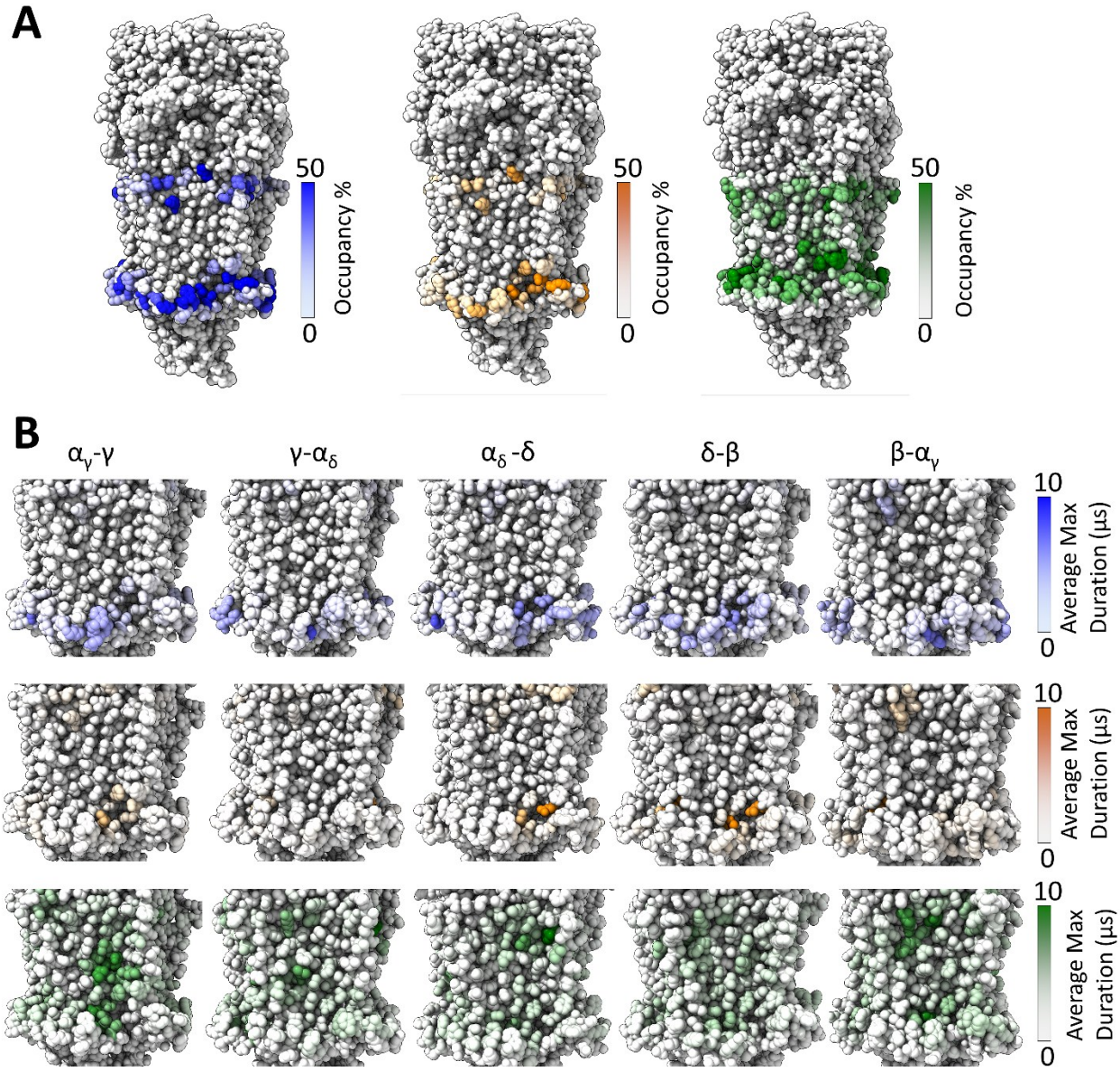
A
50
Occupancy %
0
50
Occupancy %
0
50
Occupancy %
0
B
α_γ-γ
γ-α_δ
α_δ -δ
δ-β
β-α_γ
10
Average Max Duration (µs)
0
10
Average Max Duration (µs)
0
10
Average Max Duration (µs)
0

Figure 3.10. Residues that exhibit high-occupancy interactions with lipid headgroups in the apo state. High occupancy interacting residues are shown as sticks, with key residues labelled (see Figs. S4, S6-S8). Subunit backbones are shown as cartoons.

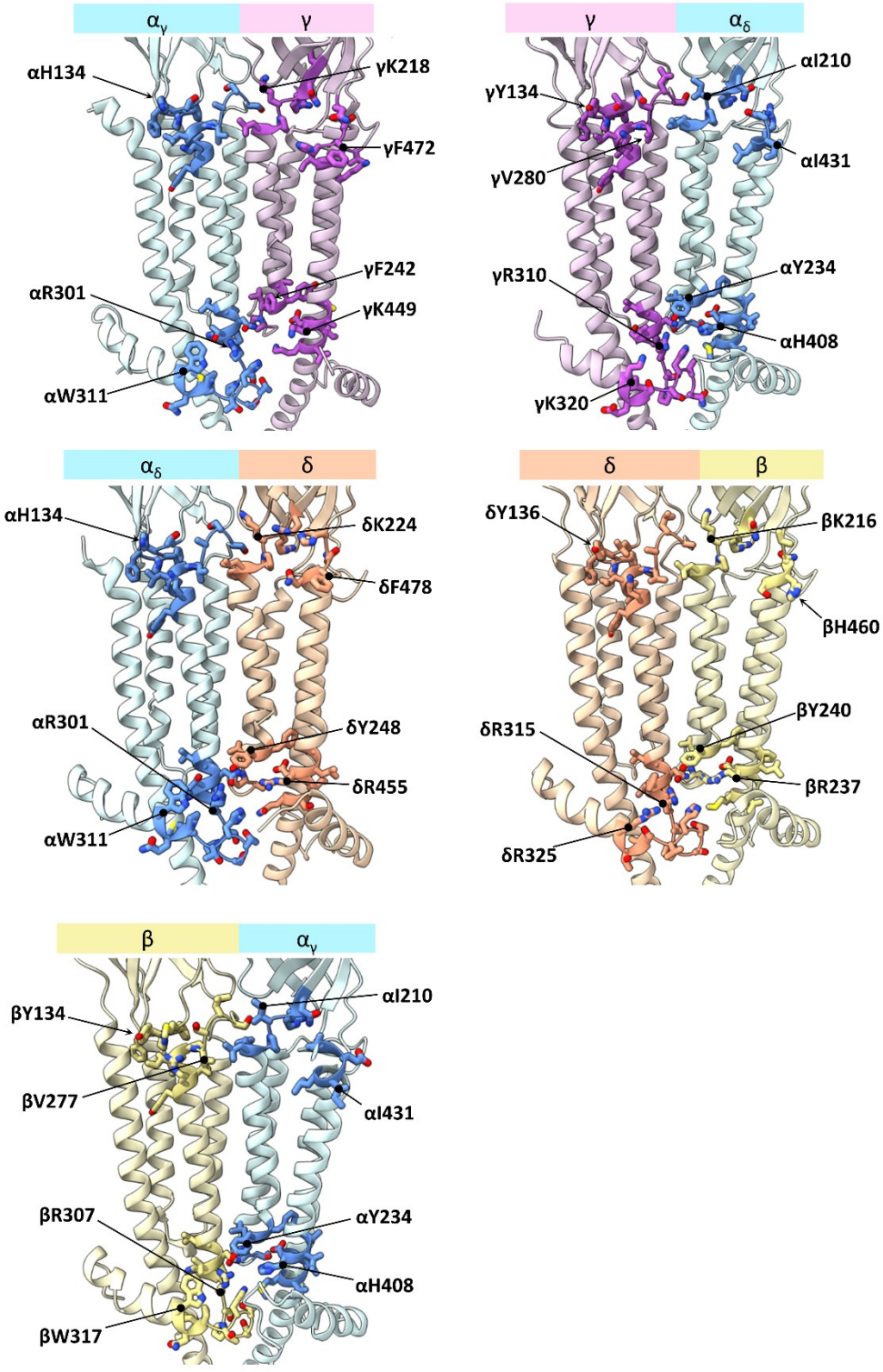
αγ
γ
αH134
γK218
γF472
γF242
αR301
γK449
αW311
γ
αδ
αI210
γY134
αI431
γV280
αY234
γR310
αH408
γK320
αδ
δ
αH134
δK224
δF478
αR301
δY248
δR455
αW311
δ
β
δY136
βK216
βH460
βY240
δR315
βR237
δR325
β
αγ
αI210
βY134
βV277
αI431
βR307
αY234
αH408
βW317

Figure 3.11. Dual axis occupancy/average maximum durations plots for PC headgroup (PO_4 bead) binding to the apo-nAChR imbedded in a pure PC membrane. Data taken from 3 x 30 μs CG-MD simulation. Error bars represent standard deviations. Structures corresponding to the lipid-interacting regions are shown in Fig. S3.

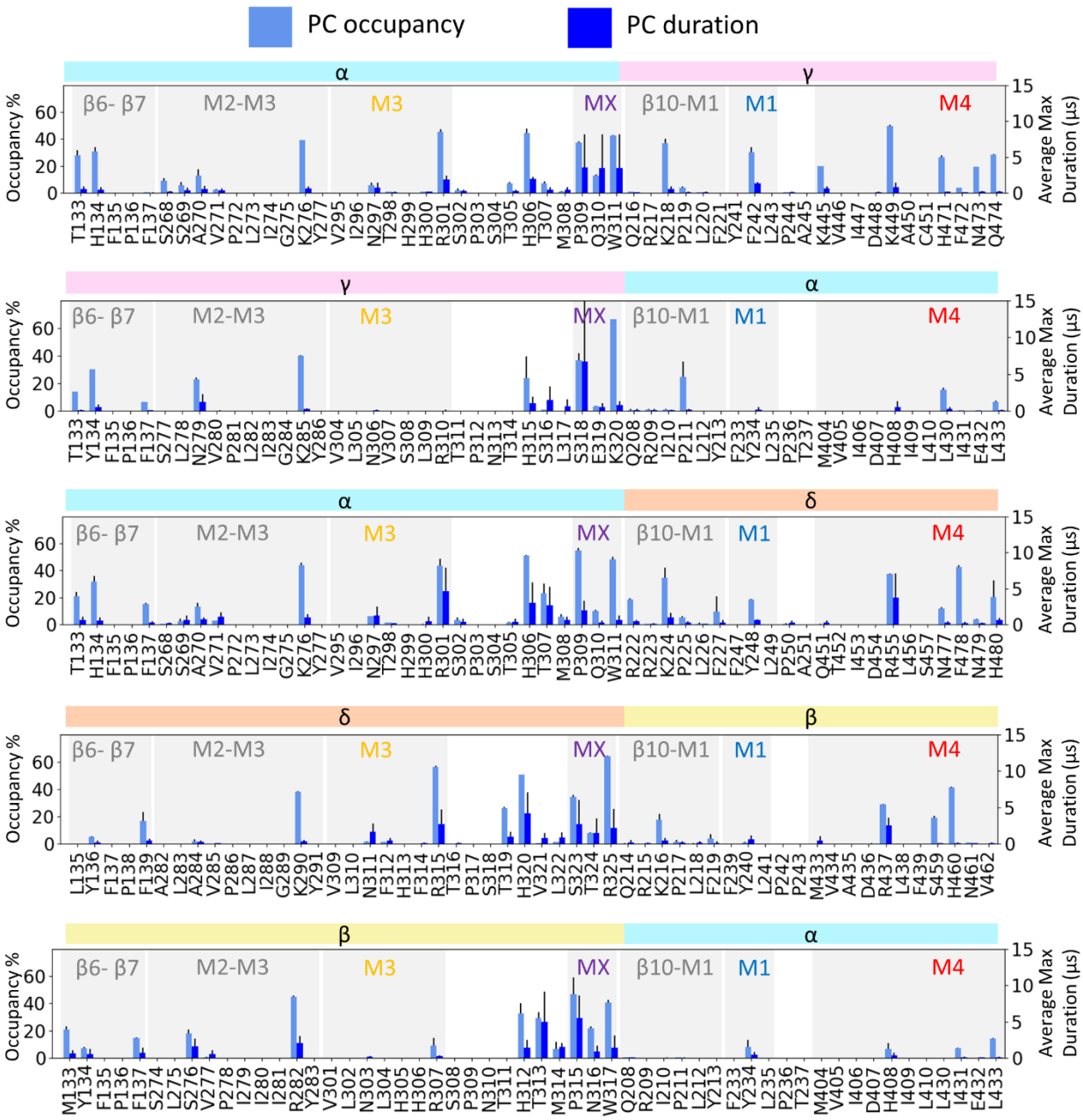
PC occupancy
PC duration
α
γ
β6- β7
M2-M3
M3
MX
β10-M1
M1
M4
Occupancy %
Average Max Duration (μs)
γ
α
α
δ
δ
β
β
α

Figure 3.12. Comparison of the lipid binding observed in the cryo-EM structures and the MD simulations. The top row shows the α_γ-γ interface of *Torpedo* nAChR structures with modelled lipids in apo and agonist-bound states. Note that for 7QKO and 7Ql5, the nAChR was purified in the *presence* of exogenous soybean azolectin, which facilitates exchange with endogenous lipids, such as Chol, and then reconstituted into azolectin MSP2N2 nanodiscs. For 7SMM, 7SMQ, and 7SMR, the nAChR was purified in the *absence* of exogenous lipid and thus retains endogenous Chol. Exogenous Chol was also added to the purified nAChR that yielded the 7SMQ structure. For these structures, the nAChR was then reconstituted into either azolectin or azolectin plus Chol (7SMQ) saposin nanodiscs. Protein subunits are shown as light cyan (α_γ) and light purple (γ) cartoons, and bound lipids are shown as spheres. The botton row shows lipid binding poses observed in atomistic simulations of the apo (7QKO) (left) and nicotine-bound (7Ql5) (right) states imbedded in 3:1:1 PC:PA:Chol membranes. In each case, a *select* representative frame from the CG-MD simulations was back-mapped to a full atom structure and then atomistic simulations run for 250 ns. The left image for both the apo and nicotine-bound structures is a swarm image, where the pose of each lipid at 8 ns intervals over the course of the 250 ns simulation is shown as sticks – the resulting 31 poses for each lipid are superimposed on top of each other. Frames were aligned to the C_α atoms of the α_γ and γ subunits. The adjacent images to the right are select frames where the bound lipids are shown as spheres. The selected frames also illustrate the variety and dynamics of lipid binding observed in the MD simulations, with some frames matching closely the lipid binding poses observed in cryo-EM structures and others capturing other distinct binding poses. For example, the two frames from the atomistic simulation for the apo state reveal lipid binding poses that match closely those observed in the apo+Chol cryo-EM structure, with some of the same poses captured in the other apo structures.

The selected frame for the nicotine-bound state reveal additional lipid binding poses as discussed in the text, such as the binding of PC with its headgroup projecting between the two MX α-helices from the principal and complementary subunits (in this frame the PC acyl chains outcompete Chol for binding) and Chol bound deeper to the high affinity inner leaflet PA binding site. The simulations also highlight sites where PA outcompetes PC for binding, particularly to inner leaflet sites. PC, blue; PA, orange; Chol, green.

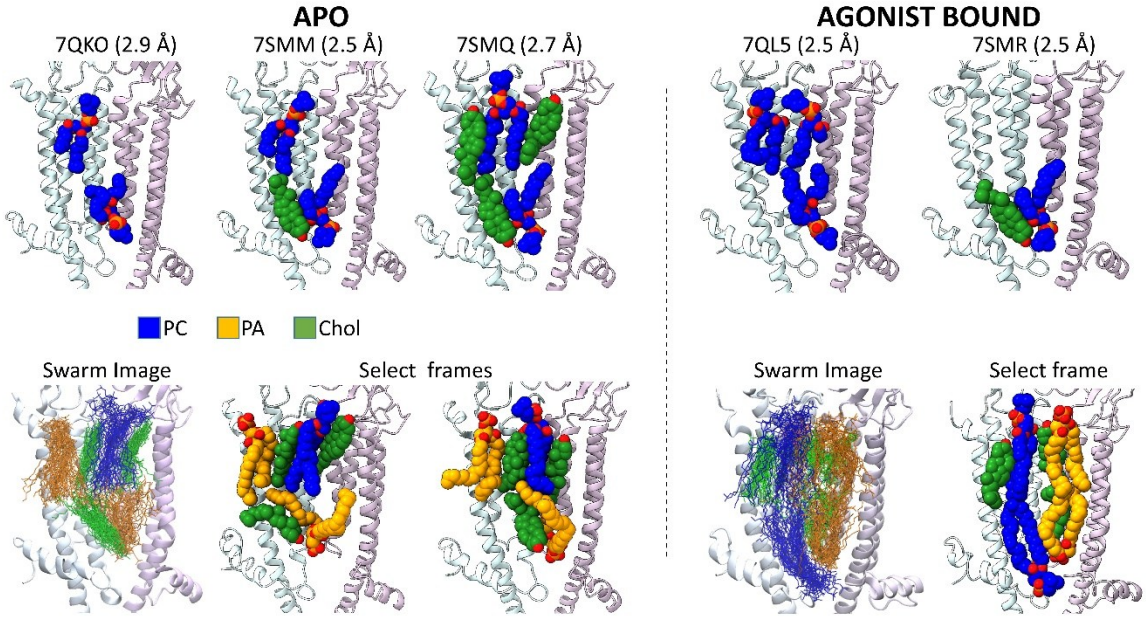
APO
AGONIST BOUND
7QKO (2.9 Å)
7SMM (2.5 Å)
7SMQ (2.7 Å)
7QL5 (2.5 Å)
7SMR (2.5 Å)
PC
PA
Chol
Swarm Image
Select frames
Swarm Image
Select frame

Figure 3.13. Dual axis occupancy/average maximum duration plots for PA headgroup (PO_4 bead) interactions with prominent residues of the apo nAChR imbedded in a 3:2 PC:PA membrane. Data taken from 3 x 30 μs CG-MD simulation. Error bars represent standard deviations. Structures corresponding to the lipid-interacting regions are shown in Fig. S3.

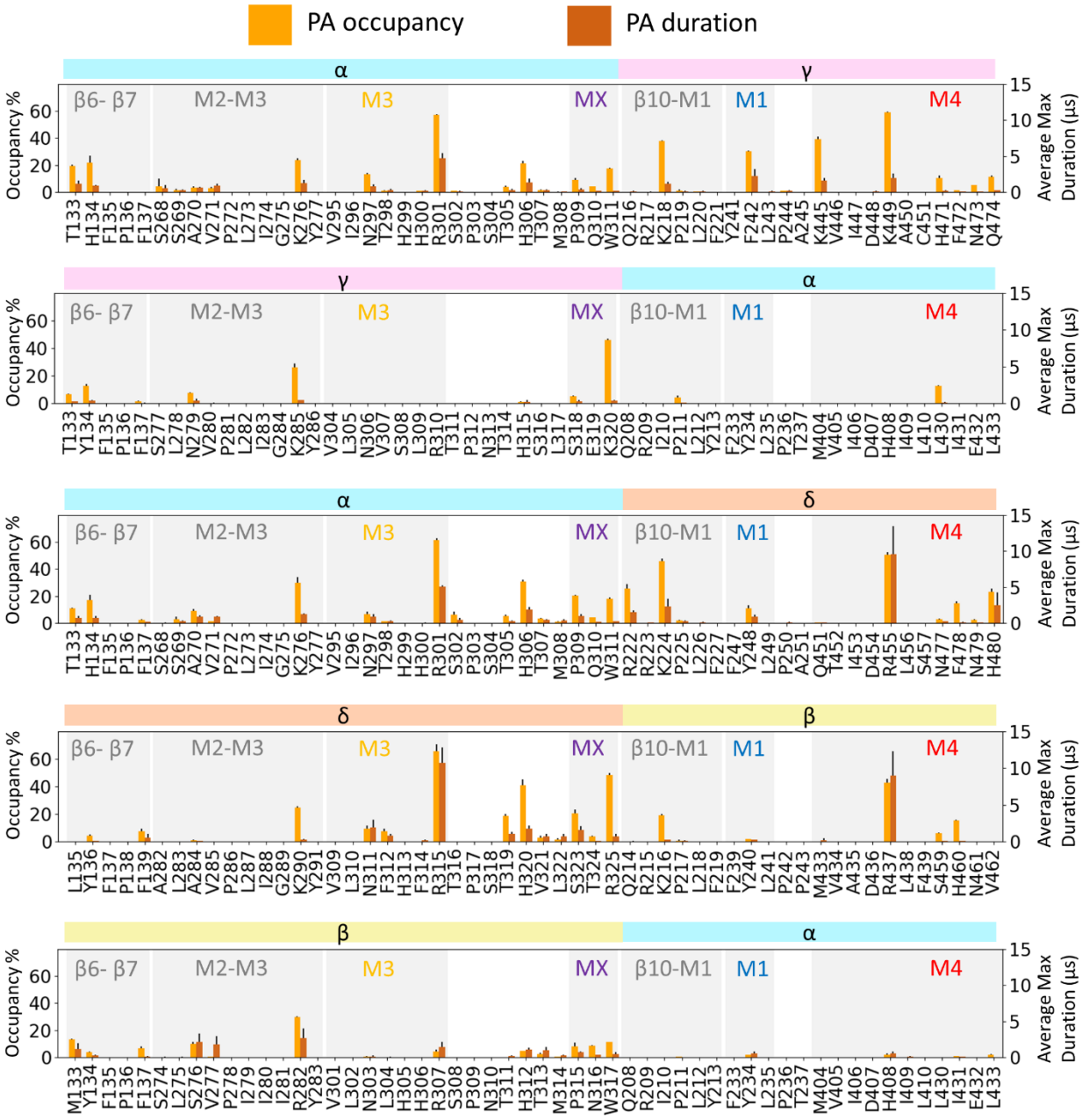
PA occupancy
PA duration
α
γ
β6- β7
M2-M3
M3
MX
β10-M1
M1
M4
Occupancy %
Average Max Duration (μs)
T133 H134 F135 P136 F137 S268 S269 A270 V271 P272 L273 I274 G275 K276 Y277 V295 I296 N297 T298 H299 H300 R301 S302 P303 S304 T305 H306 T307 M308 P309 Q310 W311 Q216 R217 K218 P219 L220 F221 Y241 F242 L243 P244 A245 K445 V446 I447 D448 K449 A450 C451 H471 F472 N473 Q474
γ
α
T133 Y134 F135 P136 F137 S277 L278 N279 V280 P281 L282 I283 G284 K285 Y286 V304 L305 N306 V307 S308 L309 R310 T311 P312 N313 T314 H315 S316 L317 S318 E319 K320 Q208 R209 I210 P211 L212 Y213 F233 Y234 L235 P236 T237 M404 V405 I406 D407 H408 I409 L410 L430 I431 E432 L433
α
δ
T133 H134 F135 P136 F137 S268 S269 A270 V271 P272 L273 I274 G275 K276 Y277 V295 I296 N297 T298 H299 H300 R301 S302 P303 S304 T305 H306 T307 M308 P309 Q310 W311 R222 R223 K224 P225 L226 F227 F247 Y248 L249 P250 A251 Q451 T452 I453 D454 R455 L456 S457 N477 F478 N479 H480
δ
β
L135 Y136 F137 P138 F139 A282 L283 A284 V285 P286 L287 I288 G289 K290 Y291 V309 L310 N311 F312 H313 F314 R315 T316 P317 S318 T319 H320 V321 L322 S323 T324 R325 Q214 R215 K216 P217 L218 F219 F239 Y240 L241 P242 P243 M433 V434 A435 D436 R437 L438 F439 S459 H460 N461 V462
β
α
M133 Y134 F135 P136 F137 S274 L275 S276 V277 P278 I279 I280 I281 R282 Y283 V301 L302 N303 L304 H305 H306 R307 S308 P309 N310 T311 H312 T313 M314 P315 N316 W317 Q208 R209 I210 P211 L212 Y213 F233 Y234 L235 P236 T237 M404 V405 I406 D407 H408 I409 L410 L430 I431 E432 L433

Figure 3.14. Interactions of monoanionic versus dianionic PA with the apo nAChR in a 3:2 PC:PA membrane. A) The top two panels are dual-axis occupancy/duration plots for monoanionic and dianionic PA binding to residues near the inner leaflet binding site at the δ-β subunit interface. Error bars represent standard deviations. The bottom panel shows interaction duration histograms for both monoanionic and dianionic lipid headgroup interactions with δR315, showing all interactions from 3 x 30 μs CG-MD simulations. **B)** Same data as in (A) but for the β-α inner leaflet binding site. Structures corresponding to the lipid-interacting regions are shown in Fig. S3.

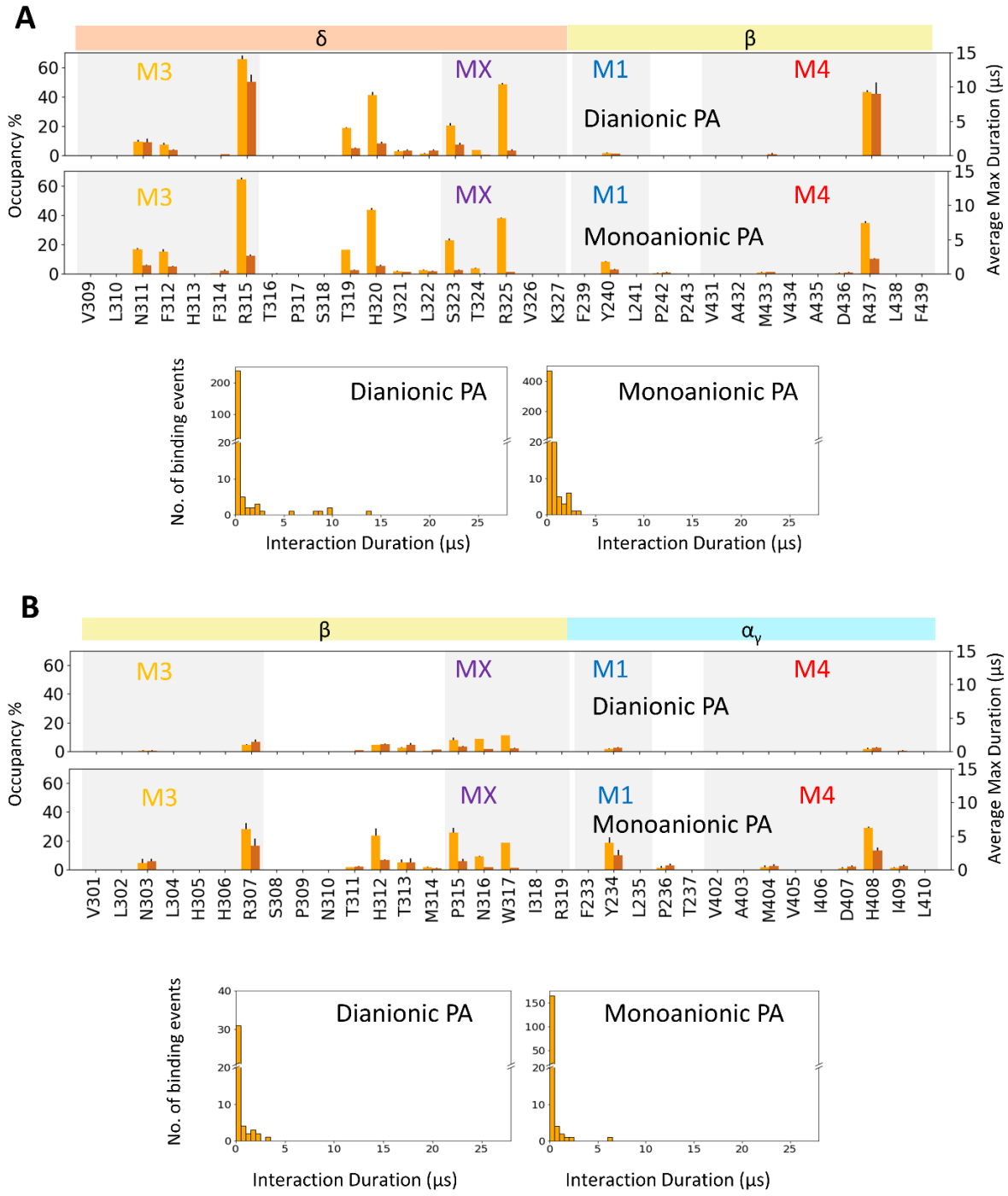
A
δ
β
M3
MX
M1
M4
Dianionic PA
Monoanionic PA
Occupancy %
Average Max Duration (μs)
V309 L310 N311 F312 H313 F314 R315 T316 P317 S318 T319 H320 V321 L322 S323 T324 R325 V326 K327 F239 Y240 L241 P242 P243 V431 A432 M433 V434 A435 D436 R437 L438 F439
No. of binding events
Interaction Duration (μs)
B
β
αγ
V301 L302 N303 L304 H305 H306 R307 S308 P309 N310 T311 H312 T313 M314 P315 N316 W317 I318 R319 F233 Y234 L235 P236 T237 V402 A403 M404 V405 I406 D407 H408 I409 L410

Figure 3.15. Dual axis occupancy/average maximum duration plots for Chol (ROH) interactions with prominent residues in a 3:2 PC:Chol membrane. Data taken from 3 x 30 μs CG-MD simulation. Error bars represent standard deviations. Structures corresponding to the lipid-interacting regions are shown in Fig. S3.

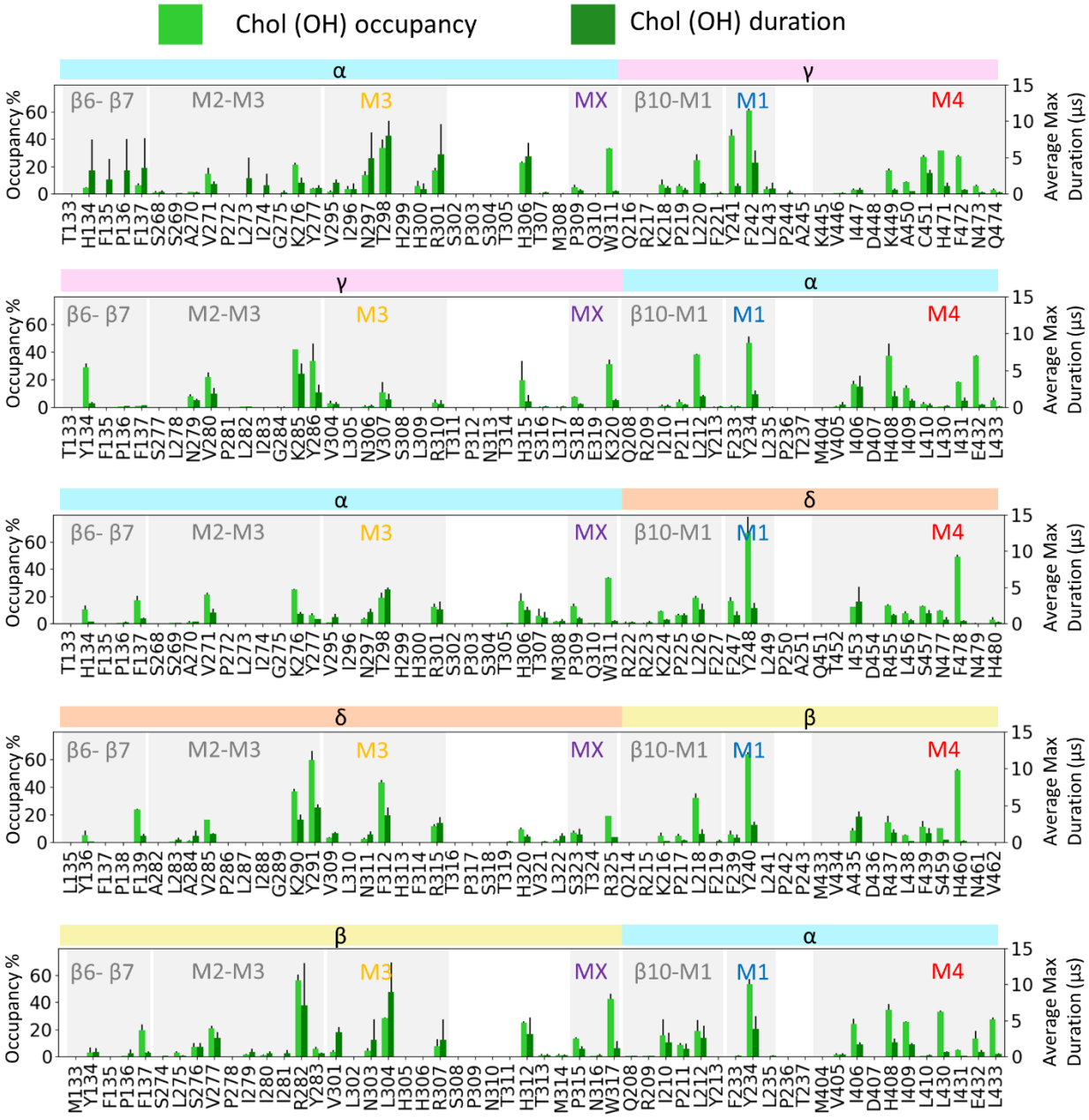
Chol (OH) occupancy
Chol (OH) duration
α
γ
β6- β7
M2-M3
M3
MX
β10-M1
M1
M4
Occupancy %
Average Max Duration (μs)
γ
α
α
δ
δ
β
β
α

Figure 3.16. Snapshots of PC and Chol binding to the apo nAChR in a 3:2 PC:Chol membrane. Images show both PC and Chol binding at 0, 125 and 250 ns corresponding to the beginning, middle and end of one atomistic simulation repeat. The left column is a top-down view of bound PC and Chol (lipids within 5 Å of the nAChR) with the lipids shown as spheres and the TMD shown as cartoon with subunits colored as in Fig. 1. The right column presents a side view of Chol interactions with the TMD. Chol bound to the canonical upper and lower leaflets is shown in light green spheres while Chol diving and bobbing into the membrane is shown as dark green spheres. In all cases, the hydroxyl is in red.

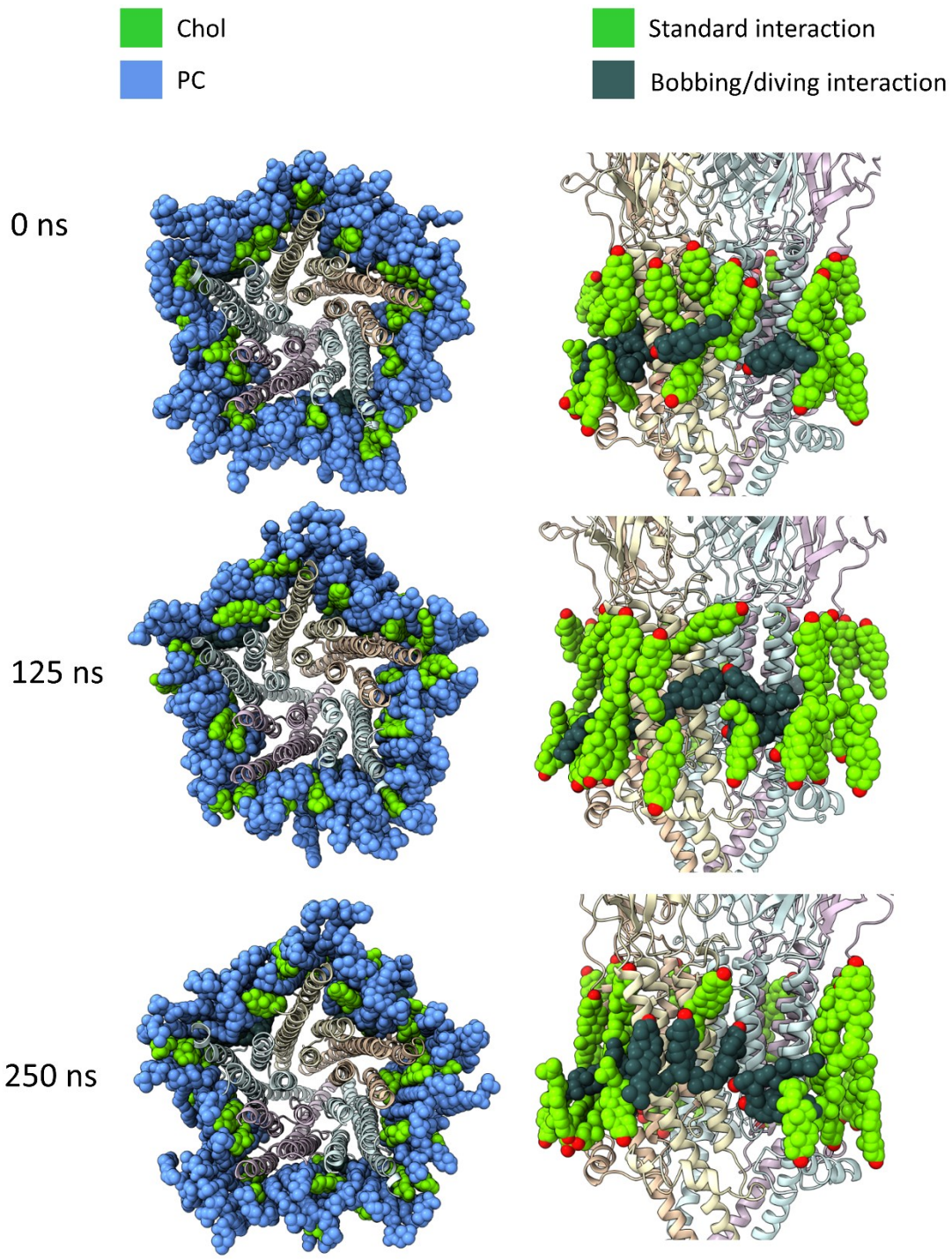
Chol
PC
Standard interaction
Bobbing/diving interaction
0 ns
125 ns
250 ns

Figure 3.17. Cholesterol leaflet distribution over time. A) Number of Chol molecules at each simulation frame in a representative 30 μs long trajectory located with their headgroups (ROH) located in the canonical outer and inner leaflets or in the middle of the bilayer. Leaflets were defined as per LiPyPhilic method[72], with a midplane cutoff of 8 Å used to select Chol molecules in the middle of the bilayer. **B)** Number of Chol molecules in each leaflet or in the middle of the bilayer at the beginning, middle and end of the 30 μs simulation. The presented values are the mean for number of Chol molecules in each region over 100 frames, with error bars representing the standard deviation. Points represent Chol counts at each frame.

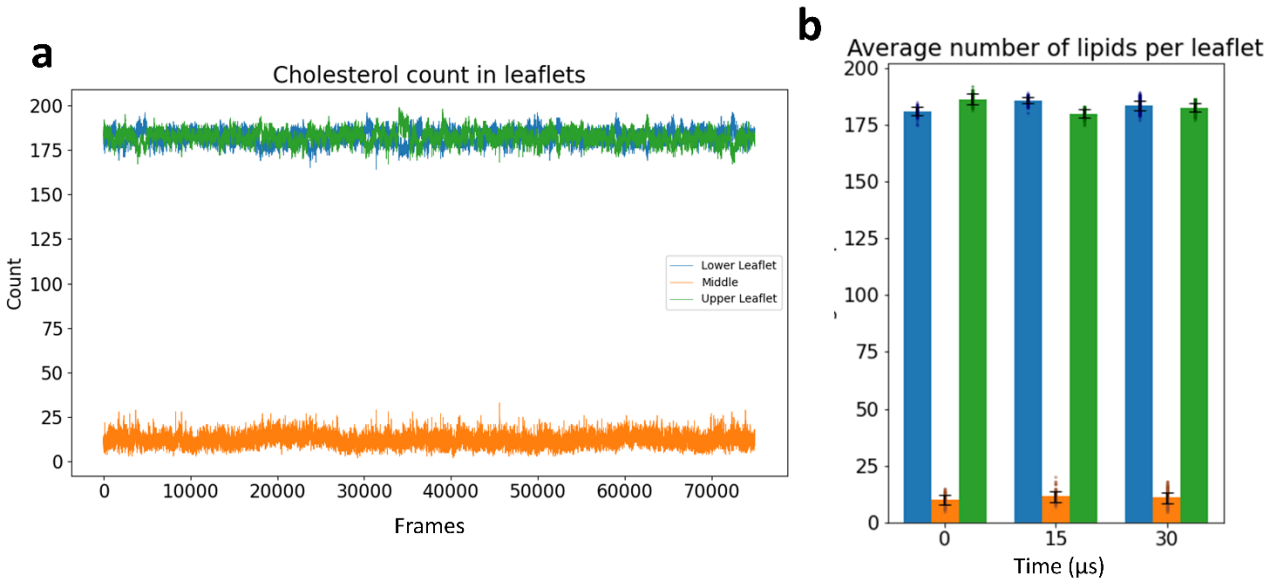
a
Cholesterol count in leaflets
Count
Frames
Lower Leaflet
Middle
Upper Leaflet
b
Average number of lipids per leaflet
Time (μs)

Figure 3.18. Chol interactions with the pore lining M2 helix in the nicotine-bound state. A) A single CG-MD simulation frame showing Chol interacting with Leu256 on the M2 α-helix of the β subunit. Protein backbone shown as sticks, with interacting residues and Chol shown as coarse-grained spheres. **B)** Average durations for Chol (ROH) interactions with residues at the β-α subunit interface in the apo (top) and nicotine-bound (bottom) states. Average interaction durations taken from 3 x 30 μs CG-MD simulations of each state in a 3:1:1 PC:PA:CHOL membrane. Error bars represent standard deviations.

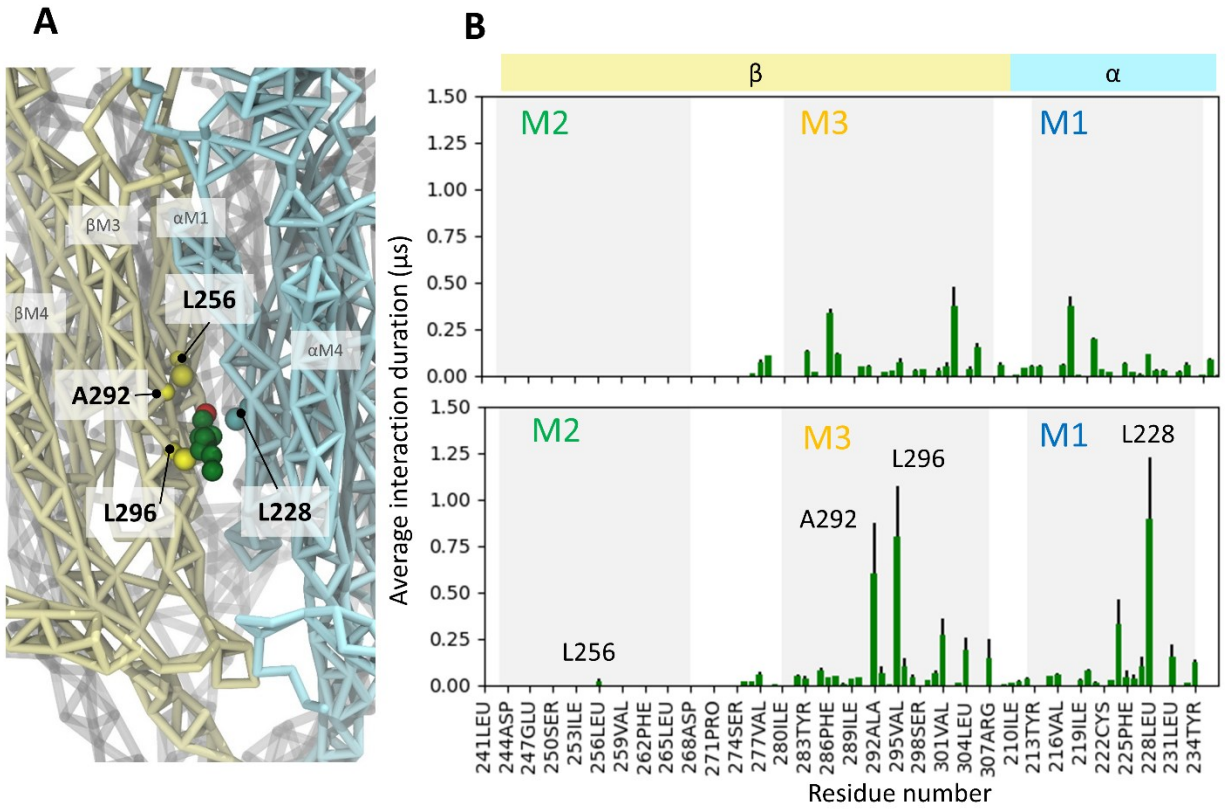
A
βM3
αM1
βM4
αM4
L256
A292
L296
L228
B
β
α
M2
M3
M1
Average interaction duration (μs)
1.50
1.25
1.00
0.75
0.50
0.25
0.00
L256
A292
L296
L228
241LEU
244ASP
247GLU
250SER
253ILE
256LEU
259VAL
262PHE
265LEU
268ASP
271PRO
274SER
277VAL
280ILE
283TYR
286PHE
289ILE
292ALA
295VAL
298SER
301VAL
304LEU
307ARG
210ILE
213TYR
216VAL
219ILE
222CYS
225PHE
228LEU
231LEU
234TYR
Residue number

Figure 3.19. Comparison of the cavity volumes observed between TMD α-helices in the apo 2BG9 (4 Å resolution) and 7QKO (2.9 Å resolution) structures. Side view (top row) and top-down (bottom row) views of the cavities in 2BG9 are shown in purple on the left with the TMD α-helices shown as silver cartoons. Grey transparent surfaces are also shown in the top-down view (bottom row). **S**ide view (top row) and top-down views (bottom row) of the cavities in 7QKO with the same coloring as for 2BG9 are shown in the middle. A side view (top row) and a top-down view (bottom row) of Chol is shown on the right. Select upper leaflet cavity volumes are labelled. The cavities in the TMD of 2BG9 are continuous. Cavities were calculated using the KVFinder web tool[75]. The output of this tool is a series of points filling each cavity, which are shown here as spheres.

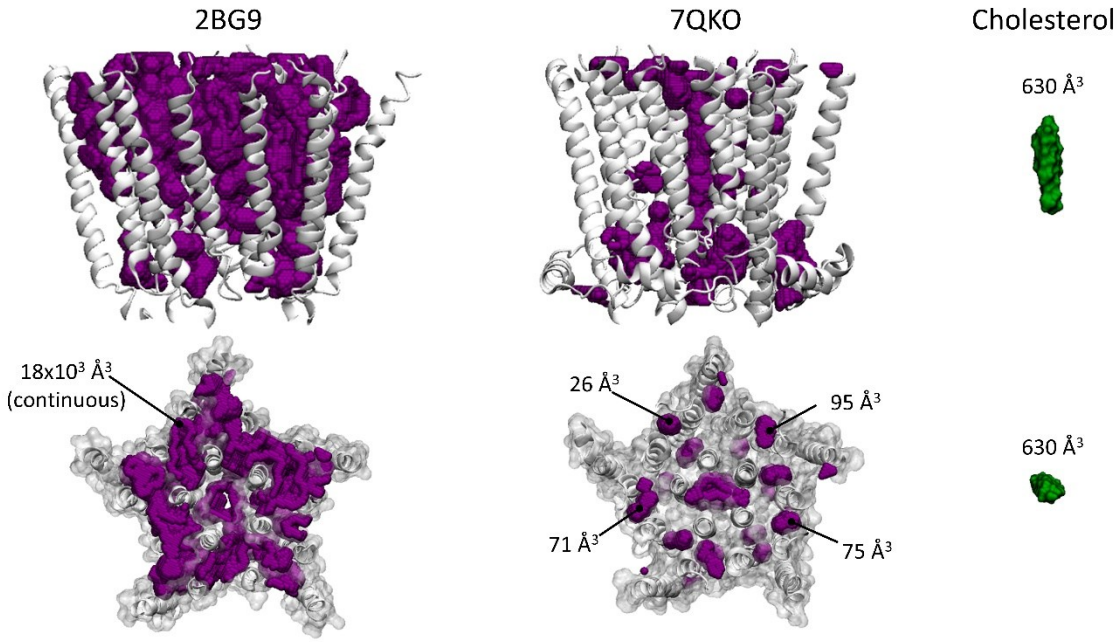
2BG9
7QKO
Cholesterol
630 Å³
18x10³ Å³
(continuous)
26 Å³
95 Å³
630 Å³
71 Å³
75 Å³

Figure 3.20. Cholesterol binding occurs in regions distinct from CRAC, CARC, and CARC-like motifs. The top row shows the location of CARC, CRAC-like and CARC-like motifs mapped onto each subunit-subunit interface in the TMD of the apo nAChR (PDB: 7QKO). The second and third rows show the average maximum duration of binding for the Chol hydroxyl and sterol groups, respectively. The fourth and fifth rows show the occupancy for the Chol hydroxyl and sterol groups, respectively. Data obtained from 3 x 30 μs CG simulation of the apo nAChR in a 3:2 PC:Chol membrane.

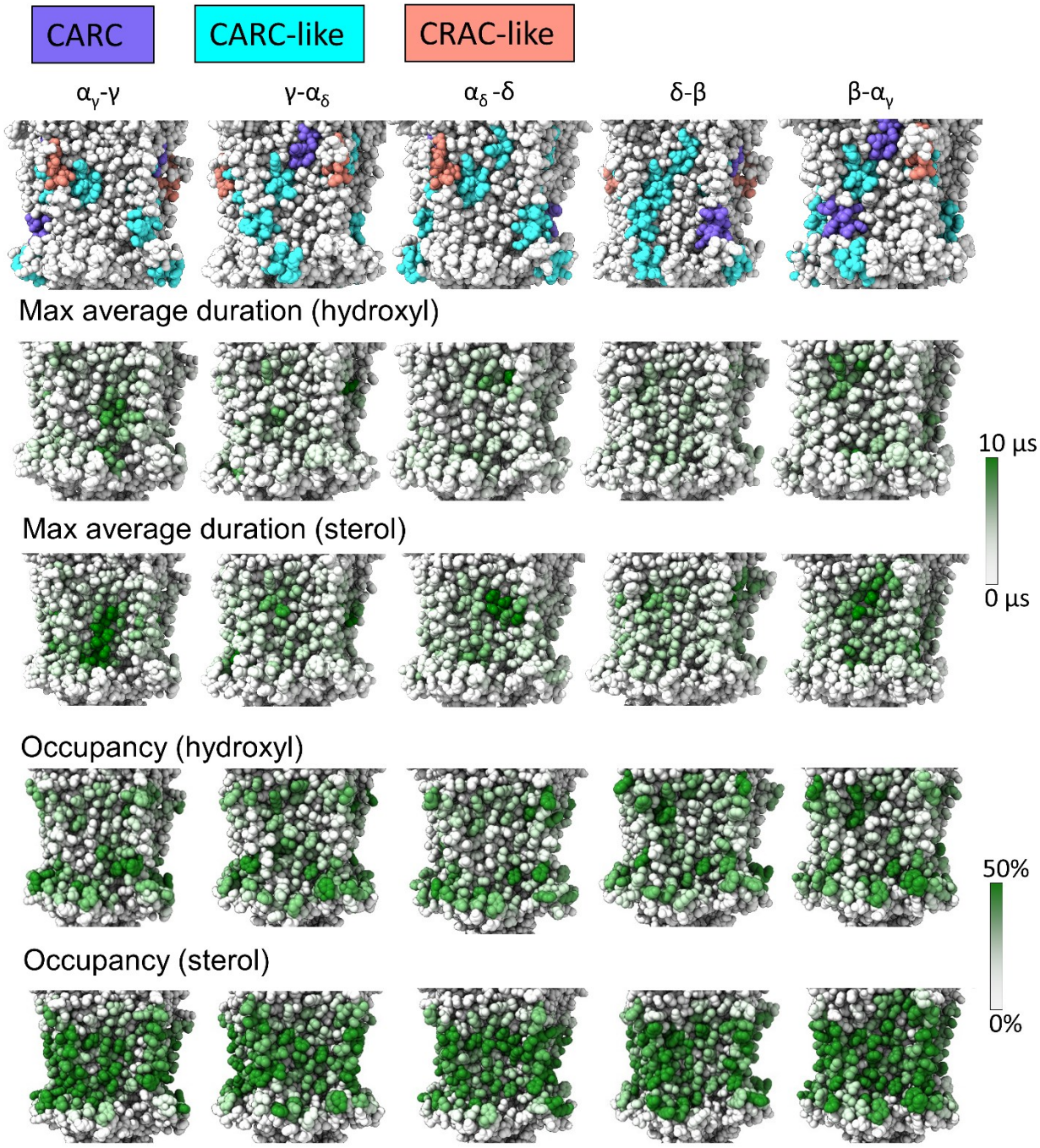
CARC
CARC-like
CRAC-like
α_γ-γ
γ-α_δ
α_δ -δ
δ-β
β-α_γ
Max average duration (hydroxyl)
Max average duration (sterol)
10 µs
0 µs
Occupancy (hydroxyl)
Occupancy (sterol)
50%
0%

Figure 3.21. Cutoff determination for PyLipID calculations. A) Probability density of interactions between lipid headgroup bead and residue sidechain beads. Interactions taken for one simulation repeat using all headgroup-residue interactions exceeding 10 simulation frames. Left: data for POPC lipids. Right: data for POPA lipids shown for comparison. **B)** Average interaction durations calculated from tested cutoff pairs. The pair (0.5, 0.85) was selected due to being able to sample long interaction durations while sampling only specific lipid interactions.

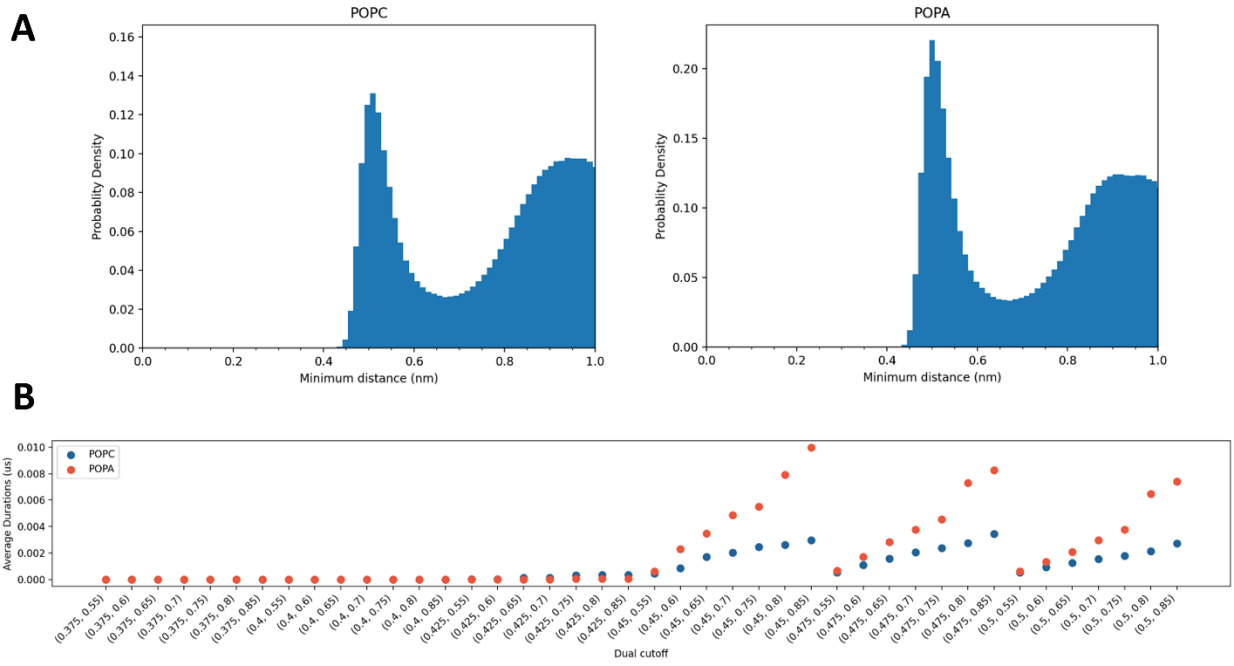
A
POPC
POPA
Probability Density
Minimum distance (nm)
B
POPC
POPA
Average Durations (us)
Dual cutoff

Supplementary Note 1

CG-MD simulations

A different initial membrane configuration with randomized lipid positions was used for each of the three independent CG-MD simulation repeats. While these simulations are of sufficient length (30 μs) to sample of lipid binding to the nAChR, several analyses suggest that the dynamic binding reflects an "equilibrated" state:

First, despite the differing initial membrane configurations, each simulation repeat leads to essentially identical top-down 2D lipid headgroup density plots (Fig. S15) showing the same reported sites of lipid binding appear regardless of the starting membrane configuration. The data suggest that the 30 μs trajectory is sufficient for the lipids to sample the entire surface of the nAChR TMD.

Second, all percent occupancy/average maximum interaction duration plots (Figs. 4, 5, S4, S6, S7, S8 and S11) that were used to characterize lipid binding contain data calculated independently from each simulation repeat, with the data from each repeat averaged and plotted with standard deviations. The small standard deviations observed in the occupancy/duration plots show that similar dynamic lipid binding is captured in each simulation repeat.

Finally, an examination of the distribution of Chol over the course of a single 30 μs CG-MD simulation trajectory (Fig. S10) shows that despite Chol moving from the outer to the inner leaflet, and vice versa, the number of Chol molecules in each leaflet remains constant.

Atomistic Simulations

In atomistic simulations, equilibration of lipid binding sites is shown by both the swarm images and distance measurements between the lipid phosphate and its coordinating residues (Figs. 7 and S3). Specifically, lipids bind stably over the course of the 250 ns simulations, albeit with the precise lipid binding pose varying according to lipid motions (see swarm plots, Fig. 7b and S3). In addition, the phosphate of PA alternates between forming a salt bridge with either the +M3 arginine or -M4 positively charged residue throughout the 250 ns simulation. Finally, the pattern and distribution of PC and Chol binding to the nAChR is shown to be consistent at three separate time points (0, 125 and 250 ns) (Fig. S9).

Figure 3.22. Top-down 2D lipid headgroup density plots for each of the three independent CG-MD simulation repeats. Density calculated over the course of each 30μs CG-MD simulation. Density is based on the "PO4" bead for both PA and PC, and the "ROH" bead for cholesterol. Results are shown for simulations of the apo state imbedded in 3:1:1 PC:PA:Chol.

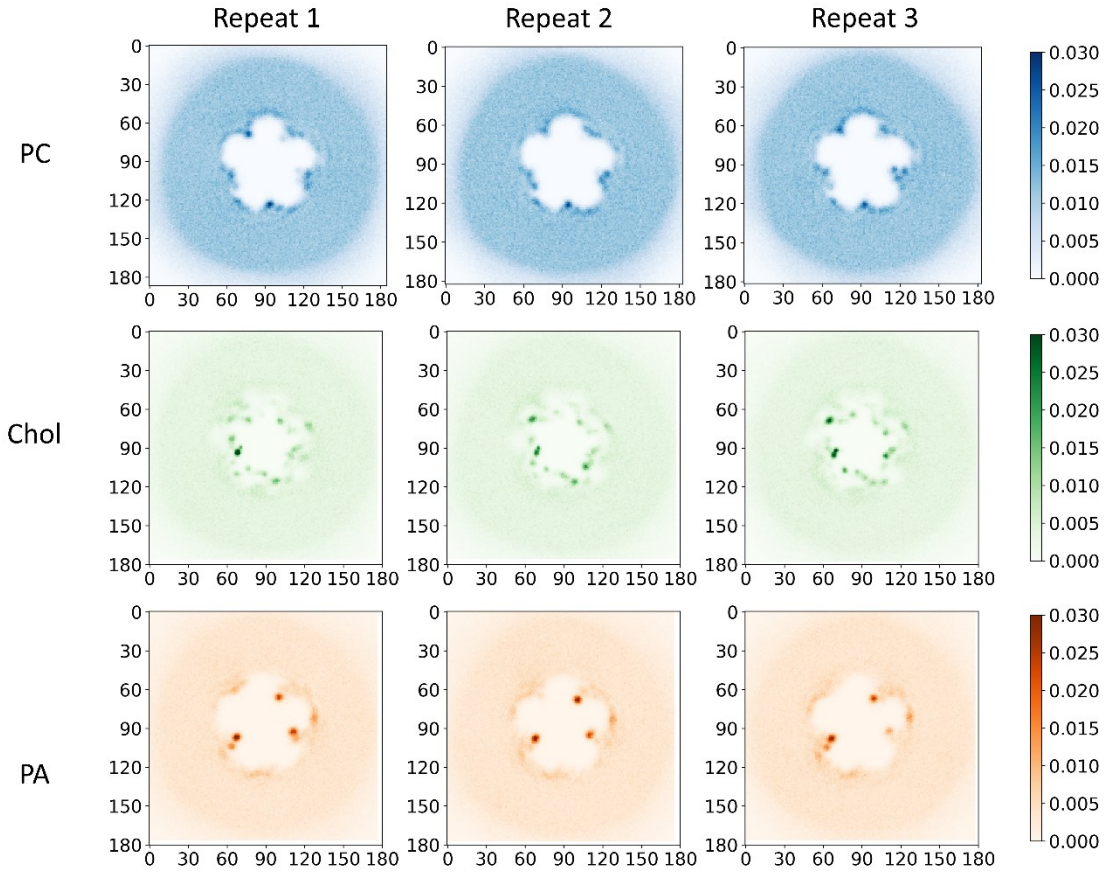
Repeat 1
Repeat 2
Repeat 3
PC
Chol
PA
0
30
60
90
120
150
180
0.030
0.025
0.020
0.015
0.010
0.005
0.000

Chapter 4: Manuscript 3: Differences in lipid affinity and binding dynamics at conserved nAChR lipid binding sites

Ananchenko, A., Szczepaniak, F., Roux, B, Baenziger, J.E., Dehez, F. (2025)

4.1 Preface

The final co-first author manuscript of my PhD builds on the data obtained in chapter 3. In this chapter I further investigate PA and PC atomistic interactions with low and high affinity inner leaflet nAChR binding sites. A major goal in the field of lipid-ion channel interactions is to define relative affinities of lipid species to different membrane protein sites in different states. I therefore use FEP to quantify the difference in binding free energy of PA and PC to the α_{γ}-γ and highlight limitations in this approach for studying ligand-LGIC interactions. In this manuscript, I further interpreted data from the atomistic simulations introduced in chapter 3. Flo Szczepaniak created the dual topology used in these FEP calculations and wrote the scripts to set up the system for alchemical transformations. I performed all the FEP calculations. Flo and I interpreted the results of the FEP calculations in consultation with Dr. Dehez, Dr. Roux and Dr. Baenziger. I wrote the majority of the manuscript with some sections written by Flo and edited the manuscript with Dr. Dehez and Dr. Baenziger.

4.2 Abstract

Recent cryo-EM and simulation studies of the *Torpedo* nAChR identify potential phospholipid binding sites at subunit-subunit interfaces in the inner leaflet. The sites located at the α_{γ}-γ, α-δ and δ-β subunit interfaces are suggested to exhibit high affinity for the anionic lipid PA, which stabilizes a coupled state of the receptor, relative to PC, which stabilizes an uncoupled state. There is not yet a clear description of the exact differences in atomic interactions between these two lipid species, nor has the difference in apparent affinity been quantified. Here we give a detailed description of the interatomic interactions between bound phospholipids lipids and residues in the putative inner leaflet binding sites. We also calculate the relative binding free energy of PA and PC using FEP at the α_{γ}-γ binding site, suggesting that longer interaction durations of PA as opposed to PC observed in CG simulations are caused by a higher relative affinity of PA to this site.

4.3 Introduction

Pentameric ligand-gated ion channels (pLGICs) are a family of membrane proteins which feature an assembly of five subunits around a central pore. They mediate fast synaptic communication by opening an ion channel in response to the binding of a ligand (Corringer et al., 2012). The agonist-induced response of many ion channels is modulated by surrounding membrane lipids. This has been particularly well studied over the last several decades in the case of the prototypic *Torpedo* nAChR, which is sensitive to the presence of anionic and/or neutral lipids for optimal function (Fong & McNamee, 1986; Sunshine & McNamee, 1992). The structure of this nAChR is composed of two α subunits, and one each of a γ, δ and β subunit arranged as a pentamer (Figure 4.1 A). nAChRs reconstituted into a membrane containing 3:1:1 ratio of phosphatidylcholine (PC), phosphatidic acid (PA) and cholesterol (Chol) exhibit native-like function, whereas they are non-functional in membranes containing pure PC (Baenziger et al., 2000; daCosta & Baenziger, 2009; Sunshine & McNamee, 1992). Lipids modulate the function of nAChRs through a conformational selection mechanism. Membranes containing both anionic and neutral lipids stabilize an activatable resting state of the receptor, in which binding of agonist to the extracellular domain (ECD) leads to pore opening in the transmembrane domain (TMD). Functional studies have shown that PA is particularly effective at stabilizing an activatable conformation (daCosta et al., 2009). In non-optimal membranes, such as those containing only the zwitterionic lipid PC, the receptor is in an uncoupled state, whereby it binds agonist with resting state-like affinity, but does not open a pore to conduct ions (daCosta et al., 2013; daCosta & Baenziger, 2009).

The localization of different lipid species at the TMD of pLGICs has been studied using multiscale MD simulations (Ananchenko & Musgaard, 2023; Dämgen & Biggin, 2021; Sharp et al., 2019; Sharp & Brannigan, 2021; Zhuang et al., 2022). In a simulation study of the *Torpedo* nAChR

embedded in simple membranes containing POPC, POPA and/or Chol, phospholipids localized to conserved, inner leaflet sites at the interface between two subunits, sites also identified in cryo-EM structures (Rahman et al., 2022; Zarkadas et al., 2022). PA was shown to preferentially occupy and thus outcompete POPC binding to inner leaflet sites at the α_γ-γ, α_δ-δ, and δ-β interfaces. These sites were deemed "high affinity" anionic lipid binding sites as PA as they exhibit longer interaction durations than PC with cationic residues in these binding pockets. At the β-α_γ and γ-α_δ sites, however, some localization of both PA and PC was observed, with no clear preference for the anionic lipid PA. These sites were deemed to have "low affinity" for anionic lipids due. Recent cryo-EM structures show variability in the poses of bound lipids at the inner leaflet sites at the interfaces between different subunits (Gharpure et al., 2019; Rahman et al., 2020; Walsh et al., 2018; Zarkadas et al., 2022) (Figure 4.1B), and even suggest the existence of both low and high affinity lipid binding sites (Rahman et al., 2022). It is possible that the effectiveness of different lipids to stabilize an activatable state of the nAChR depends on their relative affinities for different binding sites.

Figure 4.1. Cryo-EM structure of the *Torpedo* nAChR with bound lipids (PDB:7QL5). A. Top-down view of the nAChR transmembrane domain showing pentamer arrangement. The protein is shown in cartoon representation coloured by subunit. Bound lipids in the inner leaflet region are shown as sticks. **B.** Side view of resolved lipids at the transmembrane domain. The protein is shown as a surface representation coloured by subunit corresponding to those shown in A. Bound lipids are shown as dark blue spheres coloured by heteroatom.

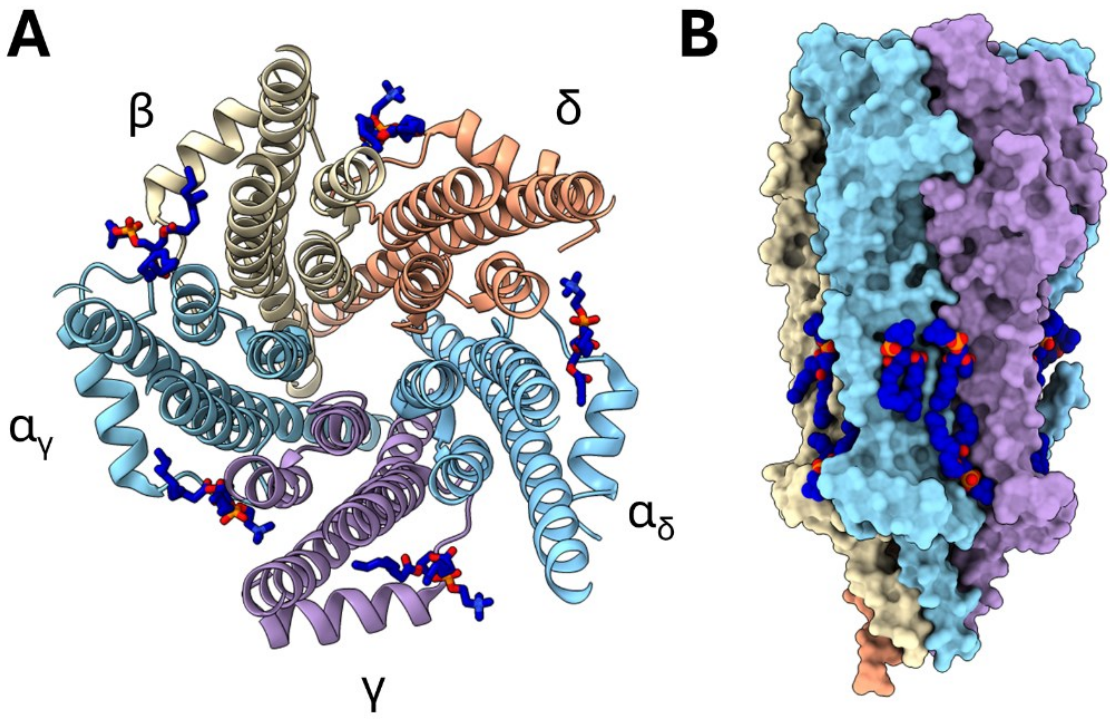
A
β
δ
α_γ
α_δ
γ
B

A major goal of the lipid-protein interactions field is to define the relative affinities in how different lipids bind to different states of a membrane protein, as this correlates directly with understanding how lipids affect function. Free energy perturbation (FEP) is widely for estimating protein:ligand affinity (Fu et al., 2022), including binding free energy of different lipid species to sites on proteins(Corey et al., 2019; Duncan et al., 2020). In a recent study, the relative binding affinities of PC, phosphatidylethanolamine (PE) and phosphatidylglycerol (PG) to a different member of the pLGIC family, ELIC, were computed (Petroff et al., 2022). This was done using the recently developed Streamlined Alchemical FEP (SAFEP) strategy (Santiago-McRae et al., 2023). The ΔΔG calculated for POPE to POPC (both zwitterionic lipids, but POPE has a smaller polar head) is around 4 kcal/mol. The ΔΔG calculated for POPE to POPG (zwitterionic to anionic lipid) is around -2 kcal/mol, consistently with the higher affinity of the protein for anionic lipids. These studies quantitatively show that similar phospholipids may bind to the same binding sites with different affinities.

The work presented on this paper builds on previous insight into the differences in anionic and zwitterionic phospholipid binding to conserved nAChR sites. We provide detailed description of the interactions between phospholipids at the previously identified phospholipid binding sites on the nAChR and the dynamic nature of these interactions. We also quantify the difference in affinity between an anionic compared to a zwitterionic lipid to one of the nAChR lipid binding sites and discuss the limitations of FEP approaches in understanding lipid-ion channel interactions.

4.4 Methods and Materials

Starting configurations

A cryo-EM structure of the *Torpedo* nAChR apo state (PDB:7QKO) at 2.9 Å resolution (Zarkadas et al., 2022) was used for all simulations. Initial lipid-bound configurations were generated by backmapping selected frames from Martini 2 coarse-grained (CG) simulations as described in (Ananchenko et al., 2024). For PA-bound systems, a frame selected from a CG simulation of the nAChR embedded in a membrane containing a 3:2 molar ratio of PC:PA, where a PA molecule occupied each of the three binding sites deemed high affinity. The exception to this were systems with PA bound to the "low affinity" β-α_γ site. Due to low occupancy of PA at this site in CG simulations, frames were picked separately for this case, with two separate frames picked where PA occupied the site. In the case of PC-bound systems, a frame was selected from a CG simulation containing the nAChR in a pure PC membrane. A PC molecule occupied each of the five lipid binding sites.

Brute Force MD simulations

Backmapped systems resulted in a box size of 130 x 130 x 190 Å containing approximately 300,000 atoms. Salt concentration was corrected to 0.15 M of NaCl after backmapping, with additional Na+ ions added to create a net zero charge in systems containing PA. The CHARMM36 (Huang & Mackerell, 2013) forcefield was used for the protein, ions and lipids, and the TIP3P (Jorgensen & Jenson, 1998) model was used for water. NAMD 3.11 (Phillips et al., 2020) was used to carry out brute force simulations. Each system was minimized for 1000 steps, equilibrated for 5 ns with soft harmonic potential restraints on all heavy protein atoms, then equilibrated for an additional 5ns with restraints only on heavy backbone atoms. Production runs were performed for

200-250 ns for two repeats of each initial backmapped system, apart from the two specially selected frames showing PA binding at β-α_γ sites, which were simulated for one repeat each.

Temperature was held constant at 300K using the Langevin thermostat (Feller et al., 1995) and pressure was held at 1 atm using the Langevin piston method. The SHAKE/RATTLE (Andersen, 1983; Ryckaert et al., 1977) algorithms were used for constraining covalent bonds involving hydrogen atoms and the SETTLE (Miyamoto & Kollman, 1992) algorithm was used for water. A timestep of 8 and 4 fs was used for long- and short-range interactions respectively, using the r-RESPA multiple time-stepping algorithm (Tuckerman et al., 1992). A timestep of 4 fs was possible due to hydrogen mass repartitioning (Hopkins et al., 2015).

FEP calculations

The same simulation parameters as above were used with two modifications. Temperature was set to 315 K, and the NAMD3b2 simulation software was used to enable GPU-resident simulations with colvars (Fiorin et al., 2013). The first repeat of the brute force simulation in which the nAChR is embedded in a 3:2 molar ratio of PC:PA was used to generate the initial state for the FEP calculation. The PA molecule bound to the α_γ-γ site was replaced with a hybrid topology lipid. This hybrid lipid topology contains common acyl chains and glycerol groups, but two separate headgroups, which correspond to the PA phosphate group and the PC phosphate and choline groups. Alchemical transformations in the bulk membrane were performed by creating a membrane-only system containing a 3:2 molar ratio of PC:PA in a 115 x 115 x 85 Å box using CHARMM-GUI (Lee et al., 2016). The same hybrid topology was used and applied to a randomly selected lipid in the bilayer for FEP calculations. FEP calculations were performed over 50 lambda windows of 1.5 ns each in both the forward and reverse direction. Each lambda window was equilibrated for 1000 steps prior to collecting FEP data.

To calculate the free energy contribution of a change to the system charge, a water molecule was transformed into a Cl- ion using the same FEP steps as above. The calculation was performed in both a membrane-only and a membrane plus nAChR system to account for differences in the relative system proportion of water.

Selection of restraints for lipid in binding site

Restraints are added to FEP calculations to reduce the configurational space to sample in the protein:ligand system and thereby enhance convergence. Applying restraints to a lipid bound to the TMD of an nAChR presents a challenge for several reasons. First, unlike a traditional ligand, a bound phospholipid moves between several energetically equivalent binding poses while in the binding pocket. The alkyl chain lipid tails are constantly in motion while the phosphate and glycerol groups are coordinated in the binding site. Because of this, imposing positional and orientational restraints leads to inadequate sampling of the lipid-binding energetic landscape.

Rather than imposing positional or orientational restraints on the lipid, we opted to include a harmonic wall at a distance from the lipid binding site, with a distance limit of 15 Å based on analysis of lipid binding from brute force simulations (Figure 4.6). Since both PA and PC remain bound to this site throughout brute force simulations, the harmonic wall is a preventative measure to prevent unbinding during lipid discharging and does not affect the FEP endpoints. A somewhat similar strategy is used in the SAFEP method, in which a distance-to-bound configuration (DBC) coordinate is defined, and an upper limit to this coordinate is set using a harmonic wall. These restraints are introduced to enhance the convergence of the calculations at a lower cost than other more usual sets of restraints used in FEP calculations (Santiago-McRae et al., 2023).

4.5 Results

Lipid-nAChR interactions in brute force simulations.

Initial studies deemed the inner leaflet α_{γ}-γ, α_{δ}-δ and δ-β sites to have high affinity for PA over PC, suggested by the much longer interaction durations of PA at these sites (Ananchenko et al., 2024). When bound at these sites, the phosphates of both PA and PC form salt bridges with positively charged residues in the binding pocket. The lipid can form salt bridge interactions with an arginine on the M3 helix of the principal subunit, for example αR301 and/or a lysine or arginine on the M4 helix of the complementary subunit, for example γK449 (Figure 4.2). While one or both salt bridge interactions are present throughout the duration of equilibrium simulations, the lipid may alternate between forming these interactions with the principal or complimentary cationic residue. Additional coordinating interactions in the form of hydrogen bonds between polar residues deep in the binding pocket and the glycerol moiety of the lipids are present, although they are variable.

Despite these common coordinating interactions and the fact that both PA and PC generally stay bound withing these pockets over the atomistic 250 ns simulation trajectories, they remain dynamic in their binding pose. While electrostatic interactions which coordinate the bound lipids are continuously present throughout the simulation trajectories, the exact interatomic pairings which participate in these interactions vary between the two lipid types, the bindings sites, and even the simulation repeats (Figures 4.2-4.4). The bound lipids adopt dynamic binding poses, with some simulations exhibiting more defined acyl chain poses than others.

The coordinating interactions and binding pose of PA are relatively well defined at the α_{γ}-γ site. In one simulation repeat, the phosphate group of PA forms a salt bridge to the conserved M3 helix arginine for almost the entire 250 ns trajectory, with additional stable electrostatic interactions of

the glycerol group with N297 on the α_γ M3 helix and K445 on the γ M4 helix (Figure 4.2 A,B). The second simulation repeat also shows the PA phosphate group participating in salt bridge interactions for much of the trajectory, albeit moving between K445 and K449 on the M4 helix of the γ subunit. PC on the other hand has a relatively lower occurrence of salt bridges between its phosphate group and the positively charged residues in this binding pocket, presumably due to greater variability in its headgroup pose (Figure 4.2 B,C).

Figure 4.2. Lipid binding poses at the α_γ-γ site in brute-force simulations. A. Bound lipid in a cryo-EM structure of the nAChR, modelled as PC (PDB: 7QL5). Protein subunits are shown as cartoon with α_γ subunit in blue and γ subunit in purple. Bound lipid and coordinating residues are shown as sticks and coloured by heteroatom. Protein helices are labelled. **B.** Interaction network between polar atoms of bound lipid and coordinating residues in the binding pocket. Lipid polar atoms corresponding to headgroup and glycerol groups are shown on the y-axis and polar atoms of binding site residues of the principal (α_γ) and complimentary (γ) subunits are shown on the x-axis. Boxes corresponding to each interaction pair are coloured by % of trajectory (250 ns) in which an electrostatic interaction is present, defined by a distance of less than 3 Å between the two atoms. **C.** Evolution of lipid binding poses throughout the trajectory, with lipid binding pose snapshot is shown every ~5 ns. Left to right: PA bound in repeat 1, PA bound in repeat 2, PC bound in repeat 1, PC bound in repeat 2.

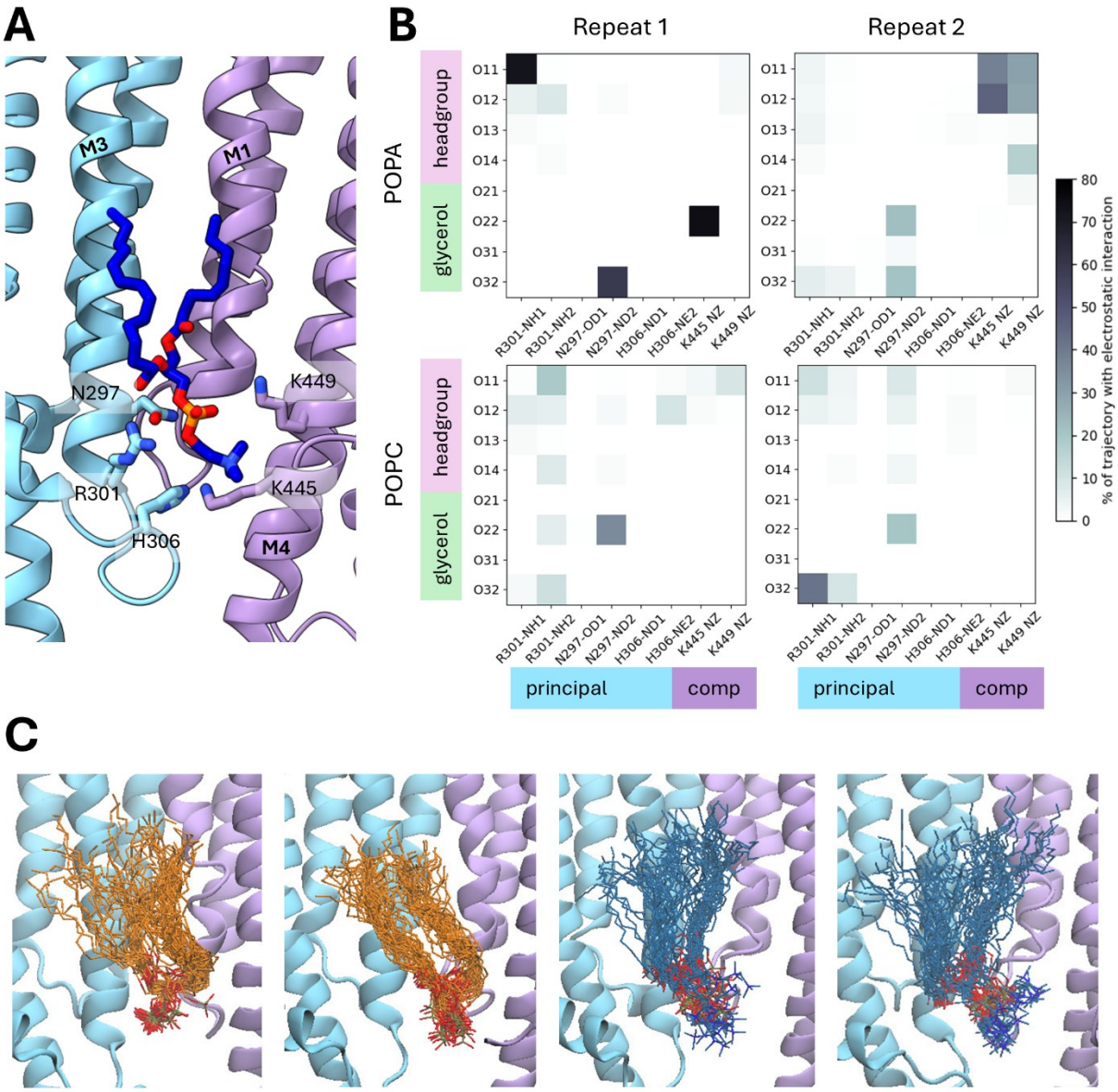
A
M3
M1
N297
K449
R301
K445
H306
M4
B
Repeat 1
Repeat 2
POPA
POPC
headgroup
glycerol
O11
O12
O13
O14
O21
O22
O31
O32
R301-NH1
R301-NH2
N297-OD1
N297-ND2
H306-ND1
H306-NE2
K445 NZ
K449 NZ
principal
comp
% of trajectory with electrostatic interaction
0
10
20
30
40
50
60
70
80
C

Another binding site deemed high affinity, the δ-β site, suggests a different pattern of interactions than the α_γ-γ site. While salt bridge interactions between the PA phosphate group and the arginine residues on the δ and β subunits are present, there is greater movement between different atom pairs. Surprisingly. The PC phosphate group participates in a stable salt bridge with βR437 in the second simulation repeat (Figure 4.3 B). Compared to PA, however, the PC glycerol moiety does not participate in any electrostatic interactions with the binding pocket (Figure 4. 3B). Compared to bound poses of both lipids at the α_γ-γ site, the positions of the acyl chain tails are more variable at the δ-β site. These results suggest that even though both high affinity sites exhibit higher PA occupancy and longer interaction durations than PC, the binding modes of lipids to these two sites are distinct.

Figure 4.3. Lipid binding poses at the δ-β site in brute-force simulations. A. Bound lipid in a cryo-EM structure of the nAChR, modelled as PC (PDB: 7QL5). Protein subunits are shown as cartoon with the δ subunit in salmon and β subunit in yellow. Bound lipid and coordinating residues are shown as sticks and coloured by heteroatom. Protein helices are labelled. **B.** Interaction network between polar atoms of bound lipid and coordinating residues in the binding pocket. Lipid polar atoms corresponding to headgroup and glycerol groups are shown on the y-axis and polar atoms of binding site residues of the principal (δ) and complimentary (β) subunits are shown on the x-axis. Boxes corresponding to each interaction pair are coloured by % of trajectory (250 ns) in which an electrostatic interaction is present, defined by a distance of less than 3 Å between the two atoms. **C.** Evolution of lipid binding poses throughout the trajectory, with lipid binding pose snapshot is shown every ~5 ns. Left to right: PA bound in repeat 1, PA bound in repeat 2, PC bound in repeat 1, PC bound in repeat 2.

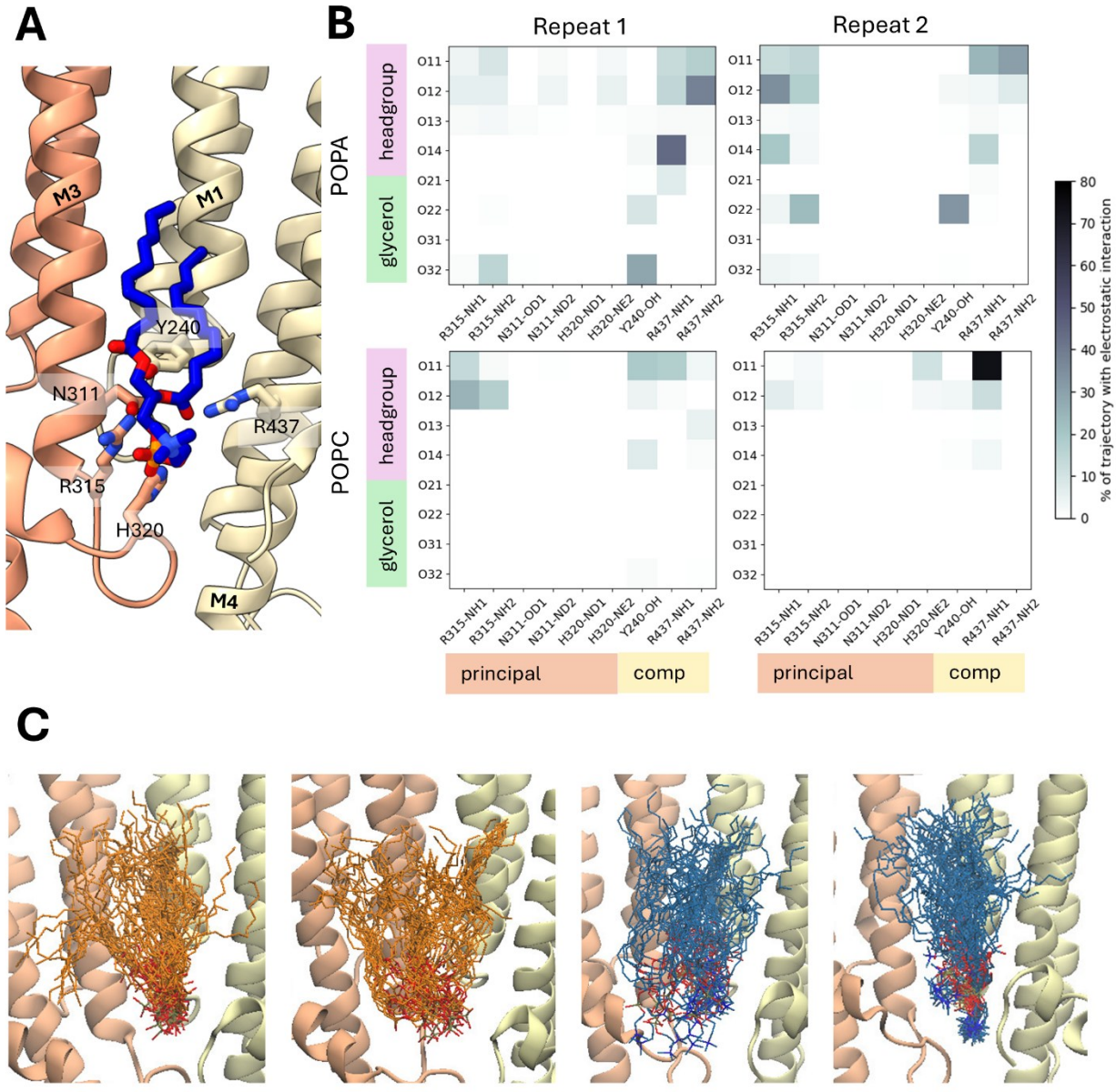
A
M3
M1
Y240
N311
R437
R315
H320
M4
B
Repeat 1
Repeat 2
POPA
POPC
headgroup
glycerol
O11
O12
O13
O14
O21
O22
O31
O32
R315-NH1
R315-NH2
N311-OD1
N311-ND2
H320-ND1
H320-NE2
Y240-OH
R437-NH1
R437-NH2
principal
comp
% of trajectory with electrostatic interaction
0
10
20
30
40
50
60
70
80
C

The β-α_γ and γ-α_δ sites were deemed low affinity PA in CG simulations, with very little sampling for PA binding at the γ-α_δ site in CG simulations of the nAChR apo state. At the β-α_γ site, both PC and PA exhibit greater variability in their binding poses (Figure 4.4 C). In both cases, the complimentary α subunit contains a neutral histidine on the M4 helix rather than a lysine or arginine (Figure 4.4 A). In general, both PA and PC adopt a more superficial binding pose at the β-α_γ site compared to the sites deemed high affinity, consistent with the lipid binding pose modelled in cryo-EM structures (Zarkadas et al., 2022). The one exception to this is the first simulation repeat starting from a selected frame in which PA was bound uncharacteristically deeply in the β-α binding pocket, effectively "trapped" by the MX helices of the two subunits (Supplementary Figure 4.7), and as a result is strongly coordinated similar to PA at high-affinity sites (Figure 4.4 B). No such poses were detected in CG or atomistic simulations with PC at this site, presumably due to the relatively larger size of the PC headgroup. The lower apparent affinity for PA at this site could therefore be due to the relative inaccessibility of this binding pocket for lipids.

Figure 4.4. Lipid binding poses at the β-α_γ site in brute-force simulations. A. Bound lipid in a cryo-EM structure of the nAChR, modelled as PC (PDB: 7QL5). Protein subunits are shown as cartoon with the β subunit in yellow and the α_γ subunit in cyan. Bound lipid and coordinating residues are shown as sticks and coloured by heteroatom. Protein helices are labelled. **B.** Interaction network between polar atoms of bound lipid and coordinating residues in the binding pocket. Lipid polar atoms corresponding to headgroup and glycerol groups are shown on the y-axis and polar atoms of binding site residues of the principal (β) and complimentary (α_γ) subunits are shown on the x-axis. Boxes corresponding to each interaction pair are coloured by % of trajectory (250 ns) in which an electrostatic interaction is present, defined by a distance of less than 3 Å between the two atoms. **C.** Evolution of lipid binding poses throughout the trajectory, with lipid binding pose snapshot is shown every ~5 ns. Left to right: PA bound in repeat 1, PA bound in repeat 2, PC bound in repeat 1, PC bound in repeat 2.

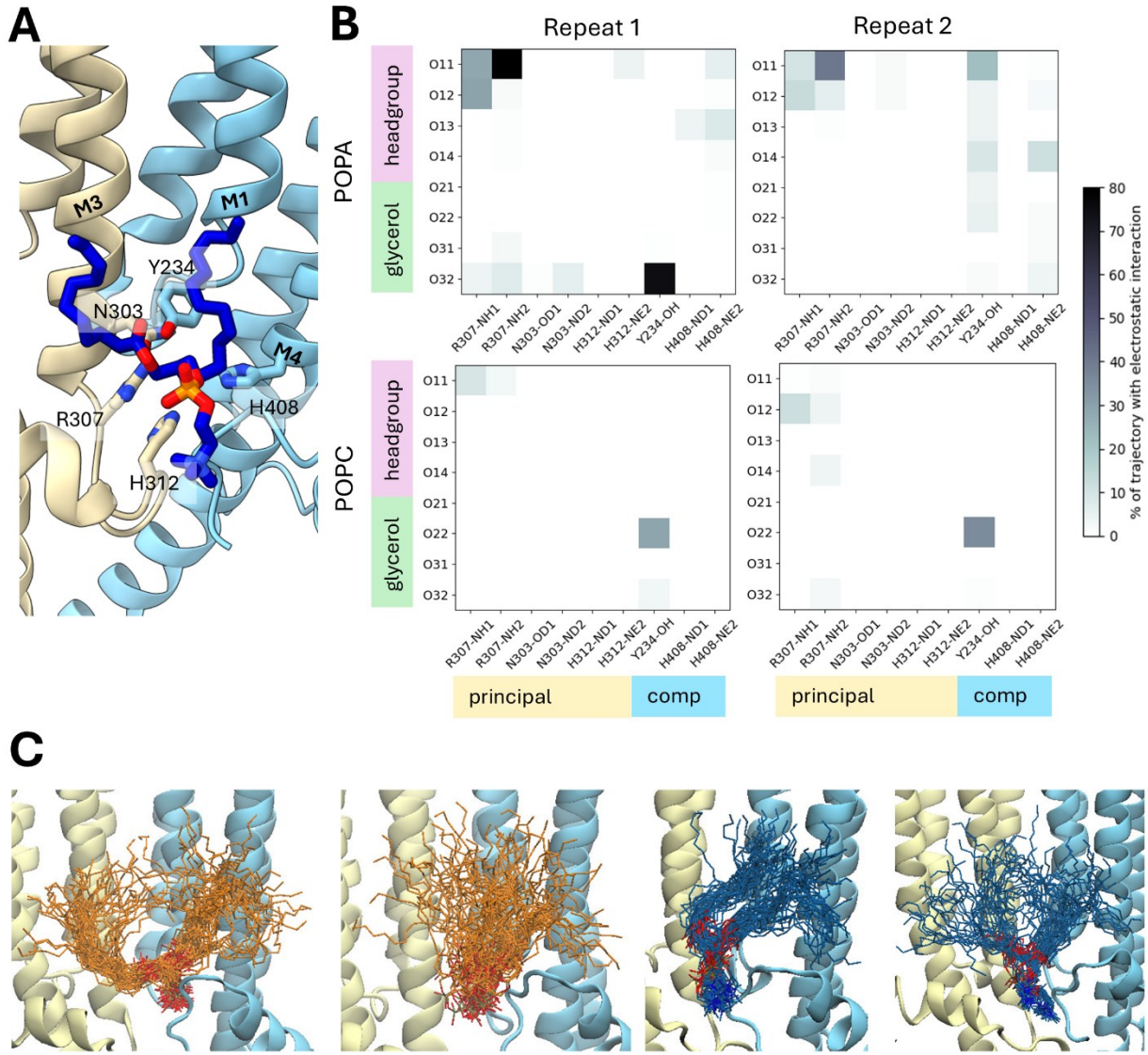
A
M3
M1
Y234
N303
M4
R307
H408
H312
B
Repeat 1
Repeat 2
POPA
POPC
headgroup
glycerol
O11
O12
O13
O14
O21
O22
O31
O32
R307-NH1
R307-NH2
N303-OD1
N303-ND2
H312-ND1
H312-NE2
Y234-OH
H408-ND1
H408-NE2
principal
comp
% of trajectory with electrostatic interaction
80
70
60
50
40
30
20
10
0
C

PA binds with higher affinity to the α_γ-γ site than PC

The difference in binding free energy (ΔΔG) between PA and PC at the α_γ-γ site was evaluated using FEP. The starting frame, where a PA lipid was bound in a representative pose as described above, was picked from a 250 ns equilibrium simulation. Transformations of the nAChR-bound lipid and a lipid in the same composition bulk membrane were performed in separate systems. The transformation of a water molecule to a chloride ion was also performed in both a bulk membrane and an nAChR-containing system to evaluate the free energy contribution of a change in system charge. These transformations are reflected in the thermodynamic scheme used to calculate ΔΔG (Figure 4.5). The ΔG values for each of these transformations are shown in Table 4.1.

Figure 4.5. Thermodynamic scheme of complete PA to PC alchemical transformation. The zero-sum nature of thermodynamic cycles is used for relative FEP calculation.

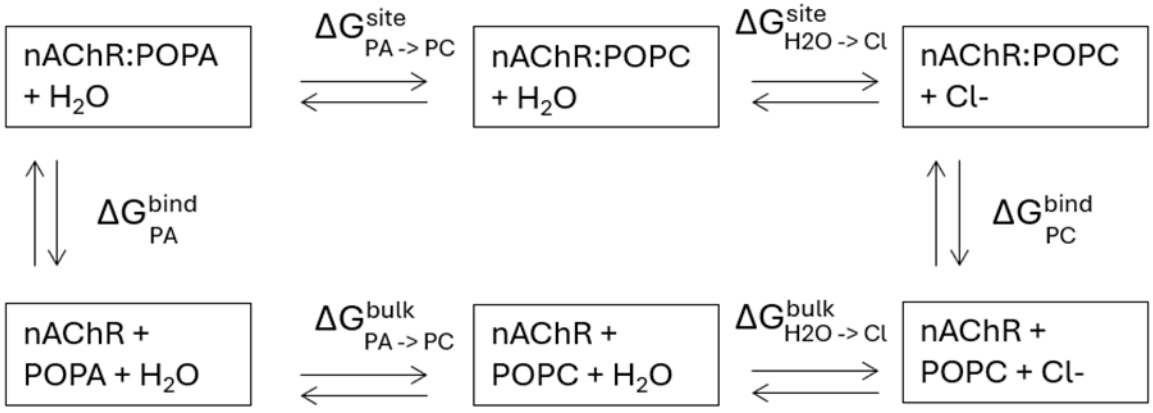
nAChR:POPA + H2O
ΔG site PA -> PC
nAChR:POPC + H2O
ΔG site H2O -> Cl
nAChR:POPC + Cl-
ΔG bind PA
ΔG bind PC
nAChR + POPA + H2O
ΔG bulk PA -> PC
nAChR + POPC + H2O
ΔG bulk H2O -> Cl
nAChR + POPC + Cl-

The equation for the binding free energy is as follows:

$$\Delta\Delta G = \Delta G_{PC}^{bind} - \Delta G_{PA}^{bind} = \left(\Delta G_{PA\rightarrow PC}^{site} + \Delta G_{H2O\rightarrow Cl}^{site}\right) + \left(\Delta G_{PC\rightarrow PA}^{bulk} + \Delta G_{Cl\rightarrow H2O}^{bulk}\right)$$

Table 4.1. Differences in free energy obtained through FEP

Transformation	ΔG
PA to PC in site	84.2 ± 0.17 kcal/mol
PC to PA in bulk	-79.7 ± 0.56 kcal/mol
Water to Cl- in protein+membrane system	-83.5 ± 0.11 kcal/mol
Water to Cl- in membrane only system	-80.5 ± 0.88 kcal/mol

FEP therefore predicts a 1.5 ± 0.55 kcal/mol difference in binding free energy between PC and PA, indicating preference for PA at this site. This relatively small difference in binding free energy is consistent with CG and brute-force simulation studies, which suggest that both PA and PC are able to bind to this site, but with PA having a relatively more stable headgroup binding pose (Figure 4.2). This finding supports the existence of common phospholipid binding sites which have different affinities for functionally relevant lipids.

4.6 Discussion

This work presents the dynamic nature of lipid interactions with conserved phospholipid binding sites on the nAChR. Rather than a set of specific coordinating interactions which determine the nature of phospholipid binding to nAChR binding sites, both PA and PC participate in variable electrostatic interactions with several coordinating residues in the lipid binding pocket. While initial CG simulations suggested large differences in apparent affinity for PA and PC at three inner leaflet sites, with PA having 10x longer interaction durations in some cases (Ananchenko et al., 2024), the atomistic simulation presented here suggest very similar binding patterns between the two phospholipids with a more subtle difference in affinity.

We quantified the relative affinity of PA and PC to the α_γ-γ binding site which showed an estimated 1.5 kcal/mol higher binding free energy for PC than PA, suggesting that this site does have higher affinity for PA than PC as predicted in unbiased CG simulations. The backwards and forwards FEP calculations converged readily after 300 ns total of sampling. We attempted to calculate the difference in binding free energy at the β-α_γ and δ-β using the same method, expecting a similar ΔΔG value at the δ-β site and a ΔΔG of around 0 at the β-α_γ site. The backwards and forwards transformations at these sites, however, did not converge after 300 ns, instead having a hysteresis of approximately 5 kcal/mol. To try and improve the convergence, we tested different distance values to be used in harmonic wall restraints, different starting point frames, and restraints which excluded bulk lipids from entering the binding sites. We also attempted to repeat the calculations with 700 ns of sampling as well as with using the DBC restraint scheme described in other works (Petroff et al., 2022; Santiago-McRae et al., 2023) (Figures 4.8, 4.9), which did not improve the convergence.

It is possible that the relatively well-defined binding poses at the α_γ-γ site as well as the consistent interaction network with coordinating residues aided in the convergence of FEP calculations. At the β-α_γ and δ-β sites, the poor definition of a consistent binding pose creates a challenge in using a minimal restraint scheme, likely requiring a significantly greater amount of sampling or the use of replicas to get a reliable $\Delta\Delta G$ measurement.

We were also unable to calculate a $\Delta\Delta G$ between PA and PC binding at the γ-α_δ site, which was deemed state-dependent (Ananchenko et al., 2024). This site is completely inaccessible to PA in CG simulations, making it impossible to select PA-bound simulation frames for subsequent simulation and analysis. The rapid transition of the nAChR from an open to collapsed-pore state in unrestrained simulations (Zarkadas et al., 2022) changes the shape of the lipid binding pocket, making this calculation also inaccessible using the nicotine-bound nAChR state.

This work demonstrates that a clear definition of lipid binding poses to cryo-EM models of stable functional ion channel states is required for the accurate estimation of relative lipid binding affinities. This presents a challenge due to the continuous movement of lipids in the binding pocket even in cases when a lipid is stably bound to the protein, highlighting the limitations of using FEP to estimate lipid-protein binding affinities. This may suggest the need for unique FEP calculation strategies on a case-by-case basis. The FEP calculation presented in this work supports the existence of binding sites on the nAChR which exhibit preference for specific lipid species. The selectivity of direct lipid binding sites for function-promoting lipid species could be part of the modulatory mechanism of pLGICs by lipids.

4.7 References

Ananchenko, A., Gao, R. Y., Dehez, F., & Baenziger, J. E. (2024). State-dependent binding of cholesterol and an anionic lipid to the muscle-type Torpedo nicotinic acetylcholine receptor. Communications Biology, 7(1), 437. https://doi.org/10.1038/S42003-024-06106-8

Andersen, H. C. (1983). Rattle: A "velocity" version of the shake algorithm for molecular dynamics calculations. Journal of Computational Physics, 52(1), 24–34. https://doi.org/10.1016/0021-9991(83)90014-1

Baenziger, J. E., Morris, M. L., Darsaut, T. E., & Ryan, S. E. (2000). Effect of membrane lipid composition on the conformational equilibria of the nicotinic acetylcholine receptor. Journal of Biological Chemistry, 275(2), 777–784. https://doi.org/10.1074/jbc.275.2.777

Corey, R. A., Vickery, O. N., Sansom, M. S. P., & Stansfeld, P. J. (2019). Insights into Membrane Protein-Lipid Interactions from Free Energy Calculations. Journal of Chemical Theory and Computation, 15(10), 5727–5736. https://doi.org/10.1021/acs.jctc.9b00548

Corringer, P. J., Poitevin, F., Prevost, M. S., Sauguet, L., Delarue, M., & Changeux, J. P. (2012). Structure and pharmacology of pentameric receptor channels: From bacteria to brain. Structure, 20(6), 941–956. https://doi.org/10.1016/J.STR.2012.05.003/ASSET/9F762FC8-D3A7-4A23-BB9B-2DA1EBCBE0E9/MAIN.ASSETS/GR5.JPG

daCosta, C. J. B., & Baenziger, J. E. (2009). A Lipid-dependent Uncoupled Conformation of the Acetylcholine Receptor. The Journal of Biological Chemistry, 284(26), 17819. https://doi.org/10.1074/JBC.M900030200

daCosta, C. J. B., Dey, L., Therien, J. P. D., & Baenziger, J. E. (2013). A distinct mechanism for activating uncoupled nicotinic acetylcholine receptors. Nature Chemical Biology 2013 9:11, 9(11), 701–707. https://doi.org/10.1038/nchembio.1338

daCosta, C. J. B., Medaglia, S. A., Lavigne, N., Wang, S., Carswell, C. L., & Baenziger, J. E. (2009). Anionic Lipids Allosterically Modulate Multiple Nicotinic Acetylcholine Receptor Conformational Equilibria. The Journal of Biological Chemistry, 284(49), 33841. https://doi.org/10.1074/JBC.M109.048280

Dämgen, M. A., & Biggin, P. C. (2021). State-dependent protein-lipid interactions of a pentameric ligand-gated ion channel in a neuronal membrane. PLoS Computational Biology, 17(2). https://doi.org/10.1371/JOURNAL.PCBI.1007856

Duncan, A. L., Corey, R. A., & Sansom, M. S. P. (2020). Defining how multiple lipid species interact with inward rectifier potassium (Kir2) channels. Proceedings of the National Academy of Sciences of the United States of America, 117(14), 7803–7813. https://doi.org/10.1073/pnas.1918387117

Feller, S. E., Zhang, Y., Pastor, R. W., & Brooks, B. R. (1995). Constant pressure molecular dynamics simulation: The Langevin piston method. The Journal of Chemical Physics, 103(11), 4613–4621. https://doi.org/10.1063/1.470648

Fiorin, G., Klein, M. L., & Hénin, J. (2013). Using collective variables to drive molecular dynamics simulations. Molecular Physics, 111(22–23), 3345–3362. https://doi.org/10.1080/00268976.2013.813594

Fong, T. M., & McNamee, M. G. (1986). Correlation between Acetylcholine Receptor Function and Structural Properties of Membranes. Biochemistry, 25(4), 830–840. https://doi.org/10.1021/bi00352a015

Fu, H., Chen, H., Blazhynska, M., Goulard Coderc de Lacam, E., Szczepaniak, F., Pavlova, A., Shao, X., Gumbart, J. C., Dehez, F., Roux, B., Cai, W., & Chipot, C. (2022). Accurate determination of protein:ligand standard binding free energies from molecular dynamics simulations. Nature Protocols 2022 17:4, 17(4), 1114–1141. https://doi.org/10.1038/s41596-021-00676-1

Gharpure, A., Teng, J., Zhuang, Y., Noviello, C. M., Walsh, R. M., Cabuco, R., Howard, R. J., Zaveri, N. T., Lindahl, E., & Hibbs, R. E. (2019). Agonist Selectivity and Ion Permeation in the α3β4 Ganglionic Nicotinic Receptor. Neuron, 104(3), 501-511.e6. https://doi.org/10.1016/J.NEURON.2019.07.030

Hopkins, C. W., Le Grand, S., Walker, R. C., & Roitberg, A. E. (2015). Long-time-step molecular dynamics through hydrogen mass repartitioning. Journal of Chemical Theory and Computation, 11(4), 1864–1874. https://doi.org/10.1021/CT5010406/ASSET/IMAGES/LARGE/CT-2014-010406_0017.JPEG

Huang, J., & Mackerell, A. D. (2013). CHARMM36 all-atom additive protein force field: Validation based on comparison to NMR data. Journal of Computational Chemistry, 34(25), 2135–2145. https://doi.org/10.1002/JCC.23354

Jorgensen, W. L., & Jenson, C. (1998). Temperature Dependence of TIP3P, SPC, and TIP4P Water from NPT Monte Carlo Simulations: Seeking Temperatures of Maximum Density. J Comput Chem, 19, 11791186. https://doi.org/10.1002/(SICI)1096-987X(19980730)19:10

Lee, J., Cheng, X., Swails, J. M., Yeom, M. S., Eastman, P. K., Lemkul, J. A., Wei, S., Buckner, J., Jeong, J. C., Qi, Y., Jo, S., Pande, V. S., Case, D. A., Brooks, C. L., MacKerell, A. D., Klauda, J. B., & Im, W. (2016). CHARMM-GUI Input Generator for NAMD, GROMACS, AMBER, OpenMM, and CHARMM/OpenMM Simulations Using the CHARMM36 Additive Force Field. Journal of Chemical Theory and Computation, 12(1), 405–413. https://doi.org/10.1021/ACS.JCTC.5B00935/ASSET/IMAGES/LARGE/CT-2015-00935E_0005.JPEG

Miyamoto, S., & Kollman, P. A. (1992). Settle: An analytical version of the SHAKE and RATTLE algorithm for rigid water models. Journal of Computational Chemistry, 13(8), 952–962. https://doi.org/10.1002/jcc.540130805

Petroff, J. T., Dietzen, N. M., Santiago-McRae, E., Deng, B., Washington, M. S., Chen, L. J., Trent Moreland, K., Deng, Z., Rau, M., Fitzpatrick, J. A. J., Yuan, P., Joseph, T. T., Hénin, J., Brannigan, G., & Cheng, W. W. L. (2022). Open-channel structure of a pentameric ligand-gated ion channel reveals a mechanism of leaflet-specific phospholipid modulation. Nature Communications 2022 13:1, 13(1), 1–16. https://doi.org/10.1038/s41467-022-34813-5

Phillips, J. C., Hardy, D. J., Maia, J. D. C., Stone, J. E., Ribeiro, J. V., Bernardi, R. C., Buch, R., Fiorin, G., Hénin, J., Jiang, W., McGreevy, R., Melo, M. C. R., Radak, B. K., Skeel, R. D., Singharoy, A., Wang, Y., Roux, B., Aksimentiev, A., Luthey-Schulten, Z., … Tajkhorshid, E. (2020). Scalable molecular dynamics on CPU and GPU architectures with NAMD. The Journal of Chemical Physics, 153(4), 44130. https://doi.org/10.1063/5.0014475

Rahman, M. M., Basta, T., Teng, J., Lee, M., Worrell, B. T., Stowell, M. H. B., & Hibbs, R. E. (2022). Structural mechanism of muscle nicotinic receptor desensitization and block by curare. Nature Structural and Molecular Biology, 29(4), 386–394. https://doi.org/10.1038/s41594-022-00737-3

Rahman, M. M., Teng, J., Worrell, B. T., Noviello, C. M., Lee, M., Karlin, A., Stowell, M. H. B., & Hibbs, R. E. (2020). Structure of the Native Muscle-type Nicotinic Receptor and Inhibition by Snake Venom Toxins. Neuron, 106(6), 952-962.e5. https://doi.org/10.1016/J.NEURON.2020.03.012

Ryckaert, J. P., Ciccotti, G., & Berendsen, H. J. C. (1977). Numerical integration of the cartesian equations of motion of a system with constraints: molecular dynamics of n-alkanes. Journal of Computational Physics, 23(3), 327–341. https://doi.org/10.1016/0021-9991(77)90098-5

Santiago-McRae, E., Ebrahimi, M., Sandberg, J. W., Brannigan, G., & Hénin, J. (2023). Computing Absolute Binding Affinities by Streamlined Alchemical Free Energy Perturbation (SAFEP). BioRxiv, 2022.12.09.519809. https://doi.org/10.1101/2022.12.09.519809

Sharp, L., & Brannigan, G. (2021). Spontaneous lipid binding to the nicotinic acetylcholine receptor in a native membrane. The Journal of Chemical Physics, 154(18), 185102. https://doi.org/10.1063/5.0046333

Sharp, L., Salari, R., & Brannigan, G. (2019). Boundary lipids of the nicotinic acetylcholine receptor: spontaneous partitioning via coarse-grained molecular dynamics simulation. Biochimica et Biophysica Acta. Biomembranes, 1861(4), 887. https://doi.org/10.1016/J.BBAMEM.2019.01.005

Sunshine, C., & McNamee, M. G. (1992). Lipid modulation of nicotinic acetylcholine receptor function: the role of neutral and negatively charged lipids. Biochimica et Biophysica Acta (BBA) - Biomembranes, 1108(2), 240–246. https://doi.org/10.1016/0005-2736(92)90031-G

Tuckerman, M., Berne, B. J., & Martyna, G. J. (1992). Reversible multiple time scale molecular dynamics. The Journal of Chemical Physics, 97(3), 1990–2001. https://doi.org/10.1063/1.463137

Walsh, R. M., Roh, S.-H., Gharpure, A., Morales-Perez, C. L., Teng, J., & Hibbs, R. E. (2018). Structural principles of distinct assemblies of the human α4β2 nicotinic receptor. Nature 2018 557:7704, 557(7704), 261–265. https://doi.org/10.1038/s41586-018-0081-7

Zarkadas, E., Pebay-Peyroula, E., Thompson, M. J., Schoehn, G., Uchański, T., Steyaert, J., Chipot, C., Dehez, F., Baenziger, J. E., & Nury, H. (2022). Conformational transitions and ligand-binding to a muscle-type nicotinic acetylcholine receptor. Neuron, 110(8), 1358-1370.e5. https://doi.org/10.1016/j.neuron.2022.01.013

Zhuang, Y., Noviello, C. M., Hibbs, R. E., Howard, R. J., & Lindahl, E. (2022). Differential interactions of resting, activated, and desensitized states of the α7 nicotinic acetylcholine receptor with lipidic modulators. Proceedings of the National Academy of Sciences, 119(43), e2208081119. https://doi.org/10.1073/PNAS.2208081119

4.8 Supplementary Information

Supplementary Figure 4.6. Depth of lipid binding in the α_γ-γ binding pocket. The distance between the lipid headgroup phosphorous atom and the C-alpha atom of γQ245, located at the bottom of the M1-M2 linker defining the deepest point of the lipid binding pocket. Distance measurement was taken over 2 repeats of 250 ns trajectories for both bound POPC and POPA. Binned frame counts at each distance are shown for both lipids.

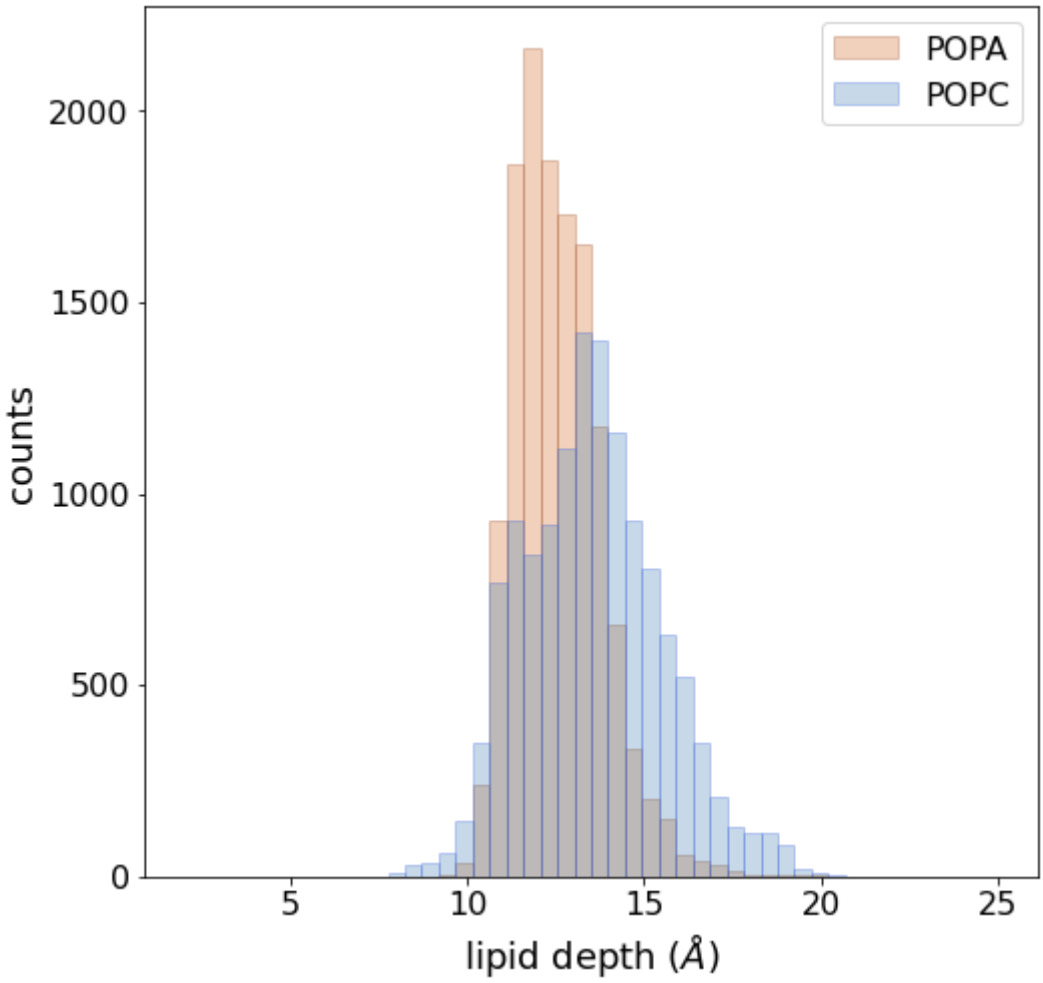
POPA
POPC
2000
1500
1000
500
0
counts
5
10
15
20
25
lipid depth (Å)

Supplementary Figure 4.7. Initial bound PA and PC positions at the β-α_γ site in brute force simulations. Deeply bound PA shown in orange, while typical cases for both PA and PC binding are shown in purple.

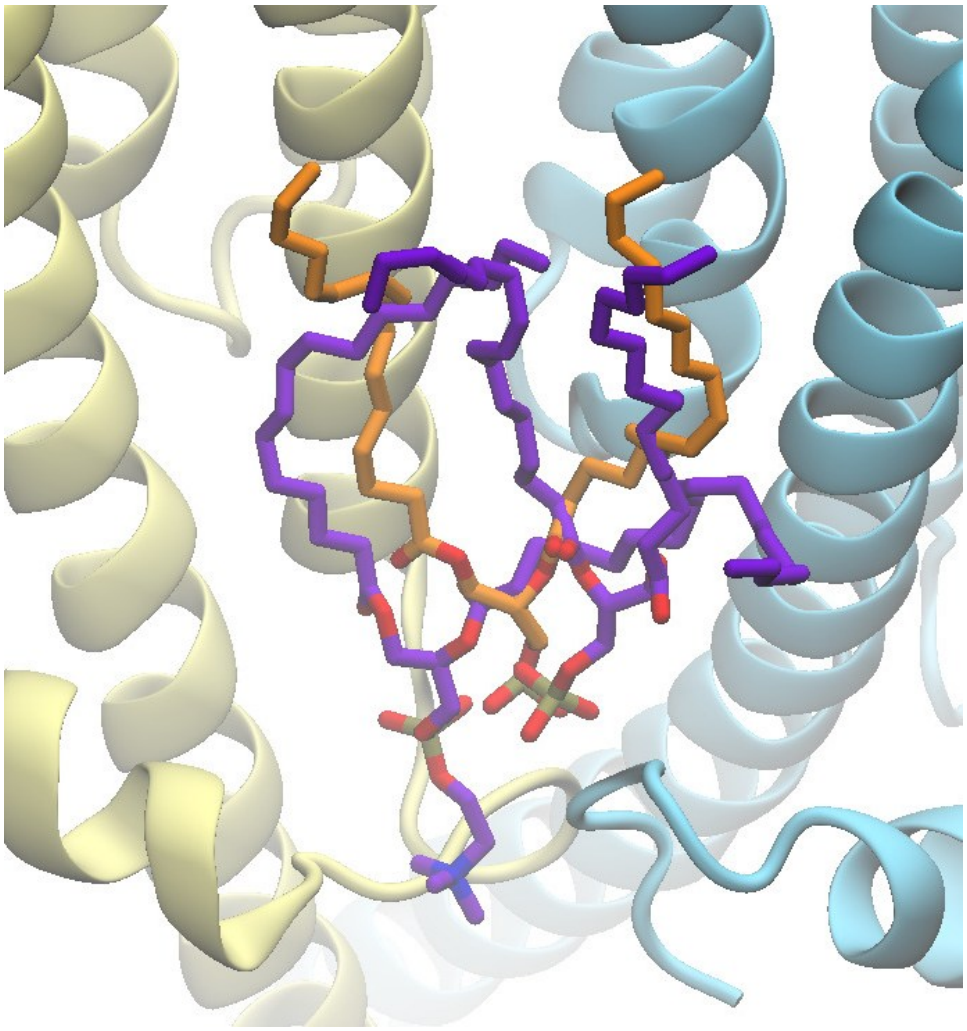

Supplementary Figure 4.8. ΔG along 300 ns alchemical FEP transformation of PA to PC at δ-β site. Forward transformation is shown in black, backward transformation is shown in red. Hysteresis between forwards and backwards transformations is about 5 kcal/mol.

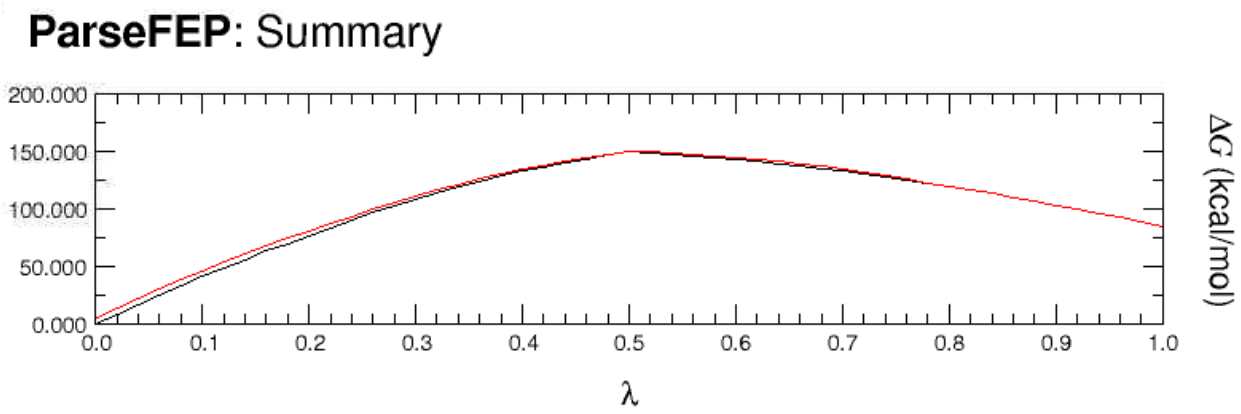
ParseFEP: Summary
200.000
150.000
100.000
50.000
0.000
0.0
0.1
0.2
0.3
0.4
0.5
0.6
0.7
0.8
0.9
1.0
λ
ΔG (kcal/mol)

Supplementary Figure 4.9. ΔG along 700 ns alchemical FEP transformation of PA to PC at δ-β site using DBC restrains. Forward transformation is shown in black, backward transformation is shown in red. Hysteresis between forwards and backwards transformations is about 8 kcal/mol.

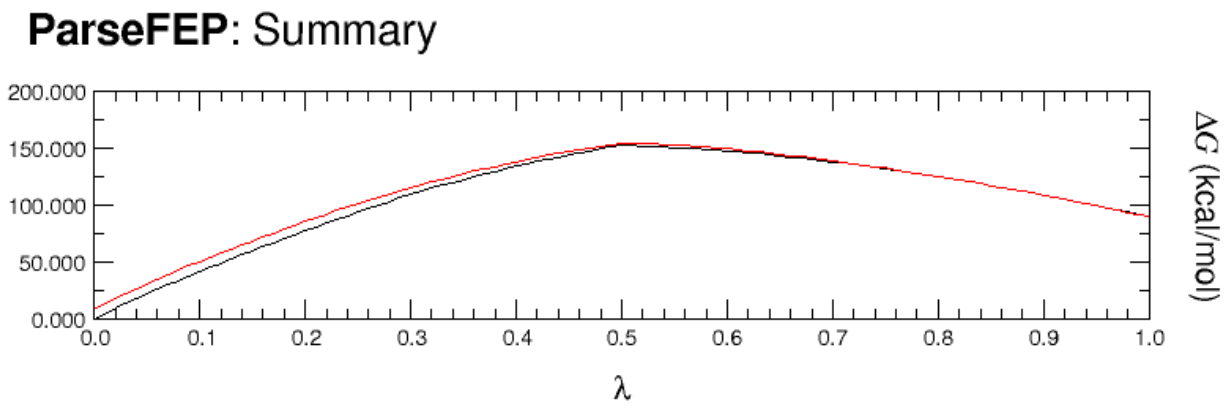
ParseFEP: Summary
200.000
150.000
100.000
50.000
0.000
0.0
0.1
0.2
0.3
0.4
0.5
0.6
0.7
0.8
0.9
1.0
λ
ΔG (kcal/mol)

Chapter 5: General Discussion and Conclusions

The overall goal of this thesis was to probe lipid binding sites on LGICs *in-silico* and to investigate the detailed intermolecular interactions that drive lipid binding. Lipids can modulate the response of ion channels to agonists, in the case of ASIC1 types and nAChRs, or can independently cause activation, such as in the case of hASIC3. The effect of ligands on protein function depends in part on their affinity for binding sites on the LGIC, which is determined by their interactions with residues at these sites. A higher relative affinity of an agonist to a specific functional state over another, for example higher affinity for an active state over an inactive state, stabilizes that functional state (Auerbach, 2016; Monod et al., 1965). One mechanism by which lipids may alter the function of LGICs is by preferentially binding to one functional state over another. This has been shown to be the case for PIP_2 activation of Kir2.2 channels, whereby PIP_2 molecules preferentially bind to open Kir2.2 channel states (Hansen et al., 2011). It is therefore of interest to characterize the behaviour of lipids at binding sites on LGICs and estimate the binding affinities of functionally relevant lipid species to different functional states.

MD simulations cannot directly measure ligand affinity. Rather, measurements such as relative occupancy and interaction durations of lipid species at predicted lipid binding sites can be used to approximate their relative affinities. Simulations additionally provide the ability to view potential time-resolved ligand-protein interactions at atomic detail under controlled conditions not yet accessible to experiments. Enhanced sampling approaches such as FEP are used to quantitatively estimate binding free energy.

The works in this thesis have generated new information on lipid-LGIC interaction in various membrane compositions. The simulations performed here have suggested the existence of lipid

binding sites which have varying affinities for lipid species. Function-promoting lipids, such as PUFAs in the case of ASICs, or anionic lipids and cholesterol in the case of nAChRs, have higher apparent affinity for these sites.

5.1 New insight into PUFA binding sites on ASICs

Simulations of ASICs in the presence of PUFAs suggest preferential interactions with outer leaflet sites. PUFAs with a greater number of tail carbons and a greater number of double bonds tend to interact more frequently with these sites, in agreement with their increased effectiveness in functional studies to modulate the function of ASICs. In addition, the binding pattern of AA differs between the hASIC1 and hASIC3 subtypes, which may explain the difference in how these subtypes are modulated by PUFAs. The residues R65 and R68 are on the same face of the TM1 helix in hASIC3, creating an area of more positive electrostatic charge in this region relative to hASIC1, possibly increasing the affinity of negatively charged PUFA headgroups to this general outer leaflet site. The reversal of the PUFA binding pattern in hASIC1 and hASIC3 through *in-silico* mutagenesis suggests that the identified interactions with $R65_{hASIC3}$, $R68_{hASIC3}$ and $Y71_{hASIC1}$ are key to PUFA-ASIC interactions.

5.2 New insight into lipid binding sites on nAChRs

The MD simulations performed in this work corroborate the lipid binding sites resolved in recent cryo-EM structures. The inner leaflet sites shown in recent structures (Rahman et al., 2022; Zarkadas et al., 2022) are suggested in simulations to be general phospholipid binding sites and appear to have preference for the PA over PC. The relative higher affinity of PA for the α_γ-γ site was quantified using FEP, further supporting the idea of conserved phospholipid sites having higher affinity for anionic lipids like PA, which stabilize a coupled receptor state, over zwitterionic lipids like PC, which stabilize an uncoupled state. Detailed insight from atomistic simulations

suggests that phospholipids bind in a dynamic manner without a defined binding pose, rather, they consistently participate in variable electrostatic interactions with key residues in the lipid binding pocket. The multiscale simulations also agree with the existence of high affinity Chol sites (Rahman et al., 2022). The simulation studies in this thesis, however, suggest that Chol binding sites are distinct from phospholipid binding sites. In addition to high affinity sites, Chol binds promiscuously to many regions of the TMD surface at patches of hydrophobic residues.

5.3 Overall conclusions and future studies of LGIC modulation by lipids

The work in this thesis suggests the idea that there exist direct lipid binding sites on LGICs which bind modulatory lipid species with higher affinity over other non-modulatory lipids. There is little similarity in the putative lipid binding sites between trimeric and pentameric LGICs, suggesting unique modulatory mechanisms for each LGIC family. It is therefore not possible to make broad conclusions about lipid-LGIC interactions, rather, lipid interactions and modulation of each type of LGIC must be evaluated individually. It is also yet to be determined how the binding of lipids to these direct sites translates into functional effects on LGICs.

The simulations in this thesis suggest that lipids associate with LGICs at defined binding sites through sets of persistent electrostatic interactions, resulting in binding that is sustained for entire simulation trajectories. At the same time, the specific atom pairings involved in these interactions are variable, and lipids typically do not adopt well-defined binding poses. This complicates the investigation of structural effects of lipid binding and attempts at calculating lipid binding affinities *in-silico*, such as with the use of FEP. These dynamic interactions, along with previous evidence that lipids may exert their effects on LGICs through both direct binding and bulk membrane effects, suggest a complex mechanism, or even multiple simultaneous mechanisms, by which lipids modulate LGIC function.

These studies were restricted to simple membrane compositions, focusing only on key interacting lipids; AA and DHA with ASICs, and PA and Chol with nAChRs. To build on these findings, I have been supervising an undergraduate student who has extended my initial studies to look at other anionic and neutral lipid interactions with the nAChR, such as PS, PI, PG and diacylglycerol. Given that there is important interplay between a variety of lipid types in neuronal membranes, and that other lipids are important to nAChR and ASIC function, it is important to extend MD simulations to more complex, perhaps even in-vivo mimetic (Marrink et al., 2019) membranes.

Following the publication of manuscript 1, another simulation study yielded unique insight into the interplay of PUFAs and PC at hASIC3 lateral fenestrations (Bandarupalli et al., 2024). In the absence of PUFAs, microsecond-long atomistic simulations show PC entering the channel pore through lateral fenestrations, dewetting the pore and blocking the flow of ions. The association of DHA to outer leaflet binding sites near the fenestrations in the region of R65/ R68 prevents POPC entry into the pore, thereby promoting pore hydration and ion flow in the open state. Curiously, density in the pore of the agonist-bound state of the nAChR was modelled as PC in cryo-EM structures (Zarkadas et al., 2022). In simulations, the PC molecules remain in the pore for the entire simulation trajectory. When removed, and in the absence of positional restraints on the pore-lining helices, the pore “collapses” to a dewetted state. It remains unclear whether the entry of PC lipids into LGIC pores occurs physiologically or is an artifact of cryo-EM sample preparation and simulation system set-up. Nevertheless, these observations present an intriguing possibility that one way by which lipids may influence LGIC function is by entering the ion channel pore itself.

It is surprising that high affinity phospholipid sites are found in the inner leaflet, relatively far from the ECD-TMD coupling region that exists at the M2-M3 linker in the outer leaflet (Thompson et al., 2024). Regions of organized lipid density were seen in the outer leaflet region in my CG

simulations; however, these were not attributed to long-duration nAChR-lipid interactions. It is unclear how the inner leaflet region of the nAChR might participate in stabilizing coupled versus uncoupled channel states. The inner leaflet phospholipid binding sites are located near a conserved salt bridge between the M2 and M4 helices, present in all subunits and in all eukaryotic pLGIC structures solved to date, which plays a key role in coupling channel gating and ion permeation (Strikwerda & Sine, 2021). The contributions of this salt bridge in different subunits of the archetypal muscle nAChR are non-equivalent, as the disruption of this salt bridge in the α or β subunits by mutagenesis decreases current amplitude, while its disruption at the δ or ε (equivalent to γ in the *Torpedo* nAChR) subunits increases current amplitude in single-channel electrophysiology recordings (Alhalhooly & Sine, 2024). Phospholipids interact with residues adjacent to this salt bridge and not with the residues forming the salt bridge directly, and no changes to the salt bridge were observed in my simulations. In the context of subunit-dependent lipid interactions seen in simulations, however, it is interesting that this region plays an important role in nAChR function in a subunit-dependent fashion.

Probing the mechanism of LGIC modulation by lipids through MD simulations is primarily limited by the short timescales which are currently available to this technology. Observing large ion channel conformational changes, which typically occur over millisecond timescales, are out of reach for atomistic brute-force simulations. Experiments such as electrophysiology recordings, on the other hand, measure the complete conformational transitions of ion channels but do not provide the atomic details of structural changes in response to ligand binding. Bridging the timescale gap between these tools would enable a more comprehensive understanding of LGIC modulation by lipids by connecting the functional effects measured experimentally directly to atomistic

interactions. MD simulations can also play a particularly important role when coupled with structural and mutagenesis data to give additional, detailed insight into lipid binding sites.

The increasing availability of LGIC structures in various functional states provides functionally relevant starting points for MD simulations, improving the extent of conformational sampling available. Enhanced sampling approaches such as steered MD or well-tempered metadynamics can also be used to predict the structural movements involved in LGIC conformational changes by sampling relevant regions of conformational space but are nonetheless limited by computational cost of observing large and complex conformational changes. Combining artificial intelligence-driven protein structure prediction tools with MD simulations could fill the gaps in the repertoire of available functional states, allowing for atomistic insight across the conformational landscape of LGICs and the roles of interacting lipids in these transitions.

References

Addona, G. H., Sandermann, H., Kloczewiak, M. A., & Miller, K. W. (2003). Low chemical specificity of the nicotinic acetylcholine receptor sterol activation site. Biochimica et Biophysica Acta (BBA) - Biomembranes, 1609(2), 177–182. https://doi.org/10.1016/S0005-2736(02)00685-5

Akk, G., & Auerbach, A. (1999). Activation of muscle nicotinic acetylcholine receptor channels by nicotinic and muscarinic agonists. British Journal of Pharmacology, 128(7), 1467. https://doi.org/10.1038/SJ.BJP.0702941

Alder, B. J., & Wainwright, T. E. (1957). Phase Transition for a Hard Sphere System. The Journal of Chemical Physics, 27(5), 1208–1209. https://doi.org/10.1063/1.1743957

Alhalhooly, L., & Sine, S. M. (2024). Ion transport in muscle acetylcholine receptor maintained by conserved salt bridges between the pore and lipid membrane. Proceedings of the National Academy of Sciences of the United States of America, 121(16), e2320416121. https://doi.org/10.1073/PNAS.2320416121

Allen, N. J., & Attwell, D. (2002). Modulation of ASIC channels in rat cerebellar purkinje neurons by ischaemia-related signals. The Journal of Physiology, 543(2), 521–529. https://doi.org/10.1113/JPHYSIOL.2002.020297

Auerbach, A. (2016). Dose-Response Analysis When There Is a Correlation between Affinity and Efficacy. Molecular Pharmacology, 89(2), 297–302. https://doi.org/10.1124/MOL.115.102509

Baconguis, I., Bohlen, C. J., Goehring, A., Julius, D., & Gouaux, E. (2014). X-ray structure of acid-sensing ion channel 1-snake toxin complex reveals open state of a Na+-selective channel. Cell, 156(4), 717–729. https://doi.org/10.1016/j.cell.2014.01.011

Baenziger, J. E., Morris, M. L., Darsaut, T. E., & Ryan, S. E. (2000). Effect of membrane lipid composition on the conformational equilibria of the nicotinic acetylcholine receptor. Journal of Biological Chemistry, 275(2), 777–784. https://doi.org/10.1074/jbc.275.2.777

Bandarupalli, R., Roth, R., Klipp, R. C., Bankston, J. R., & Li, J. (2024). Molecular Insights into Single-Chain Lipid Modulation of Acid-Sensing Ion Channel 3. The Journal of Physical Chemistry B, 128(51), 12685–12697. https://doi.org/10.1021/ACS.JPCB.4C04289

Bocquet, N., Nury, H., Baaden, M., Le Poupon, C., Changeux, J. P., Delarue, M., & Corringer, P. J. (2008). X-ray structure of a pentameric ligand-gated ion channel in an apparently open conformation. Nature 2008 457:7225, 457(7225), 111–114. https://doi.org/10.1038/nature07462

Bohlen, C. J., Chesler, A. T., Sharif-Naeini, R., Medzihradszky, K. F., Zhou, S., King, D., Sánchez, E. E., Burlingame, A. L., Basbaum, A. I., & Julius, D. (2011). A heteromeric Texas coral snake toxin targets acid-sensing ion channels to produce pain. Nature 2011 479:7373, 479(7373), 410–414. https://doi.org/10.1038/nature10607

Bozek, K., Wei, Y., Yan, Z., Liu, X., Xiong, J., Sugimoto, M., Tomita, M., Pääbo, S., Sherwood, C. C., Hof, P. R., Ely, J. J., Li, Y., Steinhauser, D., Willmitzer, L., Giavalisco, P., & Khaitovich, P. (2015). Organization and Evolution of Brain Lipidome Revealed by Large-Scale Analysis of Human, Chimpanzee, Macaque, and Mouse Tissues. Neuron, 85(4), 695–702. https://doi.org/10.1016/J.NEURON.2015.01.003

Carignano, C., Barila, E. P., & Spitzmaul, G. (2016). Analysis of neuronal nicotinic acetylcholine receptor α4β2 activation at the single-channel level. Biochimica et Biophysica Acta (BBA) - Biomembranes, 1858(9), 1964–1973. https://doi.org/10.1016/J.BBAMEM.2016.05.019

Chiang, P. H., Chien, T. C., Chen, C. C., Yanagawa, Y., & Lien, C. C. (2015). ASIC-dependent LTP at multiple glutamatergic synapses in amygdala network is required for fear memory. Scientific Reports 2015 5:1, 5(1), 1–14. https://doi.org/10.1038/srep10143

Cotman, C., Blank, M. L., Moehl, A., & Snyder, F. (1969). Lipid Composition of Synaptic Plasma Membranes Isolated from Rat Brain by Zonal Centrifugation. Biochemistry, 8(11), 4606–4612. https://doi.org/10.1021/BI00839A056/ASSET/BI00839A056.FP.PNG_V03

Criado, M., Eibl, H., & Barrantes, F. J. (1982). Effects of lipids on acetylcholine receptor. Essential need of cholesterol for maintenance of agonist-induced state transitions in lipid vesicles. Biochemistry, 21(15), 3622–3629. https://doi.org/10.1021/bi00258a015

daCosta, C. J. B., & Baenziger, J. E. (2009). A Lipid-dependent Uncoupled Conformation of the Acetylcholine Receptor. The Journal of Biological Chemistry, 284(26), 17819. https://doi.org/10.1074/JBC.M900030200

daCosta, C. J. B., Dey, L., Therien, J. P. D., & Baenziger, J. E. (2013). A distinct mechanism for activating uncoupled nicotinic acetylcholine receptors. Nature Chemical Biology, 9(11), 701–707. https://doi.org/10.1038/nchembio.1338

daCosta, C. J. B., Medaglia, S. A., Lavigne, N., Wang, S., Carswell, C. L., & Baenzinger, J. E. (2009). Anionic Lipids Allosterically Modulate Multiple Nicotinic Acetylcholine Receptor Conformational Equilibria. Journal of Biological Chemistry, 284(49), 33841–33849. https://doi.org/10.1074/JBC.M109.048280

daCosta, C. J. B., Wagg, I. D., McKay, M. E., & Baenziger, J. E. (2004). Phosphatidic acid and phosphatidylserine have distinct structural and functional interactions with the nicotinic acetylcholine receptor. Journal of Biological Chemistry, 279(15), 14967–14974. https://doi.org/10.1074/jbc.M310037200

Dämgen, M. A., & Biggin, P. C. (2021). State-dependent protein-lipid interactions of a pentameric ligand-gated ion channel in a neuronal membrane. PLoS Computational Biology, 17(2). https://doi.org/10.1371/JOURNAL.PCBI.1007856

Di Miceli, M., Bosch-Bouju, C., & Layé, S. (2020). PUFA and their derivatives in neurotransmission and synapses: a new hallmark of synaptopathies. Proceedings of the Nutrition Society, 79(4), 388–403. https://doi.org/10.1017/S0029665120000129

Fitzner, D., Bader, J. M., Penkert, H., Bergner, C. G., Su, M., Weil, M. T., Surma, M. A., Mann, M., Klose, C., & Simons, M. (2020). Cell-Type- and Brain-Region-Resolved Mouse Brain Lipidome. Cell Reports, 32(11), 108132. https://doi.org/10.1016/J.CELREP.2020.108132

Flayhan, A., Mertens, H. D. T., Ural-Blimke, Y., Martinez Molledo, M., Svergun, D. I., & Löw, C. (2018). Saposin Lipid Nanoparticles: A Highly Versatile and Modular Tool for Membrane Protein Research. Structure(London, England:1993), 26(2), 345. https://doi.org/10.1016/J.STR.2018.01.007

Fong, T. M., & McNamee, M. G. (1986). Correlation between Acetylcholine Receptor Function and Structural Properties of Membranes. Biochemistry, 25(4), 830–840. https://doi.org/10.1021/bi00352a015

Fu, H., Chen, H., Blazhynska, M., Goulard Coderc de Lacam, E., Szczepaniak, F., Pavlova, A., Shao, X., Gumbart, J. C., Dehez, F., Roux, B., Cai, W., & Chipot, C. (2022). Accurate determination of protein:ligand standard binding free energies from molecular dynamics simulations. Nature Protocols 2022 17:4, 17(4), 1114–1141. https://doi.org/10.1038/s41596-021-00676-1

Gharpure, A., Teng, J., Zhuang, Y., Noviello, C. M., Walsh, R. M., Cabuco, R., Howard, R. J., Zaveri, N. T., Lindahl, E., & Hibbs, R. E. (2019). Agonist Selectivity and Ion Permeation in the α3β4 Ganglionic Nicotinic Receptor. Neuron, 104(3), 501-511.e6. https://doi.org/10.1016/J.NEURON.2019.07.030

Gonzales, E. B., Kawate, T., & Gouaux, E. (2009). Pore architecture and ion sites in acid-sensing ion channels and P2X receptors. Nature, 460(7255), 599–604. https://doi.org/10.1038/nature08218

Gründer, S. (2018). Acid-Sensing Ion Channels. The Oxford Handbook of Neuronal Ion Channels, 646–695. https://doi.org/10.1093/OXFORDHB/9780190669164.013.12

Guros, N. B., Balijepalli, A., & Klauda, J. B. (2020). Microsecond-timescale simulations suggest 5-HT–mediated preactivation of the 5-HT3A serotonin receptor. Proceedings of the National Academy of Sciences, 117(1), 405–414. https://doi.org/10.1073/PNAS.1908848117

Hamouda, A. K., Sanghvi, M., Sauls, D., Machu, T. K., & Blanton, M. P. (2006). Assessing the lipid requirements of the Torpedo californica nicotinic acetylcholine receptor. Biochemistry, 45(13), 4327–4337. https://doi.org/10.1021/bi052281z

Handlin, L. J., & Dai, G. (2023). Direct regulation of the voltage sensor of HCN channels by membrane lipid compartmentalization. Nature Communications 2023 14:1, 14(1), 1–16. https://doi.org/10.1038/s41467-023-42363-7

Hansen, S. B., Tao, X., & MacKinnon, R. (2011). Structural basis of PIP2 activation of the classical inward rectifier K+ channel Kir2.2. Nature 2011 477:7365, 477(7365), 495–498. https://doi.org/10.1038/nature10370

Hénault, C. M., Govaerts, C., Spurny, R., Brams, M., Estrada-Mondragon, A., Lynch, J., Bertrand, D., Pardon, E., Evans, G. L., Woods, K., Elberson, B. W., Cuello, L. G., Brannigan, G., Nury, H., Steyaert, J., Baenziger, J. E., & Ulens, C. (2019). A lipid site shapes the agonist response of a pentameric ligand-gated ion channel. Nature Chemical Biology, 15(12), 1156–1164. https://doi.org/10.1038/s41589-019-0369-4

Hesselmans, L. F. G. M., Jennekens, F. G. I., Van Den Oord, C. J. M., Veldman, H., & Vincent, A. (1993). Development of innervation of skeletal muscle fibers in man: relation to acetylcholine receptors. The Anatomical Record, 236(3), 553–562. https://doi.org/10.1002/AR.1092360315

Hilf, R. J. C., & Dutzler, R. (2008). X-ray structure of a prokaryotic pentameric ligand-gated ion channel. Nature 2008 452:7185, 452(7185), 375–379. https://doi.org/10.1038/nature06717

Honerkamp-Smith, A. R., Veatch, S. L., & Keller, S. L. (2008). An Introduction to Critical Points for Biophysicists; Observations of Compositional Heterogeneity in Lipid Membranes. Biochimica et Biophysica Acta, 1788(1), 53. https://doi.org/10.1016/J.BBAMEM.2008.09.010

Ingólfsson, H. I., Carpenter, T. S., Bhatia, H., Bremer, P. T., Marrink, S. J., & Lightstone, F. C. (2017). Computational Lipidomics of the Neuronal Plasma Membrane. Biophysical Journal, 113(10), 2271–2280. https://doi.org/10.1016/j.bpj.2017.10.017

Ingólfsson, H. I., Melo, M. N., van Eerden, F. J., Arnarez, C., Lopez, C. A., Wassenaar, T. A., Periole, X., de Vries, A. H., Tieleman, D. P., & Marrink, S. J. (2014). Lipid Organization of the Plasma Membrane. Journal of the American Chemical Society, 136(41), 14554–14559. https://doi.org/10.1021/ja507832e

Klipp, R. C., & Bankston, J. R. (2022). Structural determinants of acid-sensing ion channel potentiation by single chain lipids. Journal of General Physiology, 154(7). https://doi.org/10.1085/JGP.202213156

Kumar, P., Cymes, G. D., & Grosman, C. (2021). Structure and function at the lipid-protein interface of a pentameric ligand-gated ion channel. Proceedings of the National Academy of Sciences of the United States of America, 118(23), e2100164118. https://doi.org/10.1073/PNAS.2100164118/SUPPL_FILE/PNAS.2100164118.SAPP.PDF

Ledesma, M. D., Martin, M. G., & Dotti, C. G. (2012). Lipid changes in the aged brain: Effect on synaptic function and neuronal survival. Progress in Lipid Research, 51(1), 23–35. https://doi.org/10.1016/J.PLIPRES.2011.11.004

Lingwood, D., Kaiser, H. J., Levental, I., & Simons, K. (2009). Lipid rafts as functional heterogeneity in cell membranes. Biochemical Society Transactions, 37(Pt 5), 955–960. https://doi.org/10.1042/BST0370955

Marra, S., Ferru-Clément, R., Breuil, V., Delaunay, A., Christin, M., Friend, V., Sebille, S., Cognard, C., Ferreira, T., Roux, C., Euller-Ziegler, L., Noel, J., Lingueglia, E., & Deval, E.

(2016). Non-acidic activation of pain-related Acid-Sensing Ion Channel 3 by lipids. The EMBO Journal, 35(4), 414–428. https://doi.org/10.15252/embj.201592335

Marrink, S. J., Corradi, V., Souza, P. C. T., Ingólfsson, H. I., Tieleman, D. P., & Sansom, M. S. P. (2019). Computational Modeling of Realistic Cell Membranes. In Chemical Reviews (Vol. 119, Issue 9). https://doi.org/10.1021/acs.chemrev.8b00460

Martin, M., Dotti, C. G., & Ledesma, M. D. (2010). Brain cholesterol in normal and pathological aging. Biochimica et Biophysica Acta (BBA) - Molecular and Cell Biology of Lipids, 1801(8), 934–944. https://doi.org/10.1016/J.BBALIP.2010.03.011

Monod, J., Wyman, J., & Changeux, J. P. (1965). ON THE NATURE OF ALLOSTERIC TRANSITIONS: A PLAUSIBLE MODEL. Journal of Molecular Biology, 12(1), 88–118. https://doi.org/10.1016/S0022-2836(65)80285-6

Rahman, M. M., Basta, T., Teng, J., Lee, M., Worrell, B. T., Stowell, M. H. B., & Hibbs, R. E. (2022). Structural mechanism of muscle nicotinic receptor desensitization and block by curare. Nature Structural and Molecular Biology, 29(4), 386–394. https://doi.org/10.1038/s41594-022-00737-3

Santos, R., Ursu, O., Gaulton, A., Bento, A. P., Donadi, R. S., Bologa, C. G., Karlsson, A., Al-Lazikani, B., Hersey, A., Oprea, T. I., & Overington, J. P. (2016). A comprehensive map of molecular drug targets. Nature Reviews. Drug Discovery, 16(1), 19. https://doi.org/10.1038/NRD.2016.230

Schütte, O. M., Mey, I., Enderlein, J., Savi, F., Geil, B., Janshoff, A., & Steinem, C. (2017). Size and mobility of lipid domains tuned by geometrical constraints. Proceedings of the National Academy of Sciences of the United States of America, 114(30), E6064–E6071. https://doi.org/10.1073/PNAS.1704199114/SUPPL_FILE/PNAS.1704199114.SM05.MOV

Sente, A., Desai, R., Naydenova, K., Malinauskas, T., Jounaidi, Y., Miehling, J., Zhou, X., Masiulis, S., Hardwick, S. W., Chirgadze, D. Y., Miller, K. W., & Aricescu, A. R. (2022). Differential assembly diversifies GABAA receptor structures and signalling. Nature 2022 604:7904, 604(7904), 190–194. https://doi.org/10.1038/s41586-022-04517-3

Sharp, L., & Brannigan, G. (2021). Spontaneous lipid binding to the nicotinic acetylcholine receptor in a native membrane. The Journal of Chemical Physics, 154(18), 185102. https://doi.org/10.1063/5.0046333

Sharp, L., Salari, R., & Brannigan, G. (2019). Boundary lipids of the nicotinic acetylcholine receptor: spontaneous partitioning via coarse-grained molecular dynamics simulation. Biochimica et Biophysica Acta. Biomembranes, 1861(4), 887. https://doi.org/10.1016/J.BBAMEM.2019.01.005

Simons, K., & Ikonen, E. (1997). Functional rafts in cell membranes. Nature 1997 387:6633, 387(6633), 569–572. https://doi.org/10.1038/42408

Smith, E. S., Cadiou, H., & McNaughton, P. A. (2007). Arachidonic acid potentiates acid-sensing ion channels in rat sensory neurons by a direct action. Neuroscience, 145(2), 686–698. https://doi.org/10.1016/j.neuroscience.2006.12.024

Stevens, J. A., Grünewald, F., van Tilburg, P. A. M., König, M., Gilbert, B. R., Brier, T. A., Thornburg, Z. R., Luthey-Schulten, Z., & Marrink, S. J. (2023). Molecular dynamics simulation of an entire cell. Frontiers in Chemistry, 11, 1106495. https://doi.org/10.3389/FCHEM.2023.1106495/BIBTEX

Stillwell, W. (2016). Membrane Lipids: Fatty Acids. An Introduction to Biological Membranes, 49–62. https://doi.org/10.1016/B978-0-444-63772-7.00004-X

Strikwerda, J. R., & Sine, S. M. (2021). Unmasking coupling between channel gating and ion permeation in the muscle nicotinic receptor. ELife, 10. https://doi.org/10.7554/ELIFE.66225

Sun, J., & MacKinnon, R. (2020). Structural Basis of Human KCNQ1 Modulation and Gating. Cell, 180(2), 340-347.e9. https://doi.org/10.1016/J.CELL.2019.12.003

Sunshine, C., & McNamee, M. G. (1992). Lipid modulation of nicotinic acetylcholine receptor function: the role of neutral and negatively charged lipids. Biochimica et Biophysica Acta (BBA) - Biomembranes, 1108(2), 240–246. https://doi.org/10.1016/0005-2736(92)90031-G

Tessier, C. J. G., Sturgeon, R. M., Emlaw, J. R., McCluskey, G. D., Pérez-Areales, F. J., & Dacosta, C. J. B. (2022). Ancestral acetylcholine receptor β-subunit forms homopentamers that prime before opening spontaneously. ELife, 11, e76504. https://doi.org/10.7554/ELIFE.76504

Thompson, M. J., & Baenziger, J. E. (2020). Ion channels as lipid sensors: from structures to mechanisms. Nature Chemical Biology 2020 16:12, 16(12), 1331–1342. https://doi.org/10.1038/s41589-020-00693-3

Thompson, M. J., Mansoub Bekarkhanechi, F., Ananchenko, A., Nury, H., & Baenziger, J. E. (2024). A release of local subunit conformational heterogeneity underlies gating in a muscle nicotinic acetylcholine receptor. Nature Communications 2024 15:1, 15(1), 1–15. https://doi.org/10.1038/s41467-024-46028-x

Unwin, N. (2005). Refined Structure of the Nicotinic Acetylcholine Receptor at 4 Å Resolution. Journal of Molecular Biology, 346(4), 967–989. https://doi.org/10.1016/J.JMB.2004.12.031

Walsh, R. M., Roh, S.-H., Gharpure, A., Morales-Perez, C. L., Teng, J., & Hibbs, R. E. (2018). Structural principles of distinct assemblies of the human α4β2 nicotinic receptor. Nature 2018 557:7704, 557(7704), 261–265. https://doi.org/10.1038/s41586-018-0081-7

Wang, Y. Z., Wang, J. J., Huang, Y., Liu, F., Zeng, W. Z., Li, Y., Xiong, Z. G., Zhu, M. X., & Xu, T. Le. (2015). Tissue acidosis induces neuronal necroptosis via ASIC1a channel

independent of its ionic conduction. ELife, 4(NOVEMBER2015). https://doi.org/10.7554/ELIFE.05682

Wickenden, A., Priest, B., & Erdemli, G. (2012). Ion channel drug discovery: challenges and future directions. Future Medicinal Chemistry, 4(5), 661–679. https://doi.org/10.4155/FMC.12.4

Yoder, N., & Gouaux, E. (2020). The his-gly motif of acid-sensing ion channels resides in a reentrant 'loop' implicated in gating and ion selectivity. ELife, 9, 1–18. https://doi.org/10.7554/ELIFE.56527

Yoder, N., Yoshioka, C., & Gouaux, E. (2018). Gating mechanisms of acid-sensing ion channels. Nature, 555(7696), 397–401. https://doi.org/10.1038/nature25782

Yu, J., Zhu, H., Lape, R., Greiner, T., Du, J., Lü, W., Sivilotti, L., & Gouaux, E. (2021). Mechanism of gating and partial agonist action in the glycine receptor. Cell, 184(4), 957. https://doi.org/10.1016/J.CELL.2021.01.026

Zarkadas, E., Pebay-Peyroula, E., Thompson, M. J., Schoehn, G., Uchański, T., Steyaert, J., Chipot, C., Dehez, F., Baenziger, J. E., & Nury, H. (2022). Conformational transitions and ligand-binding to a muscle-type nicotinic acetylcholine receptor. Neuron, 110(8), 1358-1370.e5. https://doi.org/10.1016/j.neuron.2022.01.013

Zhao, Y., Liu, S., Zhou, Y., Zhang, M., Chen, H., Eric Xu, H., Sun, D., Liu, L., & Tian, C. (2021). Structural basis of human α7 nicotinic acetylcholine receptor activation. Cell Research 2021 31:6, 31(6), 713–716. https://doi.org/10.1038/s41422-021-00509-6

Zhu, H., & Gouaux, E. (2021). Architecture and assembly mechanism of native glycine receptors. Nature 2021 599:7885, 599(7885), 513–517. https://doi.org/10.1038/s41586-021-04022-z

Zhuang, Y., Noviello, C. M., Hibbs, R. E., Howard, R. J., & Lindahl, E. (2022). Differential interactions of resting, activated, and desensitized states of the α7 nicotinic acetylcholine receptor with lipidic modulators. Proceedings of the National Academy of Sciences, 119(43), e2208081119. https://doi.org/10.1073/PNAS.2208081119

Curriculum Vitae

Education

Sept 2019- present **University of Ottawa** Ottawa, ON

- Doctorate in Philosophy- Biochemistry
- Transferred from: Master of Science – Chemistry (January 2021)
- Research: computational biochemistry, biophysics, molecular dynamics simulations, lipid interactions with ion channels
- Estimated graduation date: March 2025

Sept 2015- June 2019 **University of Ottawa** Ottawa, ON

- Bachelor of Science- Hon. Biomedical Science (option in Biostatistics)
- Research: Proteomics of bacterial proteins for vaccine development

Publications

Thompson, M.J, Tessier, C.J.G., **Ananchenko, A.,** Emlaw J.R., Dehex, F., Zarkadas, F., daCosta, C.J.B., Nury, H., Baenziger, J.E. (2024) Structure of an intermediate state priming acetylcholine receptor activation . *Under Review* doi: https://doi.org/10.1101/2024.12.02.626350

Ananchenko, A., Gao R., Dehez, F., Baenziger, J.E. (2024) State-dependent binding of cholesterol and an anionic lipid to the muscle-type *Torpedo* nicotinic acetylcholine receptor. *Comms. Biol.* 10;7:437. doi: 10.1038/s42003-024-06106-8

Thompson, M.J., Mansoub Bekarkhanechi, F., **Ananchenko, A.**, Nury, H., Baenziger, J.E. (2024) A release of local subunit conformational heterogeneity underlies gating in a muscle nicotinic acetylcholine receptor. *Nat. Commun.* **15**, 1803 doi: 10.1038/s41467-024-46028-x

Ananchenko A., Musgaard M., (2023) Subtype-dependent arachidonic acid binding sites in the ASIC transmembrane domain probed through MD simulations. *J. Gen. Physiol.* 155 (3): e202213259 doi: 10.1085/jgp.202213259

Ananchenko A., Hussein T.O.K., Mody D., Thomson M.J., Baenziger J.E. (2022) Recent insight into lipid binding and lipid modulation of pentameric ligand-gated ion channels. *Biomolecules* 12(6):814. doi: 10.3390/biom12060814

Baenziger J.E., **Ananchenko A**., Hussein T.O.K, Mody D. (2021) IUPAB 2021 Symposium 13: Ion channels and membrane transporters. *Biophys. Rev.* 13(6):871-873.doi: 10.1007/s12551-021-00874-x

Rook M.L.*, **Ananchenko A.***, Musgaard M., MacLean D.M. (2021) Molecular investigation of chicken ASIC1 β11-12 linker isomerization and channel kinetics, *Front. Cell. Neurosci.* *co-first authors 15:761813.doi: 10.3389/fncel.2021.761813

Fulton K.M., **Ananchenko A.**, Wolfraim L., Martin S., Twine S.M. (2019) Classical Immunoproteomics: Serological Proteome Analysis (SERPA) for Antigen Identification. *Immunoproteomics: Methods in Molecular Biology* 2024:59-78. doi: 10.1007/978-1-4939-9597-4_3

Research Experience

Sept 2019-present **University of Ottawa** Ottawa, ON

PhD Student, Research Assistant

- Used computational biochemistry approaches to research ion channel function and interactions with membrane lipids
- Gained experience in software tools and techniques for protein modelling and structure prediction, molecular dynamics simulations, and enhanced sampling simulations.

May 2018-Sept 2019 **National Research Council** Ottawa, ON

Undergraduate Researcher

- Used mass spectrometry and proteomics approaches to identify and compare immunoreactive proteins in strains of *Acinetobacter baumannii* and compare expression of MHC proteins in B cell lymphoma.
- Gained skills and experience in biochemistry, microbiology and immunoproteomics

Relevant Experience

Sept 2019-present **University of Ottawa** Ottawa. ON

Teaching Assistant

- Supervised laboratory sessions in molecular biology and biochemistry laboratory courses and demonstrated experimental techniques, evaluated student lab performance and presentations

Apr 2017-Sept 2017 **Apotex Inc.** Etobicoke, ON

Co-op Student / Intern, Global Quality Control

- Performed analysis of small-molecule pharmaceutical laboratory samples including in-process, finished products and stability samples using analytical instruments and established analytical procedures and techniques

Presentations and Awards

Ananchenko A., Dehez F., Nury, H., Baenziger J.E., (2022) Probing cholesterol and anionic lipid binding to the nicotinic acetylcholine receptor using MD simulations. Poster presentation delivered at 2022 Biophysical Society of Canada Annual Meeting, received poster award.

Ananchenko A., Musgaard M. (2021) Arachidonic Acid Interactions with Human Acid-Sensing Ion Channel 3. Oral presentation delivered at 2021 Virtual Symposium for Theoretical and Computational Chemistry in Canada, received award for top 4 speed talks.

Ananchenko A., Kinsley D., MacLean D., Musgaard M. (2021) Lipid Activation of Acid Sensing Ion Channels. Poster presentation delivered at 2021 Biophysical Society of Canada Annual Meeting, received poster award

Additional Skills	Computational Biology	Operating systems: Linux and Windows Programming languages: Python, R, bash, Tcl/Tk Molecular dynamics simulations: GROMACS, NAMD, Free energy perturbation, STRING, Steered/Targeted MD Molecular visualization software: VMD, ChimeraX, PyMol Protein structure and sequence databases: PDB, UniProt, AlphaFold
	Laboratory	Experience in tandem mass spectrometry for proteomics, western blotting, two-electrode voltage clamp and molecular biology techniques